

(Ga,In)(N,As,Sb) Solar Cells: N Incorporation using Novel
Precursor in MOVPE Growth and Solar Cell Characteristics

Dissertation

zur

Erlangung des Doktorgrades
der Naturwissenschaften
(Dr. rer. nat.)

dem

Fachbereich Physik
der Philipps-Universität Marburg

vorgelegt von

Eduard Sterzer, M.Sc.

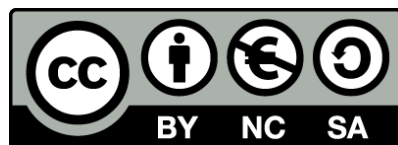
aus

Meshdureshensk, Russische Föderation

Marburg/Lahn, 2018

Vom Fachbereich Physik der Philipps-Universität Marburg
als Dissertation angenommen am: 20.07.2018
Erstgutachter: Prof. Dr. Kerstin Volz
Zweitgutachter: Prof. Dr. Carsten von Hänisch
Tag der mündlichen Prüfung: 24.07.2018
Hochschulkennziffer: 1180

Originaldokument gespeichert auf dem Publikationsserver der
Philipps-Universität Marburg
<http://archiv.ub.uni-marburg.de>



Dieses Werk bzw. der Inhalt steht unter einer
Creative Common
Namensnennung
Keine kommerzielle Nutzung
Weitergabe unter gleichen Bedingungen
3.0 Deutschland Lizenz.

Die vollständige Lizenz finden Sie unter:
<http://creativecommons.org/licenses/by-nc-sa/3.0/de/>

Danksagung (Acknowledgments)

An dieser Stelle möchte ich mich bei allen bedanken, die mir diese Promotion ermöglicht haben und allen, die mich auf diesem Weg unterstützt haben. Ganz besonderer Dank gilt dabei...

... Prof. Dr. Kerstin Volz, für die Möglichkeit die Promotion in Ihrer Arbeitsgruppe durchzuführen. Für die fruchtbaren, intensiven und zahlreichen Diskussionen. Für die sehr freundschaftliche und gleichzeitig professionelle Betreuung sowie für das Ermöglichen der zahlreichen Konferenzteilnahmen.

... Prof. Dr. Carsten von Hänisch, für die vielen Gespräche und Planungen neuer Präkursoren, sowie die Diskussionen über die Aufreinigungsmöglichkeiten der aktuellen Präkursoren.

... Prof. Dr. Martin Koch für die Bereitschaft meine Prüfungskommission zu vervollständigen.

... Prof. Dr. Gebhard für das freundliche Übernehmen der Aufgabe des Prüfungsvorsitzenden.

... Prof. Dr. Wolfgang Stolz, für die Möglichkeit immer einen Sachverhalt gemeinsam zu erörtern sowie auch die Bereitschaft einem stets unter die Arme zu greifen.

... der DFG für die Finanzierung meiner Arbeit innerhalb des Projects RTG1782 "Functionalization of Semiconductors".

... dem Techniker Team Stefan Reinhard, Celina Becker und Thomas Ochs, für das unermüdliche Kämpfen gegen die Querelen der Anlagen.

... dem Administrativem Team Elke Vaupel, Marina Koch und Isabelle Kimmel, für das schnelle und kompetente Beraten und Lösen aller Fragestellungen.

... meiner Arbeitsgruppe, für die gute Zusammenarbeit und die, schöne Zeit die wir zusammen verbracht haben.

... Lukas Nattermann, für die Wahnsinns-Zeit, die wir zusammen verbracht haben und für eine Freundschaft, die man selten wieder findet.

... Jürgen Belz, für manch legendäre Party sowie für die konstruktiven fachlichen Diskussionen.

... Christian Fuchs, für die fruchtbaren Diskussionen sowie die super Zeit in San Diego.

... dem Korrekturleser-Team Jürgen Belz, Christian Fuchs, Lukas Nattermann, India Watkins, Jan Oliver Öhlerich. Ganz besonderer Dank gilt hier Jürgen Belz, der sich durch die erste Version kämpfen musste.

... Peter Ludewig, Ulrike Häuplik, Antje Ruiz Perez, Johannes Zimmet und Michael Volk, für die bomben Stimmung im Labor und das konstruktive Zusammenarbeiten

... dem Spikeball Team Lennart Duschek, Jan Oliver Öhlerich, Andreas Beyer, Maximillian Widemann, Johannes Glowatzki und Bernard Epp, für den sehr witzigen Zeitvertreib.

... Oliver Massmeyer, Thilo Hepp und Damien Heimes, für die witzige und konstruktive Atmosphäre im Büro.

... Shalini Gupta, Shamail Ahmad, Pirmin Kükelhahn, Seyyed Firoozabadi, Johannes Glowatzki, David Krug und Manveer Munde, für die immer gute Stimmung in der Arbeitsgruppe.

... Benjamin Ringler und Christian Ritter, für das Synthetisieren und Aufreinigen der Präkursoren.

... dem Fraunhofer Institut für Solare Energiesysteme (ISE), für das Bereitstellen des *know-hows*, der Technik und der Räumlichkeiten.

... Jens Ohlmann, für ein fruchtbares und konstruktives Zusammenarbeiten. Für bereichernde Diskussionen und das Organisieren meiner Forschungswoche beim ISE.

... dem ISE Team, welches mich sehr freundlich aufgenommen und tatkräftig unterstützt hat.

... Carolin Woermann, Daniel Drolshagen, Maria Sverdlova, Tobias Stummer, Frederike Hübner, Sören Pygoch, Oxana Haid, Johann Haid, Jana Mayerose, Dennis Jagusiak, Annemarie Ullmann und Igor Kryukov, für die schönen Abende, die mich vom Schreiben der Arbeit abgelenkt haben.

... meinem Bruder Roman Sterzer und meiner Schwägerin Alina Sterzer, für die Möglichkeit mich auf der Baustelle zur Abwechslung mal körperlich zu betätigen.

... meiner gesamten Familie Sterzer und Kryukov, die mich in jeder Situation unterstützt haben und stets unterstützen.

... meiner Frau, Maria Sterzer, die immer und tatkräftig für mich da war. Für das Motivieren in schweren Zeiten und das Mitfreuen in Guten.

Ohne die Unterstützung all dieser Menschen wäre diese Promotion nicht möglich.

Vielen herzlichen Dank an jeden von euch!

*Das Ziel des Lebens ist der Weg zum Tod!
Carpe Diem, YOLO!*

Zusammenfassung (Summary in German)

Während der Energieverbrauch in Europa und den USA nur noch langsam wächst, steigt der Verbrauch in Schwellenländern wie China, Indien und Afrika stark an. Dabei steigt pro Jahr der Primärenergieverbrauch der gesamten Erdbevölkerung durchschnittlich um 1.8 %. Bis 2040 wird also ein Primärenergieanstieg von 40 % erwartet. Auf der anderen Seite, führen die hohen Umweltbelastungen durch den CO₂ Ausstoß der Automobile sowie ein erhöhtes Umweltbewusstsein bezüglich des Klimawandels zu immer größerem Interesse an Elektromobilität und alternativer Energiegewinnung. Aufgrund dessen, wird der Strombedarf voraussichtlich stärker wachsen als der Primärenergiebedarf. Während die CO₂ neutralen Atomkraftwerke erhebliche Probleme mit nuklearem Abfall und Endlagerung haben, ist die Kernfusion von der kommerziellen Nutzung noch 30-50 Jahre entfernt. Aufgrund dessen ist die Nachfrage nach erneuerbaren Energien in den letzten Jahren weiter gestiegen und wird auch in den nächsten Jahren steigen müssen, um den Energiebedarf nachhaltig decken zu können. Auch die Entwicklung im Bereich der Satelliten (Hochleistungs-Satelliten und steigende Zahl von Kleinsatelliten) führt zu höherem Strombedarf im Weltall und dementsprechend zu einem erhöhten Bedarf an Stromquellen mit hohen Leistungsdichten.

All die oben genannten Probleme und Herausforderungen können mithilfe von hocheffizienten Solarzellen gelöst werden. Ein Ansatz für solche ist eine Mehrschichtsolarzelle, die aus vier unterschiedlichen, übereinander gewachsenen Materialien besteht. Während das Wachstum drei dieser Materialien gut kontrolliert werden kann (GaAs, (Ga_{50%}In_{50%})P und Ge), sind die bei der Herstellung der nötigen 1 eV Schicht in MOVPE entstehenden Probleme noch nicht gelöst. Hier schließt die vorliegende Arbeit an und stellt einige Lösungsansätze für diese Probleme vor.

Diese Arbeit behandelt den gesamten Zyklus von der Synthese über die Untersuchung der Präkursoren beim Wachstum unterschiedlicher Halbleiter wie Ga(NAs), (GaIn)(NAs) und Ga(NAsSb) bis hin zur Herstellung von Solarzellen auf Basis des erworbenen Wissens.

Zu Beginn wurde ein neuer Präkursor, das DTBAA, im Vergleich zum etablierten Präkursor (UDMHy) beim Ga(NAs) Wachstum untersucht. Hierbei wurde festgestellt, dass die N Einbaueffizienz bei DTBAA um einen Faktor von 15 - 20 höher ist als beim UDMHy.

Weiterführende Experimente mit (GaIn)(NAs) zeigten auch hier eine 60 - 80 mal höhere N Einbaueffizienz im Vergleich zu UDMHy. Dieses Verhalten ist darauf zurückzuführen, dass der N Einbau im (GaIn)(NAs), welches mit UDMHy hergestellt wurde, extrem reduziert wird, wenn zusätzliches TMIn angeboten wird. Dieses Verhalten wurde in Verbindung mit DTBAA nicht beobachtet.

Der DTBAA Präkursor wurde im Verlauf dieser Arbeit sechs mal hergestellt, mit jeder Herstellung wurde eine Verbesserung der Präkursorqualität angestrebt. Aufgrund dessen wurde mit jedem neuen DTBAA Präkursor eine O und C Untersuchung an Ga(NAs) und (GaIn)(NAs) Strukturen durchgeführt. Diese zeigte eine deutliche Reduzierung des O Gehalts, während nur eine geringe Änderung des C Gehalts beobachtet wurde. Gleichzeitig wurde TMIn als eine Quelle für C Einbau identifiziert, da der C Gehalt sich vom Ga(NAs) zu (GaIn)(NAs) um den Faktor zwei erhöhte.

Es wurden daher weiterführende Experimente, mit dem Ziel den C Einbau zu reduzieren, durchgeführt. Hierzu wurde zum DTBAA gewachsenen (GaIn)(NAs) zusätzliches TBAs hinzugeführt, um mittels eines erhöhten V/III Verhältnisses den C Einbau zu reduzieren. Im Folgenden wurde der als C Quelle identifizierte TMIn Präkursor durch TIPIn, eine alternative In Quelle, substituiert. Beides führte zu einer C Reduktion in DTBAA gewachsenen (GaIn)(NAs) Schichten.

In (GaIn)(NAs) Schichten, die mit UDMHy hergestellt wurden, ist die Höhe des C Einbaus weiterhin ein Problem, welches die Qualität des Solarzellen-Materials reduziert. Diesbezüglich wurden Experimente mit zusätzlichem TMSb durchgeführt. In diesem Fall wurde TMSb als sogenannter *surfactant* verwendet, um den C Einbau zu reduzieren. Entgegen den Erwartungen wurde kein positiver Effekt des TMSbs auf den C Einbau beobachtet. Vielmehr wurde die Herstellung vom (GaIn)(NAs) Material noch schwieriger, da das zusätzliche TMSb den N Einbau stärker reduziert als bereits für TMIn beobachtet. Ein weiteres Material, welches mittels DTBAA hergestellt wurde, ist das Ga(NAsSb). Dieses Material wird als eine mögliche Alternative zu einer 1 eV (GaIn)(NAs) Schicht gitterangepasst auf GaAs diskutiert, konnte jedoch bis zur vorliegenden Arbeit nicht mit konventionellen Präkursoren mittels MOVPE hergestellt werden. In DTBAA gewachsenem Ga(NAsSb) wurde eine Reduktion des N Einbaus festgestellt, die jedoch um Größenordnungen niedriger war als in Verbindung mit UDMHy. Aufgrund dessen konnte zum ersten Mal eine 1 eV Ga(NAsSb) Schicht gitterangepasst auf GaAs hergestellt werden. Leider zeigten die SIMS Untersuchungen einen hohen O Einbau, der die Qualität der optoelektrischen Eigenschaften des Halbleiters reduzierte. Weitere Experimente müssen mit einem gut aufgereinigten Präkursor folgen, um das Potential des Ga(NAsSb) Materials mit (GaIn)(NAs) vergleichen zu können.

Mit dem in dieser Arbeit erzielten Ergebnissen wurden fünf unterschiedliche Solarzellen hergestellt, zwei basierend auf UDMHy und drei auf DTBAA. Dabei wurde festgestellt,

dass mit UDMHy hergestellte Solarzellen stets die besseren Charakteristika aufwiesen. Das ist darauf zurückzuführen, dass der O Einbau in den DTBAA basierten Solarzellen um Größenordnungen höher ist. Innerhalb der mittels DTBAA hergestellten Solarzellen führte der reduzierte C Einbau nur zu geringfügigen Veränderungen, da die Materialqualität aufgrund des vorhandenen O stark leidet.

Durch die Simulation der EQE konnte die aktive Schichtdicke sowie Diffusionslänge der Minoritätsladungsträger abgeschätzt werden. Hierzu wurden die besten Solarzellen, eine basierend auf UDMHy und die andere basierend auf DTBAA, ausgewählt und gegenübergestellt. Dabei wurde festgestellt, dass die UDMHy Solarzelle einen aktiven Bereich von ca. 400 nm und eine Diffusionslänge von ca. 300 nm aufweist. Im Vergleich dazu weist die mittels DTBAA hergestellte Solarzelle eine aktive Dicke von nur 180 nm und eine Diffusionslänge von nur 60 nm auf.

Experimente mit TIPIn anstelle von TMIn zeigten, dass die V_{OC} der damit hergestellten (GaIn)(NAs) Solarzellen erhöht werden kann. Gleichzeitig wurde eine Reduktion der Stromdichte beobachtet. Diese kann jedoch mit dem fluktuierenden In Gehalt, der mit TIPIn beobachtet wurde, erklärt werden.

Die Ergebnisse dieser Arbeit zeigen, dass der DTBAA Präkursor ein hohes Potential hat die Qualität des (GaIn)(NAs) Wachstums zu verbessern und den etablierten Präkursor UDMHy zu ersetzen. Für einen großflächigen Einsatz von DTBAA muss zunächst der O Einbau durch den Präkursor um zwei bis drei Größenordnungen reduziert werden. In Kombination mit TIPIn und TBAs kann ein sehr niedriger C Einbau realisiert werden. In diesem Fall müsste die Ursache der In Fluktuation evaluiert und behoben werden.

Das Ga(NAsSb), eine Alternative zu (GaIn)(NAs), wurde erstmals in der MOVPE durch DTBAA ermöglicht. Weitere Experimente mit diesem Material sowie die Herstellung von Ga(NAsSb) und (GaIn)(NAsSb) Solarzellen müssen in Zukunft mit hochreinem DTBAA durchgeführt werden, um das Potential des Präkursors auszuschöpfen und einen realen Vergleich zu etablierten (GaIn)(NAs) Solarzellen zu ermöglichen.

Contents

Danksagung (Acknowledgments)	i
Zusammenfassung (Summary in German)	v
1 Introduction	1
2 Novel Precursors and Investigated Materials	3
2.1 Synthesis of Novel Precursors	3
2.1.1 Di-Tertiary-Butyl Arsano Amine ($t\text{Bu}_2\text{AsNH}_2$, DTBAA)	4
2.1.2 Di-Tertiary-Butyl Antimony Tertiary-Butyl Amine ($t\text{Bu}_2\text{SbN(H)tBu}$, DTBSbTBA)	5
2.1.3 Tri-Iso-Propyl Indium ($i\text{Pr}_3\text{In}$, TIPIn)	6
2.2 Fundamentals of Investigated Materials	7
2.3 Fundamentals of Solar Cells	14
3 Experimental Methods	23
3.1 Metalorganic Vapor Phase Epitaxy (MOVPE)	23
3.2 High Resolution X-Ray Diffraction (HR-XRD)	26
3.3 Atomic Force Microscope (AFM)	28
3.4 Photoluminescence (PL) Spectroscopy and Rapid Thermal Annealer (RTA)	28
3.5 Hall and Electrochemical Capacitance Voltage (ECV) Measurements	30
3.6 Secondary Ion Mass Spectrometry (SIMS)	31
3.7 Solar Cell Fabrication and Characterization	31
4 Achievements with Conventional and Alternative Precursors	33
4.1 MOVPE Growth of Ga(NAs) Structures	33
4.2 MOVPE Growth of (GaIn)(NAs) Structures	35
4.2.1 (GaIn)(NAs) Growth with DTBAA	36
4.2.2 Antimony as <i>Surfactant</i> for UDMHy based Growth	38
4.2.3 Carbon Reduction in (GaIn)(NAs) with TIPIn and TBAs	43
4.3 MOVPE Growth of Ga(NAsSb) Structures	50
4.3.1 DTBAA grown Ga(NAsSb)	50

4.3.2	DTBSbTBA grown Ga(NAsSb)	51
5	(GaIn)(NAs) Solar Cell Structures	55
6	Summary and Outlook	63
7	Publications	65
7.1	Efficient nitrogen incorporation in GaAs using novel metal organic As-N precursor di-tertiary-butyl-arsano-amine (DTBAA)	65
7.2	Novel nitrogen/gallium precursor [Ga(bdma)H ₂] for MOVPE	76
7.3	(GaIn)(NAs) Growth Using Di-Tertiary-Butyl-Arsano-Amine (DTBAA) .	84
7.4	1 eV Ga(NAsSb) Grown in MOVPE Using Di-Tertiary-Butyl-Arsano-Amine (DTBAA)	90
7.5	Further Publications	100
	Bibliography	103
	List of abbreviations	119

CHAPTER 1

Introduction

The energy consumption of the earth's population is greatly increasing¹. While the energy use in MWh/capita value is around 40 in the EU and 80 in the USA, China (18 MWh/capita), India (6 MWh/capita) and Africa (7 MWh/capita) still have a lower energy consumption². Given that around half of the world's population is based in these latter three areas and that the economic growth in China and India in particular is very rapid, the need for higher energy will grow significantly in the future. The average growth of global primary energy consumption over a ten year period is 1.8 %³. Consequently, the demand for primary energy is expected to increase worldwide by around 40 % until 2040. At the same time, climate change as well as air pollution in cities are becoming more dramatic due to fossil fuels. The development in the automotive industry towards electric cars will increase the demand for electricity even more. All these developments urge for environmentally sustainable energy sources. Nuclear energy, as a CO_2 neutral energy supply has major drawbacks: nuclear waste disposal, which needs to be stored costly, and no deep geological repository has been found as of today. The potentially less harmful fusion reactor is still 30 - 50 years away from commercial use^{4,5}. Therefore, a sustainable energy supply must be developed on the basis of renewable energies like wind power, hydropower, bio energy and solar energy.

Additionally, development in the satellite industry, especially research satellites as well as the Mars expeditions, demand an energy source with a high energy production to weight ratio.

Hence, the development of commercially competitive solar cells with conversion efficiencies of around 50 % would address the environmental sustainability issues as well as the extraterrestrial energy supply issue. One approach is the fabrication of a four junction solar cell consisting of 0.7, 1, 1.42 and 1.85 eV materials⁶. Gallium indium nitride arsenide ((GaIn)(NAs)) as well as gallium nitride arsenide antimonide (Ga(NAsSb)) are the two materials discussed as a 1 eV material. So far, no sophisticated solar cell growth process was achieved with metalorganic vapor phase epitaxy (MOVPE), as precursor induced interactions and incorporation of parasitic atoms deteriorate the (GaIn)(NAs) as well

as Ga(NAsSb) material quality. The nitrogen (N) incorporation in (GaIn)(NAs) was observed to decrease by 75 % in comparison with gallium nitride arsenide (Ga(NAs)) when alloyed with 8% indium (In)⁷. The N incorporation decrease is even more dramatic when alloying Ga(NAs) with antimony (Sb). This is the reason why no 1 eV Ga(NAsSb) material was realized by MOVPE as of yet. Therefore, novel precursors, namely di-tertiary-butyl arsano amine (DTBAA) and di-tertiary-butyl antimony tertiary-butyl amine (DTBSbTBA) were synthesized by the chemistry department of the Philipps-Universität, Marburg and investigated in this work to evaluate the potential for dilute N growth.

This thesis is structured as follows: the precursor synthesis and fundamentals of the materials and solar cells will be described in Section 2. In Section 3 the experimental investigation methods and solar cell investigation procedure will be discussed. The results of this work will focus on the 1 eV material (GaIn)(NAs) and will also discuss the growth of Ga(NAsSb) material. The growth of Ga(NAs) with DTBAA will be presented in Section 4.1, followed by the (GaIn)(NAs) growth in Section 4.2. Here, several approaches will be discussed: DTBAA grown (GaIn)(NAs), (GaIn)(NAs) growth with Sb as a *surfactant* and tri-iso-propyl indium (TIPIn) for carbon (C) incorporation reduction. Section 4.3 focuses on Ga(NAsSb) grown with either DTBAA or DTBSbTBA. Finally, solar cell results will be discussed in Section 5.

As this work is written in a cumulative form the published data will be summarized only. Corresponding sections are marked with an asterisk (*). Unpublished data is presented in more detail.

CHAPTER 2

Novel Precursors and Investigated Materials

Chapter 2 will give an overview of the investigated materials and explain the demand for novel precursors, which have been investigated in this work.

2.1 Synthesis of Novel Precursors

The most recent important innovation in precursor development for III/V semiconductor growth was the invention of tertiary-butyl arsine ($t\text{BuAsH}_2$, TBAs) in 1987⁸. This precursor step by step substitutes arsine (AsH_3). TBAs is not only less toxic^{9–11}, but it also decomposes at growth temperatures below 650 °C,^{12–14} enabling arsenic (As) based low temperature MOVPE.

Challenging materials like dilute nitrides require special growth conditions such as low temperatures going along with low intrinsic doping densities as well as high growth rates for commercial use. Commercial precursors do not always meet the demands for these specific growth conditions. The substitution of ammonia (NH_3) by 1,1-dimethylhydrazine ($\text{H}_2\text{NN}(\text{CH}_3)_2$, UDMHy) shifted the investigation focus on N related problems, such as unintentional C incorporation and low N incorporation efficiency. Only small progress was achieved in this field as of yet. A further development in the search for a solution for N related problems is the invention of novel N precursors. In the past, several precursors like hydrazine, tertiary-butyl amine, n-Butyl amine, di-isobutyl amine, allyl amine, cyclopentyl amine, aniline, benzyl amine, nitrogen trifluoride were investigated. However, no advantages in comparison with the established N precursor was found^{12,13,15–20}. Tertiary-butyl hydrazine ($t\text{BuNHNH}_2$, TBHy), which has an N incorporation efficiency five times higher than UDMHy⁷, is discussed as a potential N precursor. Unfortunately the purity requirements have not been fulfilled so far¹⁷. Therefore, novel and innovative precursors for III/V materials are still of great interest, as the choice of the precursor strongly affects the growth characteristics and ultimately the material quality²¹.

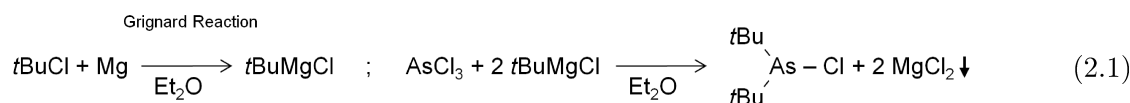
The novel precursors should be liquid and show a sufficient vapor pressure, which should optimally be higher than 10 mbar for group V and higher than 1 mbar for group III ele-

ments^{22–25}. For lower vapor pressures, different supply techniques like liquid injection^{26–29} are discussed. Further challenges for the precursor synthesis include the demand for an enormously high purity (>9N). This high level of purity must go along with high stability at room temperature while ensuring full decomposition at rather low growth temperatures in a range between 400 and 600 °C. Furthermore, economical aspects must be taken into account regarding the production costs, which include the synthesis, purification and chemical waste disposal. In summary, precursor design and synthesis is challenging in terms of the choice of ligands, purification requirements and economical aspects. We tackled these problems, in cooperation with the research group of Prof. Dr. von Hähnisch and Dr. Benjamin Ringler from the chemistry department of the Philipps-Universität Marburg. While they carried out the synthesis and purification of DTBAA and DTBSbTBA molecules, our working group was investigating the growth characteristics as well as the potential for the MOVPE growth of these precursors.

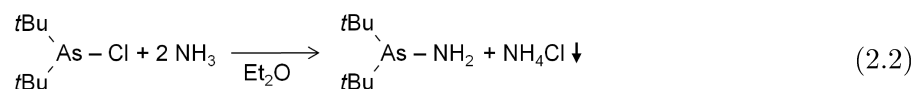
2.1.1 Di-Tertiary-Butyl Arsano Amine ($t\text{Bu}_2\text{AsNH}_2$, DTBAA)

For the synthesis of the novel N precursor, di-tertiary-butyl arsano amine ($t\text{Bu}_2\text{AsNH}_2$, DTBAA), depicted in Figure 2.1 a), firstly tertiary-butyl ($t\text{Bu}$) groups need to be attached to commercially available AsCl_3 . The so-called *Grignard Reaction*³⁰ shown on the left-hand side of Equation 2.1 is utilized to synthesize the tertiary-butyl magnesium chloride ($t\text{BuMgCl}$), which is needed for further alkylation. Therefore, magnesium (Mg) powder and diethyl ether (Et_2O) are placed in a flask equipped with a dropping funnel and a condenser. The tertiary-butyl chloride ($t\text{BuCl}$), which serves as a $t\text{Bu}$ -source, is dissolved in Et_2O and added drop-wise via the dropping funnel over a period of 3.5 hours. The Mg inset between the $t\text{Bu}$ group and the chloride results in the formation of $t\text{BuMgCl}$.

In the next step, a two-fold substitution of arsenic trichloride (AsCl_3) is carried out. Therefore, the Grignard solvent was added over a period of 3 h drop-wise to the AsCl_3 - Et_2O solution at 0 °C. This suspension was stirred for 13 h and slowly warmed to room temperature within 5 hours. Hereby, di-tertiary-butyl arsano chloride ($t\text{Bu}_2\text{AsCl}$) and magnesium chloride (MgCl_2) are formed (cf. Equation 2.1 right). The solid MgCl_2 is filtrated off in order to obtain a clear solution of $t\text{Bu}_2\text{AsCl}$ in Et_2O . The solvent was removed under reduced pressure conditions. $t\text{Bu}_2\text{AsCl}$ was obtained as a colorless oil after purification by fractional distillation with a yield of 77 %.



For the ammination, $t\text{Bu}_2\text{AsCl}$ is dissolved in Et_2O and cooled down to 0°C . An excess of NH_3 is passed through the solution. The NH_3 reacts with $t\text{Bu}_2\text{AsCl}$ and forms DTBAA as well as ammonium chloride (NH_4Cl):



The NH_4Cl is filtered off and the Et_2O removed under reduced pressure conditions. In the next step the DTBAA is purified by fractional distillation. A further distillation is done in order to bottle the precursor directly into a bubbler (cf. Figure 3.1). Detailed descriptions of the synthesis were published by Scherer et al.³¹, Sterzer et al.³² as well as Ringler et al.³³.

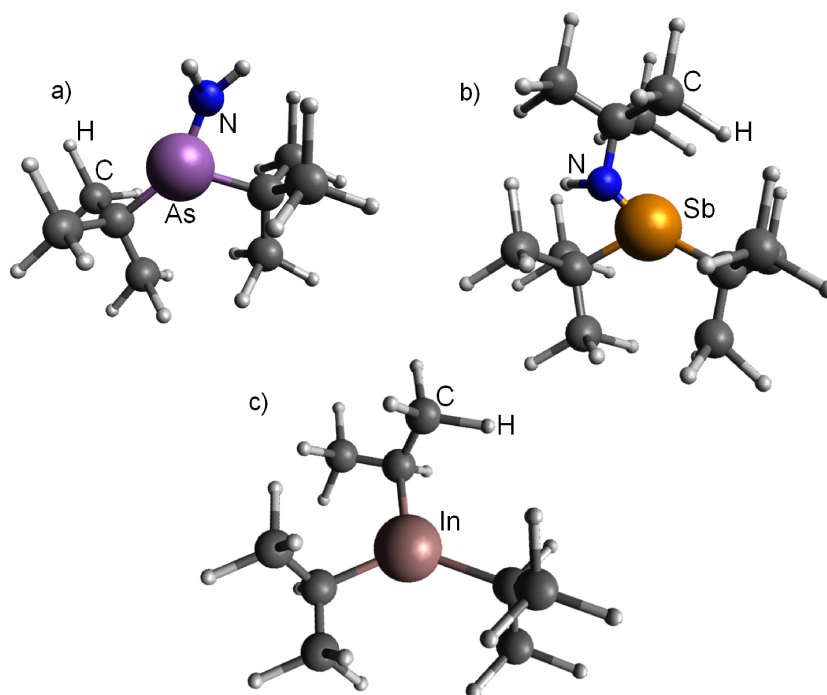
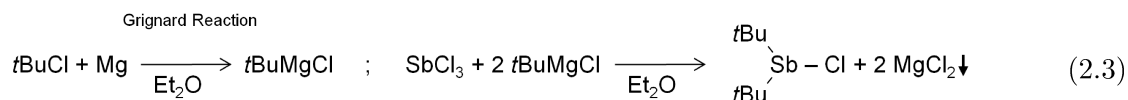


Figure 2.1: Schematic 3D representation of the three alternative molecules utilized in this work: a) DTBAA b) DTBSbTBA c) TIPIn

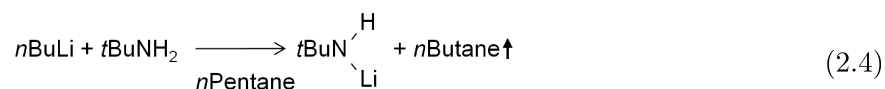
2.1.2 Di-Tertiary-Butyl Antimony Tertiary-Butyl Amine ($t\text{Bu}_2\text{SbN(H)tBu}$, DTBSbTBA)

To achieve the synthesis of di-tertiary-butyl antimony tertiary-butyl amine ($t\text{Bu}_2\text{SbN(H)tBu}$, DTBSbTBA) (depicted in Figure 2.1 b)), the reactant di-tertiary-butyl antimony chloride ($t\text{Bu}_2\text{SbCl}$) must be synthesized.

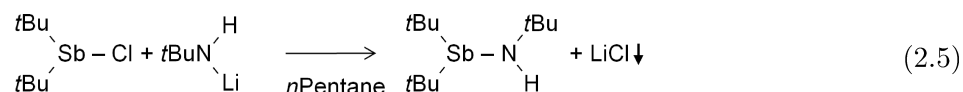
This synthesis is performed similarly to the $t\text{Bu}_2\text{AsCl}$ reactant described in Section 2.1.1. The detailed synthesis is described in more detail by Benjamin Ringler^{33,34}.



The tertiary-butyl amine ($t\text{BuNH}_2$) does not react with $t\text{Bu}_2\text{SbCl}$, and a metallisation of the amine must be performed. Hereby, normal-butyl lithium ($n\text{BuLi}$) dissolved in normal-pentane ($n\text{Pentane}$) is added drop-wise to a $t\text{BuNH}_2$ solution which is at -20°C , diluted with $n\text{Pentane}$, leading to $t\text{BuNLi}$ and gaseous $n\text{Butane}$:



In the following step, $t\text{Bu}_2\text{SbCl}$ dissolved in $n\text{Pentane}$ is added drop-wise to the $t\text{BuNLi}$ - $n\text{Pentane}$ solution at 0°C . This leads to DTBSbTBA and lithium chloride (LiCl) elimination:



Lastly, the LiCl is filtered off, and the $n\text{Pentane}$ is removed under reduced pressure. Purification by fractional distillation yields DTBSbTBA as a colorless oil with a yield of 81 %.

2.1.3 Tri-Iso-Propyl Indium ($i\text{Pr}_3\text{In}$, TIPIIn)

The synthesis of tri-isopropyl indium ($i\text{Pr}_3\text{In}$, TIPIIn) (Figure 2.1 c)) is also performed via Grignard Reaction. In this case, iso-propyl chloride ($i\text{PrCl}$), Mg and Et_2O are utilized to synthesize the iso-propyl magnesium chloride ($i\text{PrMgCl}$). The $i\text{PrMgCl}$ is subsequently added drop-wise to indium(III) iodide (InI_3), dissolved in Et_2O . This reacts with TIPIIn and magnesium chloride iodide (MgClI) elimination:



The solids were filtered off, and the purification of TIPIIn is carried out by distillation. Detailed syntheses are described by Neumueller³⁵ and Hoffman³⁶.

2.2 Fundamentals of Investigated Materials

In this section, an overview of the investigated materials will be given. Firstly, the physical background will be discussed in order to explain fundamentals, which are required for a detailed understanding of the following sections. Further sections will introduce each material system individually, beginning with the host material gallium arsenide (GaAs) and subsequently discussing the effects of the incorporation of In, N and Sb into the host matrix.

All materials investigated in this thesis are of a crystalline zinc blende structure. This structure consists of two face centered cubic (fcc) crystals shifted by $(\frac{1}{4}, \frac{1}{4}, \frac{1}{4})$ of the lattice constant in respect to each other^{37–39}. Each of these fcc structures is occupied either by a group III or a group V atom. In contrast to the energy states in a single atom, the energy levels around the valence electrons in a periodically arranged crystal are not discrete. The periodicity of the atoms in combination with valence electron interaction due to small distance leads to a splitting of the discrete energy levels and therefore to the formation of a quasi continuous band of energy states. These so-called energy bands are one of the main characteristic of crystals^{37–39}. The highest band which is occupied by electrons at $T = 0^\circ\text{C}$ is called the valence band (based on valence electron), whereas the subsequent band is referred to as the conduction band. The configuration of these two bands defines the optical and electrical properties of a crystal. The energy gap between the valence and conduction band is referred to as band gap. An other important value for describing a semiconductor is the Fermi Level^{37–39} (E_{Fermi}). It is defined by the energy up to which all energy states are filled at $T = 0\text{ K}$. Hereby, Fermi Dirac statistics^{40,41} describe the energy distribution dependent on temperature, taking into account the density of states. In a perfect crystal, no energy states are available between the bands. Nevertheless, crystal defects and impurities (e.g. O, C) result in localized energy states within the band gap. Consequently, the E_{Fermi} as well as the material properties are changed.

Materials with a fully filled valence band and an empty conduction band are either semiconductors ($E_{gap} \lesssim 4\text{ eV}$) or insulators ($E_{gap} \gtrsim 4\text{ eV}$). If the valence band is not fully filled or the conduction band overlaps with the valence band, the material is considered to be a metal.

The left part of Figure 2.2 shows an overview of the band gap in real space with some doping and defect energy states. A shallow defect level is located in close proximity to the band gap edges and strongly affects the semiconductor electron and hole transport properties. This effect is used to tailor the electrical properties of semiconductors and is referred to as doping. When substituting an atom with an atom of higher valency, the excess electron has only a weak bond to the positively charged atomic nucleus. This weakly bound electron needs only a small amount of energy to be excited to the conduction band. This so-called n-doped semiconductor has a defect energy level close to the conduction band. Semiconductors which are p-doped have an additional energy level in the band

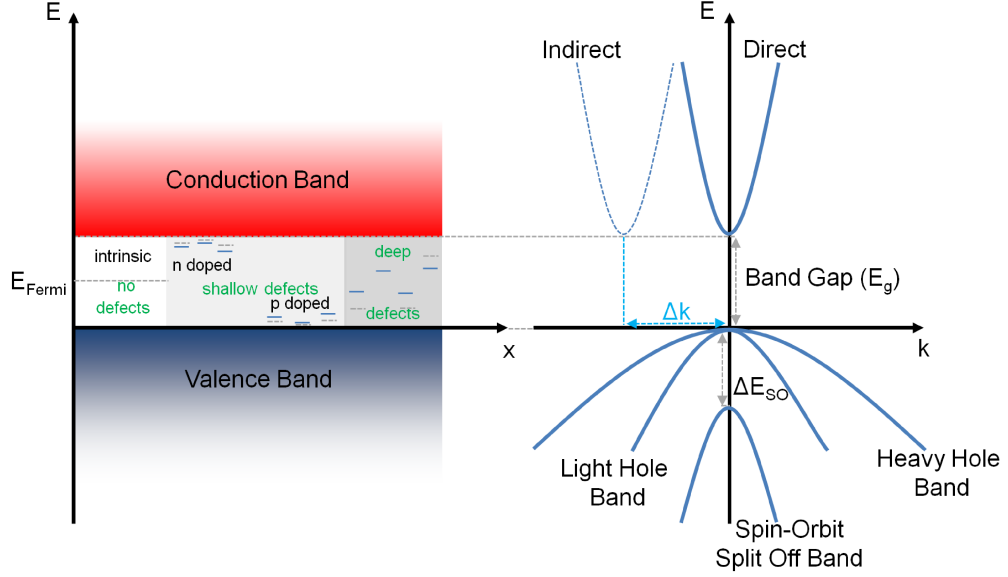


Figure 2.2: Band structure in real as well as reciprocal space. Several defect states are shown in the real space plot for a schematic overview.

gap close to the valence band edge. This kind of doping is achieved by substituting a host atom with an atom of lower valency, inducing an absence of an electron, also referred to as hole, and therefore an energy state within the band gap. Typical doping densities are in the range of 10^{16} - 10^{18} atoms/cm³, whereas the typical material densities are around 10^{22} atoms/cm³. Deep level defects such as oxygen (O) in GaAs are close to the band gap center and act as non-radiative recombination centers^{42–46}. Parasitic C incorporation occurs in different material systems due to the nature of MOVPE. This effect was investigated in detail for GaAs by Jiang et al.⁴⁷ as well as other groups^{48–51}.

The band structure in reciprocal space^{38,52,53}, which is depicted in Figure 2.2 on the right-hand side, contains additional information on a semiconductor. The relative location of the conduction band maxima and minima defines the semiconductor as either direct or indirect. In a direct semiconductor the absolute valence band maximum and the absolute conduction band minimum are both at $k = 0$ (Γ point). If the absolute conduction band minimum is not allocated at $k = 0$ (dotted parabola), additional phonons (Δk) are needed for the electron transition to fulfill momentum conservation^{54,55}. This in turn, decreases the light matter interaction probability in comparison with a direct semiconductor because an additional quasi particle is required for this process. Therefore, direct semiconductors such as GaAs, gallium antimonide (GaSb) and indium arsenide (InAs) are more favorable in terms of optoelectronics. Silicon (Si), germanium (Ge) or gallium phosphide (GaP) are examples for indirect semiconductors. The curvature of the bands in the vicinity of $k = 0$ is approximated by the parabolic function $E = \frac{\hbar^2 k^2}{2m^*}$. This concept takes the environment

of the electrons in the semiconductor into account and combines these influences into the effective mass. The effective electron mass is usually lower than the effective hole mass. This can be estimated by the curvature in the vicinity of $k = 0$ of the bands plotted in k -space. The effective electron mass increases with higher band gap⁵⁶, as seen in Table 2.1. Due to a higher electron density and therefore more interactions, the band structure of the filled valence bands is more complex than the structure of the conduction band^{55,56}. On the right-hand side of Figure 2.2, the heavy hole band has a lower curvature in comparison with the light hole band, indicating a higher effective mass for the heavy hole band. A further band is the so-called spin-orbit split off band. This band emerges from the electron spin interaction with the atomic nucleus and therefore strongly depends on the atomic mass, which is connected to the atomic number⁵⁷.

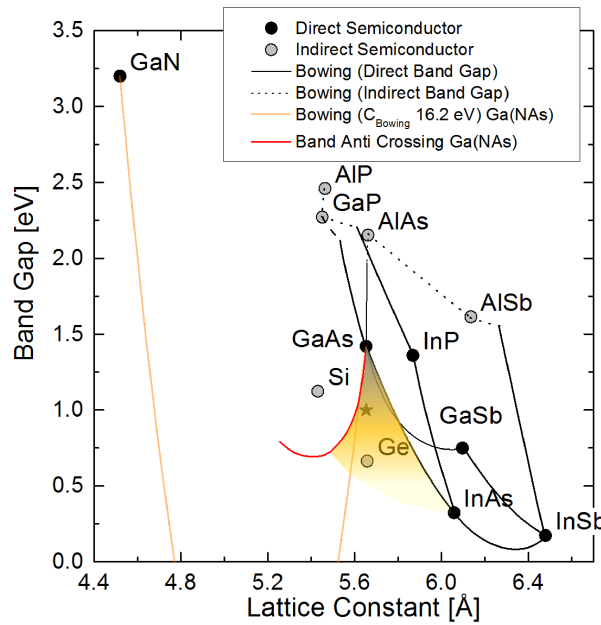


Figure 2.3: Band gap vs. lattice constant plot for direct and indirect monocrystallin and V/III semiconductors. Lines represent the ternary combination possibilities of the connected binary materials. Dotted line stands for indirect and straight line for direct semiconductor. The BAC calculation for a fix band bowing is shown in orange. Real band gap vs. lattice constant behavior is shown in red.

Gallium Arsenide

Since all experiments discussed in this thesis are based on the **gallium arsenide (GaAs)** host matrix, an insight into this material is given in the following section. GaAs is a widely used III/V semiconductor with a direct band gap of 1.422 eV and a lattice constant of 5.65325 Å (zink blende structure) at room temperature. Several applications in the optoelectronic field, i.e. light emitting diodes (LEDs) and light amplification by the stimulated emission of radiations (LASERS)⁵⁸ or solar cells⁵⁹, were realized using GaAs as a host material between 1962 and 1970. Furthermore, GaAs is utilized in various kinds

of transistors^{60–62}. Due to its popularity and the fact that the manufacturing process is established at very high quality, GaAs wafers are broadly available for a subsequent overgrowth with different kinds of III/V materials. A detailed description of GaAs can be found in literature⁶³. This work focuses on Ga(NAs), gallium indium nitride arsenide ((GaIn)(NAs)) and Ga(NAsSb) growth on GaAs.

Compound semiconductors, GaAs alloys

When alloying GaAs with InAs or gallium nitride (GaN), the characteristics of these materials begin to intermix. While the lattice constant can be linearly interpolated between two binary materials (Vegard's Law⁶⁴), band structure changes are more complex (cf. Eq 2.7). Figure 2.3 shows the band gap vs. lattice constant plot. This graph holds a tremendous amount of information for the binary III/V materials as well as their ternary alloys. Direct semiconductors are represented with solid lines, indirect ones with dotted lines. Selected material properties are summarized in Table 2.1, including the band gap values and lattice constants which are needed to calculate the characteristics of a ternary compound. The **gallium indium arsenide ((GaIn)As)** material is realized by combining GaAs and InAs. $(Ga_{1-x}In_x)As$ material with an $x(In)$ of 0.01 exhibits properties close to GaAs. The band gap and lattice constant shift towards the InAs characteristics with a higher content of In. As mentioned above, the band gap does not change linearly with the composition, as seen in Equation 2.7. Therefore, the connecting lines in Figure 2.3 between the binary materials are bent.

$$E_{gap}(M_{1-x}^A M_x^B) = (1-x)E_{gap}(M^A) + xE_{gap}(M^B) - x(1-x)C_{bowing} \quad (2.7)$$

Binary Material	GaAs	InAs	GaN	GaSb
E_{gap} [eV]	1.422	0.354	3.4	0.727
$a_{lattice}$ [Å]	5.65325	6.0583	4.52	6.0959
m_e^* [m_0]	0.067	0.026	0.13	0.039
m_h^* [001] [m_0]	0.350	0.333	0.8	0.250
m_l^* [001] [m_0]	0.090	0.027	0.21	0.044
μ_e [$cm^2 V^{-1} s^{-1}$]	$\lesssim 8500$	$\lesssim 40000$	< 1000	$\lesssim 3000$
μ_{hh} [$cm^2 V^{-1} s^{-1}$]	$\lesssim 400$	$\lesssim 500$	< 200	$\lesssim 1000$

Table 2.1: Semiconductor properties from Vurgaftman⁶⁵ and Ioffe Institute⁶⁶

Consequently, C_{bowing} is an empirical material parameter which must be determined experimentally for each material combination. C_{bowing} was determined to be 0.45 - 0.5 eV⁶⁵ for (GaIn)As. The E_{gap} decreases, while $a_{lattice}$ increases with higher In content. An In content of around 8 % is needed for the solar cell material in order to reduce the E_{gap} by 130 - 140 meV, leading to an E_{gap} of around 1.28 - 1.29 eV. Figure 2.4 depicts the

valence and conduction band bowing independently. (GaIn)As shows only small changes in the valence band but has a rather strong influence on the conduction band.

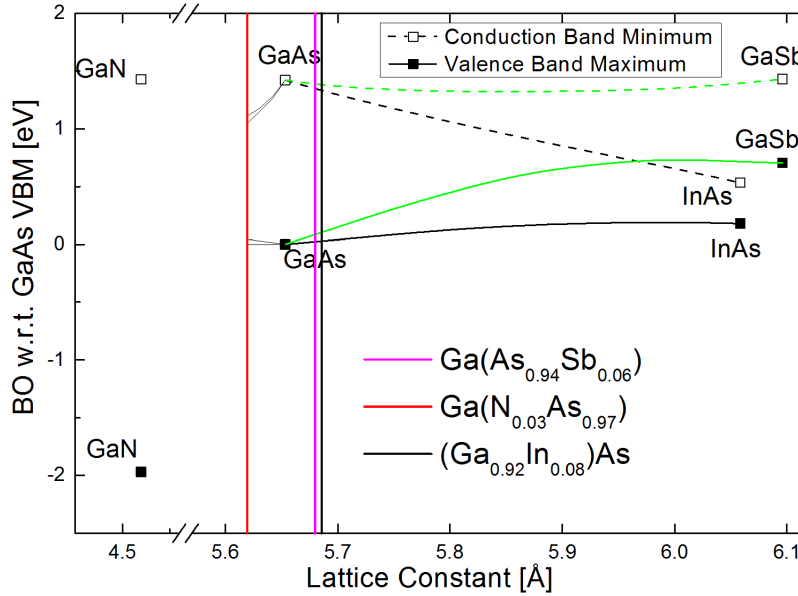


Figure 2.4: Valence and conduction band shift dependent on to the compositionally induced lattice constant for the materials of interest. Y-axis represents the band offset values with respect to GaAs valence band maximum. Sb has a stronger effect on the valence band than In, while In has a stronger effect on the conduction band. The N affects mostly the conduction band due to BAC. Data obtained from Vurgaftman⁶⁵.

The **gallium nitride arsenide (Ga(NAs))** is realized by alloying GaAs with N. In a first order approximation, Ga(NAs) material would have an increasing band gap with higher N content. Experiments, however, have shown the opposite behavior. Several groups were investigating Ga(NAs) to determine the C_{bowing} . First experimental constants were determined to be in the range of 11 - 25 eV⁶⁷⁻⁷³, leading to an unobserved negative band gap. This transition is shown in Figure 2.3 for $C_{bowing} = 16.2$ eV to be between 11 % and 77 % N (orange line). The description of N to be an isoelectric impurity, leads to a more precise theory. As the lattice constant of GaN is small in comparison with the GaAs lattice, strong local strain fields are introduced in dilute nitrides. Furthermore, the energy level of N in GaAs is calculated to be around 230 meV above the conduction band edge^{74,75} (depicted schematically in Figure 2.5). This localized energy state (broad in the reciprocal space) then interacts with the GaAs conduction band and leads to a strong band gap reduction for dilute nitrides. The so-called band anti crossing (BAC) theory^{74,76-86} is in a good agreement with the experiments for up to 15 % N. The BAC trend is shown in Figure 2.3 as a red line. Figure 2.5 schematically shows the influence of the N energy state on the GaAs band structure. The distance between conduction band minimum and the localized state within the band is important as this distance affects the so-called coupling parameter (β), a value which defines how strong the interaction and

therefore, the band gap reduction, is. The coupling matrix element V_{NM} depends on the N content x ^{82,87,88}, which explains the N related band gap reduction.

$$V_{NM} = \beta x^{\frac{1}{2}} \quad (2.8)$$

Due to the repulsion of the dispersionless N energy level and the conduction band, two bands occur: E_+ and E_- .

$$E_{\pm} = \frac{E'_N + i\Gamma_N + E_M}{2} \pm \frac{\sqrt{(E'_N + i\Gamma_N - E_M)^2 + 4\beta^2 x}}{2} \quad (2.9)$$

Zhang et al.⁸⁹ as well as Hai et al.⁹⁰ observed an unexpected strong increase of effective mass for N contents in the area of 1.5 %. This effect is connected to the dispersionless defect level of N. For a 3 % Ga(NAs) sample, the band gap reduction is around 270 meV leading to a band gap width of around 1.1 eV and a tensile strain with respect to GaAs. This material is then used in combination with 8 % (GaIn)As to achieve a 1 eV material. Figure 2.4 shows the Ga(NAs) band offsets to GaAs. There is no consensus on the exact band offsets for Ga(NAs) in the literature. Therefore, a maximum and minimum band offset is given. Nevertheless, one clearly sees the strong reduction in the conduction band due to BAC and rather small changes in the valence band.

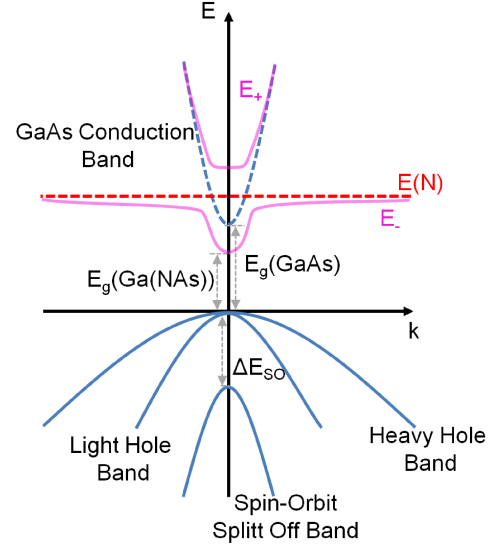


Figure 2.5: Schematic representation of the band anti crossing. The energy level of N is allocated within the GaAs conduction band. Due to interaction, a band gap splitting occurs.

The combination of two ternary materials allows for the tunability of band gap and lattice constant independently. In the case of **gallium indium nitride arsenide ((GaIn)(NAs))**, one combines the properties of (GaIn)As and Ga(NAs). In Figure 2.3 the orange filled area schematically represents the properties achievable with (GaIn)(NAs). The quaternary material fulfills the requirements of a 1 eV material lattice matched to GaAs or Ge depicted as a star in Figure 2.3. In quaternary materials, the band structure calculation is more complex. The coupling parameter β depends on the semiconductor host material defining the E_{\pm} separation. As seen in Figure 2.4, $(Ga_{0.92}In_{0.08})As$ has a lower conduction band in comparison with GaAs. This leads to a lower β and therefore, to a reduced E_{\pm} splitting in (GaIn)(NAs)⁹¹. To achieve the 1 eV (GaIn)(NAs) solar cell material lattice matched to GaAs, a composition

of 8 % In and 3 % N is needed^{92,93}. First (GaIn)(NAs) structures were realized in the mid-nineties^{94–97}. Since then, the MOVPE and molecular beam epitaxy (MBE) communities are improving growth conditions to increase the material quality^{98–101}. Typically, MBE grown (GaIn)(NAs) solar cells reveal higher conversion efficiencies^{102–105}. Secondary Ion Mass Spectrometry (SIMS) measurements revealed the C incorporation in MOVPE grown samples to be in the range of 10^{17} - 10^{18} atoms/cm³, whereas no C was detected in MBE grown samples ($<10^{16}$ atoms/cm³). This unintended C incorporation occurs through the presence of residual C groups, which exist naturally in MOVPE reactors. The C atom substitutes a group V atom and therefore, heavily p-dopes the host material.

For a functioning solar cell, a p-n junction is required (cf. Section 2.3). Therefore, high quality n-doped (GaIn)(NAs) material must be grown. This growth however, turns out not to be trivial, as the intrinsic p-doping must be compensated in the first place before the (GaIn)(NAs) material shows n-doping. This huge dopant density affects the free mean path of the carriers and in turn reduces the electric properties of the material. Furthermore, dilute nitrides show N related defects in MBE and MOVPE grown samples^{106–109}, where $N_{As} - As_{Ga}$ defects as well as N interstitials (10^{19}) are present^{110–112}. N - N defects are present as well, inducing deep level defects^{113–115}. Post growth *annealing* was found to improve the crystal quality, activating the dopants and improving the optical properties^{116–119}.

Another approach to improving the crystal quality is the *surface active agent* (**surfactant**) effect. In this approach, the surfactant material is not intended to be incorporated into the crystal. Instead, it segregates to the surface, substituting atoms, and affects the surface reconstruction^{120–122}. This thin film also induces an energy barrier: atoms which approach the surface have to pass through the Sb film before incorporating into the crystal¹²³. There are two types of surface active materials: *Type I* surfactants increase the surface diffusivity, whereas the *type II* surfactants decrease it^{123–128}. As N tends to agglomerate at the surface during low growth rates or growth rate interruptions, a *type II* surfactant prevents this aggregation by reducing the diffusivity of N on the surface^{123,129}. Several groups reported on Sb as a surfactant for (GaIn)As and other materials^{130–143} improving the optoelectronic, crystalline and surface properties. Therefore, **gallium indium nitride arsenide: antimony ((GaIn)(NAs):Sb)** material was investigated and is presented in Section 4.2.2.

A further possible combination for a 1 eV material lattice matched to GaAs is **gallium nitride arsenide antimonide (Ga(NAsSb))**. This quaternary material is a combination of Ga(NAs) and gallium arsenide antimonide (Ga(AsSb)) with a composition of 6 % Sb and 2.4 % N. In Figure 2.4, the band offsets of Ga(NAs) and Ga(AsSb) are marked orange and magenta respectively. From this figure, one would assume that Sb does not greatly influence the conduction band in comparison with the valence band, which was validated by Kudrawiec et al.^{144,145}. The lower N concentration in comparison with

(GaIn)(NAs) reduces the N related defects¹⁰⁹ as well as the C incorporation^{100,146}. So far $Ga(N_{0.024}As_{0.0916}Sb_{0.06})$ was realized only by MBE. Strong N - Sb interaction debars the growth of Ga(NAsSb) in MOVPE^{134,147–154}. This was either ascribed to gas phase interactions of metal organics or the V/V competition of Sb, N and As. Ga(NAsSb) results are discussed in Section 4.3.

2.3 Fundamentals of Solar Cells

In this section the basic concepts, of solar cells will be explained. The solar spectrum, maximum energy and limits of the current solar cells as well as theoretical limits will be discussed. For detailed solar cell theory and further concepts the books of A. Luque¹⁵⁵ and H. G. Wagemann¹⁵⁶ are recommended. The key principle of a solar cell is based

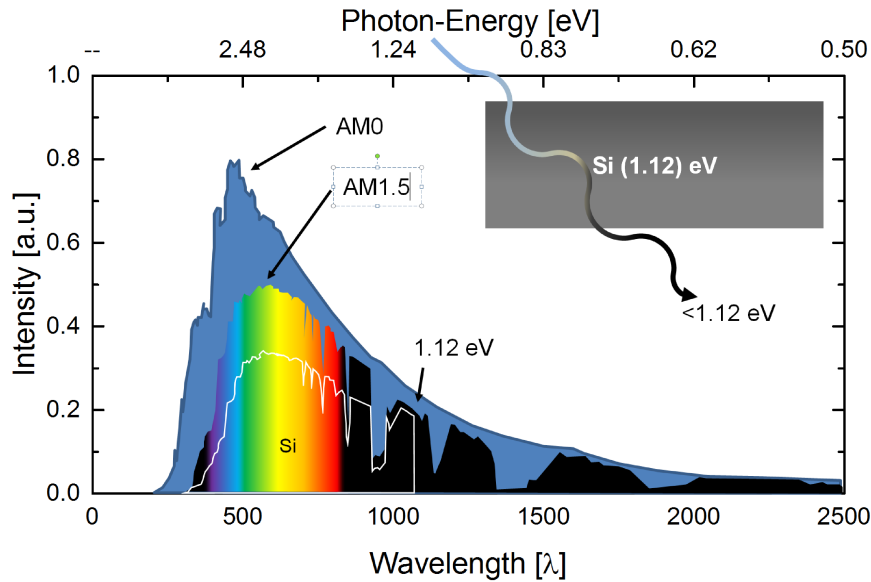


Figure 2.6: Sun spectrum for the AM0 as well as AM 1.5 condition is plotted. The extractable energy in the case of the Si solar cell is schematically depicted.

on the light matter interaction discussed in Section 2.2 and 3.4. The electron-hole pair generation due to incident light is called the photoelectric effect and was honored with a noble prize in 1921 (Albert Einstein). For a detailed understanding of the concept of the solar cell, one must discuss the energy source. In the first order approximation, the sun is a black body radiator with a surface temperature of around 5800 K, emitting mainly light from around 200 nm - 2000 nm¹⁵⁵. In Figure 2.6, the solar spectrum is depicted. However, the spectrum emitted from the sun is slightly different in comparison with the black body radiation due to absorption in the photosphere of the sun. This spectrum, which can be measured in space, is referred to as the *air mass* (AM) 0 spectrum. AM stands for the amount of air between outer space and the earth's surface. Hereby, AM is normed to the distance perpendicular to the earth's surface and calculated depending on the incidence

angle: $x(\text{AM}) = 1/(\cos(\alpha))$, where α is the angle between the impinging light and the vertical direction.

In Germany the peak impinging angle varies between 20° (summer) and 60° (winter). Consequently the AM value varies in the range of 1.06 to 2. On average over year, the AM value is approximated with 1.5. This AM 1.5 spectrum is depicted in Figure 2.6. The characteristic shape of the AM 1.5 spectra deviates strongly in comparison with the AM 0 spectrum. This is connected to the Rayleigh scattering and light molecule interaction (mainly O_3 , H_2O , O_2 , CO_2). The Rayleigh scattering is strongly depended on the wavelength ($\sim \lambda^{-4}$) and therefore scatters blue light stronger than red light, giving the sky its blue color.

In Figure 2.6 the usable area of the AM 1.5 spectrum for a Si solar cell is depicted (white line). Only the light with an energy above the Si band gap can be utilized for energy conversion. Light with lower energy (higher wavelength) either passes the solar cell or interacts with defect states and emits heat. Light

with higher energy as the band gap excites an electron into the conduction band over the band gap edge. The electrons will decay to the band gap edge emitting heat (cf. Section 3.4 and 2.2). Therefore, only the light with the energy close above the band gap is utilized efficiently, while higher energy leads to an increased heating of the solar cell.

The theoretically achievable efficiencies dependent on the band gap are plotted in Figure 2.7. Some energy gap values for prominent semiconductor materials are shown as a comparison. This so-called Shockley-Queisser-Limit¹⁵⁷ shows the theoretical limit for single junction solar cells to be around 30 % for a illumination intensity of one sun^{155,156,158}. This limit can be increased with higher photon density, which is achieved by concentrating the solar radiation by lenses¹⁵⁵. The highest efficiencies for solar cells are predicted for materials with a band gap between 1.0 and 1.5 eV as shown in Figure 2.7. Subsequently, GaAs (1.42 eV) and Si (1.12 eV) are candidates of high interest for single junction solar cells. While GaAs has a direct band gap and better electrical properties than Si, it still is toxic and more expensive than Si. Therefore, Si based solar cells are economically preferred regardless of the fact that Si is an indirect semiconductor. The highest Si solar cell conversion efficiencies of 26,6 % were achieved by the *Fraunhofer Institute for Solar Energy* (ISE)¹⁵⁹. Further increase of solar cell efficiencies for pure Si solar cells is very difficult, as the efficiencies achieved are very close to the theoretical limit.

To further increase the solar cell conversion efficiency, novel techniques are applied.

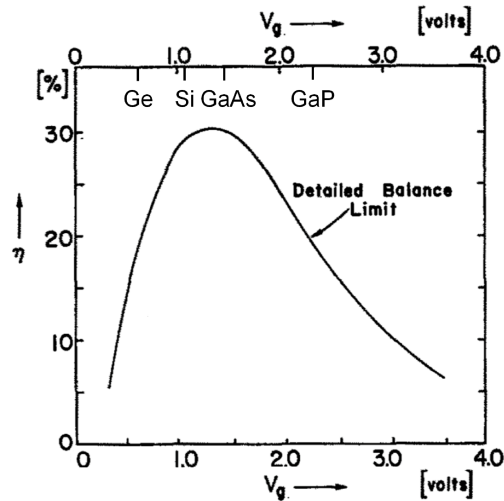


Figure 2.7: Efficiency plotted vs. band gap energy. Representative solar cells are plotted within the graph. Figure adapted from Wagemann¹⁵⁷.

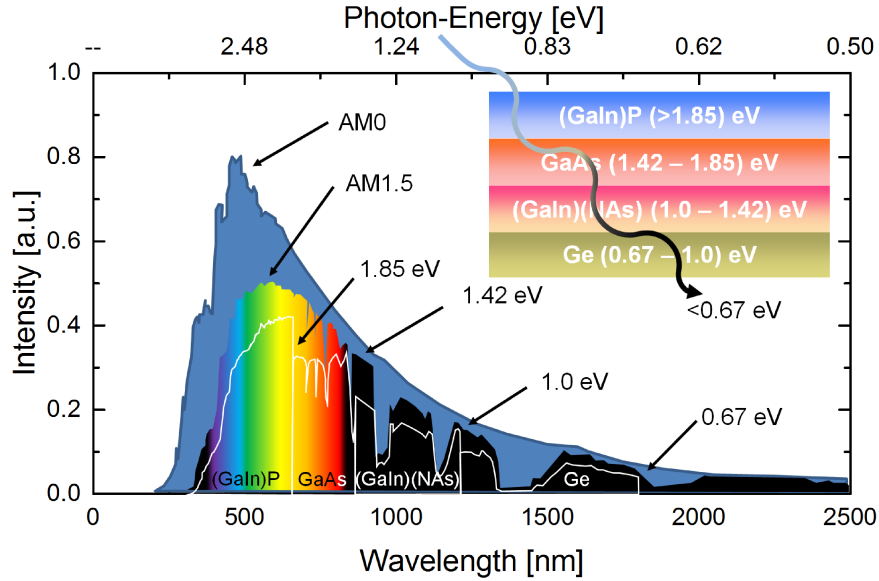


Figure 2.8: Sun spectrum for the AM 0 as well as AM 1.5 condition is plotted. The theoretical extractable energy in the case of the four junction solar cell is schematically depicted.

Stacking several semiconductor materials with different band gaps over each other leads to an increased solar cell efficiency. Hereby, several approaches are investigated. While solar cells produced by wafer stacking^{160–164} achieve 46.0 % conversion efficiencies^{159,165}, it still is cost and time intensive, making this approach economically not sustainable. Epitaxially grown layer stacks however, are generally easier to handle in terms of post growth treatment. The two most relevant approaches, lattice matched epitaxy^{147,166,167} and metamorphic growth^{168,169}, are discussed in literature. Furthermore, perovskite and organic solar cells are entering the market very aggressively. An overview of the solar cell efficiencies in different categories is summarized by Green¹⁶⁵ and NREL¹⁵⁹.

The approach discussed in this work is the epitaxial growth of four different layers lattice matched to Ge/GaAs. The inset in Figure 2.8 shows the concept of this solar cell. Hereby gallium indium phosphide ((GaIn)P), GaAs, (GaIn)(NAs), and Ge are the layers which are discussed for this four junction solar cell. In contrast to the light absorption of Si depicted in Figure 2.6, one instantly sees the higher range of absorption of the sun spectrum for the four junction solar cell solution (Figure 2.8). Marti et al.⁶ calculated for this layer combination a theoretical maximum conversion efficiency of around 50 %.

In this work, however, only the 1 eV material grown on GaAs will be investigated, as the growth of remaining materials of the layer stack is established.

A simple solar cell consists of one n- and p-doped material, the so-called *pn-junction*. In Figure 2.9 the n- and p-doped material is depicted on the right and left sides. When combining these materials, however, an electron and hole diffusion takes place due to the adjustment of the Fermi Energy.

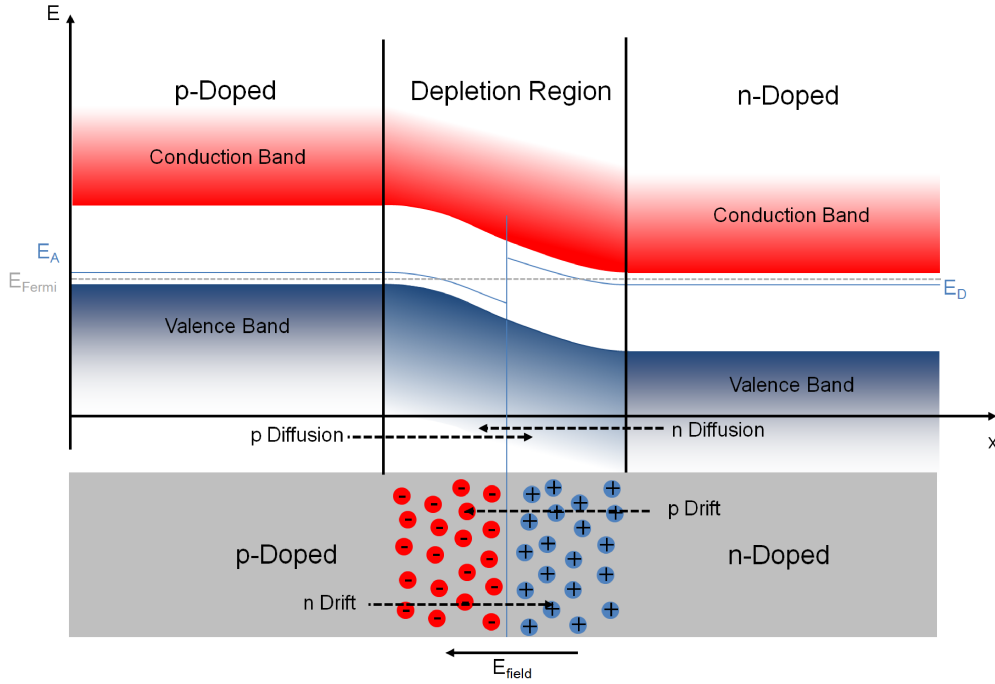


Figure 2.9: Connecting the p- and n-doped material leads to a pn-junction. The Fermi Energy adjusts to one level, leading to band bending in the junction region. Hereby, a depletion region with an E-field forms due to carrier diffusion and carrier drift. Equilibrium state is reached when diffusion current equals the drift current.

The carrier diffusion transports negative charge to the p-side and positive charge to the n-side, forming an electric field which leads to a drift current with the opposite direction of the diffusion current (Figure 2.9). Within this pn-junction, a carrier free zone, the so-called *depletion* or *space charge region*, is formed. The width of this region can be calculated for the equilibrium state as follows (equal drift and diffusion current):

$$W \approx \left[\frac{2\epsilon_0\epsilon_r}{q} \left(\frac{N_A + N_D}{N_A N_D} \right) (V_{bi} - V) \right]^{\frac{1}{2}} \quad (2.10)$$

How far the depletion region reaches into the n- and p-side depends on the doping density ratio:

$$x_n = W \frac{N_A}{N_A + N_D}; \quad x_p = W \frac{N_D}{N_A + N_D} \quad (2.11)$$

The electric field, which is connected to the derivative of the band structure bending in the real space, is the key for the charge carrier separation in a solar cell. Figure 2.10 shows how the electrons and holes are separated due to the electric field. For an efficient solar cell, the mobility of the minority charge carrier is important (electrons in p-doped and holes in n-doped). These minority charge carriers are likely to recombine with the

counterpart, as there is an excess of the countercharge. Therefore, the lifetime as well as the mobility of the minority charge carriers is of high importance.

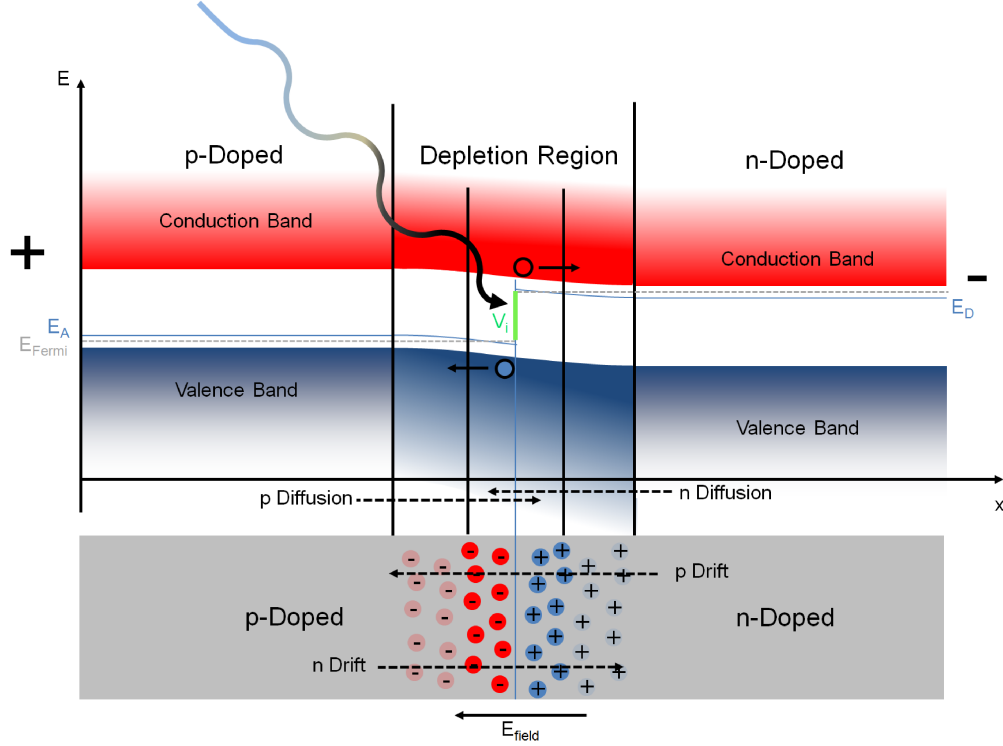


Figure 2.10: Band bending during illumination or external voltage (forward bias). In contrast to the equilibrium state, the band bending is less pronounced. V_i is the voltage either induced by illumination or external voltage (dark current).

Due to illumination the solar cell is not in the equilibrium anymore. The generation of additional charge carriers reduces the depletion region and therefore the band bending as well as the E-field. As the Fermi Energy remains at its position in each p- and n-doped material, a difference between these quasi Fermi Levels occurs (V_i). The V_i can be measured with a potentiometer when in contact with the solar cell. The same band bending is achieved when an external voltage is applied. Figure 2.10 depicts the change of the band bending with either applied voltage or illumination. Figure 2.11 shows the corresponding IV-curves for the dark and illuminated case. In the dark case, the band bends depending on the voltage applied. No current flows for low voltages, as the depletion region acts as a barrier. This barrier, however, decreases with increasing voltage. At a certain value, which is close to the open circuit voltage (V_{OC}), the potential barrier decreases so far that a current starts to flow. For the illuminated case, the IV-curve is shifted to the fourth quadrant, meaning that negative current is flowing for forward biased voltage which is the definition of energy generation. Several characteristic values are defined for the illuminated case:

- The open circuit voltage (V_{OC}) is the voltage obtained under illumination when all generated electron hole pairs are compensated by external power supply and therefore no current is flowing (lowest band bending).
- The short circuit current (I_{SC}) is the current obtained under illumination and an external voltage compensates for the light induced voltage (band bending equal to the one in equilibrium).

The power generated from the solar cell is a product of voltage and current. Therefore, no power is generated for the V_{OC} as well as I_{SC} condition. A good V_{OC} value is considered to be in the range of $E_{gap} - 400 \text{ meV}$. The difference between E_{gap} and V_{OC} is also referred to as W_{OC} . The green plot in Figure 2.11 shows the power for a given IV-curve dependent on the operating voltage. The maximum power is generated under MPP conditions which is achieved at V_{max} and I_{max} .

From these observations, IV-curves with a rectangular shape allow for the highest solar cell efficiency. The value to measure the rectangularity is the so-called fill factor (FF), which is defined as the quotient of $V_{max}I_{max}$ and $V_{OC}I_{SC}$. A good FF is considered to be in the range of 0.8 - 0.9.

The shape of the IV curve can be simulated

with the so-called equivalent circuit shown in Figure 2.12 using the following equation:

$$I = I'_{SC} - I_0 \left(e^{\frac{q(V+IR_S)}{A_0 kT}} - 1 \right) - \frac{V + IR_S}{R_{Sh}} \quad (2.12)$$

Hereby, I_0 is the dark saturation current of the whole solar cell consisting of the recombination in the quasi neutral as well as the depletion region. The ideality factor (A_0) ranges between 1 and 2 depending on whether the recombination dominates in the quasi neutral region (1) or the depletion region (2). The serial resistor (R_S) and shunt resistor (R_{Sh}) represent the deterioration of the solar cell.

The equivalent circuit consists out of the current generator (I'_{SC}), two diodes, representing the quasi neutral region (1) and the depletion region (2) and two different resistors (R_S and R_{Sh}). These resistors qualitatively represent several interactions within the crystal.

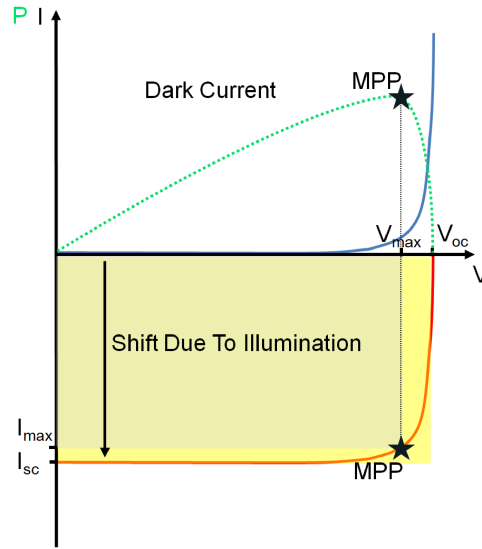


Figure 2.11: Dark current IV-curve (upper part) and illuminated IV-curve (lower part). Due to separated electron hole pairs, a negative carrier flow is measured under illumination; power is generated. The highest output power is achieved under MPP conditions.

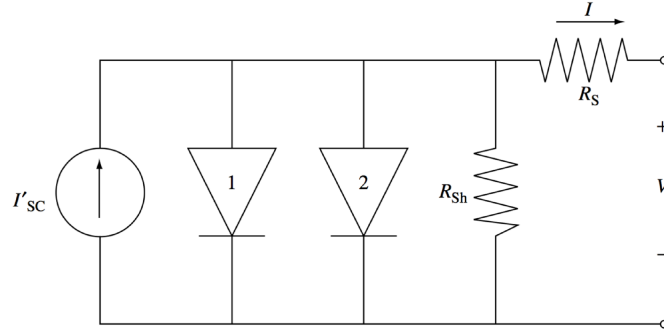


Figure 2.12: Diode 1 represents the recombination current in the quasi neutral regions, diode 2 represents recombination in the depletion region. The serial resistor (R_S) and shunt resistor (R_{Sh}) represent crystal defects and the resistivity of the contacts. Figure obtained from ¹⁵⁵

While R_S is associated with metal contacts as well as transverse current flow within in solar cell from its origin to the nickel (Ni) contacts, R_{Sh} represents leaking of current.

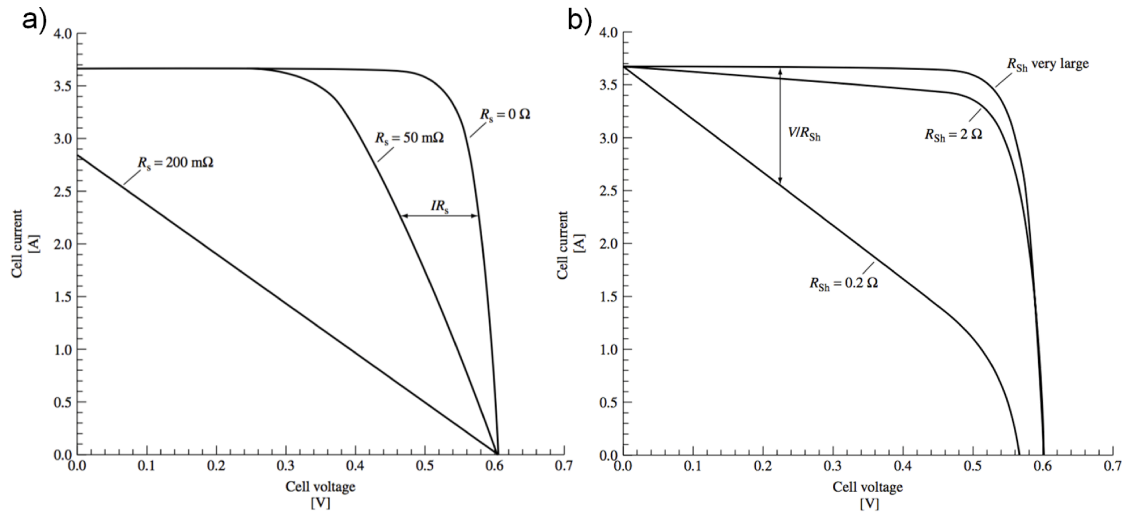


Figure 2.13: IV-curves for different resistor values. The effect of the R_S is shown in a) and the effect of the R_{Sh} is shown in b). Figure obtained from ¹⁵⁵.

Hence, one always seeks for the lowest R_S value possible, which reduces the I_{SC} (Figure 2.13 a)) and an infinite R_{Sh} , which reduces the V_{OC} (Figure 2.13 b)).

The correlation of measured and simulated IV-curves helps us understand what problem needs to be resolved in order to increase the solar cell efficiency.

Another important value is the quantum efficiency: this value is defined as the ratio between the number of carriers collected (N_c) and the incident photons (N_{ph}) dependent on the wavelength (λ) with energies above the band gap. Hereby, one must distinguish between the internal quantum efficiency (IQE), where only the absorbed photons are considered, while the external quantum efficiency (EQE) considers all impinging photons without taking reflection into account:

$$EQE = \frac{N_c(\lambda)}{N_{ph}(\lambda)} \quad (2.13)$$

$$IQE = \frac{EQE}{1 - R} \quad (2.14)$$

When folding the IQE with the spectrum of the light source, one can determine the maximum current obtainable from the solar cell. This current can then be correlated to the I_{OC} obtained from IV-characteristics.

CHAPTER 3

Experimental Methods

This chapter addresses the experimental methods utilized for the growth as well as the characterization of the samples presented in this work. The technical characteristics of the metalorganic vapor phase epitaxy (MOVPE) process will be discussed first, followed by the high resolution X-ray diffraction (HR-XRD), which was used for the first post growth feedback. Surface related investigations were performed using the atomic force microscope (AFM). Optical feedback of *as grown* as well as *annealed* samples was obtained by room temperature photoluminescence (PL) spectroscopy. Post growth *annealing* was either performed within the MOVPE reactor or in an rapid thermal annealer (RTA). Doping densities as well as mobilities were investigated via Hall and electrochemical capacitance voltage (ECV) measurements. Furthermore, dedicated samples were investigated via secondary ion mass spectrometry (SIMS). The solar cells were fabricated and investigated in the framework of a joint project at (ISE). The fabrication and investigation methods are discussed in Section 3.7.

3.1 Metalorganic Vapor Phase Epitaxy (MOVPE)

MOVPE, developed in the second half of the 20th century, is a method which is widely used to produce a variety of crystal structures using metal organics (MOs) as source molecules (precursor). The idea of supplying the source atoms in the gas phase into a reactor enables a high level of control over the growth parameters. A competing and complementary method is molecular beam epitaxy (MBE). This method requires an ultra high vacuum, which is generally more cost and maintenance intensive, and the growth rates are usually limited to 3 μm per hour. This method requires primary sources in an ultra pure form. These are heated in so-called *effusion cells*, subliming the sources to the gas phase. The kinetic energy obtained by heating leads to a molecular beam originating from the effusion cells. While the wafer throughput and the growth rate is higher by magnitudes in MOVPE, MBE grown samples are usually of higher quality. This discrepancy is related to the nature of MOVPE, where the source molecules are per definition bound to hydrocarbon groups.

These hydrocarbon groups tend to incorporate under specific process conditions, as low temperature or low V/III ratio. Nevertheless, MBE and MOVPE are complimentary, as pure gas phase and physical interactions of the pure material can be distinguished by a comparison of these two methods.

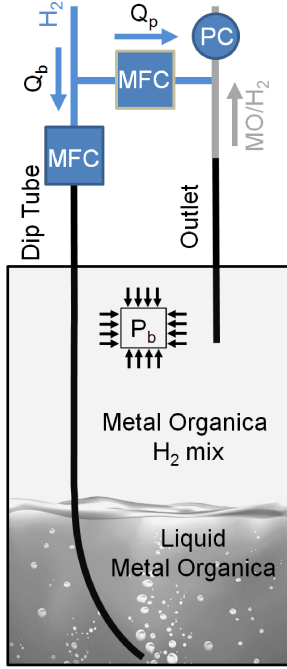


Figure 3.1: Bubbler filled with liquid precursor. H_2 flow through the dip tube is controlled with a MFC. The saturated gas phase is transported through the outlet into the line system. An additional MFC controls the dilution of the transported gas. The pressure is regulated by a PC in the range of 150 mbar - 1800 mbar.

For this work, an *Aixtron* AIX-200 reactor system equipped with a gas foil rotation (GFR) technique was used. All experiments were carried out using a reactor pressure of 50 mbar together with a total reactor flow (Q_s) of 6800 sccm. The MOs are stored in so-called *bubblers*. A schematic overview of a *bubbler* is given in Figure 3.1. These *bubblers* are stored in water baths at source-specific temperatures, because their vapor pressure is strongly temperature dependent:

$$P_v = e^{A - \frac{B}{C+T}} \quad (3.1)$$

Hereby, the A, B and C are substance-specific parameters, which need to be evaluated experimentally. Each *bubbler* has a *dip tube* and an *outlet*. The highly purified ($>9\text{N}$) inert carrier gas H_2 is passed through the *bubbler* with a flow rate Q_b resulting in a transport of the MOs into the line system of the epitaxy machine. Through an additional line system, the gas can be diluted with a flow rate of Q_p . Mass flow controllers (MFCs) are used to control the amount of transported material. Furthermore, the *bubbler* pressure (P_b) can be varied between 150 mbar and 1800 mbar. The partial pressure of the material is determined by:

$$P = \frac{Q_b}{Q_{total}} \frac{P_v}{P_b - P_v} P_R \quad (3.2)$$

Hereby, the Q_{total} represents the total flow through the reactor and P_R the reactor pressure. Figure 3.2 shows the schematic setup of the AIX200-machine used. At least two MOs are needed for the growth of a V/III-crystal (group-III: green; group-V: red). H_2 (blue) is passed through each of the *bubblers* needed. Hereby, the flow is controlled by several MFCs and PCs. Subsequently, the MO saturated gas is transported through the line system into the reactor.

In the reactor a complex interplay of temperature, surface and chemically induced decomposition, adsorption and incorporation takes place. The number of possible chemical

reactions is already very high, if only two MOs are used¹⁷⁰. This shows the complexity of MOVPE and the huge expectations for *ab initio* models of epitaxy processes when the interaction between MOs is considered. The theory of adsorption and precursor decomposition is a subject of large interest^{171–173}.

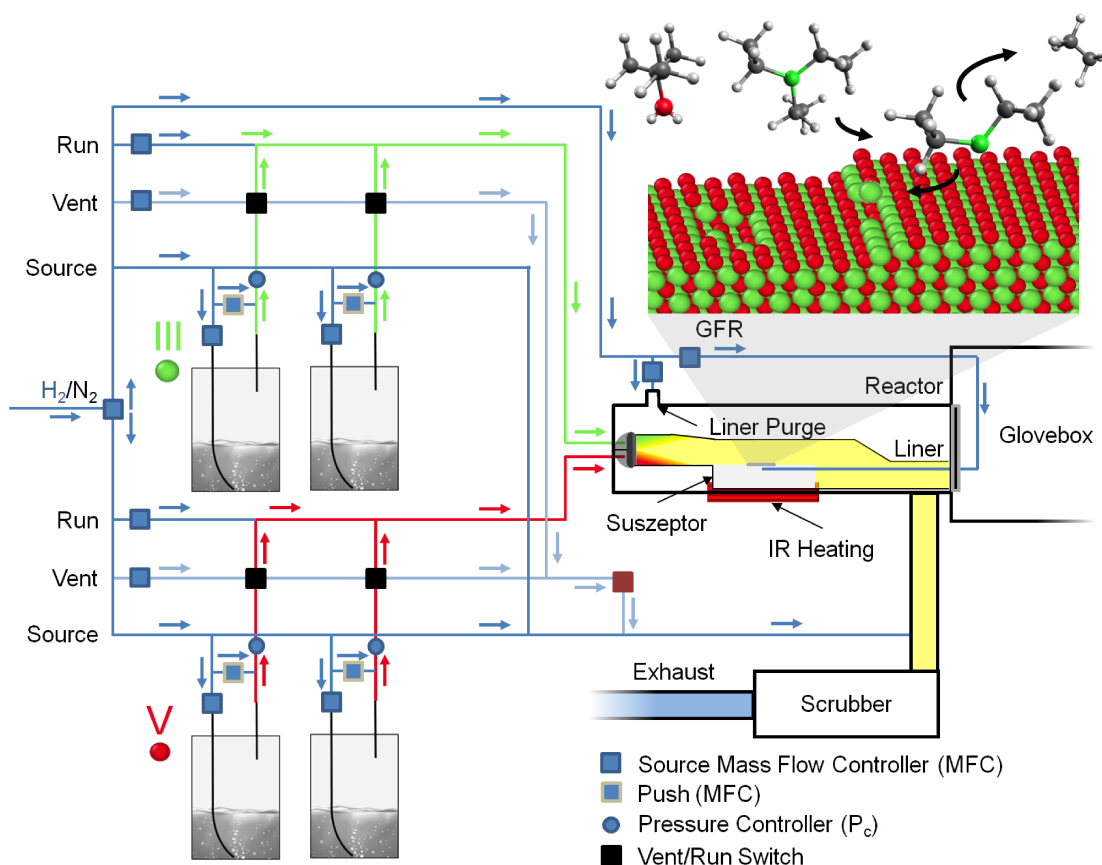


Figure 3.2: Schematic overview of the MOVPE machine. H₂ is transported through the bubbler as a carrier gas. The saturated gas (group III = green, group V = red) is transported through the line system into the reactor. Within the reactor a decomposition of the precursor takes place, leaving the group III or V atom behind at the surface in the ideal case only. Undecomposed precursor material as well as alkyl groups are subsequently filtered in the scrubber. In the next step, pure H₂ is put into the atmosphere strongly diluted with N₂.

The MO is ideally decomposed due to thermal energy and the sample surface as a catalyst. This takes place in the so-called *boundary layer*, which is close to the growth surface. After adsorption of the cracked precursor, the residual atom diffuses over the surface due to kinetic energy and either incorporates or desorbs (right inset in Figure 3.2). The individual desorption rate of each atom depends on the growth temperature as well as the epilayer grown. During the diffusion, the adsorbed residual atom passes kinks and steps, which are energetically more favorable, as there are two corresponding bonding partners instead of only one on the flat surface. Due to a much higher desorption rate of group-V atoms in comparison with group-III atoms, one usually must supply a large

group-V excess. Therefore, growth usually takes place under a V/III-ratio significantly greater than one. The waste material (undecomposed MOs, residual C groups, desorbed atoms and molecules mixed with H_2) is passed through a gas cleaning system (*scrubber*), which only lets H_2 pass through. The H_2 is subsequently diluted with N_2 so no explosive H_2 - O_2 concentration can occur and is passed into the air.

3.2 High Resolution X-Ray Diffraction (HR-XRD)

In epitaxy, one distinguishes between homo and hetero epitaxy. The growth of a material on the same substrate material is referred to as homo epitaxy, while material grown on a substrate of different material and lattice constant is referred to as hetero epitaxy. The relaxed lattice constant (b) of a hetero epitaxially grown layer is generally different from the host matrix. During epitaxial growth, the atoms are forced to accept the *in-plane* lattice constant ($b_{\parallel} \rightarrow a$) of the substrate material (pseudomorphic growth). This leads to strain ($b_{\perp} \rightarrow b'$), which is depicted in Figure 3.3. This deformation is referred to as tetragonal distortion¹⁷⁴. If the epitaxial layer has a larger lattice constant ($b > a$)

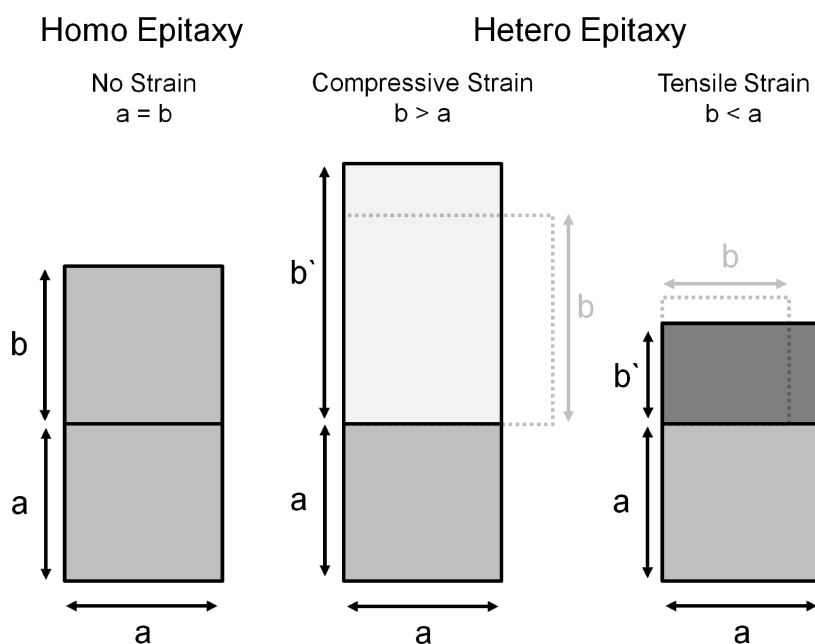


Figure 3.3: Schematic demonstration of homo epitaxy (left) and hetero epitaxy (right). In contrast to homo epitaxy, hetero epitaxial grown layers can either be compressively or tensilely strained. Hereby, a represents the lattice constant of the substrate and b the relaxed layer lattice constant and b' the strained lattice constant.

than the host matrix, it is compressively strained since its *in-plane* lattice constant is reduced. On the other hand, an epitaxial layer with a smaller lattice constant ($b < a$) is referred to as tensilely strained since its *in-plane* lattice constant is increased. The Panalytical X'Pert Pro HR-XRD machine was utilized to measure the *out-of-plane* lattice

plane distance. Hereby, a constructive and destructive interference occurs when the incident beam (copper K_α , $\lambda = 1.5405 \text{ \AA}$) is diffracted (depicted in Figure 3.4). The angle

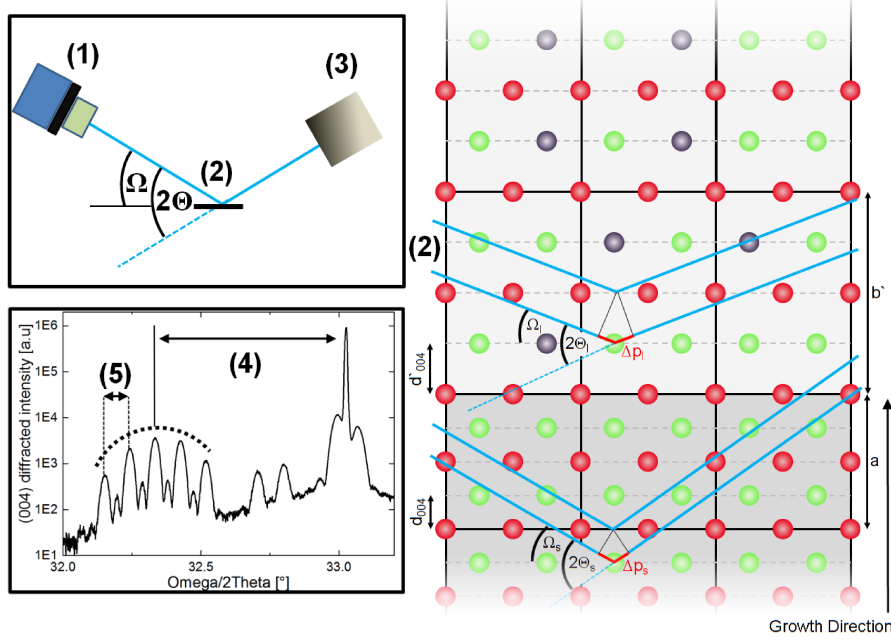


Figure 3.4: Schematic overview of the HR-XRD principle. The generated x-Ray beam (1) is directed onto the sample (2) under the angle of Ω . The beam is elastically scattered and constructive or destructive interference occurs dependent on the angle. The detector (3) follows the sample rotation with a factor of 2 (Θ). A diffraction pattern is obtained. The distance between the main peak and the envelop function (4) is related to the difference of b' and a , while the fringe distance (5) is reciprocally related to the layer thickness.

(Θ) at which constructive interference occurs depends on the distance between the lattice planes. Usually, the (004) reflex is chosen due to its high intensity. These lattice planes are parallel to the sample surface, corresponding to the *out-of-plane* distance of the atoms as depicted in Figure 3.4 (d_{004}). During the measurement a so-called $\Omega/2\Theta$ scan is performed (1). Hereby, the sample holder angle (Ω) is varied, while the detector angle (Θ) follows a factor of two. Constructive interference (2) only occurs when the path length (red) corresponds to the wavelength (λ) of the impinging beam (Bragg's Law):

$$2d\sin(\Theta) = n\lambda \quad (3.3)$$

The diffracted beams are then detected (3) and the intensity is plotted vs. $\Omega/2\Theta$ (4), (5). This leads to a diffractogram, where usually several peaks are present. In the case of GaAs-(004), the main peak corresponds to the (004) lattice planes at 33.024° , while the peaks around it originate from the compressively (lower angle, left) or tensilely (higher angle, right) strained epitaxially grown layers. The distance between the envelope and main peak corresponds to the (004) lattice planes from the epitaxial layer (4) while the distance between the fringe peaks (5) is related to the layer thickness in a multi quantum

well (QW) structure. The strained *out-of-plane* distance is determined by Equation 3.4, utilizing Equation 3.3 and approximations for small angles:

$$(\Theta_s - \Theta_{l'}) \cdot \cot(\Theta_s) = \frac{b' - a}{a} \quad (3.4)$$

To determine the relaxed lattice constant b , elastic constants (C_{11} and C_{12}) of the specific material systems are needed. Equation 3.5 shows the correlation between the relaxed lattice constant b and the tetragonally strained lattice constant b' :

$$\frac{\Delta a}{a} = \frac{b - a}{a} = \frac{C_{11}}{C_{11} + 2C_{12}} \frac{b' - a}{a} \quad (3.5)$$

Hereby, the $\frac{\Delta a}{a}$ represents the lattice mismatch of the unrelaxed crystals. The strain however, is defined as follows:

$$\varepsilon = \frac{a - b}{b} \quad (3.6)$$

The composition is determined by the relaxed lattice constant in combination with Vegard's Law⁶⁴. This composition determination is only possible for ternary materials, as a further degree of freedom is added for quaternaries. To solve this an additional investigation tool like PL spectroscopy is required to reduce one degree of freedom (cf. Section 3.4).

3.3 Atomic Force Microscope (AFM)

A *Nanoscope IIIa, Digital Instrument* AFM was utilized for surface related investigations. A needle vibrating at its resonance frequency in z-direction is scanned over a surface area in x- and y-direction. Changes in the lower nm range in z-direction strongly affects the vibration frequency due to *Van der Waals* and *Coulomb* interactions. The potential of surface and needle is approximated with a *Lennard-Jones potential*. In the *constant height mode*, the distance between the needle and the surface is adjusted via piezo elements until the initial frequency (and height) is measured again. The adjustment of the piezo crystals is then mapped as a function of the needle position. The vibration frequency is measured by a four zone photo diode. The diode is illuminated by a laser beam which is reflected by the needle. Due to the vibration of the needle, the four zone photo detector illumination varies periodically, detecting the vibration frequency.

3.4 Photoluminescence (PL) Spectroscopy and Rapid Thermal Annealer (RTA)

PL spectroscopy allows optical characterization. This technique was used to determine the PL peak position as well as intensity at room temperature conditions. The PL setup is depicted in Figure 3.5. In this setup, the 532 nm line of a frequency doubled Nd:YAG

Laser with a spot size of 1.85 ± 0.20 mm was passed through a prism monochromator to reduce the line width of the laser beam. To fine tune the output power, a grey scale was used in combination with a mobile power meter. The *Lock-In* technique was utilized to increase the *signal-to-noise* ratio. Therefore, a chopper was put into the laser path, which was blocking the laser beam periodically. After the chopper, the laser beam was directed onto the sample. The diffuse light originating from the sample was coupled into the monochromator with two lenses (L_1 collimate: 120 mm, L_2 focus: 400 mm). A long pass filter (570 nm) was put right before the monochromator to cut off the laser induced reflections. The 1 m grating monochromator (THR 1000, Jobin-Yvon) filters the incident light depending on the wavelength and couples it into a liquid N_2 cooled Ge detector. The detector signal as well as the chopper signal were processed in the Lock-In amplifier. Finally, the monochromator position as well as the Lock-In amplifier signal are sent to the computer where the signal was normalized and PL spectra are plotted.

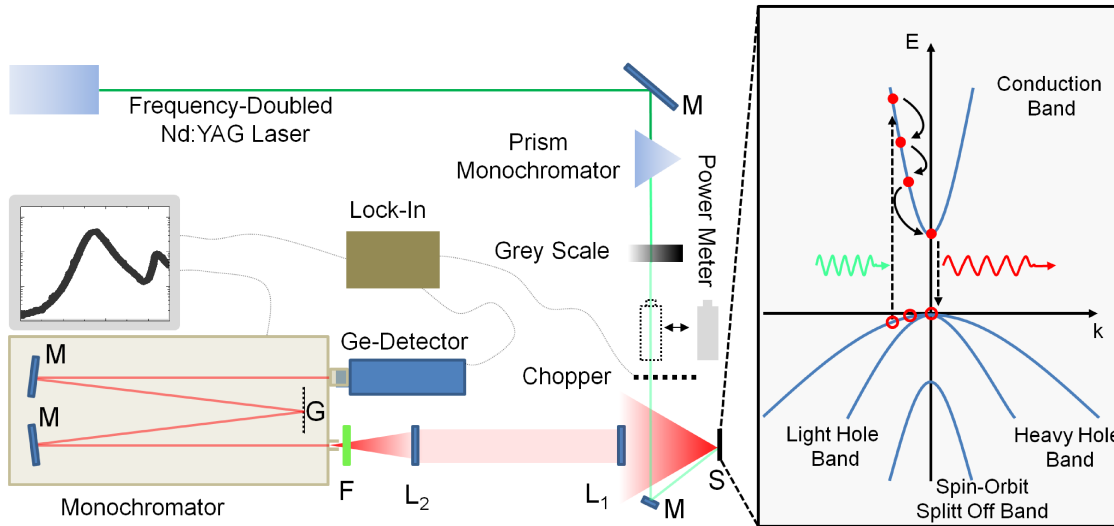


Figure 3.5: Schematic overview of the PL setup. The frequency-doubled Nd:YAG laser emits light at 532 nm, passing the prism monochromator to reduce the line width. A grey scale is used to fine tune the laser power, which is detected by a power meter. A chopper periodically blocks the laser beam, which is directed onto the sample. The light emitted by the sample is coupled into the monochromator by two lenses, and the dispersed light into the Ge detector.

Since the material investigated in this work has a band gap between 1.0 and 1.42 eV, electrons are excited by the incidenting 2.33 eV (532 nm) laser beam into the conduction band. The excited electron relaxes to the band gap edge emitting heat (phonons) as depicted in Figure 3.5 on the right-hand side. From the band gap edge, the electron either recombines radiatively or non-radiatively. Several loss mechanisms like Auger and Shockley Read Hall recombination^{175,176} are responsible for the non-radiative recombination. Furthermore, the GaAs host matrix periodicity is affected by the local disorder induced by dilute nitrides. This effect increases the non-radiative recombination¹⁷⁷ (cf. Section 2.2). Some of these

defects can be annihilated by thermal *annealing*. While one can use the MOVPE reactor for *annealing*, a JetFirst 200 C rapid thermal annealer (RTA) was utilized for the post growth *ex-situ annealing*. Hereby, 20 IR-lamps heat the samples with heating ramps up to 50 K per second. This heat treatment supplies energy to the crystal. N atoms begin to move due to kinetic energy. Hereby, interstitials and anti-sites are partially annihilated. Thus, the PL peak intensity generally increases and the full width of half maximum (FWHM) reduces after *annealing*. Furthermore, a PL peak position shift is observed in dilute nitrides. This shift is related to the surplus hydrogen (H) incorporated parasitically into the crystal during MOVPE. H annihilates the influence of N onto the band gap. *Annealing* activates the passivated N atoms and therefore, a red shift is observed^{178–181}.

In (GaIn)(NAs), one additionally has a further degree of freedom of the N environment. Theoretical calculations have shown that for the same N and In content, the band gap is less reduced for the N in an In environment than for the N in a gallium (Ga) environment. Furthermore, the local stress is reduced for the N in an In environment, which is the driving force for the N to diffuse into an In rich environment during the *annealing* process. This reordering leads to a blue shift.^{118,182,183}

3.5 Hall and Electrochemical Capacitance Voltage (ECV) Measurements

The electronic characteristics were determined by Hall and ECV measurements. Hall measurements allow us to determine the majority carrier density, its type and mobility in epitaxy layers on semi insulating (s.i.) substrates. The van-de-Pauw-Method¹⁸⁴ allows us to neglect the shape of the measured sample. For the measurement, In contacts are alloyed onto the roughly 1 cm² sample. Subsequently, the sample is glued onto an 8-pin DIP socket where four of the pins are connected to the In by copper wires. The water cooled magnet reaches field strengths up to 0.9 T, while the current usually is in the range of several μ A. This method, however, only allows measurements for one layer grown on a s.i. substrate.

As a solar cell material is grown on either p- or n-doped material, another technique was utilized to determine the active carrier type and density. This so-called **electrochemical capacitance voltage (ECV)** is based on the measurement of the capacity between the sample and the chosen electrolyte. This electrolyte is in contact with a well defined sample surface area. Due to sophisticated measurement techniques, the doping density can be determined depending on the depth. Therefore, the sample is etched and measured after a chosen etch depth. The doping density depth, however, consists out of the etch depth as well as the depletion region width. This technique allows us to determine the doping density and type for several layers on any doped substrate. A detailed description of the theory and function of the Hall and ECV measurements can be found in literature^{39,54,185–188}.

3.6 Secondary Ion Mass Spectrometry (SIMS)

The detection of parasitic incorporation is performed via secondary ion mass spectrometry (SIMS) externally by *RTG Mikroanalyse GmbH* in Berlin. Hereby, primary ions are focused onto the surface, extracting secondary ions from the sample. These secondary ions are then investigated with a mass spectrometer. Therefore, the count rate as well as the charge to mass ratio is determined. The knowledge about possible cluster formation during the sputtering process is important for adjusting the mass spectrometer and therefore for detecting the relevant atoms. The composition of the investigated sample is determined by a comparison with the count rate of a calibrated sample, which is always sputtered simultaneously with the sample of interest.

3.7 Solar Cell Fabrication and Characterization

This section focuses on the fabrication and characterization of solar cells, which was performed at the *Fraunhofer Institute of Solar Energy-Systems* (ISE) in the framework of a joint dilute N project.

Quick Cell Fabrication

The usual full solar cell fabrication procedure takes more than one month. This increases the feedback loop of the solar cell production and characterization drastically. For quick feedback within several days, an approach for solar cell fabrication was developed at ISE. This so-called *quick cell* fabrication is based on the electroplating principle. Firstly, a u-shaped mask was placed on the roughly 1 cm^2 sample and the corners were sealed with electrolyte proof varnish. The sample was then put into the electroplating machine, where the full back surface as well as the u-shaped front surface was coated with Ni. The edges were not coated due to the varnish protection to prevent a short circuit. After electroplating the mask was removed from the surface and the samples were treated with acetone to remove the varnish from the sample edges. Finally, the samples were cleaned with isopropanol.

Citric acid was used to etch down the 400 nm GaAs cap selectively. The 50 nm thick (GaIn)P was not etched by citric acid and therefore, generally acts as an etch stop material. In contrary to the conventional fabrication, no anti-reflection coating was performed. Furthermore, the mean distance of each point of the solar cell to the Ni contact varies strongly, which strongly increases the R_S value. Nevertheless, this fabrication method allows a quick and reliable comparison relatively to each other. The Ni coated area at the front (u-shape) and back (full area) are contacted externally for further investigations.

IV-characteristic

The IV-characteristic was obtained by voltage variation from $V = 0$ until $I = 0$. Hereby, the Oriel Instruments sun simulator, with a Si reference/monitor cell, was utilized. The solar cell was illuminated with a light intensity of one sun by a xenon lamp. The obtained IV-characteristics were then interpreted as discussed in Section 2.3, taking into account the sample area.

Quantum Efficiency (QE) measurements

The quantum efficiency (QE) measurements were obtained by LOANA system from PV-Tool. The EQE is measured by a spectral light impinging onto the solar cell. At the same time the generated current is detected. This current is normed to the current obtained under the same light for a calibrated sample. In a second measurement, the spectral reflectance of the solar cell surface is recorded in order to determine the IQE. Knowing the IQE as well as the spectra of the xenon lamp allows us to determine the I_{SC} value.

CHAPTER 4

Achievements with Conventional and Alternative Precursors

In this chapter, the N incorporation of DTBAA in comparison with UDMHy will be discussed for each grown system individually. Already published work, which is reprinted in Section 7, will be summarized only. The corresponding sections are marked with an asterisk (*). Figures and results of publications referenced throughout this work. Unpublished work will be discussed in more detail.

Firstly, N incorporation was investigated in pure GaAs, followed by N incorporation in (GaIn)As and Ga(AsSb). The usage of Sb as a *surfactant* during the growth of (GaIn)(NAs) (cf. Section 2.2) will be discussed in Section 4.2.2. Section 4.2.3 addresses the C incorporation in (GaIn)(NAs) with the use of novel precursors like TIPIn and DTBAA as well as C reduction techniques with TBAs. Furthermore, the growth of Ga(NAsSb) will be discussed in Section 4.3, in comparison with the UDMHy and DTBAA based growth in Section 4.3.1. Di-tertiary-butyl antimony tertiary-butyl amine ($t\text{Bu}_2\text{SbN}(\text{H})t\text{Bu}$, DTBSbTBA) results will be presented in Section 4.3.2.

4.1 MOVPE Growth of Ga(NAs) Structures*

In order to compare the N incorporation of DTBAA and UDMHy, Ga(NAs) QW structures were grown on s.i. exact (001) GaAs substrates with each precursor and investigated with HR-XRD, AFM and PL. Dedicated bulk samples were investigated with SIMS.

First results obtained in Eduard Sterzer's Masters thesis¹⁸⁹ revealed that Ga(NAs) structures can be grown with DTBAA and tri-ethyl gallium ($(\text{C}_2\text{H}_5)_3\text{Ga}$, TEGa) only. This result shows that As and N are both supplied by the novel precursor DTBAA, making additional TBAs supply optional. Hence, all DTBAA experiments, if not mentioned otherwise, were realized with TEGa and DTBAA only.

* Parts of this work are published³² and presented in Section 7.1

Two PL spectra of samples containing 0.8 % N each grown with UDMHy and DTBAA, respectively, are shown in Figure 4.1. Both samples show almost the same PL peak position, in which the DTBAA grown sample even shows a slightly higher PL peak intensity. AFM measurements presented in Section 7.1 show smooth surfaces. From this we conclude that high quality samples are achieved when grown with DTBAA instead of UDMHy.

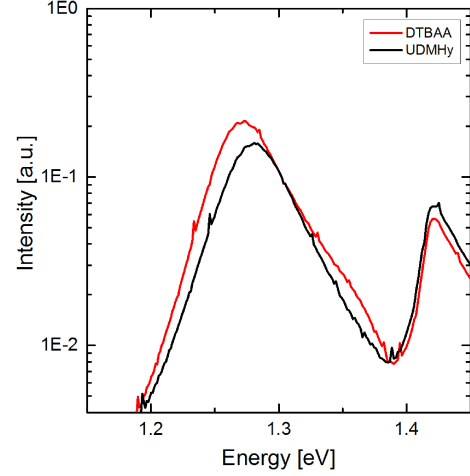


Figure 4.1: PL spectra of a UDMHy and DTBAA grown Ga(NAs) sample with an N content of 0.8 %. These data was obtained at room temperature and 100 mW laser power.

Furthermore, the N incorporation efficiency of DTBAA and UDMHy was investigated. Therefore, Ga(NAs) samples containing 3 % N were grown with DTBAA and UDMHy under similar conditions. A 15 - 20 times higher N incorporation efficiency of DTBAA in comparison with UDMHy was determined, for the DTBAA vapor pressure was assumed to be in the range of 0.6 - 0.8 mbar. The activation energies obtained from exponential N incorporation behavior vs. temperature observed for UDMHy as well as DTBAA grown Ga(NAs) samples underline this finding (cf. Section 7.1 Figure 6 b))^{32,100}.

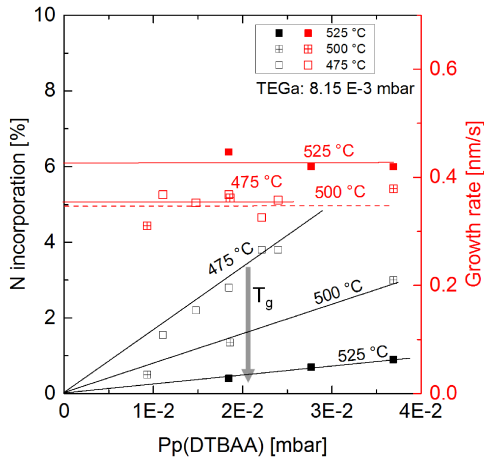


Figure 4.2: N incorporation on the left and growth rate on the right plotted dependent on DTBAA. The linear N incorporation behavior is shown for three different temperatures. Increasing temperature decreases the N incorporation.

Gas phase computations performed by the group of PD Dr. Ralf Tonner suggest that UDMHy decomposes mainly to N_2 (cf. Section 7.1 Figure 1 a). This leads to low N incorporation efficiency as N_2 desorbs easily. DTBAA, however, decomposes to N-As, which is less volatile (cf. Section 7.1 Figure 1 b). Recent research by Oliver Maßmeyer with the *In-Situ Mass Spectrometer* shows that DTBAA might decompose into NH_3 and tBu_2As molecules¹⁹⁰. Yet NH_3 is believed to desorb very efficiently as well. However, this research is still ongoing and will determine the reason for the high N incorporation efficiency in the future.

In UDMHy grown Ga(NAs), the N incorporation is controlled by the so-called V/V gas phase ratio of UDMHy and TBAs⁷. This is possible due to the fact that As and N both are group V elements and, therefore, both compete for the same lattice site. Yet, N

incorporation control in DTBAA grown Ga(NAs) is more complex. Due to the fixed As/N ratio within the DTBAA molecule and no additional TBAs supplied, a common V/V ratio variation is not possible. Nevertheless, the N incorporation can be adjusted by varying the DTBAA partial pressure only. These experiments were performed for three different temperatures as depicted in Figure 4.2. For each temperature, a linear increase of the N incorporation at a constant growth rate was observed. Additionally, a strong N incorporation increase with lower temperature for the same DTBAA partial pressure was discovered. These results suggest that either the sticking coefficient

or the desorption rate of As and N are changed dependent on the DTBAA partial pressure. This behavior is still not fully understood and is the subject of current research with a highly efficient mass spectrometer¹⁴ and reflectance anisotropy spectroscopy (RAS)¹⁹¹ setup.

Growth rate experiments were performed for two different temperatures to expand the understanding of the N incorporation behavior from the DTBAA. While no N incorporation variation was observed for the 525 °C experiments, an N incorporation decrease with higher TEGa was detected in the 475 °C case. In the future, further experiments must follow in order to understand this behavior fully. An explanation may be the constant diffusing rate of N to the surface. The growth rate increase would therefore reduce the N adsorption in a specific layer thickness and, with that, the N incorporation.

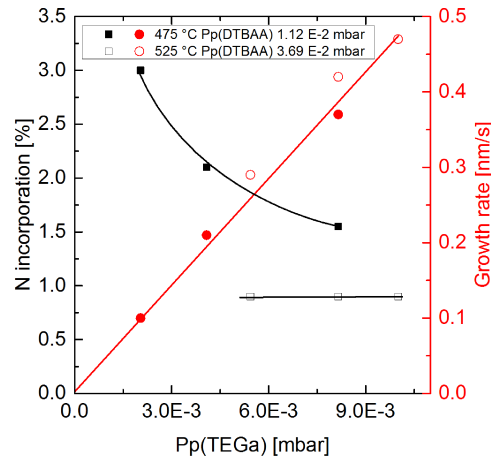


Figure 4.3: N incorporation on the left and growth rate on the right dependent on the TEGa partial pressure for two different temperatures.

4.2 MOVPE Growth of (GaIn)(NAs) Structures

After discussing Ga(NAs) growth in Section 4.1, this section focuses on (GaIn)(NAs) growth with different precursor constellations. Firstly, a comparison between the trimethyl indium ((CH₃)₃Ga, TMIIn) grown (GaIn)(NAs) material realized with DTBAA is given in Section 4.2.1. Secondly, Section 4.2.2 comprises results of TMIIn and UDMHy grown (GaIn)(NAs) samples with additional tri-methyl antimony ((CH₃)₃Sb, TMSb) as a *surfactant*. Lastly, C reduction experiments with TIPIn and/or additional TBAs for UDMHy and DTBAA grown samples are addressed in Section 4.2.3.

4.2.1 (GaIn)(NAs) Growth with DTBAA*

In Section 4.1, the N incorporation efficiency of DTBAA in comparison with UDMHy was discussed. In this section additional TMIn is added to the Ga(NAs) growth. Volz et al.⁷ showed an N incorporation reduction in the UDMHy grown (GaIn)(NAs) samples when alloying Ga(NAs) with In. This observation is depicted in Section 7.3, Figure 3 as a dotted line. The N incorporation drops by 70 % relative to the initial concentration in Ga(N_{0.03}As_{0.97}) when aiming for 8 % In. This urges to an N incorporation compensation by either higher UDMHy or lower TBAs partial pressure (higher UDMHy/TBAs ratio). Both options lead to a reduced surface quality together with a higher C incorporation. When increasing the UDMHy supply, the precursor consumption is increased, along with a growth rate reduction. The reason for that is the high UDMHy supply (around 2 % of the total gas phase in the reactor), which changes the conditions in the *boundary layer* and therefore affects the growth process. All these effects emphasize the need of novel precursors with a higher N incorporation efficiency and less precursor interactions.

Therefore, the same experiments were carried out with DTBAA. No N incorporation decrease was observed with higher In concentration for the TEGa, DTBAA and TMIn precursor combination, as depicted in Section 7.3, Figure 3. In contrast to the UDMHy grown case, an N incorporation increase was observed with higher In content. Therefore, the overall N incorporation efficiency increases from 15 - 20 times (Ga(NAs)) up to around 60 - 80 times ((GaIn)(NAs)) with respect to UDMHy grown samples.

Despite the significant benefits of DTBAA, the growth of (GaIn)(NAs) is still challenging. Firstly, the O content of the DTBAA grown samples is in the range of $4 \cdot 10^{18}$ atoms/cm³ as depicted in Section 7.3, Figure 5. And secondly, the C incorporation is still in the range of 10^{17} - 10^{18} atoms/cm³. Nevertheless, the DTBAA experiments revealed TMIn as one main source of C incorporation.

SIMS investigations on DTBAA grown (GaIn)(NAs) and Ga(NAs) layers are presented in Section 7.3, Figure 5. The only difference between both layers is the additional supply of TMIn in (GaIn)(NAs) without changing other growth parameters. In addition to the expected In content, double the C content was observed in (GaIn)(NAs) in comparison with Ga(NAs). As TMIn is the only variation, the surplus C must originate from the residual methyl groups of this precursor. In our case, C is presumably incorporating on group V lattice sites, leading to an intrinsically p-doped (GaIn)(NAs) material, whereas O is incorporating as a deep impurity.

The initial assumption for the source of C and O incorporation was the DTBAA precursor impurity. Therefore, a very challenging synthesis procedure was performed by the group

* Parts of this work are published¹⁹² and presented in Section 7.3

of Prof. von Hänisch to enhance the DTBAA quality. Figure 4.4 represents the O, C and N incorporation obtained by SIMS for Ga(NAs) (a) and (GaIn)(NAs) (b) dependent on different batches synthesized by the chemistry department. While the O content decreases sharply with increasing batch number, no C content reduction was observed. This makes the assumption that C originates from DTBAA impurity unlikely, but does not exclude it. A key point for a reduced O content was the usage of highly purified NH_3 (5N) as well as further reactants with higher purity. While the Ga(NAs) samples reveal a C incorporation in the range of $1 \cdot 10^{18}$, (GaIn)(NAs) samples have a C content twice as high. This is related to the additionally supplied TMIn as discussed before. Experimental results concerning this C reduction are discussed in Section 4.2.3.

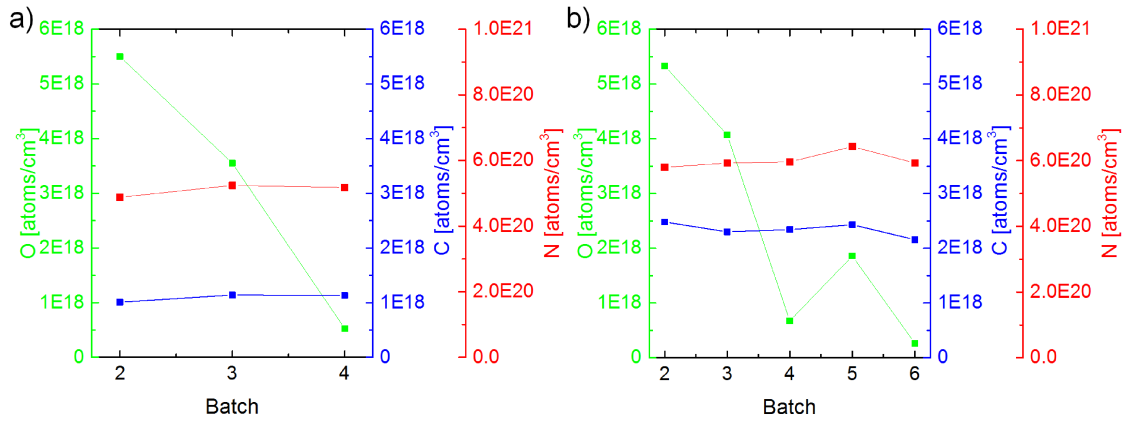


Figure 4.4: O, C and N content of DTBAA grown Ga(NAs) (a) and (GaIn)(NAs) (b) plotted dependent on increasing synthesis experience.

Batches 5 and 6 were both synthesized in a novel and bigger apparatus that allows a higher outcome. The (GaIn)(NAs) layer grown with batch 6 shows the lowest O content observed so far and values $2.6 \cdot 10^{17}$ atoms/cm³ only. (GaIn)(NAs) material grown with batch 5, however, reveals an O content seven times higher (cf. Figure 4.4 b)). While batch 6 was distilled three times, two distillations were performed only on batch 5. This has a strong effect on the O content and shows how big the impact of the reactant purity and distillation number is. Consequently, further purification with more distillation cycles and higher material purity must follow in order to allow for a sophisticated usage of DTBAA.

4.2.2 Antimony as *Surfactant* for UDMHy based Growth

Jones-Albertus et al.¹⁴⁷ showed that MBE grown gallium indium nitride arsenide antimonide ((GaIn)(NAsSb)) 1 eV samples with dilute amounts of Sb exhibit the highest solar cell efficiency observed so far. Sb is often utilized as a *surfactant* and is known to improve the crystal and the optoelectronic properties of (GaIn)As as well as other structures^{130–141}. Furthermore, group V *surfactants* were observed to reduce C incorporation^{142,143}. Due to these facts, (GaIn)(NAs) samples were produced with tri-methyl gallium ((CH₃)₃Ga, TMGa) or TEGa together with TBAs, TMIn and UDMHy while supplying additional TMSb.

The HR-XRD results of (GaIn)As:Sb and Ga(NAs):Sb growth are presented individually for the TMGa/TMSb combination (a) as well as the TEGa/TMSb combination (b) in Figure 4.5. Regarding the TMGa/TMSb combination, two trends are observed: the In content increases with higher TMSb/III ratio, going along with a decreasing growth rate of around 25 % (TMSb/III = 0.35). This leads to the assumption that either the TMGa decomposition or the Ga incorporation itself is hindered by the TMSb supply. Sb incorporation can be excluded, as SIMS measurements depicted in Figure 4.8 show an Sb content in the range of 10¹⁹ atoms/cm³. This corresponds to 0.05 % Sb incorporation which is negligible for HR-XRD investigations.

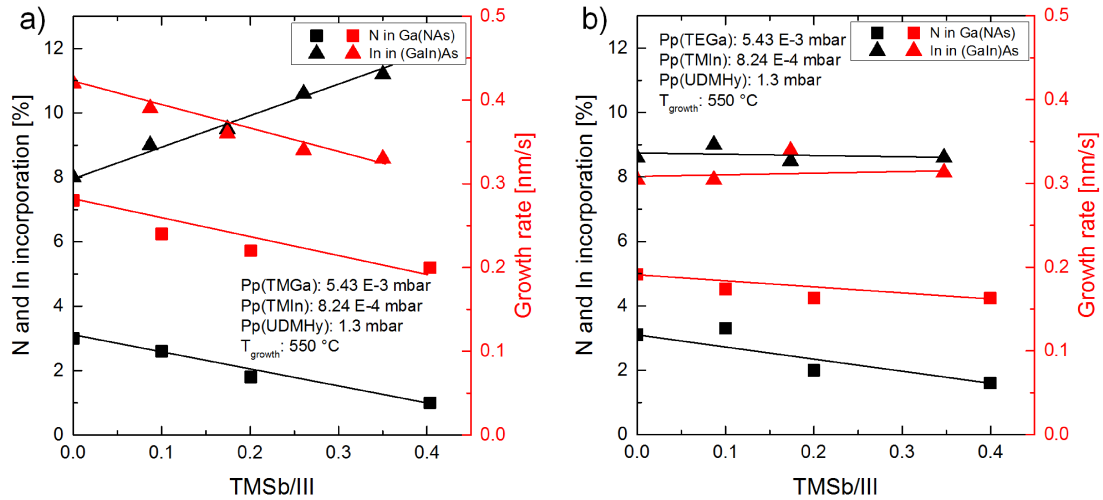


Figure 4.5: N and In incorporation dependent on TMSb/III. The results of the TMGa/TMSb are presented in a) and of the TEGa/TMSb in b).

In a comparison of (GaIn)As results of the two precursor combinations, no In incorporation increase or (GaIn)As growth rate decrease was observed for the TEGa/TMSb combination. This hints at a methyl group interaction between TMGa and TMSb. At the same time, the growth rate is lower for TEGa grown (GaIn)As and Ga(NAs) in comparison with TMGa, although the same Ga partial pressure was used. The N incorporation shows an opposite trend for both precursor combinations: higher Sb supply (higher TMSb/TBAs)

reduces the N incorporation as well as the growth rate. But here as well, the Sb influence on N incorporation and growth rate is stronger for the TMGa/TMSb combination. After the evaluation of the Sb effect on both ternary material systems, investigations on quaternary (GaIn)(NAs) material follow with by much lower TMSb supply. As mentioned in Section 4.2.1, the N incorporation is drastically reduced in (GaIn)(NAs) with respect to Ga(NAs) when grown with UDMHy and TMIn. A huge amount of UDMHy must be supplied due to the very low N incorporation efficiency of this precursor. As the UDMHy variations affect growth conditions strongly, the UDMHy partial pressure was fixed at a value of 0.7 mbar, while the TBAs partial pressure was varied to control N incorporation. After achieving a 1 eV (GaIn)(NAs) layer lattice matched to GaAs, Sb experiments were performed by supplying TMSb in addition to the $(Ga_{0.92}In_{0.08})(N_{0.03}As_{0.97})$ -growth conditions.

As already shown in Figure 4.5, the N incorporation decreases for both precursor combinations as soon as TMSb is supplied during growth. This is also observed for the growth of quaternary materials. Accordingly, the N incorporation had to be increased by decreasing the TBAs partial pressure. In Figure 4.6, the reduction of TBAs, which is needed to compensate for the TMSb induced N incorporation decrease, is plotted versus TMSb/III. For the same Ga, UDMHy and TMIn partial pressures, a different initial TBAs partial pressure is observed for $(Ga_{0.92}In_{0.08})(N_{0.03}As_{0.97})$ growth (TMSb/III = 0). This shows that the N incorporation is slightly more efficient with TEGa than with TMGa. The slope a_{slope} of each trend demonstrates how strong the TMSb affects N incorporation. For the TMGa/TMSb combination, a slope of -0.4 TBAs/(TMSb/III) was determined, whereas the slope for the TEGa/TMSb combination is 25 % lower (-0.3 TBAs/(TMSb/III)). This a_{slope} allows us to determine the required TBAs reduction for a given TMSb/III value:

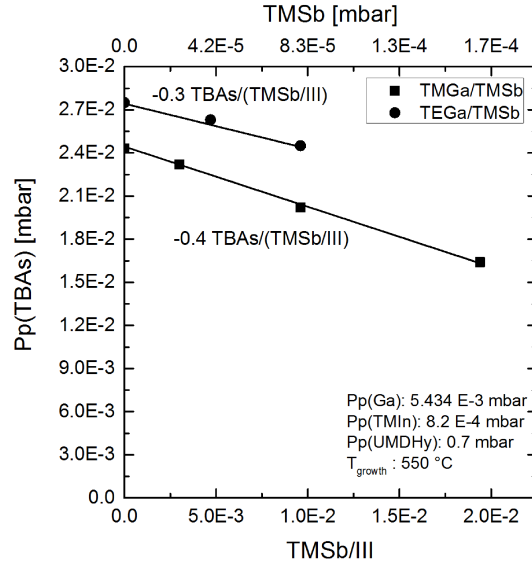


Figure 4.6: TBAs adjustment to annihilate the N incorporation decrease induced by TMSb.

$$Pp(TBAs_{new}) = Pp(TBAs) + a_{slope} \frac{TMSb}{III} \quad (4.1)$$

If one extrapolates this linear behavior, one theoretically would supply no TBAs at all to compensate for the TMSb impact already at the following values: $4.8 \cdot 10^{-4}$ mbar for the TMSb/TMGa and $6.6 \cdot 10^{-4}$ mbar for the TMSb/TEGa combination ($6 \cdot 10^{-2}$; $9 \cdot 10^{-2}$ TMSb/III respectively). This behavior underlines the complexity of growing Sb containing

(GaIn)(NAs) structures in MOVPE using UDMHy, especially as no significant Sb incorporation was achieved as determined by SIMS experiments. Hence, (GaIn)(NAsSb) samples containing around 3 % N and a sufficient amount of Sb grown with UDMHy by MOVPE have not been realized as of yet.

Figure 4.7 shows the PL and Hall measurements of 10 s 700 °C *annealed* 500 nm thick (GaIn)(NAs):Sb bulk samples with different TMSb treatments. These samples were investigated by Stresser¹⁹³ and Maßmeyer¹⁹⁴ under my supervision for a Masters and Bachelors thesis, respectively.

The TMSb was supplied in two different ways:

Preflow: TMSb supply for a given amount of time before (GaIn)(NAs) layer growth, no TMSb during (GaIn)(NAs) growth ($P_p(\text{TMSb}) = 2.29 \cdot 10^{-4}$ mbar).

Equivalent: Integral amount of *preflow* TMSb supplied during 1800 s (GaIn)(NAs) growth.

The TMSb/III ratio for a 160 s *equivalent* sample is calculated as follows: the 160 *pre-flow* sample was treated 160 s before layer growth with a TMSb partial pressure of $2.29 \cdot 10^{-4}$ mbar. The supply time (160 s) is divided by the growth time of the *equivalent* sample (1800 s). This factor, in this case $\frac{4}{45}$, leads to the TMSb partial pressure of $2.04 \cdot 10^{-5}$ and a TMSb/III ratio of $3.26 \cdot 10^{-3}$.

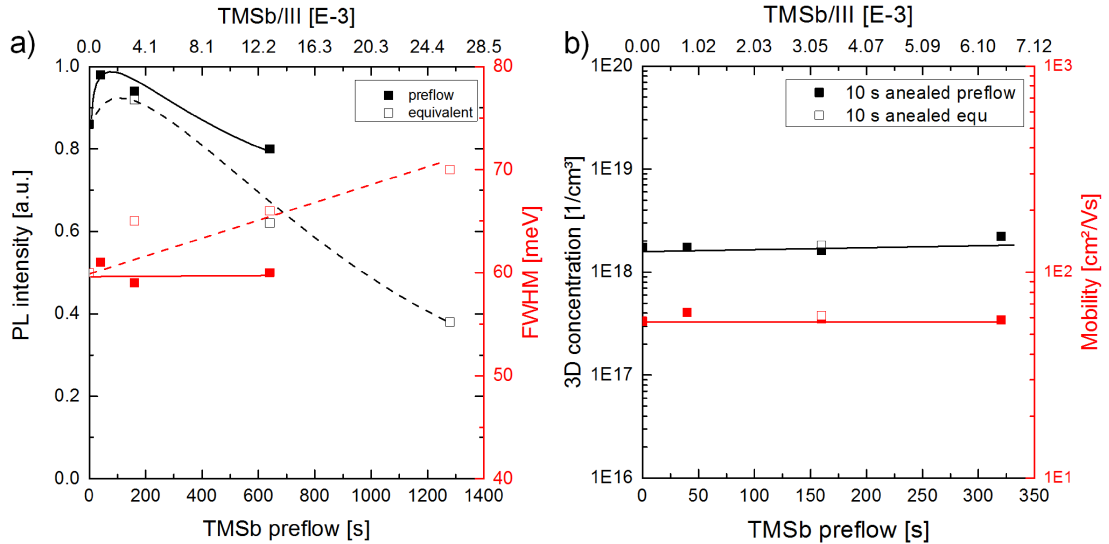


Figure 4.7: PL and Hall results for the TMGa/TMSb combination. Figure a) shows the PL peak intensity on the left and the FWHM on the right y-axis. The bottom x-axis represents the time of TMSb *preflow*. Upper x-axis shows the corresponding TMSb/III ratios for the *equivalent* case. Figure b) depicts the 3D concentration on the left and the mobility on the right y-axis obtained by Hall measurements for the TMGa/TMSb combination. The data was obtained from Stresser¹⁹³ and Maßmeyer¹⁹⁴.

The (GaIn)(NAs) samples with a TMSb *preflow* show no drastic PL peak intensity increase or FWHM decrease (solid squares in Figure 4.7 a)). Only a maximum increase of 15 %

in PL peak intensity was observed for the 40 s *preflow* sample. The higher value of the TMSb *preflow* only deteriorates the PL peak intensity without changing the FWHM. The empty squares in Figure 4.7 a) represent the *equivalent* samples. The PL peak trend is similar to the *preflow* experiments. The FWHM, however, increases with higher TMSb supply during growth.

To investigate the impact of Sb as a *surfactant* on the majority carrier mobility and intrinsic doping level, Hall measurements were performed. Figure 4.7 b) shows the 3D-concentration as well as the mobility dependent on the *preflow* TMSb (solid line). The high intrinsic doping level originates from the unintentional C incorporation of hydrocarbon groups from the MO precursors. An investigation of an *equivalent* sample shows no difference from the *preflow* sample (empty square Figure 4.7). Unfortunately, no improvements in terms of either a lower intrinsic doping level or a higher majority carrier mobility was observed with additional TMSb. Detailed investigations of the Hall-Mobility, doping level and PL spectroscopy were performed by Patrik Stresser¹⁹³ and Oliver Maßmeyer¹⁹⁴.

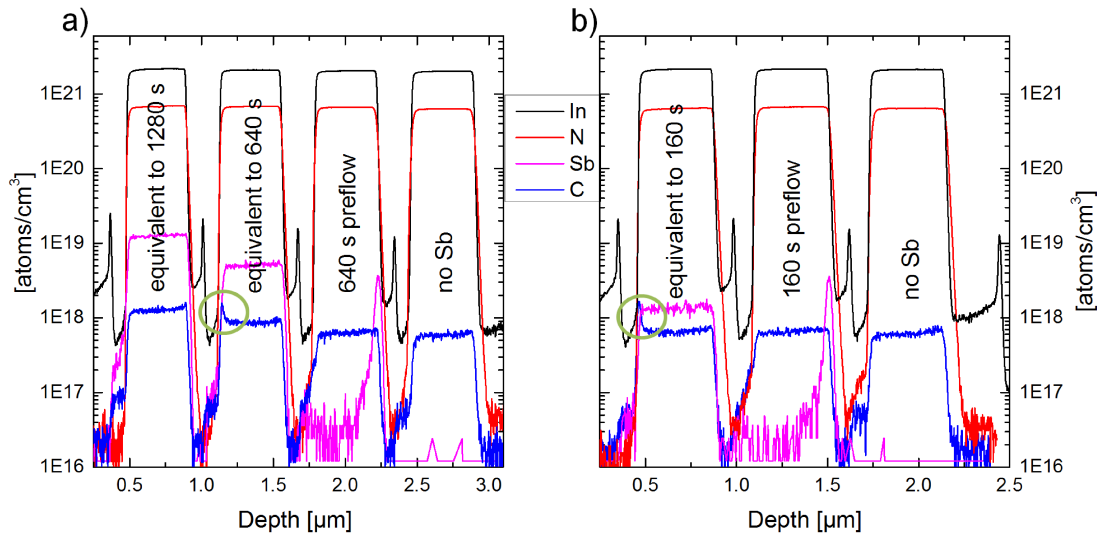


Figure 4.8: SIMS results in a) and b) for the TMGa/TMSb combination with either TMSb *preflow* or the *equivalent* amount supplied during growth.

To verify the results observed so far, SIMS investigations on samples alloyed with various amounts of TMSb are presented.

Each group of peaks presented in Figure 4.8 represents a (GaIn)(NAs) layer grown with the TMGa/TMSb combination. The "no Sb" layer always represents the reference structure without Sb treatment. The remaining (GaIn)(NAs) layers were either treated with a TMSb *preflow* or an equivalent of the *preflow* TMSb amount was supplied during the growth. Unfortunately, no positive effect on the C incorporation was observed. Instead, additional TMSb increases the C incorporation. This might be linked to the small methyl groups present in the TMSb precursor, which can incorporate in addition to the C incorporation observed in the reference structure. Furthermore, the (GaIn)(NAs) structures alloyed

with TMSb during growth demanded for a lower TBAs/III ratio, as the Sb induced N incorporation decrease had to be compensated. Therefore, these layers reveal an even higher C incorporation in comparison with the *preflow* ones.

Some C incorporation profiles of the TMSb treated (GaIn)(NAs) layers, in particular the *equivalent* grown ones, show a sharp peak at the end of the layer growth (highlighted with green circles). One reason for that might be the Sb induced *surfactant* effect, which could lead to an accumulation of C atoms at the growth surface originating from the methyl groups of TMSb, TMIn and TMGa. These features have never been observed in samples grown in an Sb-free environment. The C peak in the "no Sb" layer in Figure 4.9 (b) (highlighted with a yellow circle) occurs due to the huge amount of TMSb supplied the previous experimental run.

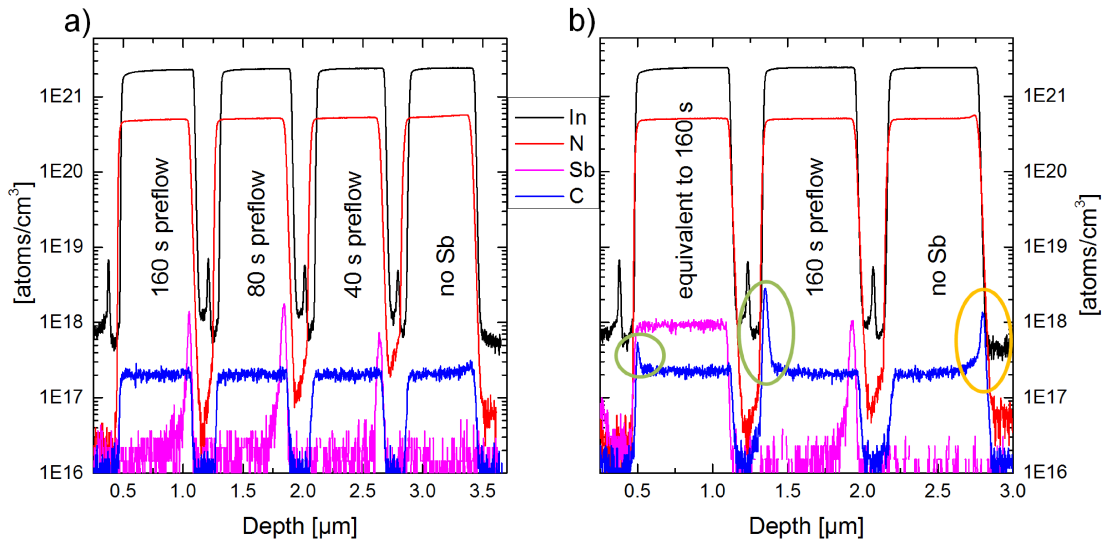


Figure 4.9: SIMS results for the TEGa/TMSb combination with either TMSb *preflow* or the *equivalent* amount supplied during growth.

The results of the TEGa/TMSb combination are presented in Figure 4.9. Unfortunately, this combination did not show a positive effect on C incorporation also when using TMSb as *surfactant*. If one compares the "no Sb" layers in Figure 4.8 and 4.9, one clearly observes the lower initial C incorporation for the TEGa/TMSb combination. This is connected to either the slightly lower TBAs partial pressure needed for the growth with TMGa instead of TEGa, or to additional methyl groups originating from the TMGa precursor.

The Sb incorporation itself is in the doping level. Highest amounts were observed for the TMGa/TMSb combination in the 1280 s *equivalent* grown layer with around $1 \cdot 10^{19}$ atoms/cm³, which corresponds to an Sb content of 0.05 %. Therefore, strain and band gap influence from the Sb incorporation can be ignored.

In summary, the usage of TMSb as a *surfactant* for (GaIn)(NAs) growth did not show any improvements. On the contrary, the growth of a 1 eV sample lattice matched to GaAs becomes even more challenging due to strong TMSb and UDMHy interactions.

Furthermore, either a negligible or negative influence on the optical as well as electrical properties were observed.

4.2.3 Carbon Reduction in (GaIn)(NAs) with TIPIIn and TBAs

In this section, C reduction strategies for DTBAA and UDMHy grown (GaIn)(NAs) samples will be discussed. The N incorporation control techniques were discussed in Section 4.1 and 7.1. As the V/III ratio has a strong influence on the incorporation of parasitic atoms, it is often used as a mechanism to control C incorporation^{8,195}. The N incorporation reduction with additional TBAs supply for DTBAA grown Ga(NAs) is shown in Figure 4.10. It was observed that the N incorporation behavior is linear depending on the DTBAA partial pressure for both cases, with and without TBAs. Therefore, the choice was made to describe this behavior with the TBAs/TEGa rather the TBAs/DTBAA ratio as a V/V related interaction is non-linear.

The N incorporation drops for the TBAs grown case by 50 % at a TBAs/TEGa ratio of only 0.9. For a quantitative comparison, the slopes are calculated and amounts for the TBAs-free case to $91 \frac{\%N}{1 \text{ mbar} P_p(\text{DTBAA})}$ and for the TBAs case to $47 \frac{\%N}{1 \text{ mbar} P_p(\text{DTBAA})}$. To finally determine the reason for this behavior, further experiments with a higher data density are needed. Nevertheless, the assumption of a linear N incorporation behavior for a given TBAs/TEGa ratio is accurate for the experimental range in this work. Consequently, a V/III ratio variation for the DTBAA grown (GaIn)(NAs) layers of the same composition is only possible when changing at least two growth parameters at the same time:

TEGa variation: In order to sustain the same N content at a higher TEGa partial pressure, the DTBAA supply must be increased as well. As the N incorporation efficiency increases with higher growth rate, the factor of the DTBAA partial pressure increase is lower than the TEGa. This partial pressure increase reduces the V/III ratio.

TBAs variation: Additional TBAs must be compensated by an increased DTBAA supply. This increases the overall V/III ratio.

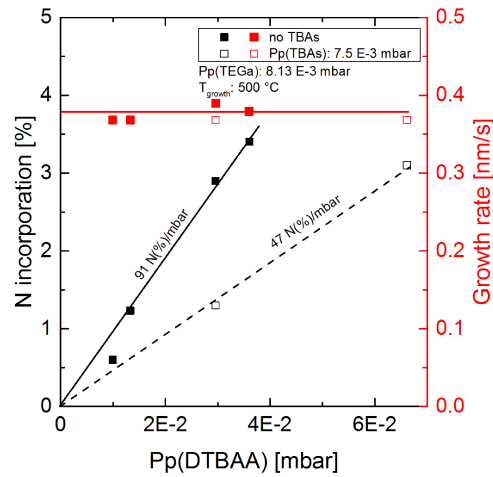


Figure 4.10: TBAs' influence on the N incorporation in DTBAA grown layers.

The epitaxy community assumed the residual groups of methyl based MOs as well as the UDMHy itself was responsible for that C incorporation (cf. Section 2.2)¹⁹⁶. Due to strong interactions between TMIn and UDMHy, no direct evidence was found for the source

of the C incorporation in (GaIn)(NAs). As no such severe interactions were observed during (GaIn)(NAs) growth with DTBAA and TMIn, C incorporation in Ga(NAs) and (GaIn)(NAs) can be compared depending on the In content: a doubling of C incorporation was observed in (GaIn)(NAs) in comparison with Ga(NAs) (Section 7.3, Figure 5 a) and Section 4.2.1, Figure 4.4). These findings make the use of a novel methyl free In precursor inevitable.

Consequently, the alternative In precursor **tri-iso-propyl indium (TIPIn)** was used for (GaIn)(NAs) growth with DTBAA as well as UDMHy. The TIPIn growth characteristics in (GaIn)As are shown in Figure 4.11. Here, the In incorporation is plotted vs. the In/III ratio. The partial pressure was calculated with an approximate vapor pressure of 0.3 mbar obtained from literature^{197,198}. Unfortunately, the In content of TIPIn grown (GaIn)As samples fluctuated. The filled data in Figure 4.11 represent the TIPIn grown (squares and circles) and the empty circles the TMIn grown samples. A clear trend can be seen for the TMIn grown layers, whereas TIPIn grown layers do not follow a common trend. Usually, no V/III dependence is observed for the In incorporation in (GaIn)As, for TIPIn, however, a V/III ratio dependence seems to occur (filled squares and circles). The growth rate of all TMIn and TIPIn grown layers increase with a higher In supply, as depicted with the red background, an observation in line with expectations.

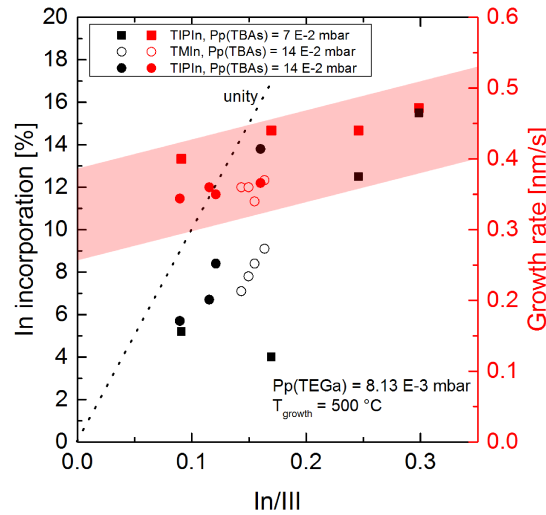


Figure 4.11: In incorporation in GaAs using TIPIn and TMIn. Growth rate increases with higher In/III as indicated with the red background.

The In incorporation fluctuations were also observed in (GaIn)(NAs). Figure 4.12 a) shows the deviation of In incorporation from the lattice matched conditions ($\Delta\text{In} = 0\%$) for TIPIn grown (GaIn)(NAs) samples, gained from the HR-XRD strain with the assumption of a constant N incorporation. The filled squares represent the DTBAA grown samples. The error bars represent the composition range during the growth of the (GaIn)(NAs) samples. Figure 4.12 b) shows the HR-XRD measurements of a lattice matched sample

(green) and another sample where several peak fluctuations were observed (red). This fluctuation is an indication for composition changes during the growth.

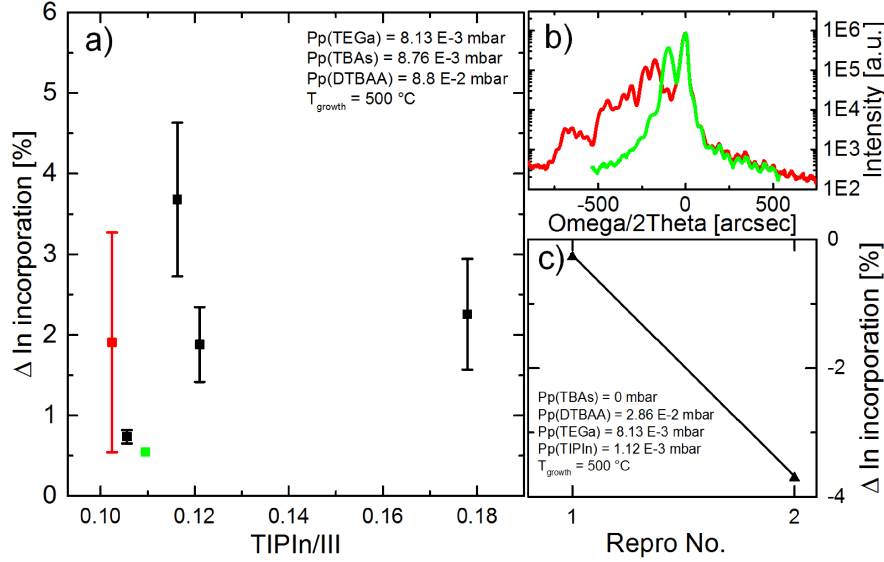


Figure 4.12: The TIPIn grown DTBAA based (GaIn)(NAs) data (a) as well as two representative and color-coded HR-XRDs (b) are presented to show the In incorporation fluctuation. Figure c) represents two samples which were grown under identical growth conditions but with extremely different In contents.

No clear trend with decreasing TIPIn supply was detected. For lower TIPIn partial pressures, an increased In content is observed. Figure 4.12 c) shows two layers with identical (GaIn)(NAs) growth conditions. Here, an In incorporation reduction of around 4 % from initially 8 % was observed. This makes highly controlled (GaIn)(NAs) growth far more challenging.

Neither the V/III dependence shown in Figure 4.11 nor the In incorporation fluctuation was confirmed by our project partners. However, they found strong indications for an intrinsic precursor decomposition within the bubbler^{199,200}. This assumption is based on

No.	TEGa	TMIn	TIPIn	N Precursor	TBAs
1	1x ($8.13 \cdot 10^{-3}$)	1x ($1.5 \cdot 10^{-3}$)		1x ($3 \cdot 10^{-2}$)	
2	1x	1x		2x	1x ($7.5 \cdot 10^{-2}$)
3	1x	1x		3x	1.15x
4	2x	2x		1.5x	
5	1x		1x ($1.12 \cdot 10^{-3}$)	1x	
6	1x		1.6x	3x	1.15x
7	1x	1x ($1.39 \cdot 10^{-2}$)		1x ($9.5 \cdot 10^{-1}$)	1x ($1.35 \cdot 10^{-2}$)
8	1x		1x ($1.07 \cdot 10^{-3}$)	1x	1x

Table 4.1: Growth conditions corresponding to the SIMS layer depicted in Figure 4.13. The N precursors are color coded: cyan represents the DTBAA and brown the UDMHy grown data.

the bubbler pressure increase from 300 mbar up to 800 mbar within 5 months. Furthermore, experiments with a concentration measurement technique called *Epison* showed a molecule density 100 times higher than usually originating from the TIPIn bubbler which was not used over 5 months. The value of the *Epison* measurement stabilized after 10 - 15 minutes at a bubbler flow of around 600 ml/min. This behavior must be investigated further to allow for precise control of the In incorporation.

To determine the C- and O incorporation levels, dedicated SIMS samples were grown with DTBAA as well as UDMHy (cf. Figure 4.13). Table 4.1 summarizes the growth conditions used for each SIMS layer. Hereby, layers 1 - 6 were grown with DTBAA, while layer 7 and 8 were realized with UDMHy.

The results obtained show a strong influence of the V/III ratio on the C- as well as O incorporation, as depicted in Figure 4.13. The reference sample without tertiary-butyl arsine (TBAs) is layer 1. One must distinguish between TBAs (blue background) and TEGa (orange background) variation. Additional TBAs (2 & 3) leads to a C incorporation reduction down to the 10^{17} atoms/cm³ magnitude, whereas higher TEGa (4) not only increases the N- but also makes the C incorporation efficiency even more severe. While the DTBAA supply was increased by a factor of 1.5 to compensate for the N incorporation decrease due to doubled TEGa, the C incorporation increases by a factor of two. This

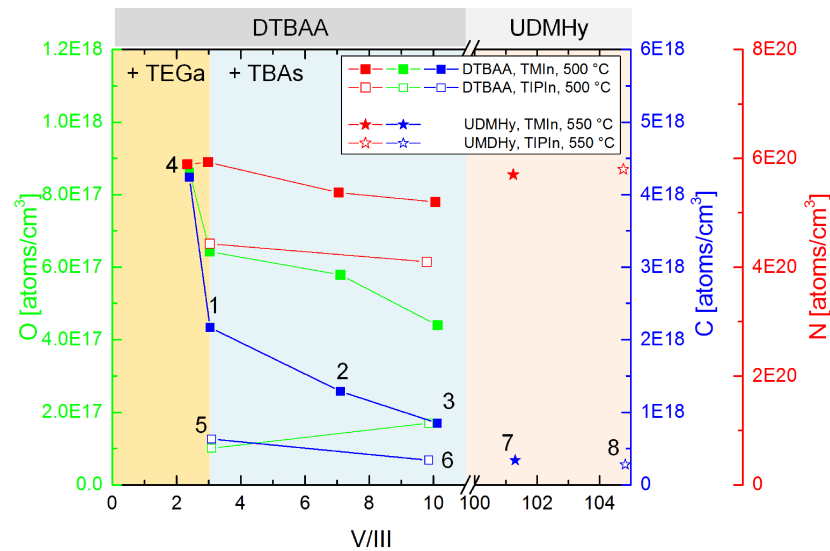


Figure 4.13: SIMS results from TEGa and TBAs experiments for C and O incorporation reduction. Higher V/III ratio reduces the C as well as O content. For simplicity, In is not included in the data. In content is $2 \cdot 10^{22}$ atoms/cm³ with a relative error of 10%.

increase can be explained by the reduced V/III ratio, which is known to increase incorporation of parasitic atoms. Combined experiments with a lower TEGa partial pressure and additional TBAs are potentially a key for an even lower C content. This, however, would

reduce the growth rate, which is not worthwhile for industrial solar cell growth from an economical point of view.

A further TBAs increase is extremely challenging, as the low C incorporation achieved (Figure 4.13 layer 3) was already grown with two DTBAA bubblers in parallel. The gas flow through both bubblers was around 25 % (1700 ml/min) of the total gas flow through the reactor (6800 ml/min). The low DTBAA vapor pressure of around 0.6 - 0.8 mbar is the limiting factor for higher TBAs supply. A third DTBAA bubbler would help to decrease the C incorporation, by increasing the relative DTBAA flow to around 40 % (2700 ml/min) of the total reactor flow, and bringing the standard technical abilities for further DTBAA gas phase supply to an absolute limit.

The empty squares in Figure 4.13 represent the TIPIn grown samples. Substituting TMIn with TIPIn leads to several effects: the N content is reduced by around 25 %, whereas simultaneously the C content is reduced by 70 % and the O by even 80 % (5 vs. 1). With additional TBAs, C incorporation decreases even further, while the O content increases (6). In a comparison of layer 3 and 6, the O content is still 60 % lower for the TIPIn case in comparison with the tri-methyl indium (TMIn) case.

UDMHy grown (GaIn)(NAs) layers were produced as a reference (red background). In Figure 4.13 the data is depicted as stars (7 & 8). The O content is not plotted as the incorporation was below the detection level of the SIMS machine ($<10^{16}$ atoms/cm³). The C incorporation, however, is still the lowest achieved in this work, if normed to the N content. Substituting TMIn did not show any obvious difference.

First, optoelectronic studies dependent on *annealing* were performed. Therefore, three different *annealing* treatments were applied: 700 °C, 10 s and 20 s in the RTA as well as 700 °C 90 minutes in the AIX-200 reactor. Hereby, the 90 minutes *reactor annealing* divides in 45 minutes H₂-TBAs stabilized and 45 minutes unstabilized (N₂) treatment. These samples were investigated with Hall (s.i. substrates), ECV (p-dot substrates) as well as PL. The summary of the results is shown in Table 4.2.

The following nomenclature is introduced to identify the layers as well as the *annealing* conditions:

D: DTBAA MIn: TMIn IIn: TIPIn U: UDMHy As: TBAs

R45: *reactor annealing* at 700 °C for 45 minutes TBAs stabilized and 45 minutes unstabilized.

RTA10: RTA *annealing* at 700 °C for 10 s

RTA20: RTA *annealing* at 700 °C for 20 s

General Information			Opt. Res.			Electr. Res.	
	SIMS [at./cm ³]	Anneal.	Int-PL [a.u.]	PL-P. [eV]	FWHM [meV]	Mobility [cm ² /Vs]	Density [1/cm ³]
D-MIn							
DTBAA, TMIn	O: $6.4 \cdot 10^{17}$	RTA10	$6.9 \cdot 10^{-4}$	1.05	93	p 40	$6.2 \cdot 10^{17}$
TEGa	C: $2.2 \cdot 10^{18}$	RTA20	$1.3 \cdot 10^{-4}$	1.05	83	n 1500	$1.4 \cdot 10^{16}$
s.i. substrate		R45	$2.0 \cdot 10^{-2}$	1.06	77	p 30	$2.3 \cdot 10^{18}$
D-IIIn							
DTBAA, TIPIIn	O: $1.0 \cdot 10^{17}$	RTA10	$1.4 \cdot 10^{-3}$	1.10	71	p 38	$2.4 \cdot 10^{17}$
TEGa	C: $6.3 \cdot 10^{17}$	RTA20	$9.5 \cdot 10^{-4}$	1.11	81	p 50	$1.2 \cdot 10^{17}$
s.i. substrate		R45	$3.6 \cdot 10^{-2}$	1.12	72	p 56	$2.6 \cdot 10^{18}$
D-MIn-As							
DTBAA, TMIn	O: $4.4 \cdot 10^{17}$	RTA10	$3.7 \cdot 10^{-4}$	1.13	84	p -	$5.2 \cdot 10^{17}$
TEGa, TBAs	C: $8.5 \cdot 10^{17}$	RTA20	$1.4 \cdot 10^{-4}$	1.12	76	p -	$3.1 \cdot 10^{17}$
p-dop substrate		R45	$5.5 \cdot 10^{-3}$	1.12	75	p -	$9.8 \cdot 10^{16}$
D-IIIn-As							
DTBAA, TIPIIn	O: $1.7 \cdot 10^{17}$	RTA10	$3.1 \cdot 10^{-4}$	1.12	85	p -	$4.9 \cdot 10^{17}$
TEGa, TBAs	C: $3.4 \cdot 10^{17}$	RTA20	$2.9 \cdot 10^{-4}$	1.11	76	p -	$3.3 \cdot 10^{17}$
p-dop substrate		R45	$8.7 \cdot 10^{-3}$	1.15	70	p -	$6.3 \cdot 10^{15}$
U-MIn-As							
UDMH _y , TMIn	O: -	RTA10	$4.2 \cdot 10^{-2}$	1.07	64	p -	$1.2 \cdot 10^{18}$
TEGa, TBAs	C: $3.4 \cdot 10^{17}$	RTA20	$1.2 \cdot 10^{-2}$	1.07	63	p -	$9.8 \cdot 10^{17}$
p-dop substrate		R45	$1.2 \cdot 10^{-1}$	1.08	55	p -	$2.6 \cdot 10^{17}$
U-IIIn-As							
UDMH _y , TIPIIn	O: -	RTA10	$3.0 \cdot 10^{-2}$	1.07	65	p -	$1.2 \cdot 10^{18}$
TEGa, TBAs	C: $2.8 \cdot 10^{17}$	RTA20	$1.1 \cdot 10^{-2}$	1.07	62	p -	$4.1 \cdot 10^{17}$
p-dop substrate		R45	$1.1 \cdot 10^{-1}$	1.08	59	p -	$3.5 \cdot 10^{17}$

Table 4.2: Optoelectronic results of (GaIn)(NAs) samples grown with various combinations of TEGa, TMIn, TIPIIn, TBAs, UDMHy and DTBAA. Additionally, three different *annealing* conditions were applied to these samples.

Consequently, the D-IIIn-As-R45 layer was grown with DTBAA, TIPIn and TBAs and was *annealed* in the reactor for 90 min, which divides in 45 minutes H₂-TBAs stabilized and 45 minutes unstabilized (N₂) treatment.

While no sufficient PL intensity was obtained from *as grown* samples, *annealing* drastically increased the PL intensity. Throughout all samples, the *reactor annealed* ones show the highest PL intensities and the lowest FWHM values. This must be investigated in more detail, as this means that no comparable *annealing* conditions for the RTA were found as of yet. The PL intensity decreases for the 20 s *annealed* sample in comparison with the 10 s *annealed* sample. This result indicates that the integral thermal energy (temperature + time) supplied for *annealing* is too high under given RTA conditions. Furthermore, the UDMHy grown (GaIn)(NAs) samples show the highest total intensities as well as lowest FWHM values. There is at least one magnitude of difference in the PL intensity between the DTBAA and UDMHy grown samples. This probably is connected to the unintentional O incorporation originating from the DTBAA precursor. Furthermore, the growth temperature of the DTBAA grown (GaIn)(NAs) samples was 500 °C, whereas UDMHy grown (GaIn)(NAs) layers were realized at 550 °C. This difference in growth temperature has an effect on the intrinsically incorporated crystal defects and therefore on the optoelectronic properties as well.

The (GaIn)(NAs) layer grown on p-doped substrate cannot be investigated via Hall. Therefore, mobility data is presented only for (GaIn)(NAs) layers grown on s.i. substrates. In contrast to the PL intensity and the FWHM, the mobility increases in the given order for the D-IIIn sample: RTA10, RTA20, R45. The D-MIn-RTA20 sample shows a very large major carrier mobility of 1500 cm²/Vs as well as untypical n-doping. Ga vacancies are described in literature as potentially n-doping^{201,202}. Therefore, an explanation might be temperature-induced Ga vacancies, leading to a compensation of the p-doping, as well as over-compensation of these, thus leading to an n-doped material. Why this happens only for this layer and whether this is the mechanism that is occurring, needs to be investigated in the future in more detail.

The doping densities were investigated with Hall and ECV, as shown in Table 4.2. When comparing RTA10 and RTA20 samples, one instantly observes a decrease in the active doping density for longer *annealing*. In literature, the C_{As}-As_i-C_{As} clusters which act as an p-dopant are believed to dissolve due to temperature and form C interstitials, reducing the p-doping^{47,203}. Hereby, the As_i is an interstitial, and C_{As} incorporates onto the group V lattice site.

The comparison between the RTA and *reactor annealed* samples in terms of active doping density is difficult to interpret. ECV based measurements always show the lowest doping density for the R45 samples, whereas Hall measurements show opposite results. This leads

to the assumption that a systematic difference in the investigation techniques leads to the different values.

Additionally, the C incorporation obtained by SIMS (cf. Figure 4.13) is also presented in Table 4.2. As discussed previously, C incorporation is related to p-doping. When comparing the doping densities obtained by Hall and ECV, one observes the discrepancy between the C content and the measured active doping density. As mentioned above, further defects like vacancies (V_x) are a potential source of n- and p-doping, for example V_{Ga} and V_{As} , respectively. Furthermore, O incorporation is known to compensate the C acceptors²⁰⁴. To gain better insight in to the physical processes, further experiments need to be performed in the future, aiming for systematic ECV and Hall results.

4.3 MOVPE Growth of Ga(NAsSb) Structures

In this section, the Sb incorporation in Ga(NAs) is discussed. As observed in Section 4.2.2 and according to literature^{134,153}, the growth of 1 eV Ga(NAsSb) lattice matched to GaAs is very challenging, if not impossible, with the commercially available N precursor UDMHy. Therefore, Ga(NAsSb) growth utilizing the novel precursor DTBAA was investigated in Section 4.3.1. Furthermore, results of a second precursor DTBSbTBA, designed especially for N and Sb incorporation, will be presented in Section 4.3.2.

4.3.1 DTBAA grown Ga(NAsSb)*

In Section 4.2.2, Sb was utilized as a *surfactant* and unfortunately did not meet the expectations of leading to a better (GaIn)(NAs) material quality. The sharp N incorporation decrease with additional Sb was discussed and is one of the main reasons why no 1 eV Ga(NAsSb) material lattice matched to GaAs was realized in MOVPE as of yet. In Section 4.2.1, the N incorporation efficiency of DTBAA in comparison with UDMHy was discussed. As no N incorporation decrease was observed for (GaIn)(NAs) growth with DTBAA and TMIIn, experiments on Ga(NAsSb) were carried out with similar expectations.

For the first time, a 1 eV Ga(NAsSb) layer lattice matched on GaAs grown in MOVPE was realized with TEGa, DTBAA and tri-ethyl antimony ($(C_2H_5)_3Sb$, TESb) (Section 7.4). Hereby, a complex incorporation behavior of Sb and N was found. An important result was the requirement for low V/III ratios (1.0 - 2.0) to achieve sufficient Sb as well as N incorporation in combination with a smooth surface. Higher V/III ratios lead to a lower Sb incorporation, which coincides with higher root mean square (RMS) values for surface roughness obtained by AFM. The reason for that is presumably the group V competition,

* Parts of this work are published²⁰⁵ and presented in Section 7.4

in which Sb is obviously not dominating. Consequently, surplus Sb accumulates on the surface and leads to 3D growth.

Figure 4.14 shows the same data as presented in Section 7.4 (Figure 1) with additional UDMHy data obtained from the (GaIn)(NAs):Sb results in Section 4.2.2 (Figure 4.5 b)). The N incorporation in UDMHy grown Ga(NAs) decreased by 50 % when realized with a TMSb partial pressure of $2.52 \cdot 10^{-3}$ mbar (grey solid line). The grey dashed line is an extrapolation of the UDMHy grown Ga(NAs) results. Despite the differences in growth conditions between the UDMHy and DTBAA grown samples like growth temperature (550°C , 500°C) and TEGa partial pressure ($5.4 \cdot 10^{-3}$ mbar, $8 \cdot 15^{-3}$ mbar), the deviation between the

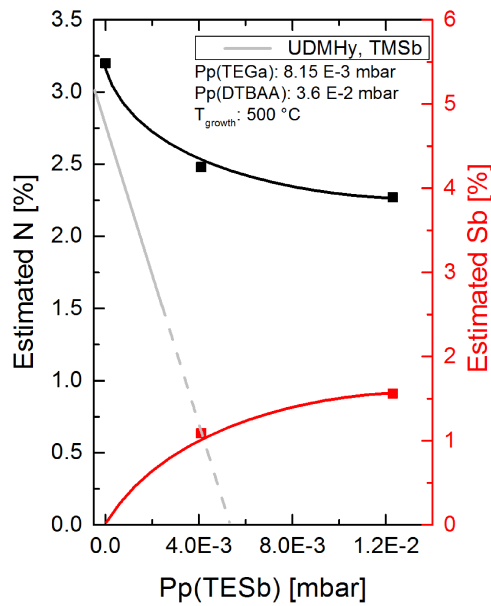


Figure 4.14: N content in Ga(NAsSb) dependent on Sb supply for DTBAA and UDMHy. UDMHy data obtained from Figure 4.5 b). Grey dashed line is an extrapolation of the UDMHy data.

growth conditions for a positive Sb *surfactant* effect were found, or no such effect exists in terms of C incorporation for this material. Further experiments with higher data density as well as higher growth temperatures must follow to increase the crystal quality.

4.3.2 DTBSbTBA grown Ga(NAsSb)

Because of the enormous advantages of DTBAA in comparison with the conventional N precursor UDMHy, a similar molecule, namely DTBSbTBA with Sb instead of As and one more tertiary butyl group, was designed and synthesized by the chemistry department in Marburg (Section 2.1.2). TEGa, TBAs and DTBSbTBA were used for the following Ga(NAsSb) experiments. Therefore, 5 QW structures on s.i. exact (001) GaAs

solid grey and solid black line shows representatively how strong the Sb supply affects the N incorporation in UDMHy grown Ga(NAs)(Sb) in comparison with the DTBAA grown layers. At the same time, no Sb incorporation was achieved for the UDMHy grown samples, whereas DTBAA grown Ga(NAsSb) reveals a sufficient Sb content (cf. Figure 4.14). With the knowledge of the complex interaction of Sb and N, which is discussed in more detail in Section 7.4, a 1 eV Ga(NAsSb) sample lattice matched to GaAs was realized in MOVPE. Figure 5 in Section 7.4 shows the HR-XRD and PL data of this sample grown at 475°C , confirming the statement of a lattice matched 1 eV sample. However, SIMS studies showed that the Ga(NAsSb) sample is deteriorated by O and C incorporation, which generally is higher for lower growth temperatures (Figure 6, Section 7.4). Unfortunately, either no

substrates were grown by MOVPE. Unfortunately, the experiments show N incorporation only in the doping level as seen in the SIMS results (Figure 4.15). So far, no sufficient N incorporation was achieved with this precursor. Nevertheless, the Sb incorporation behavior was investigated. The results are shown in Figure 4.16.

Figure 4.16 a), c) and e) represent the data obtained by HR-XRD with the assumption of no N incorporation, whereas b) d) and f) are derived from the SIMS measurement shown in Figure 4.15. Additionally, AFM micrographs of the marked samples are presented below. The RMS values of the surface roughness are denoted within the micrographs, which are color-coded and assigned to the highlighted data points.

The DTBSbTBA variation depicted in Figure 4.16 a) shows a very low impact on the Sb incorporation for the range investigated. The solid line represents the results obtained with higher TBAs partial pressure. Here, the Sb content seems to saturate after a DTBSbTBA supply of 350 ml/min, as also confirmed by the SIMS results presented in Figure 4.16 b) (magenta).

At the same time, O incorporation increases with higher DTBSbTBA supply, indicating that the O originates from the novel precursor. Furthermore, no drastic change in C incorporation was observed. The graph in Figure 4.16 a) contains additional results obtained with a lower TBAs partial pressure. This TBAs reduction of 50 % increases the Sb incorporation from around 5 to 19 %. The observed strong V/V dependence of Ga(AsSb) samples is also known from other Sb precursors and described in literature²⁰⁶. AFM measurements revealed smooth surfaces for the DTBSbTBA range investigated.

Temperature variation results in the range between 490 °C and 550 °C are shown in Figure 4.16 c) and d). Here, a decrease of all measured contents as Sb, N, C and O was observed. This agrees with the results obtained with a conventional precursor and is explained by a higher desorption rate of the atoms from the surface. The growth rate, however, increases due to higher TEGa precursor decomposition. At the same time, the surface roughness decreases with the higher temperature from 0.29 to 0.20 nm (RMS). The final interrelation investigated is presented in Figure 4.16 e) and f). In this context, an Sb incorporation increase by a factor of three was observed when doubling the TEGa partial pressure. At the same time, N incorporation shows only minor changes, whereas C and O incorporation increases due to lower V/III ratio. The surface morphology, however, reveals

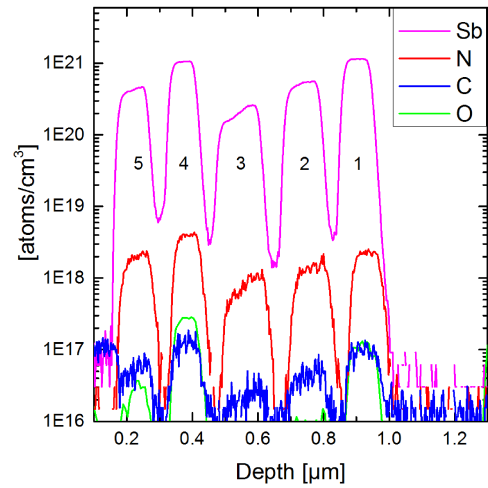


Figure 4.15: SIMS results for Ga(NAsSb) structures grown with DTBSbTBA. Sb incorporation dominates, while no sufficient N incorporation was achieved.

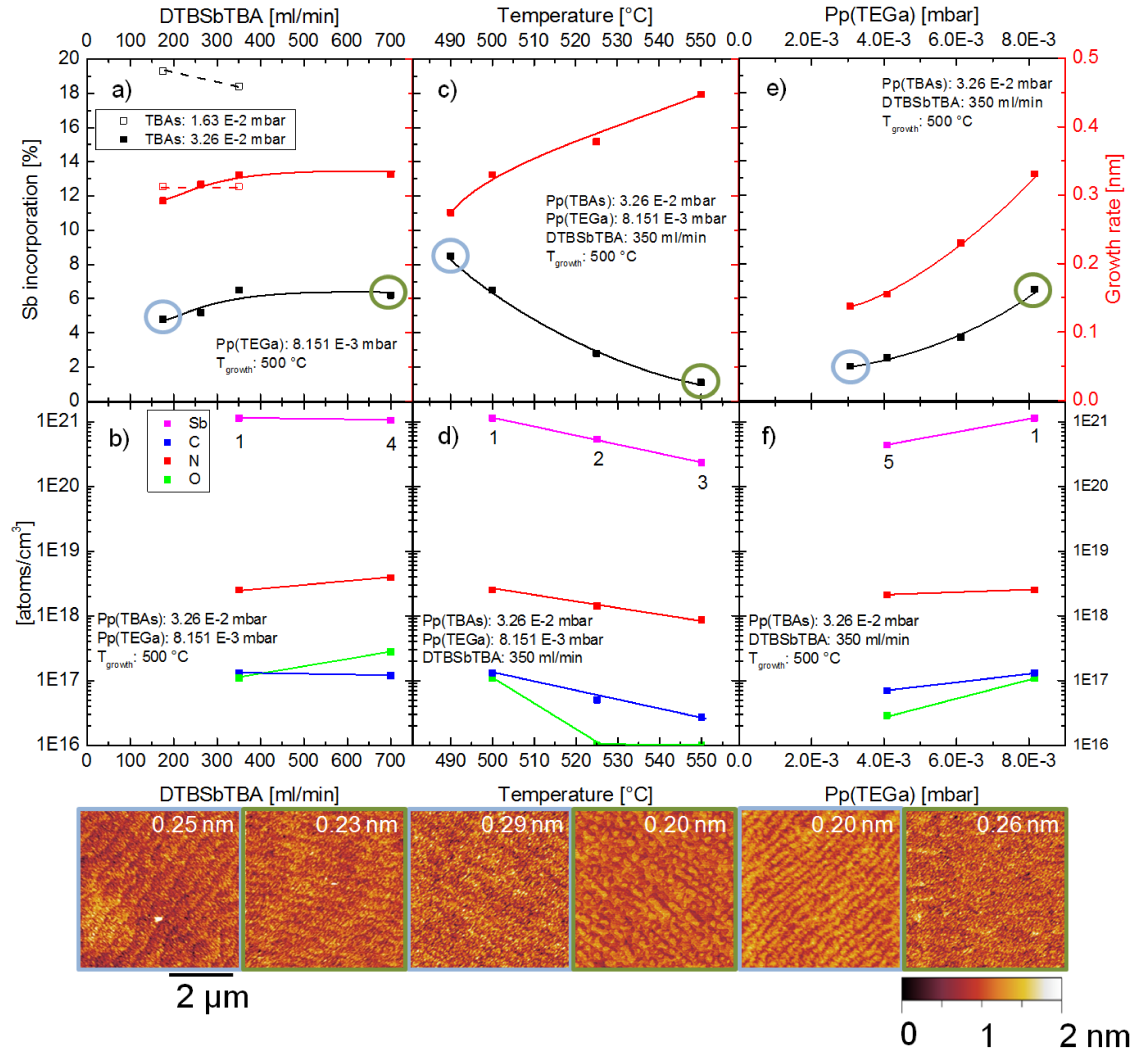


Figure 4.16: HR-XRD (a, c, e) and SIMS (b, d, f) data plotted vs. DTBSbTBA and growth temperature as well as TEGa supply. AFM micrographs are presented below for the circled data. The numbers next to the data points are related to the layer number shown in Figure 4.15.

a low surface roughness between 0.20 and 0.26 nm (RMS), indicating a high quality surface.

Even if this precursor has not shown sufficient N incorporation, further testing and comparison with a conventional Sb precursor like TMSb and TESb are interesting in terms of parasitic O and C incorporation. So far, only qualitative comparison is possible, as no systematic investigations were performed on this topic.

CHAPTER 5

(GaIn)(NAs) Solar Cell Structures

This chapter focuses on the discussion of the solar cell results obtained at *Fraunhofer Institute of Solar Energy-Systems* (ISE) in the framework of a joint dilute N project. The growth as well as *annealing* conditions and nomenclature will be addressed first, followed by the results. In the results section, the V_{OC} and short circuit current density (J_{SC}) variations dependent on precursor combinations will be discussed. Furthermore, selected light IV-curves and EQE measurements will be presented.

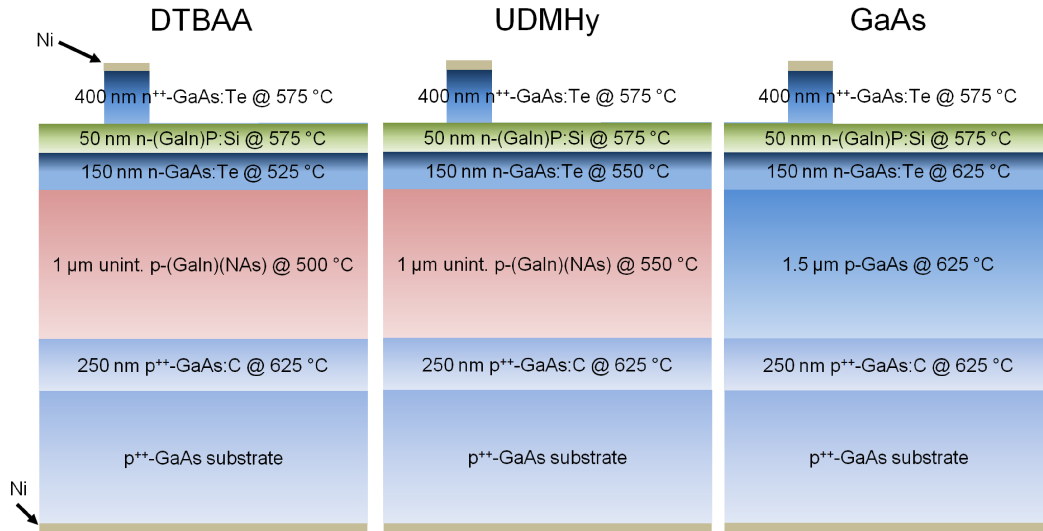


Figure 5.1: Solar cell structure of three different sets: DTBAA, UDMHy and GaAs. The growth temperature of the (GaIn)(NAs) material based on DTBAA is 500 °C, whereas the UDMHy based material was grown at 550 °C. Highly n-doped GaAs was chosen to be the emitter, while the unintentionally p-doped (GaIn)(NAs) material acts as the base. The GaAs reference cell was grown at 625 °C. The Ni contacts on the top and bottom were deposited by electroplating.

All solar cells were grown on p-doped exact (001) GaAs substrate. The structure of the cells is shown in Figure 5.1. A 250 nm highly p-doped ($2 \cdot 10^{18}$ atoms/cm³) GaAs buffer layer was grown on top, followed by the intrinsically p-doped 1000 nm thick (GaIn)(NAs)

base material. A hetero solar cell design was chosen to focus only onto the intrinsically p-doped (GaIn)(NAs) material. Hence, a $1.5 \cdot 10^{18}$ atoms/cm³ n-doped GaAs emitter was grown. The $2 \cdot 10^{18}$ atoms/cm³ n-doped (Ga_{0.50}In_{0.50})P layer functions on the one hand as an etch stop and on the other hand as a window layer, which acts as a barrier for minority carriers in the emitter. The $6 \cdot 10^{18}$ atoms/cm³ n-doped top GaAs layer is used as a contact layer, to lower the front side contact resistance. After processing, it remains only beneath the metal fingers. For the front and back contacts, Ni-films were deposited by electroplating. While the back side received a full area coverage, a simple u-shaped grid design was used for the front side.

Five (GaIn)(NAs) solar cell sets were grown using TEGa. Two of them based on UDMHy in combination with TMIn and TBAs or TIPIn and TBAs. The other three (GaIn)(NAs) solar cells based on DTBAA were grown either with TMIn, TMIn and TBAs or TIPIn and TBAs. Additionally, a GaAs solar cell was grown as a reference sample to allow the classification of the general sample and fabrication quality. Furthermore, each of the solar cells mentioned above was *annealed* at 700 °C in five different ways. Three pieces were *annealed* in the RTA at atmospheric pressure under N₂ environment for either 10 s, 20 s or 30 s. The other two pieces were *annealed* in the Aix-200 reactor at the following conditions:

R45 *annealing*: 50 mbar reactor pressure, 45 min TBAs stabilized under H₂ followed by 45 min unstabilized under N₂, 90 minutes in total.

R60 *annealing*: 50 mbar reactor pressure, 60 min TBAs stabilized under H₂ followed by 30 min unstabilized under N₂, 90 minutes in total.

All of these samples were fabricated and investigated with the methods introduced in Section 3.7 with the knowledge of the solar cell fundamentals introduced in Section 2.3. The nomenclature introduced on page 47 will be used to identify the solar cell type as well as the *annealing* condition.

Each solar cell set was grown at different temperatures. The DTBAA based solar cell was grown at 500 °C, the UDMHy based at 550 °C and the GaAs based at 625 °C. Higher growth temperatures of GaAs based dilute N materials require an exponentially higher DTBAA supply (cf. Section 7.1). Therefore, the DTBAA based material was limited in growth temperature, due to a limited supply by the available DTBAA source.

The doping densities as well as O and C contents of each individual (GaIn)(NAs) layer were determined in test structures and are summarized in Table 4.2.

The applied processing technique leads to some restrictions on interpreting the cell results. Due to the simple grid design, high contact resistance and thin metal layer thickness, a high distributed series resistance is present. Additionally, parasitic Ni coating on the solar cell edges can occur and lead to a possible short circuit, therefore lowering the R_{Sh} .

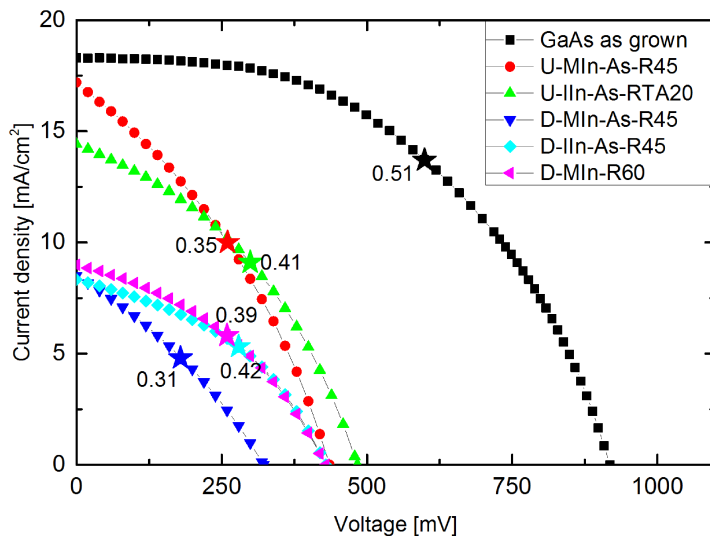


Figure 5.2: Light IV-curves of the *quick cell* processed solar cells. Due to the applied processing method, a high R_S , including the transversal flow resistivity, and a low R_{Sh} are present, hindering detailed interpretation of these data. MPPs are marked as stars, the labels represent the FF value.

These effects can be seen in the light IV-curves of selected solar cells in Figure 5.2. The influence of the R_S , including the transversal current flow, and R_{Sh} is clearly present, lowering the FF significantly. While the applied processing method limits the possibility for interpretation of the whole light IV-curve, the V_{OC} and J_{SC} (for low enough R_{Sh}) remain unaltered. This allows quantum efficiency measurements and their interpretation in combination with the voltages as a function of growth conditions.

Figure 5.2 shows as expected the highest V_{OC} value for GaAs solar cells. The next best V_{OC} value is obtained from the UDMHy cells followed by the lowest values from DTBAA grown solar cells. A similar trend can be observed for J_{SC} values.

One must keep in mind that no GaAs filter was applied for the light IV-curves measurement leading to higher current density compared to an application in a multi-junction solar cell as photon-energies above 1.42 eV also contribute to the current.

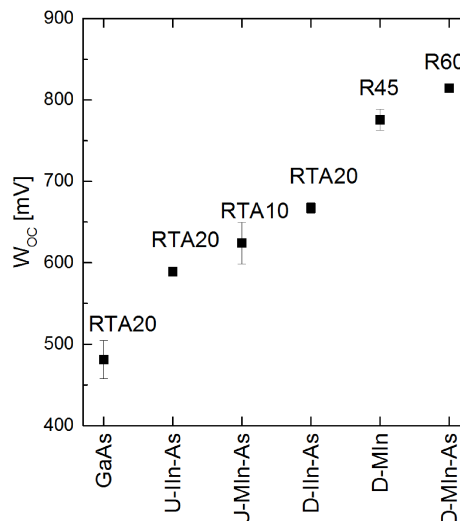


Figure 5.3: Best W_{OC} data plotted vs. solar cell category. The label represents the *annealing* condition.

Nevertheless, the V_{OC} gives a good impression of the material quality. To exclude the influence of the band gap and the voltage, the best W_{OC} values are plotted dependent on the solar cell growth conditions in Figure 5.3.

We neglect the impact of the different *annealing* treatments, as no general trend was observed. A solar cell is considered to be of higher quality if the W_{OC} is low. As discussed in Section 2.3, a W_{OC} of around 400 mV represents a good solar cell. In our case, the best GaAs solar cell shows a W_{OC} value of 470 mV. In this case, the solar cell structure as well as growth was not optimized and therefore leads to lower J_{SC} . Furthermore, the applied back surface field was not intense enough to prevent minority electrons within the base material to diffuse into the substrate. Due to the high doping of the substrate, higher recombination takes place, increasing the J_0 , which in turn decreases the V_{OC} .

However, GaAs based solar cells show the lowest W_{OC} as expected, followed by the UDMHy based (GaIn)(NAs) material. The U-In-As solar cell with a W_{OC} of around 600 mV is slightly better than the U-MIn-As solar cell, whose W_{OC} value is higher and amounts to around 630 mV. Therefore, a slight improvement of the W_{OC} is observed when the UDMHy based (GaIn)(NAs) material is grown with TIPIIn instead of TMIn.

The DTBAA based material exhibits overall a higher W_{OC} . Hereby, the lowest W_{OC} was determined for the D-In-As layer. This lower value corresponds to the O and C content, which is the lowest for the D-In-As case. Consequently, D-MIn-As and D-MIn layers show both a higher O and C content and therefore exhibit a higher W_{OC} . In Section 4.2.3, additional TBAs

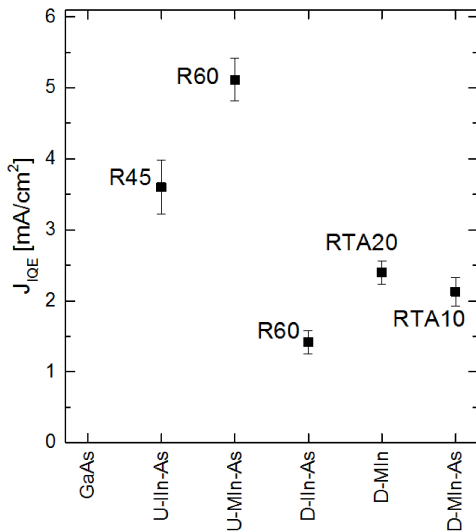


Figure 5.4: Plotted is the current calculated from the IQE measurements for wavelengths between 890 nm and 1200 nm and AM 1.5g spectrum. The label represents the *annealing* conditions.

was supplied to DTBAA based (GaIn)(NAs) growth to reduce the C incorporation by 60 %. This reduction was believed to enhance the solar cell performance. Unfortunately, the W_{OC} of the D-MIn-As solar cell is even higher than the W_{OC} of the TBAs-free D-MIn material. One explanation might be the by three times higher DTBAA partial pressure, which was supplied for the D-MIn-As case to compensate the N reduction. Hence, either unknown impurities were incorporated or the general crystal quality was deteriorated under given growth conditions.

Overall, the W_{OC} shows that the UDMHy based material is still of higher quality than the DTBAA based solar cells. This, however, is probably related to much higher O content in DTBAA grown material. Furthermore,

TIPIIn was observed to reduce the W_{OC} in both cases.

As no GaAs filter was used, photon-energies higher than 1.42 eV were absorbed by the solar cell too. Therefore, the J_{SC} obtained by the light IV-curves cannot be used for the evaluation of the (GaIn)(NAs). To determine the (GaIn)(NAs) solar cell quality in the range of interest, the current obtained from photon-energies in the range of around 1.0 - 1.4 eV (890 nm and 1200 nm) was calculated for each cell. For that, the IQE was determined by measuring the EQE and taking the reflection into account. Consequently, the current density was obtained by folding the IQE spectra in the range mentioned above with the AM 1.5g spectra. The error was estimated from the current density calculated for the full EQE and correlated with the J_{SC} from the light IV-curves. Theoretically, highest current densities achievable with a fully active structure of the present design, amounts to around 10.5 mA/cm².

These current densities are plotted in Figure 5.4. The UDMHy grown solar cells show higher current densities, similar to the W_{OC} data. Highest current densities were observed for the U-MIn-As solar cell. The TIPIn grown U-IIn-As solar cell shows significantly lower current density in comparison with the U-MIn-As solar cell. A similar behavior is found for the D-MIn-As vs. D-IIn-As case. This finding is an indication for a very high R_S . The usage of TIPIn improves the W_{OC} slightly, however, the current densities are greatly reduced. This reduction is probably related to the In fluctuations during growth, which affects the band offsets and therefore also the diffusion length of the minority carriers within the (GaIn)(NAs) solar cell base.

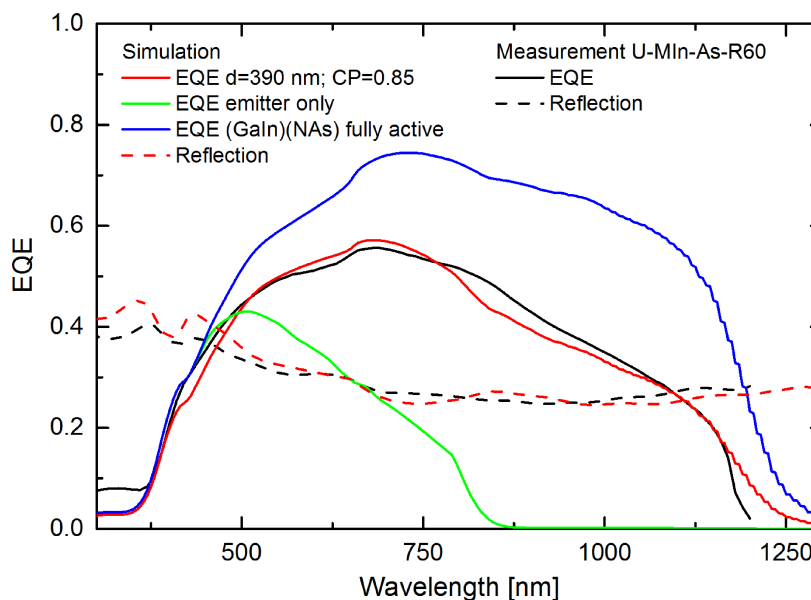


Figure 5.5: The EQE and reflection measurements are shown in black, while the simulations are presented in green, red and blue. The simulations performed by Dr. Jens Ohlmann reveal an active (GaIn)(NAs) material thickness of only 390 nm.

In comparison with the best UDMHy grown solar cell, the best DTBAA based material shows only 50 % of the current densities. D-MIn-As and D-MIn solar cells show a current

density in the range of 2 - $2.5 \frac{mA}{cm^2}$. Unfortunately, additional TBAs supply for the D-MIn-As case did not increase the J_{SC} . This can be explained by the high O incorporation.

Within the DTBAA grown solar cells, the D-IIIn-As solar cell shows the best W_{OC} of around 680 mV. The current density, however, is the lowest observed. These trends are at odds with each other and need to be investigated in the future.

Selected EQE measurements were simulated to evaluate the solar cell quality in higher detail. Therefore, U-MIn-As-R60 and D-MIn-As-R45 solar cells were chosen. With the transfer-matrix method the absorption and reflection of each layer were simulated, assuming perpendicular impinging light.

In Figure 5.5, the measured EQE as well as the reflection are plotted vs. the wavelength in black solid and dotted lines. The green, red and blue solid lines represent three different EQE simulations, while the red dotted line is the simulated reflection. The green solid line represents the GaAs emitter only, the blue line includes a fully active 1000 nm (GaIn)(NAs) layer. The red solid line is a simulation that comes close to the measured EQE. Hereby, an active thickness of 390 nm (GaIn)(NAs) was assumed, with a total carrier collection probability (CP) of only 85 %. In reality, the collection probability is wavelength dependent, which is neglected here for simplicity. The assumption of 390 nm active is based on low diffusion length, which hinders carriers generated in the lower 610 nm absorber material to reach the depletion region.

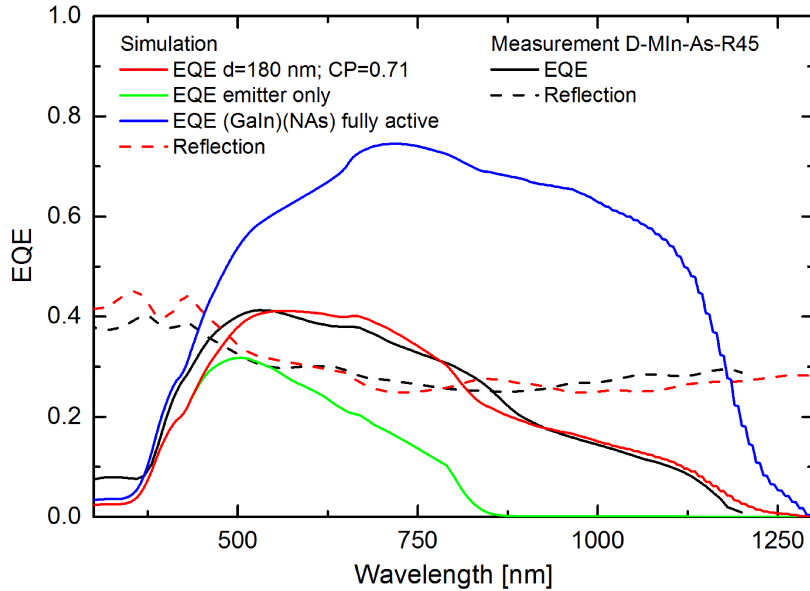


Figure 5.6: The EQE and reflection measurements are shown in black, while the simulations are presented in green, red and blue. The simulations performed by Dr. Jens Ohlmann reveal an active (GaIn)(NAs) material thickness of only 180 nm. This low value is connected to the high O content and high background doping.

With the assumption that the intrinsic doping level of the U-MIn-As-R60 sample is similar to the U-MIn-As-R45 sample from Table 4.2 (ca. $3 \cdot 10^{17}$ atoms/cm³), a build in potential

of 1 V as well as the dielectric constant of GaAs (12.9), the depletion width amounts to around only 80 nm. This thickness divides into 13 nm within the GaAs material and 67 nm within the (GaIn)(NAs) material. From these values, one can estimate the diffusion length of the minority charge carrier to be in the range of 320 nm.

The same procedure was performed with the D-MIn-As-R45 solar cell. The corresponding EQE measurement and simulations are presented in Figure 5.6. One instantly observes the lower EQE for the DTBAA grown solar cell in comparison with the U-MIn-As-R45 case. The simulations reveal an active (GaIn)(NAs) layer of only 180 nm. When assuming the intrinsic doping to be in the range of $1 \cdot 10^{17}$ atoms/cm³, a depletion width of 125 nm is calculated. This leaves around 8 nm within the GaAs and 117 nm in the (GaIn)(NAs) material, leading to a diffusion length value of only 63 nm. This value is around five times lower than the U-MIn-As-R45 solar cell and therefore drastically reduces the solar cell efficiency. The lower diffusion length of the DTBAA based solar cell is presumably related to the O content, which acts as a deep level impurity.

One must keep in mind that *quick cell* fabrication is still under development and the data obtained has strong fluctuations. Therefore, this data must be handled very carefully. Nevertheless, the data showed that the UDMHy based solar cells are still of better quality. This, however, is strongly related to the O incorporation that originates from the DTBAA precursor. The C reduction with additional TBAs for the D-MIn-As case did not show significant solar cell quality improvement in comparison with the D-MIn material. This is probably related to the fact that O deteriorates the (GaIn)(NAs) material more strongly than the C. The usage of TIPIn instead of TMIn lead to an decrease of the W_{OC} . Simultaneously, a reduction of the current density was observed. DTBAA based solar cell growth must follow with a precursor of significantly higher purity to allow comparable or better results in comparison with UDMHy grown material.

CHAPTER 6

Summary and Outlook

This work presents a full investigation cycle of a new precursor, beginning with the synthesis of the precursors of interest. The first MOVPE investigations in different material systems like GaAs, (GaIn)As and Ga(NAsSb) were performed and finally the realization and investigation of several solar cell sets was achieved.

First experiments with Ga(NAs) material showed an extremely high N incorporation of DTBAA in comparison with the UDMHy grown material. Consequently, experiments on (GaIn)(NAs) material followed. In contrast to UDMHy grown (GaIn)(NAs) material, no N incorporation reduction was observed for the DTBAA grown (GaIn)(NAs) layer. This led to an even higher N incorporation efficiency, 60 - 80 times higher than for UDMHy. Higher purification of the DTBAA precursor reduced the O content in the Ga(NAs) and (GaIn)(NAs) layer, however, no C incorporation reduction was observed with increasing DTBAA purity. The comparison between the C incorporation between Ga(NAs) and (GaIn)(NAs) revealed TMIn to be one main C source. Therefore, additional C incorporation investigations for Ga(NAs) and (GaIn)(NAs) were performed.

A significant C incorporation reduction in DTBAA based (GaIn)(NAs) was found by either additional TBAs supply or by substituting TMIn with TIPIn. While N incorporation was reduced with additional TBAs, the TIPIn growth was not trivial, due to the fluctuation of In content.

In UDMHy based (GaIn)(NAs) material, the C incorporation reduction was attempted by the usage of Sb as a *surfactant*. The results show no beneficial interaction between Sb treated and untreated (GaIn)(NAs) material. In fact, Sb even increased the challenges of the (GaIn)(NAs) growth due to strong N incorporation reduction with additional Sb supply.

The interaction between TESb and DTBAA was investigated: it was found that the N incorporation decreased with additional TESb. However, the effect on the UDMHy based material is significantly larger. While the growth of a 1 eV Ga(NAsSb) material with MOVPE was not possible as of yet, the low negative interactions observed with the DTBAA precursor made the realization of the first 1 eV Ga(NAsSb) material grown by

MOVPE possible. SIMS investigations revealed a high amount of O, which originates from the DTBAA precursor and must be dealt with and resolved.

The knowledge obtained in the first part of this work was utilized for solar cell growth: five (GaIn)(NAs) solar cell sets, three of which were based on the DTBAA and two on the UDMHy precursor, were realized. The results revealed the UDMHy based material to be of higher quality. The C incorporation reduction led only to small solar cell quality improvement, which is probably related to the high O content that drastically reduces the material quality. The simulation of the best EQE measurements showed an active (GaIn)(NAs) thickness of around 400 nm for the UDMHy based material. DTBAA based material, however, revealed an active (GaIn)(NAs) material of only 180 nm. Among with the active doping densities obtained from test structures, the depletion region was calculated, and an indication for the diffusion lengths was found. For the UDMHy based material, the diffusion length was estimated to be around 300 nm while the DTBAA based material was estimated to have a diffusion length of around only 60 nm. The poor solar cell characteristics of DTBAA grown material is related to the high O content, which deteriorates the solar cell quality drastically.

Additionally, TIPIn was found to increase the open circuit voltage of the DTBAA as well as UDMHy based (GaIn)(NAs) solar cell. However, the current of the same solar cell material was significantly lower than the TMIn grown pendant. This, however, is probably connected to the In incorporation fluctuation during the growth.

The results summarized above show that the DTBAA precursor has a huge potential to improve the (GaIn)(NAs) material growth and therefore to replace the conventional N precursor UDMHy. However, the DTBAA purity must be improved. Furthermore, TIPIn was found to reduce C incorporation in comparison with TMIn. However, the In incorporation fluctuation when using TIPIn is an issue that must be resolved. As the Sb-N interaction is drastically lower for DTBAA based dilute N materials, (GaIn)(NAs):Sb growth with DTBAA needs to be investigated in terms of potential C incorporation reduction. Additionally, Ga(NAsSb) as well as (GaIn)(NAsSb) solar cells need to be grown in future experiments with highly purified DTBAA, as this kind of solar cells grown with MBE showed the highest solar cell qualities observed so far.

CHAPTER 7

Publications

This chapter presents the publications related to this thesis. An abstract as well as the authors contribution will be given for each publication.

7.1 Efficient nitrogen incorporation in GaAs using novel metal organic As-N precursor di-tertiary-butyl-arsano-amine (DTBAA)*

E. Sterzer, A. Beyer, L. Duschek, L. Nattermann, B. Ringler, B. Leube, A. Stegmüller, R. Tonner, C. von Hänisch, W. Stolz, K. Volz, *Journal of Crystal Growth* **439**, 19-27 (2016). DOI: 10.1016/j.jcrysgro.2015.12.032.

Abstract

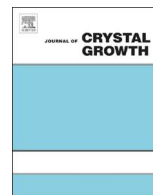
III/V semiconductors containing small amounts of nitrogen (N; dilute nitrides) are discussed in the context of different solar cell and laser applications. The efficiency of these devices is negatively affected by carbon (C) incorporation, which comes either from the direct C-N bond in the N precursor unsymmetrical 1,1-dimethylhydrazine (UDMH₂) used conventionally or from the alkyl groups of the conventional precursors for gallium (Ga), indium and arsenic (As) containing carbon. This C is incorporated together with the N due to the strength of the C-N bond. A further important issue in dilute nitride growth is the very low N incorporation efficiency in the crystal from UDMH₂, which can be as little as 1% of the N supplied in the gas phase. Therefore, new metal organic chemicals have to be synthesized and their growth characteristics and suitability for dilute nitride growth have to be explored. This work presents the chemical di-tertiary-butyl-arsano-amine (DTBAA), which was synthesized, purified and tested as an N precursor for metal organic vapor phase epitaxy (MOVPE). Computational investigations show β -hydrogen and isobutane

* Reprinted from *Journal of Crystal Growth* **439** (2016) 19-27, Copyright 2016, with permission from Elsevier.

elimination to be the main reaction channel in the gas phase with high reaction barriers and absence of small fragments containing C as products. The loss of N via N_2 , as in UDMHy, can be excluded for unimolecular reactions of DTBAA. The Ga(NAs)/GaAs heterostructures were grown by MOVPE as initial test material and a systematic N incorporation study is presented in this paper. It is shown that high quality Ga(NAs) can be grown using DTBAA. The N incorporation was confirmed by high resolution X-ray diffraction and photoluminescence studies. All samples grown exhibit as grown room temperature photoluminescence and smooth surface morphologies. Furthermore, DTBAA shows extremely high N incorporation efficiency, which makes this molecule a very promising candidate for further research into dilute nitride material growth.

The Authors contribution

My contribution to this work was the planning, executing and investigation of all samples including MOVPE growth and HR-XRD, AFM as well as PL measurements. B. Leube, A. Stegmüller and R. Tonner did perform the decomposition calculation, which was interpreted by all authors. A. Beyer and L. Duschek performed the STEM measurements which were interpreted by all authors. All co-authors helped to interpret the data for the publication which was written by me.



Efficient nitrogen incorporation in GaAs using novel metal organic As–N precursor di-tertiary-butyl-arsano-amine (DTBAA)



E. Sterzer^{a,*}, A. Beyer^a, L. Duschek^a, L. Nattermann^a, B. Ringler^b, B. Leube^b, A. Stegmüller^b, R. Tonner^b, C. von Hänisch^b, W. Stolz^a, K. Volz^a

^a Material Sciences Center and Faculty of Physics, Philipps-Universität Marburg, Germany

^b Material Sciences Center and Faculty of Chemistry, Philipps-Universität Marburg, Germany

ARTICLE INFO

Article history:

Received 15 October 2015

Received in revised form

22 December 2015

Accepted 24 December 2015

Available online 2 January 2016

Keywords:

A3. Metalorganic chemical vapor deposition

B1. Nitrides

B2. Semiconducting III–V materials

B2. Semiconducting gallium arsenide

ABSTRACT

III/V semiconductors containing small amounts of nitrogen (N; dilute nitrides) are discussed in the context of different solar cell and laser applications. The efficiency of these devices is negatively affected by carbon (C) incorporation, which comes either from the direct C–N bond in the N precursor unsymmetrical 1,1-dimethylhydrazine (UDMHy) used conventionally or from the alkyl groups of the conventional precursors for gallium (Ga), indium and arsenic (As) containing carbon. This C is incorporated together with the N due to the strength of the C–N bond. A further important issue in dilute nitride growth is the very low N incorporation efficiency in the crystal from UDMHy, which can be as little as 1% of the N supplied in the gas phase. Therefore, new metal organic chemicals have to be synthesized and their growth characteristics and suitability for dilute nitride growth have to be explored. This work presents the chemical di-tertiary-butyl-arsano-amine (DTBAA), which was synthesized, purified and tested as an N precursor for metal organic vapor phase epitaxy (MOVPE). Computational investigations show β -hydrogen and isobutane elimination to be the main reaction channel in the gas phase with high reaction barriers and absence of small fragments containing C as products. The loss of N via N_2 , as in UDMHy, can be excluded for unimolecular reactions of DTBAA. The Ga(NAs)/GaAs heterostructures were grown by MOVPE as initial test material and a systematic N incorporation study is presented in this paper. It is shown that high quality Ga(NAs) can be grown using DTBAA. The N incorporation was confirmed by high resolution X-ray diffraction and photoluminescence studies. All samples grown exhibit as grown room temperature photoluminescence and smooth surface morphologies. Furthermore, DTBAA shows extremely high N incorporation efficiency, which makes this molecule a very promising candidate for further research into dilute nitride material growth.

© 2016 Elsevier B.V. All rights reserved.

1. Introduction

Dilute nitrides (III/V semiconductors, containing small amounts of nitrogen: N), such as Ga(NAs) and GaInNAs, promise a variety of applications. By incorporating N in GaAs, the band gap reduces strongly, which can be described by the anti-crossing model [1–4]. The strong redshift of the energy gap upon the introduction of small amounts of N makes the dilute N compounds very interesting for high-efficiency solar cell [5,6] and laser applications [7–9]. Unintentional carbon (C) incorporation during growth (especially MOVPE: metal organic vapor phase epitaxy), however, is a major challenge for dilute nitride optoelectronic devices. It has been shown, for example, that C increases the threshold current density in GaInNAs lasers

linearly [10]. Conventionally, UDMHy (1,1-dimethylhydrazine) is used as an N precursor. The high C incorporation could arise from the incorporation of the dimethylamine half of the UDMHy. Another possibility is the C incorporation from the radicals of the other MO precursors for arsenic (As), gallium (Ga) and indium (In) containing C, which are incorporated together with the N due to the C–N bond strength once N encounters an alkyl radical containing C on the surface. It should be noted that “larger” radicals, such as propyl and butyl, are most probably sterically hindered from being incorporated, whereas methyl, especially, and also ethyl radicals might incorporate easily. Hence, novel precursors are needed, especially an N precursor without a direct C–N bond [10–13]. These precursors should be liquid at room temperature, have a sufficient vapor pressure and the organic fragments should, if possible, be larger than ethyl or the decomposition characteristics at low temperatures should not favor the formation of small radicals containing C. Furthermore, it is important for

* Corresponding author.

E-mail address: eduard.sterzer@physik.uni-marburg.de (E. Sterzer).

dilute nitride growth that the molecule decomposes at the low growth temperature (around 500 °C), because dilute nitrides are highly metastable and, consequently, low growth temperatures have to be applied. A further challenge during dilute nitride growth – even at low temperatures – is the extremely low N incorporation efficiency from UDMHy (in the percent range [14]) leading to an extraordinarily high consumption of the N precursor for only dilute N incorporation. Not only does this lead to high production costs, but also to a drastic change of the gas phase during MOVPE growth, which, in turn, affects all other growth conditions [15,16]. Loss of molecular N₂ will be discussed in the gas phase chemistry chapter as the reason for N loss using UDMHy.

This paper will present an incorporation study of N from a new N precursor with no direct C–N bond (*di-tertiary-butyl-arsano-amine*: DTBAA) which has been synthesized and purified on a laboratory scale. The avoidance of a direct C–N bond might result in a reduction of C incorporation after all growth conditions have been optimized. Furthermore, as the N incorporation mechanisms into GaAs from UDMHy are not entirely clarified, using DTBAA might also enhance our understanding at this point and even higher N incorporation efficiencies might be achieved.

2. Synthesis of *t*Bu₂AsNH₂ (DTBAA)

The preparation of *t*Bu₂AsNH₂ was described by Scherer and Janssen in 1969. The *t*Bu₂AsCl is prepared in a two-step synthesis via the reaction of the Grignard reagent *t*BuMgCl and AsCl₃. Amination to *t*Bu₂AsNH₂ occurs by exposing the chloroarsine to gaseous ammonia [17,18].

2.1. Experimental part

In general, all our working procedures were conducted under rigorous exclusion of oxygen and moisture using a standard Schlenk technique and an argon atmosphere. Solvents were dried and freshly distilled before use. The starting material *tert*-butyl-chloride was purchased from Acros Organics, and magnesium and arsenic trichloride from Sigma Aldrich. Arsenic trichloride was purified by distillation prior to use. Nuclear magnetic resonance (NMR) spectra were recorded with a Bruker Avance 300 spectrometer. The abbreviations for the multiplicity of the signals are s=singlet and bs=broad singlet.

2.2. *t*Bu₂AsCl

An amount of 6.08 g Mg powder (250 mmol) was suspended in 250 ml Et₂O and 27.6 ml *t*BuCl (250 mmol) dissolved in 250 ml Et₂O, which was added drop by drop. This Grignard solution was refluxed for 1 h and, after cooling to room temperature, was subsequently added drop by drop to a solution of 8.4 ml AsCl₃ (100 mmol) in 400 ml Et₂O at 0 °C. The suspension obtained was slowly warmed to room temperature. After filtration and rinsing of the solid with *n*-pentane, the solvent was removed under reduced pressure. The purification was achieved by fractional distillation at 13.3 mbar to afford 17.14 g *t*Bu₂AsCl at 70 °C as a colorless liquid in a yield of 76%.

2.3. *t*Bu₂AsNH₂

An amount of 17.14 g *t*Bu₂AsCl (76 mmol) was dissolved in 600 ml Et₂O and cooled to 0 °C. An excess of ammonia was passed into the solution until no more NH₄Cl precipitated. The solids were filtered off and the solvent was removed under reduced pressure. An amount of 11.96 g *t*Bu₂AsNH₂ was obtained as a colorless liquid in a yield of 77% by fractional distillation at 2.7 mbar at 40 °C.

3. Quantum chemical calculations

Comprehensive decomposition reaction catalogues were established for UDMHy and DTBAA, including alkene, H₂, β-hydrogen and alkane elimination and homolytical cleavage mechanisms based on our previous work on tertiarybutylphosphine (TBP) [19]. Gibbs reaction energies and barriers were calculated following unconstrained structural optimization using density functional theory with a generalized gradient approximation functional (PBE [20]), together with the def2-TZVPP [21] basis set. Dispersion effects were considered in an atomic pairwise, semi-empirical approach (DFT-D3) [22]. An auxiliary basis set was used to speed up the computations [23] and tightened convergence criteria were applied in the self-consistent field cycle (scfconv 10^{−8} a.u., grid m4).

The character of stationary points on the potential energy surface and derivation of thermodynamic data was achieved by computing the Hessian and vibrational frequency analysis. Minima were characterized by zero and transition states by one imaginary mode. Transition states (TS) were located and confirmed via intrinsic reaction coordinate computations for selected thermodynamically accessible reactions at growth conditions. Thermodynamic corrections were computed via statistical thermodynamic approaches for *T*=400, 500 and 675 °C at *p*=50 mbar in the rigid rotor, harmonic oscillator approximation (Sackur–Tetrode equation for atoms). Entropy corrections are sensitive to even small errors in the low-frequency vibrations of the molecule. Thus, absolute Gibbs energies at high temperatures have to be interpreted with care, but trends are much less sensitive to this issue. The Gaussian 09 [24] and Turbomole 6 [25] packages were used. The full reaction catalogue investigated is found in the Supporting information.

4. Growth and characterization of the Ga(NAs) layers

Ga(NAs)/GaAs heterostructures were grown on exact semi-insulating GaAs (001) substrates using an Aixtron AIX 200 reactor which is an infrared heated horizontal reactor system with gas foil rotation (50–70 rpm). The reactor pressure was held constant at 50 mbar with a total flow of 6800 sccm palladium (Pd) purified hydrogen (H₂) carrier gas.

A GaAs buffer layer 250 nm thick grown homoepitaxially at optimal conditions (625 °C) ensures a high quality surface for further growth. The growth temperature (475–550 °C) between buffer and multiquantum well (MQW) was changed under stabilization with tertiarybutylarsine (TBAs) to prevent As desorption from the surface. The MQWs with Ga(NAs) layers 6–8 nm thick and GaAs barriers at least 10 nm thick were grown as test structures for N incorporation. The growth temperature and the triethylgallium (TEGa), TBAs partial pressures and the DTBAA offer were varied to investigate the N incorporation of DTBAA systematically. As the vapor pressure of the newly synthesized N precursor is unknown, the DTBAA offer will be represented in the following in flow units (ml/min) at a source temperature of 20 °C and source pressure of 200 mbar. From the consumption of the DTBAA, its vapor pressure at 20 °C is around 1 mbar, as detailed in the paper.

A Panalytical X'Pert Pro high resolution X-ray diffraction (HRXRD) system using an X-ray wavelength of 0.15405 nm (Cu Kα1) was used to determine the N incorporation and the growth rate for each growth experiment. The HRXRD patterns obtained around the (004) GaAs reflection were simulated using the X'Pert Expitaxy software.

As the last layer of each sample was a Ga(NAs) quantum well (QW), which was cooled down to 350 °C with TBAs stabilization, atomic force microscopy (AFM) investigations of the surface were used to address the morphology of the ternary system.

The as grown optical properties were investigated by room temperature photoluminescence (RTPL). The 514 nm line of an argon-ion laser with 100 mW power was used to excite the samples. A 1 m grating monochromator (THR 1000, Jobin-Yvon) and a liquid N cooled germanium detector were applied to disperse and detect the signal applying a standard lock-in technique.

The nanostructure of the samples was characterized by scanning transmission electron microscopy (STEM) to investigate layer quality and interfaces between the individual layers. Electron transparent samples were prepared via conventional mechanical grinding and final argon-ion milling. The thin foils were analyzed in a JEOL 2200FS microscope operating at 200 kV equipped with aberration correctors for the probe forming as well as the imaging lenses, which allows imaging at an atomic scale resolution. In scanning mode, the camera length and, accordingly, the detection angles of the annular detector were varied to visualize the layers containing N [26,27].

5. Results and discussion

This work is organized as follows: At first, we clarify the decomposition pathways of DTBAA compared to UDMHy by means

of DFT calculations. Then we will show evidence of N incorporation in GaAs using DTBAA, followed by systematic investigation of the dependence of the N incorporation on TBAs, DTBAA and TEGa (growth rate) partial pressures and growth temperature. The as grown optical characteristics of different samples will be presented, followed by a STEM study. Finally, an estimate of the N incorporation efficiency from DTBAA compared to UDMHy will be given.

5.1. Gas phase chemistry from computations

The gas phase decomposition channels of the DTBAA are key factors determining C incorporation and growth characteristics, especially the N incorporation. We carried out quantum chemical investigations on a large set of possible reactions. We also investigated the gas phase chemistry of UDMHy as a comparison. While the decomposition characteristics of hydrazine and its monomethylated derivative have received some attention in the past [28], less is known about UDMHy. In a cluster model of GaInNAs material, dissociative chemisorption of N at the GaIn-rich surface was found to be the most probable surface reaction. However, all reactions for removal of C species were found to exhibit high

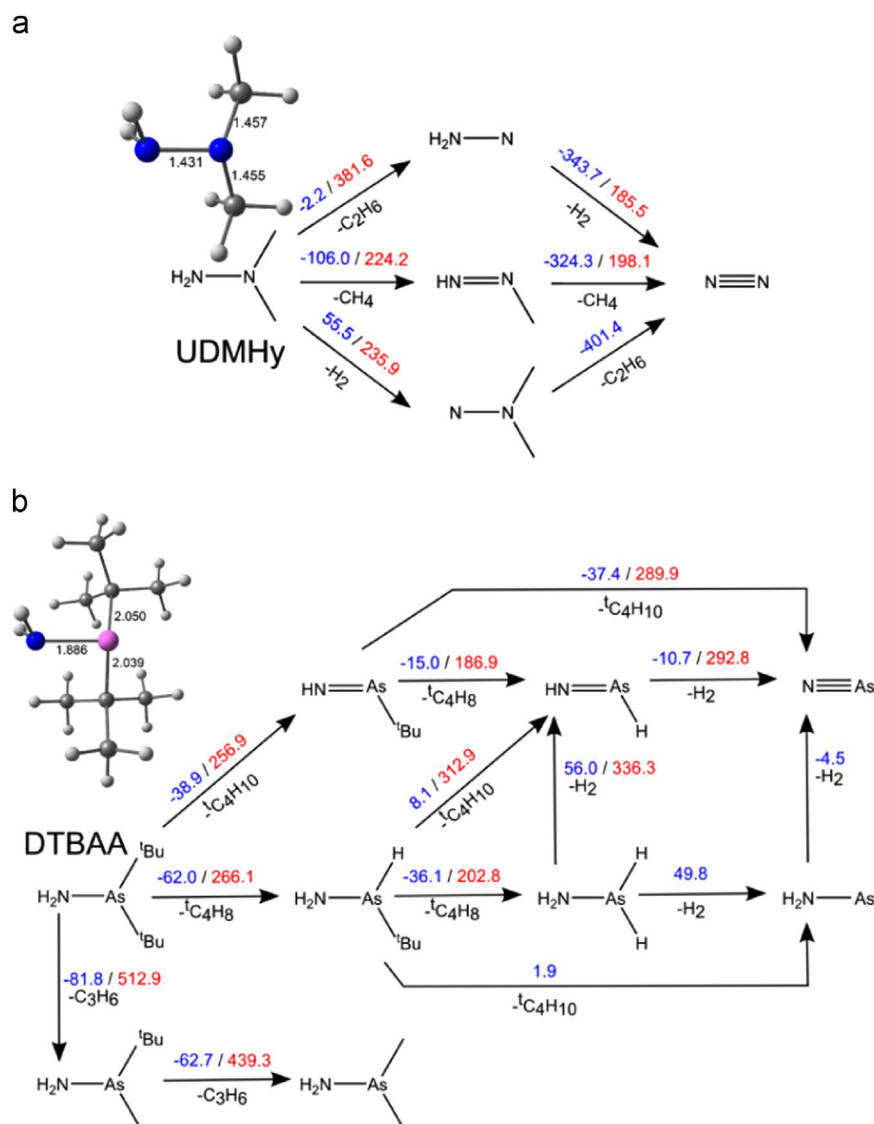


Fig. 1. Important decomposition reactions for (a) UDMHy and (b) DTBAA with Gibbs reaction energies (blue, left) and barriers (red, right) given in kJ mol⁻¹ from quantum chemical calculations (PBE-D3/def2-TZVPP, $p=50$ mbar, $T=400$ °C). The full set of reactions can be found in the [Supporting information](#). (For interpretation of the references to color in this figure legend, the reader is referred to the web version of this article.)

barriers [29]. Pyrolysis of UDMHy showed unimolecular reactions to dominate, followed by radical cleavages at rather low temperatures ($T_{50} \sim 420^\circ\text{C}$). Adduct formation and CH_4 elimination were found in the presence of TEGa. Direct N–N cleavage was found to be unlikely. Relatively high dissociation efficiency was shown even at low temperatures [30].

Since the surface reactivity has been studied already, we will focus instead on the gas phase characteristics here, as shown in Fig. 1. The main reaction channels for UDMHy are shown in the upper part, with reaction energies (in blue) and barriers (in red). As proposed earlier from experimental investigations, CH_4 abstraction exhibits the lowest barrier and the most favorable thermodynamics. Further reaction to molecular N is possible from the resulting intermediate. Other reaction channels (see Fig. 1 (a) and Tables S1 and S2 in the Supporting information) are also exothermic at growth temperatures and small molecules containing C result as products (CH_4 , C_2H_6 , CH_3) in the majority of reactions. This is in line with the high C content of the films deposited by using UDMHy.

The reaction network of DTBAA is shown in Fig. 1(b) and exhibits very different characteristics. The reactions are generally less exothermic and exhibit higher reaction barriers compared to UDMHy. The kinetically most accessible decomposition reactions for the reactant are β -hydrogen elimination, as shown before for TBP and homologues [31], or an elimination of isobutane. Even these reactions exhibit barriers of $256.9\text{--}266.1\text{ kJ mol}^{-1}$ at $T=400^\circ\text{C}$ (Fig. 1(b)). If the growth temperature is high enough to overcome such a barrier, the resulting intermediate can decompose via different channels to the N–As dimer. Notably, all decomposition reactions of DTBAA result in bulky fragments containing C, such as isobutene or isobutane, which are unlikely to be incorporated during growth. From the full reaction catalogue (see Tables S1 and S3 in the Supporting information), the only reaction leading to a small C fragment – the β -methyl abstraction reaction – is highly endergonic (263 kJ mol^{-1} at 400°C). As a side note, the homolytic bond-breaking of the precursor is even more endergonic for DTBAA (As–N bond) compared to UDMHy (N–N bond).

The computational investigation of the gas phase reactivity points towards a very small set of reactions accessible for DTBAA in the kinetically limited regime. The β -hydrogen and isobutane elimination reactions exhibit the lowest barriers and all possible decomposition reactions lead to C fragments that are unlikely to be incorporated into the surface during growth. In UDMHy, evaporation of N_2 gas is a major source of N loss. Since DTBAA cannot form N_2 in a unimolecular reaction, this can be an important fact influencing the N incorporation, as will also be supported by the experimental findings discussed below.

5.2. MOVPE growth experiments

First evidence of N incorporation using DTBAA was obtained for all samples presented in this study by HRXRD. A diffraction pattern is shown in Fig. 2 as an example. As the satellite peaks are very prominent and the profile agrees well with the dynamical simulation, the pattern indicates a high quality layer. All samples shown in the following exhibit similarly well resolved diffraction profiles. The diffraction patterns will not be shown for each sample, but rather the relevant parameters, such as N content and growth rate, will be plotted.

Fig. 3(a) shows the N incorporation and growth rate in dependence of TBAs partial pressure at constant temperature (525°C), constant TEGa partial pressure ($5.43 \cdot 10^{-3}\text{ mbar}$) and a constant DTBAA flow of 1000 ml/min . The dependence between N incorporation and TBAs partial pressure is linear and the highest N incorporation was obtained without offering TBAs. Thus, we

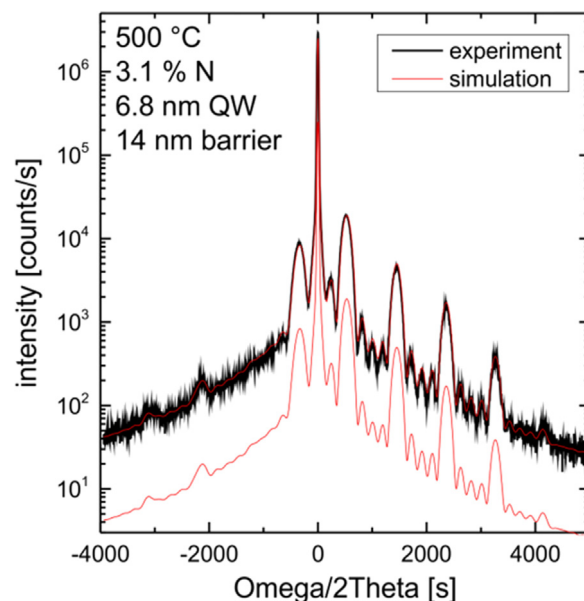


Fig. 2. An HRXRD pattern of a Ga(NAs) sample grown with TEGa and DTBAA is shown as an example. The experimental profile is shown in black and the dynamical simulation in red. (T_{growth} : 550°C , $P_{\text{p}}(\text{TEGa})$: $8.15 \cdot 10^{-3}\text{ mbar}$; $\text{Flow}(\text{DTBAA})$: 1000 ml/min .) (For interpretation of the references to color in this figure legend, the reader is referred to the web version of this article.)

conclude, on the one hand, that the N and As are both competing for the same lattice site and the V/V ratio is crucial, as has already been observed for the growth with the N precursor UDMHy [10,12,15]. On the other hand, we see that DTBAA incorporates both N and As. Furthermore, the TBAs variation had, as expected, no effect on the growth rate. The AFM micrograph shown as an inset in Fig. 3(a) is representative of most Ga(NAs) morphologies observed in this study and reveals a high quality surface with atomic steps. The spectroscopic investigation of the three samples shown in Fig. 3(a) is presented in Fig. 3(b). As grown room temperature PL is achieved for all samples grown using DTBAA, indicating a good sample quality. Comparison between DTBAA and UDMHy grown samples has revealed a similar FWHM and PL intensity. The PL intensity increases with higher N incorporation (lower TBAs partial pressure), probably due to better electron confinement in the MQW for higher N concentrations. At this point, the experiment with no TBAs shows the highest PL intensity and the highest N incorporation. Hence, the experiments presented in the following were performed without offering TBAs during Ga(NAs) growth to achieve a high N incorporation. All these samples also exhibit high quality surfaces.

We concluded from Fig. 3 that the V/V ratio is crucial for the N incorporation. As the N/As ratio in our molecule is fixed to unity, one would assume that the variation of DTBAA flow has no strong effect on the N incorporation. The results shown in Fig. 4(a) clearly illustrate the opposite. By increasing the DTBAA flow at constant temperature (525°C), constant TEGa partial pressure ($8.15 \cdot 10^{-3}\text{ mbar}$) and without offering TBAs as a further As source, we observe a linear increase in N incorporation. This might be caused by a changing desorption rate of N or As with the changing DTBAA offer. A reduced N desorption from the surface, for example, with an increasing amount of DTBAA on the surface could explain the findings. As the growth rate does not change, pre-reactions of the DTBAA with the TEGa cannot be the explanation for the dependence observed. This behavior might also highlight a way to maximize the N incorporation in dilute nitride alloys. As pointed out, the growth rate does not change with increasing DTBAA flows. Using UDMHy, the growth rate decreases with increasing UDMHy

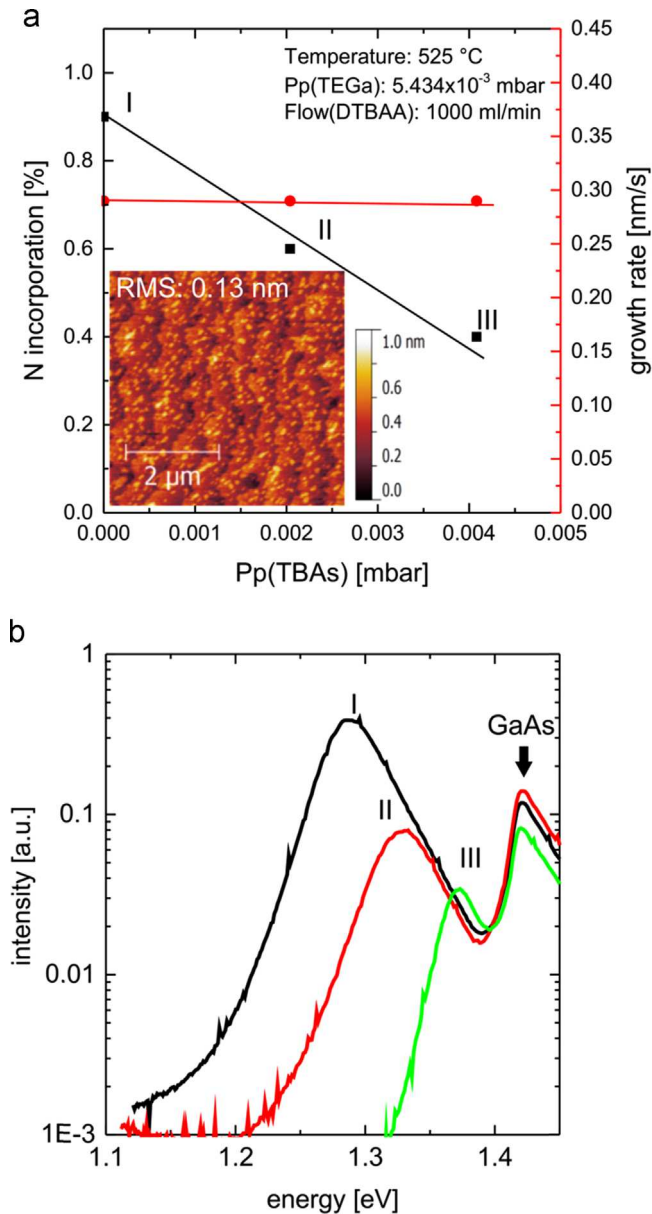


Fig. 3. N incorporation (black data points, left axis) and growth rate (red data points, right axis) as a function of TBAs partial pressure. The inset in (a) shows the AFM micrograph of sample I. Similar good surface qualities were observed during all experiments. (b) The as grown RTPL spectra are relating to the samples shown in (a). (For interpretation of the references to color in this figure legend, the reader is referred to the web version of this article.)

partial pressure due to the high amount of UDMHy in the gas phase (up to 2%, i.e. partial pressures of 1 mbar) necessary to achieve similar N concentrations, as shown here for DTBAA [10,14,15]. Hence, we conclude that the gas phase is not dominated by DTBAA in the experiments presented here. Indeed, it will be estimated later that the N incorporation efficiency from DTBAA is significantly larger than from UDMHy and, consequently, lower partial pressures are needed for identical incorporation. The spectroscopic investigation in Fig. 4(b) shows as grown RTPL and an increasing PL intensity with higher N incorporation (higher DTBAA flow).

The TEGa partial pressure was varied at a constant temperature (525 °C), constant DTBAA flow (1000 ml/min) and without TBAs offer to determine whether the N incorporation is dependent on the growth rate. If N desorption was one of the main reasons limiting the N incorporation, this should result in an increasing N

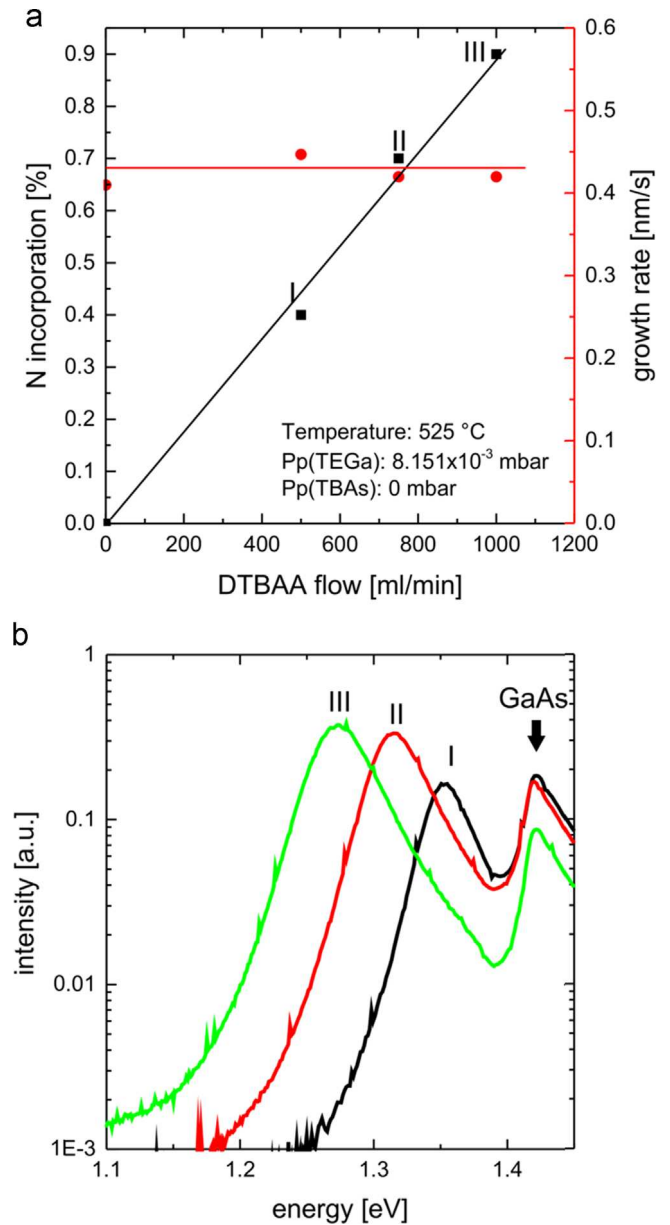


Fig. 4. (a) N incorporation and growth rate as a function of DTBAA flow. (b) As grown RTPL spectra of the samples shown in (a).

incorporation at increasing growth rates. One would expect a decrease of N content with increasing growth rate for a constant N sticking. Fig. 5(a) summarizes the results of the growth rate variation. One can clearly see (in the TEGa partial pressure range examined) no change in the N incorporation and a growth rate that increases with TEGa partial pressure. Hence, the growth rate has a negligible influence on N incorporation in GaAs using DTBAA. However, from this dependence, one is also not able to clarify whether N desorption or constant N sticking is the mechanism governing the N incorporation, as the growth rate characteristic does not support either explanation. This points, regarding the results discussed in the context of Fig. 4, towards a complex incorporation behavior where rates changing with temperature and partial pressures might also play a major role. Additionally, processes on the surface, which are certainly not in equilibrium with the gas phase at our growth temperatures, might play a decisive role. Fig. 5(b) shows a slight decrease of the as grown PL intensity at the highest TEGa partial pressure. That may be due to the fact that the As/Ga ratio decreases with a higher

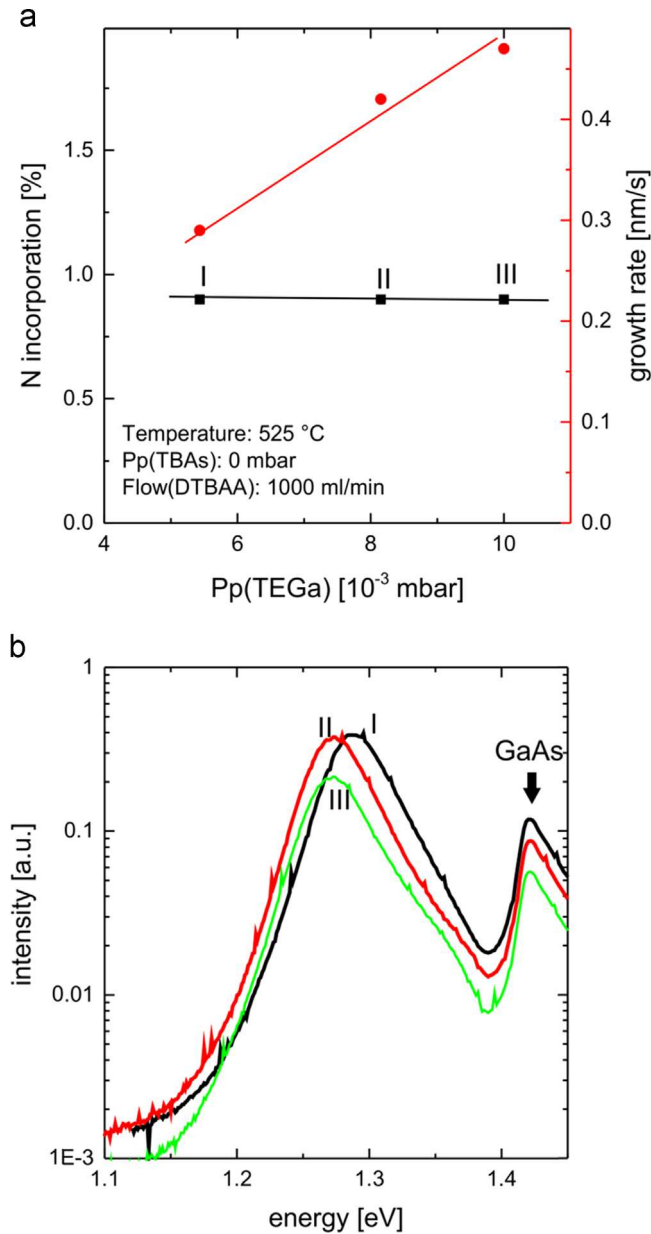


Fig. 5. (a) N incorporation and growth rate as a function of TEGa partial pressure. (b) As grown RTPL spectra for the samples shown in (a).

TEGa offering and, consequently, the crystal quality if the As/Ga falls under a certain critical value, which should be between 2 and 4 at the growth temperatures used here. The difference in the PL peak position does not arise from different N concentrations, but from slightly different layer thicknesses, hence, from quantization effects.

A strong dependence of the Ga(NAs) composition on the growth temperature would be expected, as Ga(NAs) is a metastable material system and as all MO sources used are within their kinetically limited regime for the temperature range under investigation. For metastable materials, an increasing N concentration with increasing temperature would be anticipated. However, as the equilibrium solubility of N at our growth temperatures is in the range of 10^{14} N/cm³ [32], this effect can most probably be neglected. Hence, N desorption from the surface, decomposition of the MO sources and/or reactions of the MO sources or of their fragments with each other, which all have temperature-dependent rates, are expected to have the main

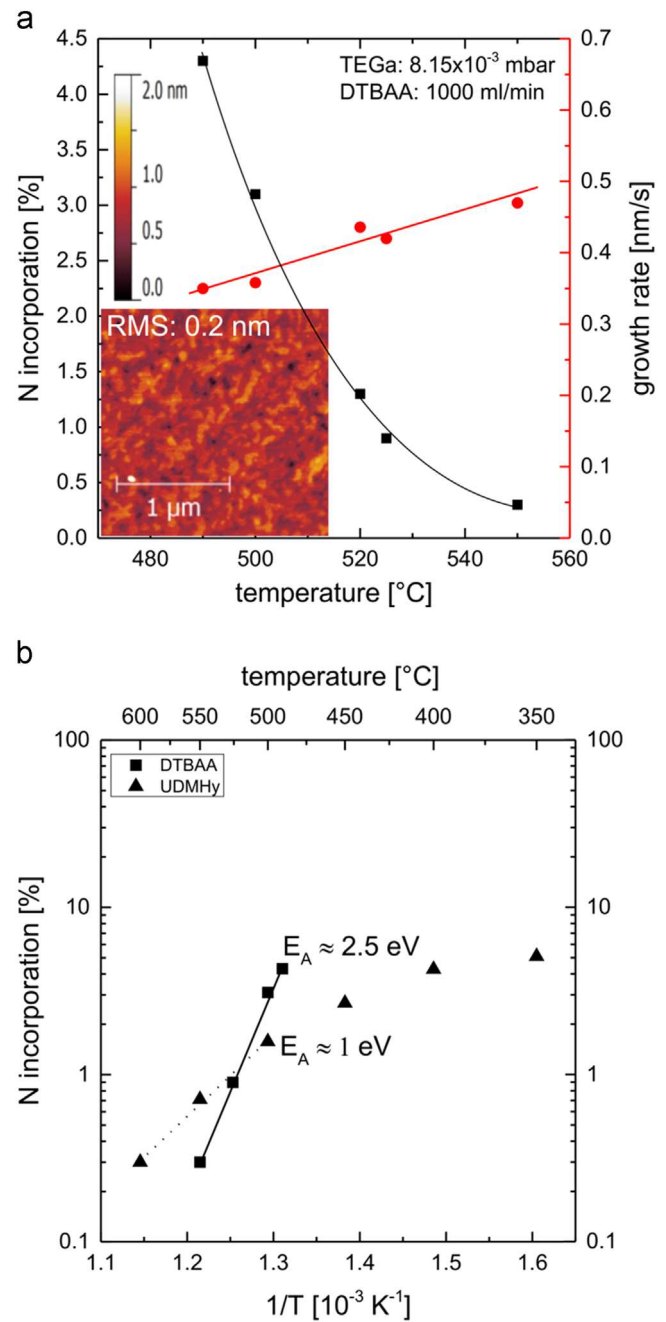


Fig. 6. (a) N incorporation and growth rate as a function of growth temperature. The inset shows an AFM micrograph of the sample with the highest N incorporation. In (b), the N incorporation is plotted as a function of the growth temperature in an Arrhenius plot. UDMHy data (triangles) is given in addition to the DTBAA data (squares). The slopes of the curves show apparent activation energies E_A .

influence. The results of the growth temperature variation are shown in Fig. 6. One can see in Fig. 6(a) that the N incorporation decreases exponentially with increasing temperature, as it is also observed for the conventional N precursor UDMHy [10,14,15]. The growth rate increases linearly with temperature because of higher decomposition of the Ga-precursor (TEGa) with increasing temperature. Under the conditions used, we achieved a maximum N incorporation of 4.2% N at 490 °C for Ga(NAs) growth with DTBAA. This is very promising and might be increased when the flow or pressure characteristics are changed during growth. The inset in Fig. 6(a) shows an AFM micrograph of the sample with the highest N concentration. One can see that the quality of the Ga(NAs) surface has two to four atoms per step and, therefore, is still very

good. Fig. 6(b) shows the N incorporation vs. temperature in an Arrhenius plot. The data can be fitted with a line, having a slope indicating an apparent activation energy (E_A) for N incorporation from DTBAA around 2.5 eV. In the same figure, UDMHy data points from [14] are also included. The apparent activation energy for Ga (NAs) growth using UDMHy amounts to roughly 1 eV. At the present stage, we refrain from interpreting these differences, as more growth conditions have to be exploited to have a larger parameter set. However, it immediately becomes clear from these results that more processes have to be taken into account than “simple” N desorption from the surface. As discussed above, the MO sources used are in their kinetically limited regime for the growth temperatures used and there might also be reactions between decomposition fragments, which have temperature-dependent rates.

Fig. 7(a) depicts the result of the as grown RTPL investigations. The PL peaks are at positions which we would expect from the N content. Starting at an N incorporation above 1%, the PL intensity decreases, due to higher disorder and defects in the crystal. The same behavior has been observed using UDMHy. Fig. 7(b) shows the energy gap concluded from PL measurements vs. N content obtained from HRXRD and simulations. The black squares represent UDMHy data points. The black line depicts the bowing behavior of the band gap independent of N incorporation using a square fit to the data. The red circles represent the DTBAA samples. The data obtained are in agreement with the reference data. Hence, one can unambiguously conclude that N is incorporated from the DTBAA source, as HRXRD shows tensile strain and the N concentration derived from this strain fits the band gaps known for Ga(NAs).

In order to investigate the crystalline quality of the samples grown with DTBAA, a specific STEM structure was deposited containing Ga(NAs) QWs grown under different conditions. As an example, only one of these QWs will be discussed. Fig. 8(a) depicts an ADF image obtained using optimized imaging conditions to visualize the QWs containing N [26,27]. The three Ga(NAs) layers are marked by arrows. The overview image already reveals smooth interfaces and the absence of crystal defects. To prove this, the interface between GaAs and the Ga(NAs) layer with 3.1% of N (marked by the black square) is depicted in a higher magnification in Fig. 8(b). The crystal exhibits a high quality and the interface between the GaAs buffer and the QW containing N is well established. This can be seen clearly from the intensity profile drawn as a red line. The atomic resolution image acquired at the region marked by the black square depicted in Fig. 8(c) proves a high crystalline quality.

6. Estimation of the N incorporation efficiency

The vapor pressure of the chemicals has to be known in order to estimate the N incorporation efficiency from different precursors. As the vapor pressure of DTBAA is not known exactly, we first estimate it by a consumption calculation and afterwards compare the N incorporation efficiency from DTBAA with that from UDMHy. The DTBAA consumption for several experiments is well known, as the bubbler can be weighed before and after the growth experiments (C). As the hydrogen flow through the bubbler (Q_s), the time the bubbler was used (t) and the pressure in the bubbler (P_c), as well as, of course, the mole number of DTBAA is known (M_{mol}), one can estimate the total consumption in grams ($C = Q_s \cdot \frac{P_c}{P_s - P_c} \cdot \frac{M_{mol}}{V_{mol}} \cdot t$). From this calculation, the estimated vapor pressure (P_s) of DTBAA is about 1 mbar at 20 °C. To compare the efficiency of DTBAA with UDMHy, the N incorporation in two structures grown under similar conditions has to be compared.

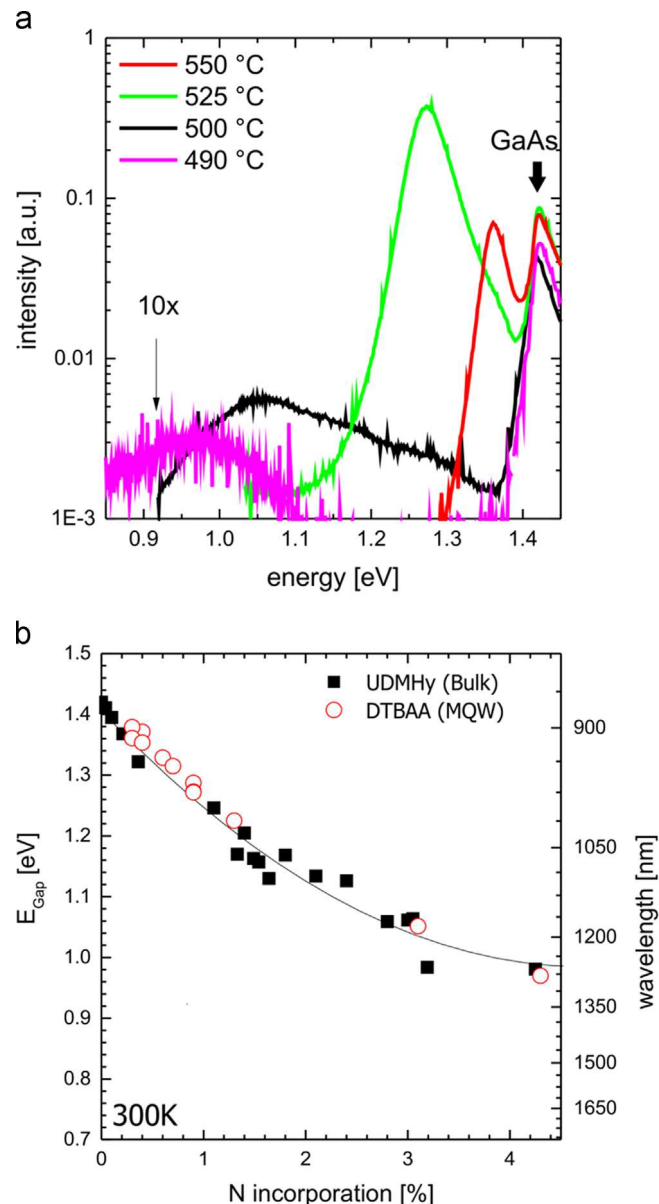


Fig. 7. (a) The as grown RTPL spectra of the samples discussed in the context of Fig. 6 (growth temperature variation), (b) depicts the band gaps (RTPL peak position) of all DTBAA grown samples (red circles) in comparison to several UDMHy grown samples (black squares). The excellent agreement between data from two different precursors, furthermore, proves the N incorporation from the DTBAA. (For interpretation of the references to color in this figure legend, the reader is referred to the web version of this article.)

Therefore, a growth temperature of 500 °C was chosen, as this is a typical dilute nitride growth temperature. The partial pressure of the TEGa was set to $8.15 \cdot 10^{-3}$ mbar in both cases. A pressure of $3.7 \cdot 10^{-2}$ mbar (1000 ml/min at 20 °C and 200 mbar) DTBAA was used for the DTBAA experiment, a pressure of 0.5 mbar UDMHy for the UDMHy experiment. The partial pressure of the TBAs in the UDMHy experiment was $5.43 \cdot 10^{-2}$ mbar. No additional TBAs was offered during the DTBAA experiment, however, the DTBAA molecule itself offers one As atom per molecule to the surface. The N incorporation into both samples turned out to be similar: 3.1% for the sample grown with DTBAA and 3.3% for the sample grown with UDMHy. If one assumes that only the N from the amine side of the UDMHy is incorporated and not the N from the dimethylamine side, this result leads to the conclusion that the DTBAA is nearly a factor of 13 more efficient with respect to N incorporation

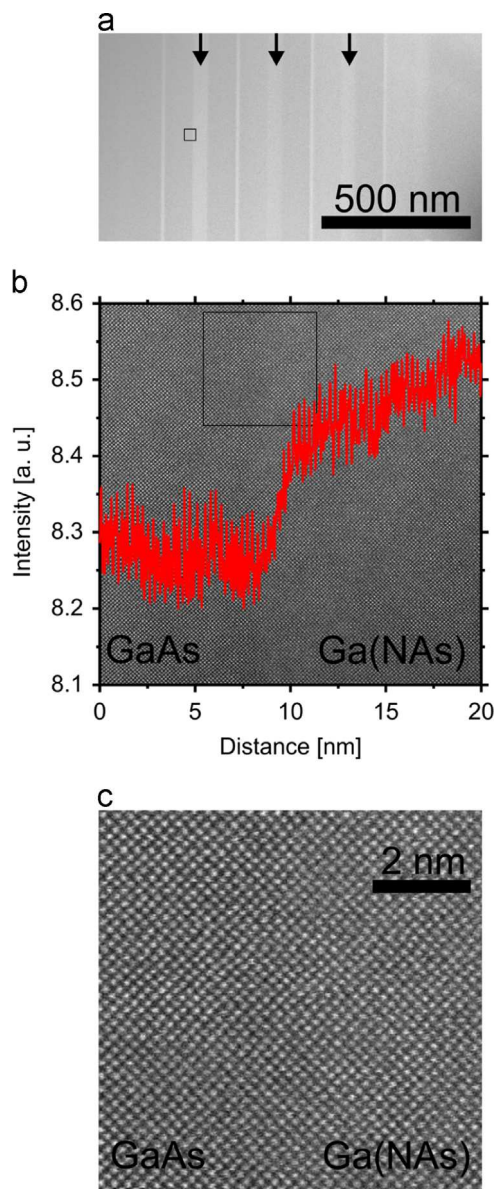


Fig. 8. STEM investigation of Ga(NAs) layers grown with DTBAA. (a) An overview of the sample structure. Due to the imaging conditions used, the QWs containing N (marked by arrows) can be detected. An interface between GaAs and Ga(NAs) (marked by the black square) is shown in higher magnification in (b). The intensity profile (red curve) reveals the QW containing N. The atomic resolution image of the interface (c) acquired at the region marked by the black square confirms a high crystal quality. (For interpretation of the references to color in this figure legend, the reader is referred to the web version of this article.)

than the UDMHy. This is, of course, only a crude estimate, as the N fraction in samples grown with DTBAA can be increased by increasing the partial pressure of the molecule in the reactor, which increases the As partial pressure at the same time. Similar experiments using UDMHy and TBAs would yield no N increase. This estimate, however, also shows the large potential behind the DTBAA as an N precursor for low temperature dilute nitride growth. Naturally, a possible origin of this by about an order of magnitude increased the incorporation efficiency of N using DTBAA could be the lack of the N_2 desorption channel, which is present for UDMHy, as discussed previously. Certainly, mechanisms as discussed in the context of Fig. 4 might also have an impact on the efficiency: if the desorption of N can be controlled by the amount of DTBAA present on the surface, which does not seem to be possible for UDMHy, the molecular structure of the DTBAA

might play a large role in explaining the observations. In addition, larger molecule fragments, sticking to the surface at low growth temperatures, might play a role. Of course, future growth experiments will explore a wider parameter range and are intended to clarify the complex incorporation characteristics. In addition, SIMS (secondary ion mass spectrometry) measurements of samples grown with UDMHy and DTBAA are planned to compare the C levels in dilute nitrides grown with the different precursors.

7. Summary

With this work, we introduced the N MOVPE precursor DTBAA (*di-tertiary-butyl-arsano-amine*) and presented a systematic investigation of the N incorporation behavior from DTBAA into GaAs. We were able to prove by HRXRD and as grown PL measurements that significant N incorporation takes place, while having good structural and optoelectronic properties.

In some respects, the N incorporation characteristics are similar to the ones known for UDMHy. Exemplarily, there is a clear competition between As from TBAs and the N for the group V lattice sites. Additionally, there is no dependence of the N incorporation on the growth rate observed. The N incorporation decreases with higher temperature.

For growth with DTBAA, Ga(NAs) crystal growth with good structural and optoelectronic properties is, however, possible without TBAs, as the DTBAA also supplies As.

Computational gas phase investigations show DTBAA to exhibit high barriers for decomposition and the β -hydrogen and isobutane elimination as the most probable channels for the reactant, which are not possible for UDMHy. While DTBAA leads to large C fragments in the gas phase, if it decomposes at all, UDMHy forms mainly methane and ethane, as found previously. In contrast to UDMHy, DTBAA does not provide a unimolecular reaction channel for the loss of N_2 , which is a possible explanation for its N incorporation efficiency.

It is very interesting to note that the N incorporation from DTBAA increases with its partial pressure, which is surprising, as this also increases the As offer at the same time. Possible mechanisms for this behavior have been discussed and might also be capable of explaining the N incorporation efficiency from DTBAA, which is about an order of magnitude larger than that from UDMHy. This is definitely very promising for future studies using DTBAA.

Acknowledgments

This work was supported by the German Science Foundation (GRK 1782: “Functionalization of Semiconductors”).

Appendix A. Supplementary material

Supplementary data associated with this article can be found in the online version at [doi:10.1016/j.jcrysgro.2015.12.032](http://dx.doi.org/10.1016/j.jcrysgro.2015.12.032).

References

- [1] W. Shan, W. Walukiewicz, K.M. Yu, J.W. Ager III, E.E. Haller, J.F. Geisz, D.J. Friedman, J.M. Olson, S.R. Kurtz, H.P. Xin, C.W. Tu, Band anticrossing in III–N–V alloys, *Phys. Status Solidi B* 223 (1) (2001) 75–85, [http://dx.doi.org/10.1002/1521-3951\(200101\)223:1<75::AID-PSSB75>3.0.CO;2-1](http://dx.doi.org/10.1002/1521-3951(200101)223:1<75::AID-PSSB75>3.0.CO;2-1).
- [2] W. Shan, W. Walukiewicz, J.W. Ager III, E.E. Haller, J.F. Geisz, D.J. Friedman, J.M. Olson, S.R. Kurtz, Band anticrossing in GaInNAs alloys, *Phys. Rev. Lett.* 82 (1999) 1221–1224, [doi: http://dx.doi.org/10.1103/PhysRevLett.82.1221](http://dx.doi.org/10.1103/PhysRevLett.82.1221).
- [3] W. Shan, K.M. Yu, W. Walukiewicz, J. Wu, J.W. Ager, E.E. Haller, Band anticrossing in dilute nitrides, *J. Phys.: Condens. Matter* 16 (31) (2004) S3355–S3372, <http://dx.doi.org/10.1088/0953-8984/16/31/024>.

- [4] J. Wu, W. Shan, W. Walukiewicz, Band anticrossing in highly mismatched III V semiconductor alloys, *Semicond. Sci. Technol.* 17 (8) (2002) 860–869, <http://dx.doi.org/10.1088/0268-1242/17/8/315>.
- [5] D.J. Friedman, J.F. Geisz, S.R. Kurtz, J.M. Olson, 1-eV solar cells with GaInNAs active layer, *J. Cryst. Growth* 195 (1998) 409–415, [http://dx.doi.org/10.1016/S0022-0248\(98\)00561-2](http://dx.doi.org/10.1016/S0022-0248(98)00561-2).
- [6] S. Kurtz, A.A. Allerman, E.D. Jones, J.M. Gee, J.J. Banas, B.E. Hammons, InGaAsN solar cells with 1.0 eV band gap, lattice matched to GaAs, *Appl. Phys. Lett.* 74 (1999) 729–731, <http://dx.doi.org/10.1063/1.123105>.
- [7] F. Höhnsdorf, J. Koch, S. Leu, W. Stolz, B. Borchert, M. Druminski, Reduced threshold current densities of (GaIn)(NAs)/GaAs single quantum well lasers for emission wavelengths in the range 1.28–1.38 μm , *Electron. Lett.* 35 (7) (1999) 571–572, <http://dx.doi.org/10.1049/el:19990421>.
- [8] S. Sato, S. Satoh, 1.3 μm continuous-wave operation of GaInNAs lasers grown by metal organic chemical vapour deposition, *Electron. Lett.* 35 (15) (1999) 1251–1252, <http://dx.doi.org/10.1049/el:19990858>.
- [9] M. Kawaguchi, T. Miyamoto, E. Gouardes, D. Schlenker, T. Kondo, F. Koyama, K. Iga, Lasing characteristics of low-threshold GaInNAs lasers grown by metalorganic chemical vapor deposition, *Jpn. J. Appl. Phys.* 40 (2001) L744, <http://dx.doi.org/10.1143/JJAP.40.L744>.
- [10] K. Volz, T. Torunski, B. Kunert, O. Rubel, S. Nau, S. Reinhard, W. Stolz, Specific structural and compositional properties of (GaIn)(NAs) and their influence on optoelectronic device performance, *J. Cryst. Growth* 272 (1–4) (2004) 739–747, <http://dx.doi.org/10.1016/j.jcrysgro.2004.09.012>.
- [11] U.W. Pohl, C. Mo, Tertiarybutylhydrazine: a new precursor for the MOVPE of group III-nitrides, *Mater. Sci. Eng.* 59 (1999) 20–23, [http://dx.doi.org/10.1016/S0921-5107\(98\)00406-1](http://dx.doi.org/10.1016/S0921-5107(98)00406-1).
- [12] B. Beaumont, P. Gibart, J.P. Faurie, Nitrogen precursors in metalorganic vapor phase epitaxy of (Al,Ga)N, *J. Cryst. Growth* 156 (3) (1995) 140–146, ISSN 0022-0248, [http://dx.doi.org/10.1016/0022-0248\(95\)00296-0](http://dx.doi.org/10.1016/0022-0248(95)00296-0).
- [13] S. Kurtz, R. Reedy, G.D. Barber, J.F. Geisz, D.J. Friedman, W.E. McMahon, J. M. Olson, Incorporation of nitrogen into GaAsN grown by MOCVD using different precursors, *J. Cryst. Growth* 234 (2–3) (2002) 318–322, [http://dx.doi.org/10.1016/S0022-0248\(01\)01711-0](http://dx.doi.org/10.1016/S0022-0248(01)01711-0).
- [14] K. Volz, J. Koch, F. Höhnsdorf, B. Kunert, W. Stolz, MOVPE growth of dilute nitride III/V semiconductors using all liquid metalorganic precursors, *J. Cryst. Growth* 311 (8) (2009) 2418–2426, <http://dx.doi.org/10.1016/j.jcrysgro.2008.09.210>.
- [15] F. Höhnsdorf, J. Koch, C. Agert, W. Stolz, Investigations of (GaIn)(NAs) bulk layers and (GaIn)(NAs)/GaAs multiple quantum well structures grown using tertiarybutylarsine (TBAs) and 1,1-dimethylhydrazine (UDMH), *J. Cryst. Growth* 195 (1998) 391–396, [http://dx.doi.org/10.1016/S0022-0248\(98\)00651-4](http://dx.doi.org/10.1016/S0022-0248(98)00651-4).
- [16] I. Suemune, K. Uesugi, T.Y. Seong, Growth and structural characterization of III–N–V semiconductor alloys, *Semicond. Sci. Technol.* 17 (8) (2002) 755–761, <http://dx.doi.org/10.1088/0268-1242/17/8/303>.
- [17] O.J. Scherer, W. Janssen, Elementorganische amin/imin-Verbindungen VII. Überführung eines N-silylierten aminoarsins in ein N-silyarsinin, *J. Organomet. Chem.* 16 (1969) 69–70.
- [18] A. Tzschach, W. Deylig, Arsen-organo-Verbindungen. V. Zur Darstellung der Lithiumderivate des Mono- und Di-tert-butylarsins, *J. Inorg. Gen. Chem.* 336 (1–2) (1965) 36–41.
- [19] A. Stegmüller, P. Rosenow, R. Tonner, A quantum chemical study on gas phase decomposition pathways of triethylgallane/TEG, $\text{Ga}(\text{C}_2\text{H}_5)_3$ and tert-butylphosphine (TBP, $\text{PH}_2(\text{t-C}_4\text{H}_9)$) under MOVPE conditions, *Phys. Chem. Chem. Phys.* 16 (2014) 17018–17029, <http://dx.doi.org/10.1039/C4CP01584C>.
- [20] J.P. Perdew, K. Burke, M. Ernzerhof, Generalized gradient approximation made simple, *Phys. Rev. Lett.* 77 (1996) 3865, <http://dx.doi.org/10.1103/PhysRevLett.77.3865>.
- [21] F. Weigend, R. Ahlrichs, Balanced basis sets of split valence, triple zeta valence and quadruple zeta valence quality for H to Rn: design and assessment of accuracy, *Phys. Chem. Chem. Phys.* 7 (18) (2005) 3297, <http://dx.doi.org/10.1039/b508541a>.
- [22] (a) S. Grimme, J. Antony, S. Ehrlich, H. Krieg, A consistent and accurate ab initio parametrization of density functional dispersion correction (DFT-D) for the 94 elements H–Pu, *J. Chem. Phys.* 132 (15) (2010) 154104, <http://dx.doi.org/10.1063/1.3382344>;
(b) C. Steffen, K. Thomas, U. Huniar, A. Hellweg, O. Rubner, A. Schroer, TmolX—a graphical user interface for TURBOMOLE, *J. Comput. Chem.* 31 (16) (2010) 2967–2970, <http://dx.doi.org/10.1002/jcc>.
- [23] (a) K. Eichkorn, F. Weigend, O. Treutler, R. Ahlrichs, Auxiliary basis sets for main row atoms and transition metals and their use to approximate Coulomb potentials, *Theor. Chem. Acc.* 97 (1–4) (1997) 119–124, <http://dx.doi.org/10.1007/s002140050244>;
(b) R. Ahlrichs, Efficient evaluation of three-center two-electron integrals over Gaussian functions, *Phys. Chem. Chem. Phys.* 6 (22) (2004) 5119, <http://dx.doi.org/10.1039/b413539c>.
- [24] M.J. Frisch, G.W. Trucks, H.B. Schlegel, G.E. Scuseria, M.A. Robb, J.R. Cheeseman, G. Scalmani, V. Barone, B. Mennucci, G.A. Petersson, H. Nakatsuji, M. Caricato, X. Li, H.P. Hratchian, A.F. Izmaylov, J. Bloino, G. Zheng, J.L. Sonnenberg, M. Hada, M. Ehara, K. Toyota, R. Fukuda, J. Hasegawa, M. Ishida, T. Nakajima, Y. Honda, O. Kitao, H. Nakai, T. Vreven, J.A. Montgomery, Jr., J.E. Peralta, F. Ogliaro, M. Bearpark, J.J. Heyd, E. Brothers, K.N. Kudin, V.N. Staroverov, R. Kobayashi, J. Normand, K. Raghavachari, A. Rendell, J.C. Burant, S.S. Iyengar, J. Tomasi, M. Cossi, N. Rega, J.M. Millam, M. Klene, J.E. Knox, J.B. Cross, V. Bakken, C. Adamo, J. Jaramillo, R. Gomperts, R.E. Stratmann, O. Yazyev, A.J. Austin, R. Cammi, C. Pomelli, J.W. Ochterski, R.L. Martin, K. Morokuma, V.G. Zakrzewski, G.A. Voth, P. Salvador, J.J. Dannenberg, S. Dapprich, A.D. Daniels, Ö. Farkas, J.B. Foresman, J.V. Ortiz, J. Cioslowski, D.J. Fox, Gaussian, Inc., Gaussian 09, Revision C.01, Wallingford CT (2009).
- [25] (a) R. Ahlrichs, M. Bär, M. Häser, H. Horn, C. Kölmel, Electronic structure calculations on workstation computers, *Chem. Phys. Lett.*, 162 (1989) 165–169;
(b) Turbomole, 6.6, 2014, a development of University of Karlsruhe and Forschungszentrum Karlsruhe GmbH, 1989–2007, Turbomole GmbH, since 2007; available from <http://www.turbomole.com> (last accessed 27.07.15).
- [26] X. Wu, M.D. Robertson, J.A. Gupta, J.-M. Baribeau, Strain contrast of $\text{GaN}_y\text{As}_{1-y}$ ($y=0.029$ and 0.045) epitaxial layers on (100) GaAs substrates in annular dark field images, *J. Phys.: Condens. Matter* 20 (7) (2008) 075215, <http://dx.doi.org/10.1088/0953-8984/20/7/075215>.
- [27] V. Grillo, K. Mueller, K. Volz, F. Glas, T. Grieb, A. Rosenauer, Strain, composition and disorder in ADF imaging of semiconductors, *J. Phys.: Conf. Ser.* 326 (2011) 012006, <http://dx.doi.org/10.1088/1742-6596/326/1/012006>.
- [28] (a) L. Zhang, A.C.T. Van Duin, S.V. Zybin, W.A. Goddard, Thermal decomposition of hydrazines from reactive dynamics using the reaxff reactive force field, *J. Phys. Chem. B* 113 (31) (2009) 10770–10778, <http://dx.doi.org/10.1021/jp900194d>;
(b) A.A. Konnov, J. De Ruyck, Kinetic modeling of the decomposition and flames of hydrazine, *Combust. Flame* 124 (1–2) (2001) 106–126, [http://dx.doi.org/10.1016/S0010-2180\(00\)00187-5](http://dx.doi.org/10.1016/S0010-2180(00)00187-5);
(c) H. Sun, C.K. Law, Thermochemical and kinetic analysis of the thermal decomposition of monomethylhydrazine: an elementary reaction mechanism, *J. Phys. Chem. A* 111 (19) (2007), <http://dx.doi.org/10.1021/jp0675911>.
- [29] A. Jenichen, C. Engler, G. Leibiger, V. Gottschalch, Growth and annealing of GaInAsN: density-functional calculations on the reactions of surface and bulk structures, *Surf. Sci.* 574 (2–3) (2005) 144–152, <http://dx.doi.org/10.1016/j.susc.2004.10.038>.
- [30] R.T. Lee, G.B. Stringfellow, Pyrolysis of 1,1 dimethylhydrazine for OMVPE growth, *J. Electron. Mater.* 28 (8) (1999) 963–969, <http://dx.doi.org/10.1007/s11664-999-0205-9>.
- [31] (a) A. Stegmüller, R. Tonner, β -Hydrogen elimination mechanism in the absence of low-lying acceptor orbitals in EH2 (t-C₄H₉) (E=N–Bi), *Inorg. Chem.* 2 (2015) 6363–6372, <http://dx.doi.org/10.1021/acs.inorgchem.5b00687>;
(b) A. Stegmüller, R. Tonner, A quantum chemical descriptor for CVD precursor design: predicting decomposition rates of TBP and TBAs isomers and derivatives, *Chem. Vap. Depos.* 21 (2015) 161–150622100321165, <http://dx.doi.org/10.1002/cvde.201504332>.
- [32] I.-hsiu Ho, G.B. Stringfellow, Solubility of nitrogen in binary III–V systems, *J. Cryst. Growth* 178 (1–2) (1997) 1–7, ISSN 0022-0248, doi: [http://dx.doi.org/10.1016/S0022-0248\(97\)00078-X](http://dx.doi.org/10.1016/S0022-0248(97)00078-X).

7.2 Novel nitrogen/gallium precursor [Ga(bdma)H₂] for MOVPE*

E. Sterzer, A. Beyer, L. Nattermann, W. Schorn, K. Schlechte, S. Pulz, J. Sundermeyer, W. Stolz, K. Volz, *Journal of Crystal Growth* **454**, 173-179 (2016). DOI: 10.1016/j.jcrysgro.2016.08.061.

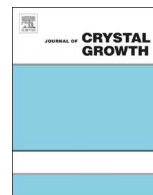
Abstract

Dilute nitrogen (N) containing III/V semiconductors are promising candidates for solar cell and laser applications. The N incorporation efficiency of 1,1-dimethylhydrazine (UDMHy) in metal organic vapor phase epitaxy (MOVPE), however, happens to be only in the one percentage range and below. This leads to an extremely high offer of UDMHy in the MOVPE reactor and, therefore, a drastic change in the growth conditions. Furthermore, the device efficiency of dilute nitride materials is currently hampered by carbon (C) incorporation, which is believed to be incorporated either jointly with the N from the dimethylamine radical of the UDMHy or from short hydrocarbon radicals originating from the decomposition of the other metal organics. Therefore, this work presents a novel N precursor N,N'-Bis(dimethylamino)acetamidinato-galliumdihydride [Ga(bdma)H₂], which provides not only N but also gallium (Ga) during MOVPE. The direct NâGa bond in this molecule might facilitate the N incorporation and hence increase the efficiency. For a systematic N incorporation study Ga(NAs)/GaAs heterostructures were grown by MOVPE. The N content was determined via high resolution X-ray diffraction and photoluminescence (PL) studies. Good structural quality and as grown room temperature PL were obtained. It will be also shown that the N incorporation efficiency in GaAs using [Ga(bdma)H₂] is significantly higher than for growths using UDMHy under comparable conditions, making this class of molecules promising candidates for the growth of dilute nitride materials.

The Authors contribution

W. Schorn, K. Schlechter and S. Pulz synthesized the precursor. My contribution to this work was the planning, executing and investigation of all samples including MOVPE growth and HR-XRD, AFM as well as PL measurements. All co-authors helped to interpret the data of the publication, which was written by me.

* Reprinted from *Journal of Crystal Growth* **454**, 173-179 (2016), Copyright 2017, with permission from Elsevier.



Novel nitrogen/gallium precursor [Ga(bdma)₂] for MOVPE



E. Sterzer^{a,*}, A. Beyer^a, L. Nattermann^a, W. Schorn^b, K. Schlechter^b, S. Pulz^b,
J. Sundermeyer^b, W. Stolz^a, K. Volz^a

^a Material Sciences Center and Faculty of Physics, Philipps-Universität Marburg, Germany

^b Material Sciences Center and Faculty of Chemistry, Philipps-Universität Marburg, Germany

ARTICLE INFO

Article history:

Received 27 June 2016

Received in revised form

17 August 2016

Accepted 29 August 2016

Communicated by G. Stringfellow

Available online 30 August 2016

Keywords:

Metalorganic chemical vapor deposition A3

Nitrides B1

Semiconducting III-V materials B2

Semiconducting gallium arsenide B2

ABSTRACT

Dilute nitrogen (N) containing III/V semiconductors are promising candidates for solar cell and laser applications. The N incorporation efficiency of 1,1-dimethylhydrazine (UDMH₂) in metal organic vapor phase epitaxy (MOVPE), however, happens to be only in the one percentage range and below. This leads to an extremely high offer of UDMH₂ in the MOVPE reactor and, therefore, a drastic change in the growth conditions. Furthermore, the device efficiency of dilute nitride materials is currently hampered by carbon (C) incorporation, which is believed to be incorporated either jointly with the N from the dimethylamine radical of the UDMH₂ or from short hydrocarbon radicals originating from the decomposition of the other metal organics. Therefore, this work presents a novel N precursor N,N'-Bis(dimethylamino)acetamidinato-galliumdihydride [Ga(bdma)₂], which provides not only N but also gallium (Ga) during MOVPE. The direct N–Ga bond in this molecule might facilitate the N incorporation and hence increase the efficiency. For a systematic N incorporation study Ga(NAs)/GaAs heterostructures were grown by MOVPE. The N content was determined via high resolution X-ray diffraction and photoluminescence (PL) studies. Good structural quality and as grown room temperature PL were obtained. It will be also shown that the N incorporation efficiency in GaAs using [Ga(bdma)₂] is significantly higher than for growths using UDMH₂ under comparable conditions, making this class of molecules promising candidates for the growth of dilute nitride materials.

© 2016 Published by Elsevier B.V.

1. Introduction

Nitrogen (N) containing semiconductors, such as Ga(NAs) and (GaIn)(NAs), open up new possibilities for laser and solar cell applications. The strong band gap reduction when adding small amounts of N–GaAs is described, for example, by the band anti crossing model, changes the crystal's characteristics drastically. For 1% N in GaAs one observes a band gap reduction up to 180 meV and due to the small size of N, tensile strain is added to the material [1–4]. In quaternary materials, one can hence adjust the band gap and lattice constant independently. Therefore, this kind of materials is very interesting for solar cell and laser applications [5–14].

There are, however, several challenges associated with the metal organic vapor phase epitaxy (MOVPE) growth of these materials. The N incorporation efficiencies from UDMH₂ (1,1-Dimethylhydrazine), which is the commonly used precursor for dilute N growth, are in the order of only one percent and below [11]. Therefore, extremely large UDMH₂ overpressures have to be

applied in order to incorporate a sufficient amount of N. This, in turn, affects several other growth conditions, like the growth rate [15,16].

Another severe drawback of dilute N containing semiconductors grown by MOVPE is the unintentional carbon (C) incorporation into the material. C incorporation leads for example to higher threshold current densities in (GaIn)(NAs) lasers [14] and lower minority carrier diffusion lengths in (GaIn)(NAs) solar cells [5,6]. Two reasons for unintentional C incorporation in dilute nitrides are discussed in literature. Either the C arises from the dimethylamine radical of the conventionally used N precursor UDMH₂, and/or the N is so strongly C affine that it binds to hydrocarbon radicals, which result from the decomposition of the other metal organic precursors such as tertiarybutylarsine (TBAs), triethylgallium (TEGa) or trimethylindium (TMIn) on the surface and consequently, C is simultaneously incorporated with N into the crystal. Smaller radicals – such as methyl and ethyl – are incorporated easily, whereas propyl and butyl are probably hindered sterically.

Therefore, novel liquid precursors with a different molecular structure, some of them with larger alkyl groups (e.g. tertiarybutyl hydrazine, TBHy) and some without a direct C–N bond (ditertiarybutylarsanoamine, DTBAA), have been synthesized to alter

* Corresponding author.

E-mail address: eduard.sterzer@physik.uni-marburg.de (E. Sterzer).

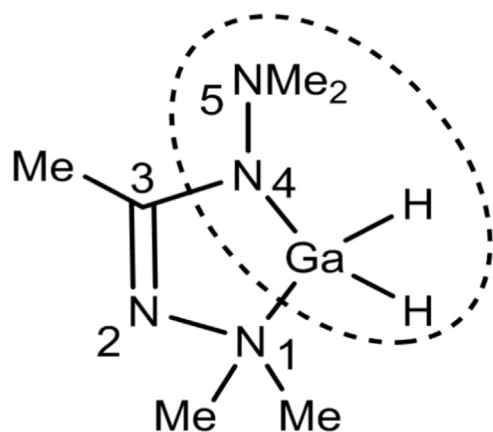


Fig. 1. Molecular structure of $[\text{Ga}(\text{bdma})\text{H}_2]$.

incorporation characteristics [17–20]. When designing the precursors, a sufficient vapor pressure is mandatory. Moreover, the alkyl fragments of the precursors should be as large as propyl, butyl or just substituted by hydrogen. On top of that, the precursors have to decompose at rather low temperatures around 500 °C, as this growth temperature is applied for the growth of dilute nitride III/V semiconductors due to the metastability of this class of alloys.

This paper will present a systematical investigation of dilute nitride growth using a new N precursor with a direct N–Ga bond, which is thought to facilitate N incorporation, *N,N'*-Bis(dimethylamino)acetamidinato-galliumdihydride: $[\text{Ga}(\text{bdma})\text{H}_2]$. The valence formula of the molecule is shown in Fig. 1. This molecule consists out of a 5-membered ring system, which contains three out of four N atoms. Due to the UDMHy based ligand system each N atom is neighbored by at least one C atom. We assume, that the amidic covalently bound N_4 atom is going to be incorporated into the crystal, as the $\text{Ga}-\text{N}_1$ bond is weak due to the donor-acceptor character, this part is going to be cleaved off and therefore probably desorbs easily. A closer look to the molecular structure shows that the N_1-N_2 single bond is less stable and labile due to the extended bond length. The instability of the C_3-N_4 bond is related to the stabilization of the generated radical and can cleave easily. This molecule still has two methyl groups attached to the N_5 atom (circled part in Fig. 1), which might result in a high C incorporation. But due to affordable educts and a rather easy up scaling of the synthetization as well as purifying, this molecule was the first choice to work with. In order to evaluate guidelines of carbon versus nitrogen uptake, we performed detailed incorporation studies to investigate the N incorporation using $[\text{Ga}(\text{bdma})\text{H}_2]$ so that the effort for the synthesis of more advanced molecules of the same class, without any dimethylamino groups, can be justified based on these results. To cover the parameter space in our investigations, the growth temperature as well as the TEGa, TBAs and $[\text{Ga}(\text{bdma})\text{H}_2]$ partial pressures have been varied. This may also help to understand the N incorporation from different N precursors, which has been shown to exhibit highly different characteristics [20].

2. Experimental Part

2.1. Growth and characterization of the Ga(NAs) layers

Ga(NAs) test structures were grown on semi-insulating exact GaAs (001) substrates in an Aixtron AIX 200 reactor equipped with an infrared heated horizontal reactor. To ensure homogeneity the substrate is rotating using the gas foil rotation technique (approx.

60 rpm). For all experiments the reactor pressure was held constant at 50 mbar under a total flow of 6800 sccm palladium purified hydrogen carrier gas.

A GaAs buffer layer (approx. 250 nm thick) – grown at 625 °C before each experiment – provides a high quality surface for on-going growth. To prevent As desorption, the samples have been TBAs stabilized during temperature variations between buffer and layer growth. A multi quantum well (MQW) structure, consisting of five GaAs (10 nm) and Ga(NAs) (10–20 nm) layers, was grown at temperatures of 475–550 °C. For detailed understanding of the N incorporation behavior, growth temperature, TEGa and TBAs partial pressures as well as $[\text{Ga}(\text{bdma})\text{H}_2]$ offer have been varied. Due to the unknown $[\text{Ga}(\text{bdma})\text{H}_2]$ vapor pressure, the offer of the new precursor will be represented in ml/min at a source pressure of 200 mbar and 20 °C source temperature. In a later section, a vapor pressure estimation of the $[\text{Ga}(\text{bdma})\text{H}_2]$ will be given based on its consumption during growth.

N incorporation and layer thickness were investigated via high resolution X-ray diffraction (HRXRD) in a Panalytical X'Pert Pro diffractometer with an incident wavelength of 0.15405 nm (Cu $\text{K}\alpha_1$). The diffraction around the (004) reflection was measured and simulated with the X'Pert Epitaxy software. Room temperature photoluminescence (RTPL) was used to characterize the optical properties. Therefore, the 514 nm line of an argon-ion laser was used for sample excitation. The signal was dispersed with a THR 1000, Jobin-Yvon monochromator and was detected in a liquid N_2 cooled germanium detector. To investigate the morphology of the ternary material with a Nanoscope IIIa tapping mode atomic force microscope (AFM), no GaAs cap was grown on the last Ga(NAs) layer. Instead, the sample was cooled down to 350 °C under TBAs stabilization.

3. Results and discussion

This work is organized as follows: We will show a systematic investigation of the dependence of the N incorporation – obtained by HRXRD – in GaAs on temperature, $[\text{Ga}(\text{bdma})\text{H}_2]$ flow, TEGa partial pressure, growth rate and TBAs partial pressure. The as grown optical characteristics of different samples will be presented, followed by a secondary ion mass spectrometry (SIMS) study. Finally, an estimation of the N incorporation efficiency from $[\text{Ga}(\text{bdma})\text{H}_2]$ compared to UDMHy will be given showing the potential of this class of molecules for dilute nitride growth.

3.1. MOVPE growth experiments

Fig. 2(a) shows the N incorporation as well as the growth rate of Ga(NAs) MQWs at a constant TEGa and TBAs partial pressure of 8.15×10^{-3} mbar and a $[\text{Ga}(\text{bdma})\text{H}_2]$ flow of 500 ml/min in dependence on the growth temperature. Similar to Ga(NAs) growth with UDMHy one observes an exponentially decreasing N incorporation with increasing growth temperature [11]. A decreasing N sticking coefficient at the surface with higher temperature is believed to be the reason for that behavior. As group III atoms are the driving force for growth rate, the observed increase of the growth rate with increasing temperature is explained with more efficient TEGa as well as $[\text{Ga}(\text{bdma})\text{H}_2]$ decomposition. It should be noted here, that $[\text{Ga}(\text{bdma})\text{H}_2]$ might also contribute to the growth rate, as it also contains Ga. The AFM shows improving surface quality with higher growth temperature (lower N content), with an RMS roughness ranging from 0.46 nm at 475 °C to an RMS roughness of 0.19 nm at 550 °C. Fig. 2(b) shows the associated RTPL measurements of the samples presented in (a). In these growth temperature regions, one associates a lower PL intensity with lower growth temperature, due to lower crystal quality. It is,

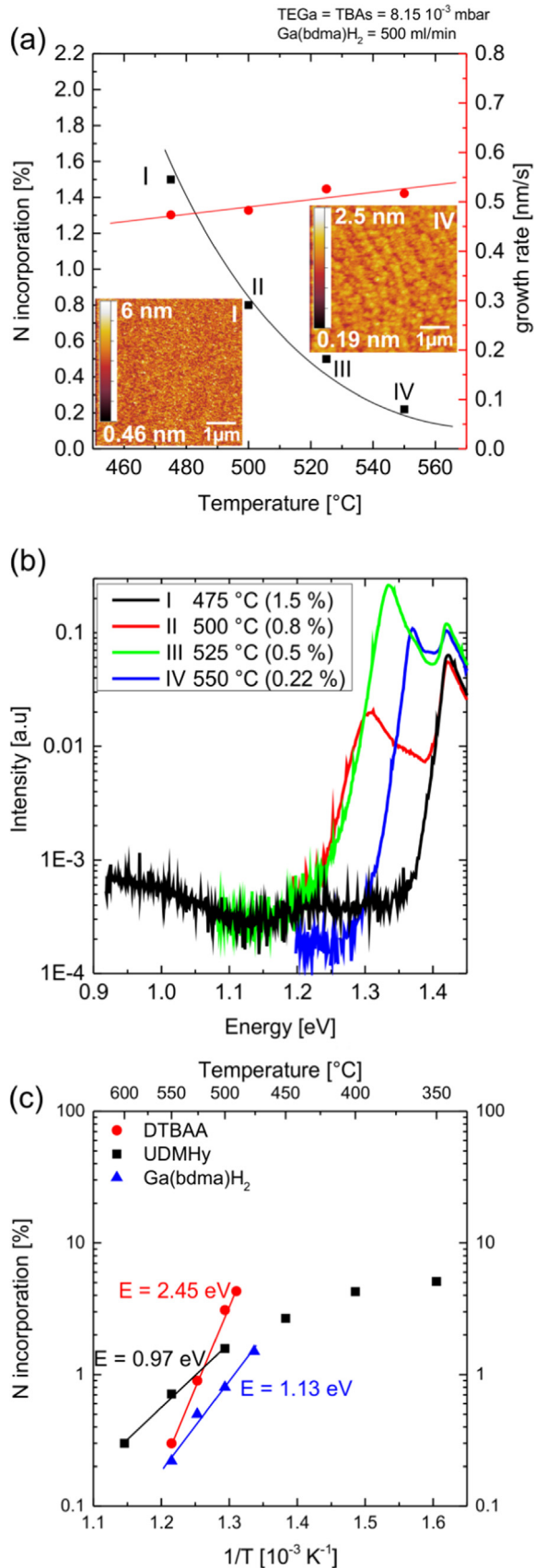


Fig. 2. (a) Temperature dependence of N incorporation including guides to the eye. The N incorporation decreases with higher temperature. The growth rate changes with temperature due to the higher precursor decomposition with higher temperatures. AFM investigation show lower surface roughness with higher growth temperature and lower N fractions. (b) PL intensity versus energy. RTPL is observed up to 0.8% N content. (c) Apparent activation energies of UDMHy, DTBAA [20] and [Ga(bdma)H₂] in comparison. Relating these energies to the N desorption leads to the assumption of increasing N incorporation efficiencies in with higher activation energies.

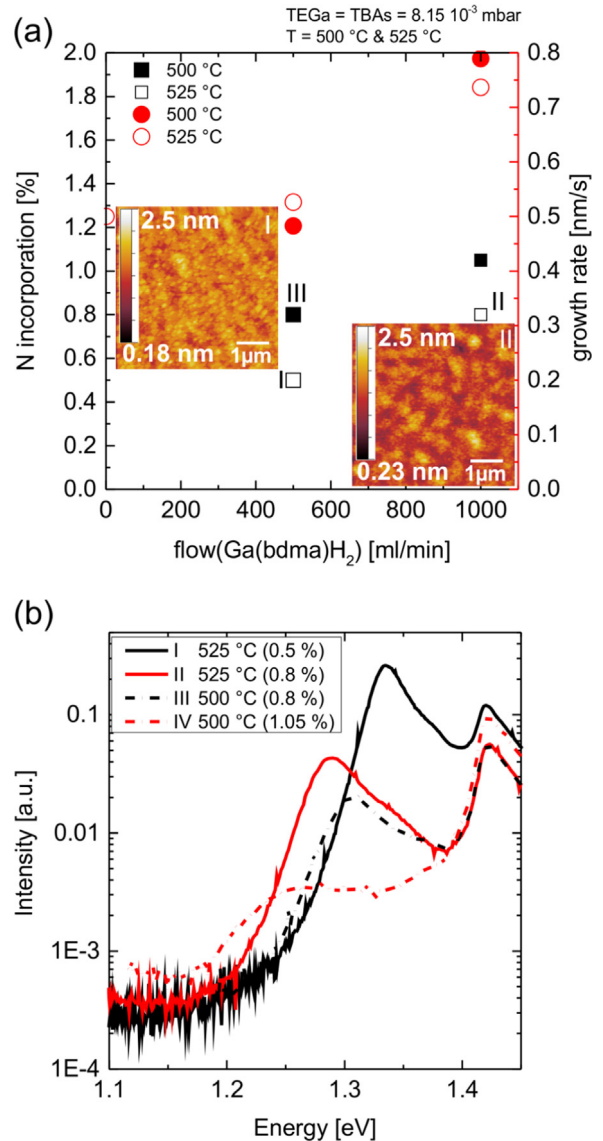


Fig. 3. N incorporation in dependence of [Ga(bdma)H₂] flow in two different temperatures including guides to the eye. (a) N incorporation increases with higher [Ga(bdma)H₂] offer. A higher growth rate is also observed. Therefore, not only N is incorporated, but also Ga. Surface quality decreases with higher [Ga(bdma)H₂] offer due to lower As/III ratio. (b) RTPL measurements for 500 °C and 525 °C grown Ga (NAs) show a decrease of PL intensity with higher N incorporation and lower growth temperature.

however, also expected that for small amounts of N the PL intensity increases with increasing N content due to improved electron confinement and decreases again with higher N incorporation due to the formation of N related defects. Here, we observe a PL intensity decrease for N contents higher than 0.5%. For the sample grown at 475 °C (1.5% N) no RTPL-peak was observed. As discussed above, these trends might be overlaid by a dependence of the crystal quality on the growth temperature, which was varied here. It is, however, remarkable that RTPL is observed for dilute nitride alloys grown using a novel precursor without further optimization of the growth conditions and post growth thermal annealing. Plotting the temperature dependence of the N incorporation into an Arrhenius plot allows to determine an apparent activation energy, which can be related to precursor decomposition or N desorption etc. The Arrhenius plot in Fig. 2 (c) shows data from UDMHy, DTBAA and [Ga(bdma)H₂]. If one

relates the data to N desorption, as already done in [20], a higher N incorporation efficiency using $[\text{Ga}(\text{bdma})\text{H}_2]$ is concluded.

In Fig. 3(a) the offer of $[\text{Ga}(\text{bdma})\text{H}_2]$ was varied at constant TEGa and TBAs partial pressures of 8.15×10^{-3} mbar for two different growth temperatures (500 and 525 °C). As already shown in Fig. 2(a) more N is incorporated at lower growth temperature. Furthermore, the N incorporation increases with higher $[\text{Ga}(\text{bdma})\text{H}_2]$ flow for both temperatures, as more N is offered for incorporation. Moreover, we observe an increase in growth rate with increasing $[\text{Ga}(\text{bdma})\text{H}_2]$ flow. This has been expected, as $[\text{Ga}(\text{bdma})\text{H}_2]$ also provides Ga. For no $[\text{Ga}(\text{bdma})\text{H}_2]$ we observe a similar growth rate as for the sample with a $[\text{Ga}(\text{bdma})\text{H}_2]$ flow of 500 ml/min. This will be discussed in detail in the next section. The AFM micrographs in Fig. 3(a) show a slightly increasing surface roughness with higher $[\text{Ga}(\text{bdma})\text{H}_2]$ flow and higher N content. The RTPL spectra in Fig. 3(b) show a decrease of PL intensity with higher N incorporation (higher $[\text{Ga}(\text{bdma})\text{H}_2]$ flow) for both temperatures, which is probably also linked to either a critical As/III or increasing N content. As one can see, the samples grown at higher temperature exhibit a higher PL intensity in general, underpinning that the crystal quality improves with increasing growth temperature.

To examine the competition between the Ga supplied from $[\text{Ga}(\text{bdma})\text{H}_2]$ and TEGa, TEGa variation experiments were carried out. Fig. 4(a) shows the N incorporation in dependence on TEGa partial pressure. One clearly observes a decrease of N incorporation with higher TEGa partial pressure, which indicates that the TEGa is competing with the $[\text{Ga}(\text{bdma})\text{H}_2]$, from which the N is incorporated together with the Ga. Another possible explanation would be a constant sticking of N on the growth surface, which would also lead to a lower N incorporation with higher growth rate. But in that case, one would assume halved N incorporation for doubled growth rate, which was not observed. Results discussed in the context of Fig. 5 also support the assumption that TEGa and $[\text{Ga}(\text{bdma})\text{H}_2]$ compete on the surface. It should be highlighted that growth without TEGa is not only possible, but also results in the highest N incorporation. This underpins that $[\text{Ga}(\text{bdma})\text{H}_2]$ could also be used as a single source precursor. Using $[\text{Ga}(\text{bdma})\text{H}_2]$ as single source precursor, the N content should be adjusted by the temperature and the $[\text{Ga}(\text{bdma})\text{H}_2]$ flow as well as the TEGa/ $[\text{Ga}(\text{bdma})\text{H}_2]$ ratio. Investigations of the surface morphology reveal a smooth surface with atomic steps for the Ga(NAs) growth without TEGa. Additional TEGa leads to less N incorporation and rougher surfaces. Here we see that the surface quality decreases with higher Ga supply even for decreasing N content. Based on that, we assume low As/III ratios to be the reason for surface roughness. The increase of the growth rate in Fig. 4 is not as high as it would be expected for an additive growth rate behavior of both Ga supplying precursors. For GaAs growth at 525 °C at a TEGa partial pressure of 1×10^{-2} mbar a growth rate of 0.56 nm/s is observed in our reactor. Starting at a growth rate of approximately 0.5 nm/s with $[\text{Ga}(\text{bdma})\text{H}_2]$ only (500 ml/min), one would assume a total growth rate of roughly 1 nm/s when flowing TEGa at partial pressure of 1×10^{-2} mbar additionally. However, a growth rate increase of only about 30–40% of the expected value is observed. That again indicates a competition of TEGa and $[\text{Ga}(\text{bdma})\text{H}_2]$ probably on the surface, which we have already concluded from the drop in N incorporation when adding TEGa. If we assume that the decomposition of the precursors mainly takes place at the surface at the low growth temperatures used here, a higher partial pressure of TEGa would lead to a higher TEGa coverage. Consequently, less surface sites are available for $[\text{Ga}(\text{bdma})\text{H}_2]$ and therefore less Ga from $[\text{Ga}(\text{bdma})\text{H}_2]$ and with that also less N is incorporated in the growing crystal. RTPL measurements in Fig. 4(b) show decreasing PL intensity with higher N incorporation, which is probably linked to the decreasing

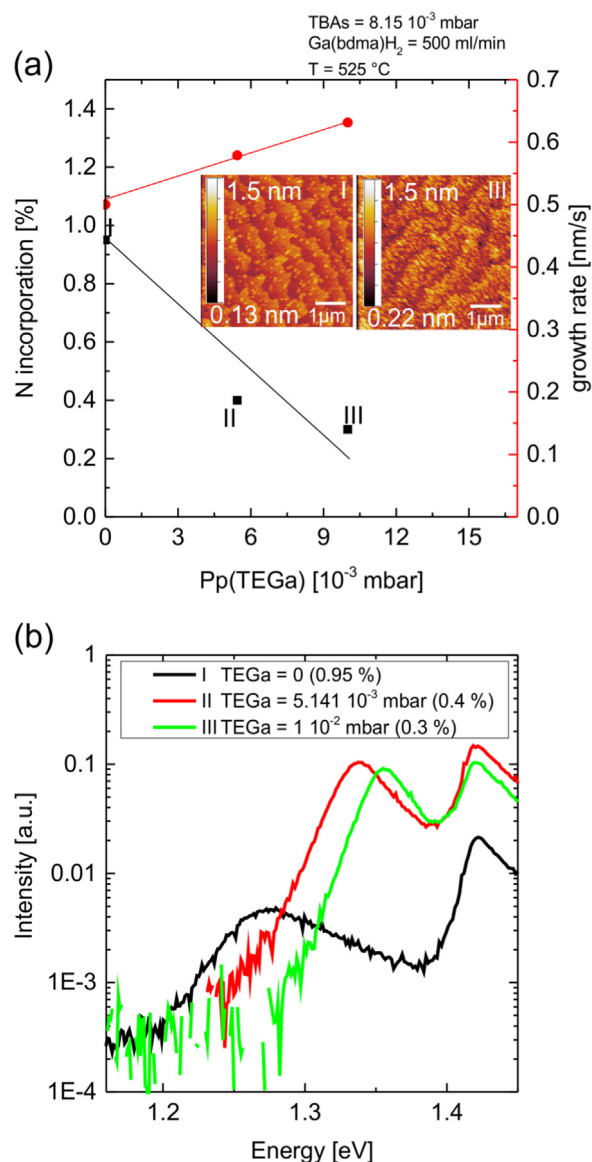


Fig. 4. Variation of TEGa with fixed TBAs and $[\text{Ga}(\text{bdma})\text{H}_2]$ including guides to the eye. (a) N incorporation decreases with higher TEGa offer. Therefore a surface competition between $[\text{Ga}(\text{bdma})\text{H}_2]$ and TEGa has to take place, as probably less $[\text{Ga}(\text{bdma})\text{H}_2]$ arrives at the surface and therefore provides less Ga and N. AFM investigations show a surface with atomic steps at growth conditions without TEGa. (b) PL intensity decreases with higher N incorporation.

crystal quality with decreasing As/III ratio and N related defects.

In the next step the gas phase ratios of the precursors were kept constant, but the partial pressure of each precursor was varied by the same factor. In Fig. 5(a) the results are represented in square data points. For comparison the data points of Fig. 4(a) are also plotted into the same graph (stars). One can see that no growth rate dependence of the N incorporation can be observed if we increase the entire gas phase by a factor of 1.8. However, if only TEGa is increased, the N incorporation drops due to TEGa and $[\text{Ga}(\text{bdma})\text{H}_2]$ surface competition as discussed before. AFM measurements show almost no change of the morphology. These results confirm that the N incorporation using $[\text{Ga}(\text{bdma})\text{H}_2]$ is also controlled by the TEGa/ $[\text{Ga}(\text{bdma})\text{H}_2]$ ratio. RTPL measurements in Fig. 5(b) show a slightly higher PL intensity of the Ga(NAs) layer with higher growth rate, but a lower PL intensity of the barrier.

The N incorporation using conventional N precursor UDMHy depends linearly on the V/V ratio, due to the competition of As and N for the same lattice site. In Fig. 6(a) we can see the N

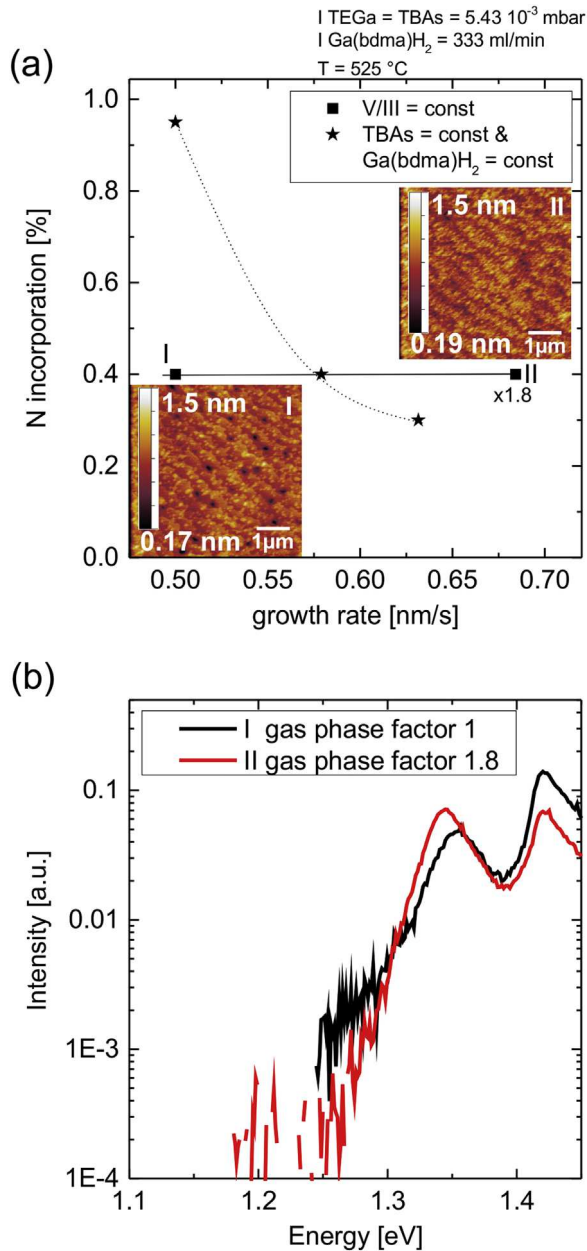


Fig. 5. Growth rate variation at fixed V/III ratio compared to results from Fig. 4 (constant TBAs and $[\text{Ga}(\text{bdma})\text{H}_2]$, stars) including guides to the eye. (a) By holding the V/III ratio constant, the growth rate increases with higher Ga offer, but N incorporation stays the same. (b) Slightly higher RT PL intensity with higher growth rate.

incorporation and growth rate dependence on the TBAs partial pressure using $[\text{Ga}(\text{bdma})\text{H}_2]$. By doubling the TBAs offer from 4×10^{-3} to 8×10^{-3} mbar we observe almost no change in N incorporation. If one assumes an N incorporation which is proportionally linked to the Ga incorporation from $[\text{Ga}(\text{bdma})\text{H}_2]$ this behavior is perspicuous. Furthermore, one can see an increase in growth rate with higher TBAs. Usually the group III elements are the driving force for growth rate if this V/III ratio exceeds 1. If the V/III is close to 1, TBAs also influences the growth rate. This is an indication for a V/III ratio close to 1, which has been used for the experiments presented here, and a first hint for the partial pressure and vapor pressure of $[\text{Ga}(\text{bdma})\text{H}_2]$. The AFM measurement

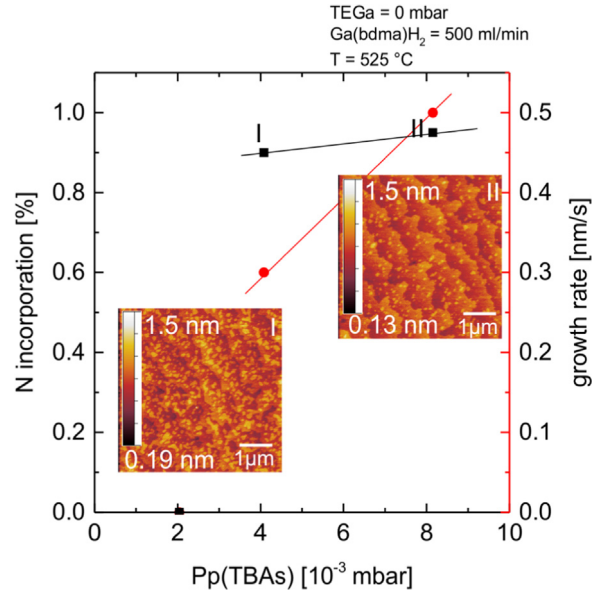


Fig. 6. N incorporation vs. TBAs variation including guides to the eye. (a) The growth rate increases with higher TBAs offer. That may hint to a critical As/III ratio. Slightly increasing N incorporation in dependence of TBAs. AFM micrographs show a smoother surface with higher TBAs.

shows a decrease of the RMS roughness with higher TBAs partial pressure, which goes in line with the assumption of a As/III ratio close to 1. The growth with a TBAs partial pressure of 2×10^{-3} mbar was not possible with a $[\text{Ga}(\text{bdma})\text{H}_2]$ flow of 500 ml/min hinting to a V/III significantly < 1 . With the assumption of a vapor pressure of 3 mbar, the partial pressure under these experimental conditions would be roughly 5.5×10^{-2} mbar.

4. SIMS investigation and N segregation

One sample was grown especially for SIMS investigations. In Fig. 7(a) the results of the O, C and N investigations are presented. The layers have all been grown with fixed TE Ga and TBAs of 8.15×10^{-3} mbar. At the same time the $[\text{Ga}(\text{bdma})\text{H}_2]$ flow was varied from 400 (layer 2) over 500 (layer 1 and 3) to 800 ml/min (layer 4). The O incorporation stays below the detection level throughout the whole sample. This is remarkable for a novel precursor, which has been synthesized and purified for epitaxy for the first time. The C incorporation however, increases with higher N incorporation. This has been expected due to the C–N bond still present in the molecule. There is, however, also a peculiar C incorporation characteristic after the end of the growth of each dilute nitride layer. The C incorporation first increases after the closure of the $[\text{Ga}(\text{bdma})\text{H}_2]$ bubbler (marked with circles) and only drops to the GaAs level after several tens of nanometers of GaAs have been grown. Furthermore, this increase in C goes along with a continued N incorporation (marked with arrows), however, at a much lower level than during the dilute nitride growth. Having a closer look at layer 2 (400 ml/min) and layer 4 (800 ml/min) one observes that the plateau is significantly wider with higher $[\text{Ga}(\text{bdma})\text{H}_2]$ flow, so probably the overall offer of $[\text{Ga}(\text{bdma})\text{H}_2]$ leads to an increased N memory effect in the reactor. Moreover, the N plateau shows that $[\text{Ga}(\text{bdma})\text{H}_2]$ segregation in to the GaAs layer has to take place. As the V/III ratio was close to unity in our experiments, $[\text{Ga}(\text{bdma})\text{H}_2]$ segregation might also be affected by that. Further experiments varying V/III ratio will clarify this behavior. By heating the sample up to 625 °C for optimal GaAs cap growth (marked with square) the N content decreases, due to desorption, abruptly. Fig. 7(b) presents the N and C incorporation

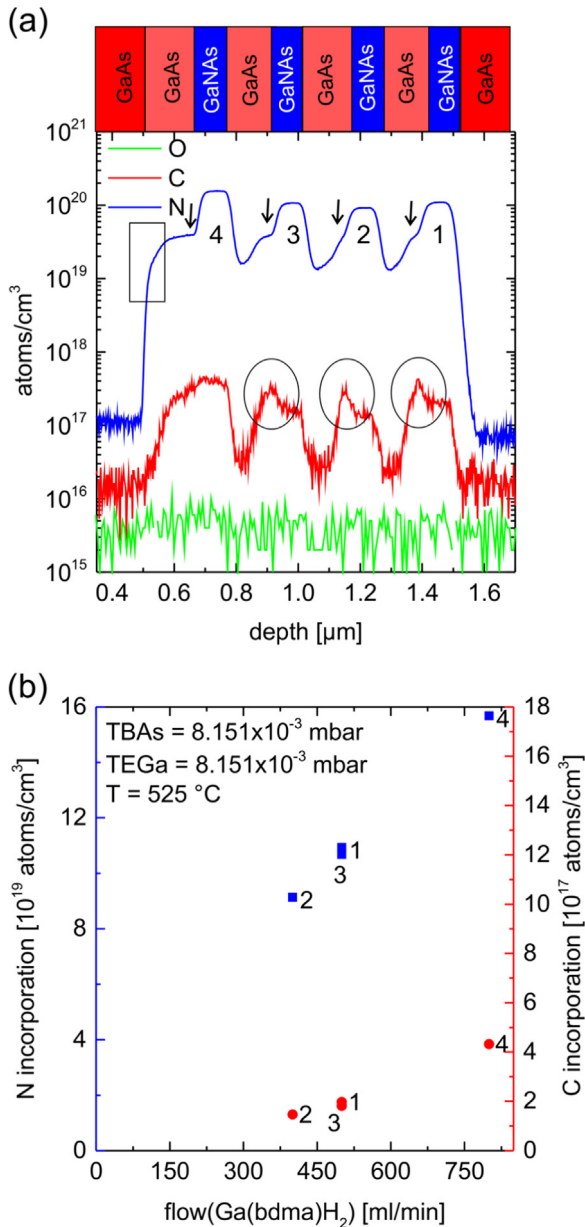


Fig. 7. SIMS measurement on a Ga(NAs) sample with four Ga(NAs) layers and GaAs barriers (growth direction from right to left). (a) SIMS measurements show no O incorporation during Ga(NAs) growth. C incorporates during Ga(NAs) growth and does not stay constant during growth, but accumulates apparently at the end of each Ga(NAs) layer (circles). N incorporation also shows some kind of accumulation and segregation (arrows). Segregation of [Ga(bdma)H₂] stops at 625 °C (square) and therefore the N incorporation drops. (b) Plot of N/C incorporation versus [Ga(bdma)H₂] flow. One clearly sees the linear link between [Ga(bdma)H₂] offer and N/C incorporation.

dependence of [Ga(bdma)H₂] flow. One notices a higher N and C incorporation with higher [Ga(bdma)H₂] offer. The C incorporation ranges in the 17th magnitude, which is comparable to the C incorporation in Ga(NAs) growth with UDMHy.

To verify the reliability of the HRXRD results and prove that N is responsible for the QW signal, all peak positions of the PL measurements were compared with the PL peak positions of UDMHy grown Ga(NAs) bulk samples having similar N contents. Fig. 8 shows a plot of PL peak position and N incorporation determined by HRXRD. The good agreement of the data underpins the accuracy and reliability of the HRXRD simulations and proves the N incorporation to the extent stated above using [Ga(bdma)H₂] as N precursor. As the test structures have been 5 QW's, some of the [Ga

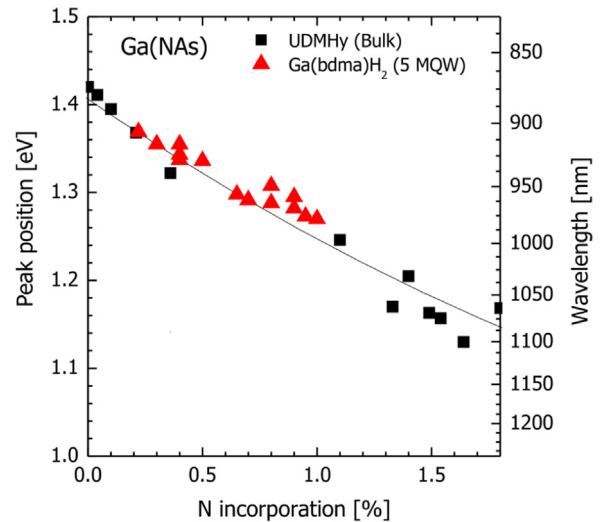


Fig. 8. PL peak vs. N incorporation (HRXRD) plotted to verify the reliability of HRXRD measurements. The small difference between [Ga(bdma)H₂] and UDMHy is due to the quantization effect.

(bdma)H₂) data lie slightly above the UDMHy values, which can be explained by the quantization effect.

After the first experimental session the bubbler was examined for intrinsic decomposition of the precursor. NMR measurements showed no decomposition of the molecule. During bubbler exchange, however, some [Ga(bdma)H₂] remains on the bubbler connections were observed, which have to be investigated in detail in future experiments.

5. Estimation of the N incorporation efficiency

For comparison of the N incorporation efficiency one has to know the vapor pressure of the used N precursor [Ga(bdma)H₂] and UDMHy. While it is known for UDMHy, the vapor pressure for [Ga(bdma)H₂] has to be determined. Analogous to the estimation of the vapor pressure of DTBAA in [20] we calculate the vapor pressure of [Ga(bdma)H₂]. The [Ga(bdma)H₂] consumption (c) is well known for several experiments, as the bubbler was weighted before and after the experiments. Also the hydrogen flow through the bubbler (Q_s), usage of the bubbler in minutes (t) and the bubbler pressure (P_c) are known. With the mol mass M_{mol}, the total consumption in grams can be determined by $c = Q_{s \frac{P_c}{P_c - P_s}} \frac{M_{mol}}{V_{mol}} t$. From that equation we estimate a vapor pressure of roughly 3 mbar for [Ga(bdma)H₂] at 20 °C.

For the comparison of N incorporation between UDMHy and [Ga(bdma)H₂] two samples with similar N content grown at 525 °C with UDMHy and [Ga(bdma)H₂] have been compared. The partial pressure of TBAs was approx. 8.2×10^{-3} mbar and the [Ga(bdma)H₂] flow was 500 ml/min (5.5×10^{-2} mbar). The TEGa in the UDMHy grown samples was fixed to 8.15×10^{-3} mbar with a TBAs partial pressure of 5.43×10^{-2} mbar and UDMHy of 0.194 mbar. By norming the consumption to the growth rate, we estimate a roughly 5 times higher N incorporation efficiency with [Ga(bdma)H₂] than with UDMHy. Of course, this is only a fairly crude estimation, as we have seen that dilute nitride growth using [Ga(bdma)H₂] is influenced also by the TEGa/[Ga(bdma)H₂] ratio. This estimate, however, shows that N incorporation using the novel precursor can be significantly more efficient than using UDMHy.

6. Summary

In this work we presented a systematic study of N incorporation behavior into GaAs utilizing the new N precursor [Ga(bdma) H_2]. N incorporation was determined by HRXRD and verified by as grown RTPL. Ga(NAs) growth with [Ga(bdma) H_2] showing good structural and optical properties was achieved.

N incorporation in dependence on temperature behaves similar for Ga(NAs) growth with [Ga(bdma) H_2] and UDMHy which we link to reduced N sticking at higher temperatures. Significant differences between [Ga(bdma) H_2] and UDMHy have been observed when varying the TEGa. The N incorporation, using the conventional N precursor UDMHy, is controlled by the UDMHy/TBAs ratio due to the competition of As and N for the same lattice site. [Ga(bdma) H_2] however, shows no such behavior for the TBAs partial pressure range studied which indicates a totally different incorporation behavior of [Ga(bdma) H_2] in comparison to UDMHy. The N incorporation of [Ga(bdma) H_2] can be controlled with TEGa/[Ga(bdma) H_2] ratio, whereas N incorporation is not affected by TEGa variation in Ga(NAs) growth with UDMHy. This can be explained with Ga source (TEGa and [Ga(bdma) H_2]) competition on the surface. In addition to N the new precursor also incorporates Ga. Therefore, no TEGa is needed for Ga(NAs) growth. It should be noted that the samples without TEGa offer exhibit smooth surfaces with atomic steps and also RTPL without applying post growth annealing.

[Ga(bdma) H_2] has a higher N incorporation efficiency in comparison to UDMHy and hence it is promising to further research dilute nitride growth using this class of molecules. Of course, one of the next steps will be to synthesize and test a molecule with a similar structural motif, but not based on 1,1-dimethylhydrazine without any N-methyl-units to also suppress the unintentional C incorporation. Moreover, it might be interesting to study GaN growth using [Ga(bdma) H_2].

Acknowledgments

This work was supported by the German Science Foundation (GRK 1782: "Functionalization of Semiconductors").

Appendix A. Supporting information

Supplementary data associated with this article can be found in the online version at <http://dx.doi.org/10.1016/j.jcrysgro.2016.08.061>.

References

- [1] W. Shan, W. Walukiewicz, K.M. Yu, J.W. Ager III, E.E. Haller, J.F. Geisz, D. J. Friedman, J.M. Olson, S.R. Kurtz, H.P. Xin, C.W. Tu, Band anticrossing in III–N–V alloys, *Phys. Status Solidi (b)* 223 (1) (2001) 75–85, [http://dx.doi.org/10.1002/1521-3951\(200101\)223:1<75::AID-PSSB75>3.0.CO;2-1](http://dx.doi.org/10.1002/1521-3951(200101)223:1<75::AID-PSSB75>3.0.CO;2-1).
- [2] W. Shan, W. Walukiewicz, J.W. Ager III, E.E. Haller, J.F. Geisz, D.J. Friedman, J.M. Olson, S.R. Kurtz, Band anticrossing in GaInNAs alloys, *Phys. Rev. Lett.* 82 (1999) 1221–1224, <http://dx.doi.org/10.1103/PhysRevLett.82.1221>.
- [3] W. Shan, K.M. Yu, W. Walukiewicz, J. Wu, J.W. Ager, E.E. Haller, Band anticrossing in dilute nitrides, *J. Phys.: Condens. Matter* 16 (31) (2004) S3355–S3372, <http://dx.doi.org/10.1088/0953-8984/16/31/024>.
- [4] J. Wu, W. Shan, W. Walukiewicz, Band anticrossing in highly mismatched III V semiconductor alloys, *Semicond. Sci. Technol.* 17 (8) (2002) 860–869, <http://dx.doi.org/10.1088/0268-1242/17/8/315>.
- [5] D.J. Friedman, J.F. Geisz, S.R. Kurtz, J.M. Olson, 1 eV solar cells with GaInNAs active layer, *J. Cryst. Growth* 195 (1998) 409–415, [http://dx.doi.org/10.1016/S0022-0248\(98\)00561-2](http://dx.doi.org/10.1016/S0022-0248(98)00561-2).
- [6] J.F. Geisz, D.J. Friedman, J.M. Olson, S.R. Kurtz, B.M. Keyes, Photocurrent of 1 eV GaInNAs lattice-matched to GaAs, *J. Cryst. Growth*, vol. 195, pp. 401–408, doi: [http://dx.doi.org/10.1016/S0022-0248\(98\)00563-6](http://dx.doi.org/10.1016/S0022-0248(98)00563-6).
- [7] S. Kurtz, A.A. Allerman, E.D. Jones, J.M. Gee, J.J. Banas, B.E. Hammons, InGaAsN solar cells with 1.0 eV band gap, lattice matched to GaAs, *Appl. Phys. Lett.* 74 (1999) 729–731, <http://dx.doi.org/10.1063/1.123105>.
- [8] F. Hohnsdorf, J. Koch, S. Leu, W. Stolz, B. Borchert, M. Druminski, Reduced threshold current densities of (GaIn)(NAs)/GaAs single quantum well lasers for emission wavelengths in the range 1.28–1.38 μ m, *Electron. Lett.* 35 (7) (1999) 571–572, <http://dx.doi.org/10.1049/el:19990421>.
- [9] S. Sato, S. Satoh, 1.3 μ m continuous-wave operation of GaInNAs lasers grown by metal organic chemical vapour deposition, *Electron. Lett.* 35 (15) (1999) 1251–1252, <http://dx.doi.org/10.1049/el:19990858>.
- [10] M. Kawaguchi, T. Miyamoto, E. Gouardes, D. Schlenker, T. Kondo, F. Koyama, K. Iga, Lasing characteristics of low-threshold GaInNAs lasers grown by metalorganic chemical vapor deposition, *Jpn. J. Appl. Phys.* 40 (2001) L744, <http://dx.doi.org/10.1143/JJAP.40.L744>.
- [11] K. Volz, J. Koch, F. Hohnsdorf, B. Kunert, W. Stolz, MOVPE growth of dilute nitride III/V semiconductors using all liquid metalorganic precursors, *J. Cryst. Growth* 311 (8) (2009) 2418–2426, <http://dx.doi.org/10.1016/j.jcrysgro.2008.09.210>.
- [12] N. Miyashita, N. Ahsan, Y. Okada, Effect of antimony on uniform incorporation of nitrogen atoms in GaInNAs films for solar cell application, *Sol. Energy Mater. Sol. Cells* 111 (2013) 127–132, <http://dx.doi.org/10.1016/j.solmat.2012.12.036>.
- [13] V. Polojärvi, A. Aho, A. Tukiainen, M. Raappana, T. Aho, A. Schramm, M. Guina, Influence of As/group-III flux ratio on defects formation and photovoltaic performance of GaInNAs solar cells, *Sol. Energy Mater. Sol. Cells* 149 (2016) 213–220, <http://dx.doi.org/10.1016/j.solmat.2016.01.024>.
- [14] K. Volz, T. Torunski, B. Kunert, O. Rubel, S. Nau, S. Reinhard, W. Stolz, Specific structural and compositional properties of (GaIn)(NAs) and their influence on optoelectronic device performance, *J. Cryst. Growth* 272 (1–4) (2004) 739–747, <http://dx.doi.org/10.1016/j.jcrysgro.2004.09.012>.
- [15] F. Hohnsdorf, J. Koch, C. Agert, W. Stolz, Investigations of (GaIn)(NAs) bulk layers and (GaIn)(NAs)/GaAs multiple quantum well structures grown using tertiarybutylarsine (TBAs) and 1,1-dimethylhydrazine (UDMHy), *J. Cryst. Growth* 195 (1998) 391–396, [http://dx.doi.org/10.1016/S0022-0248\(98\)00651-4](http://dx.doi.org/10.1016/S0022-0248(98)00651-4).
- [16] I. Suemune, K. Uesugi, T.Y. Seong, Growth and structural characterization of III–N–V semiconductor alloys, *Semicond. Sci. Technol.* 17 (8) (2002) 755–761, <http://dx.doi.org/10.1088/0268-1242/17/8/303>.
- [17] U.W. Pohl, C. Mo, Tertiarybutylhydrazine: a new precursor for the MOVPE of Group III-nitrides, *Mater. Sci. Eng.* 59 (1999) 20–23, [http://dx.doi.org/10.1016/S0921-5107\(98\)00406-1](http://dx.doi.org/10.1016/S0921-5107(98)00406-1).
- [18] B. Beaumont, P. Gibart, J.P. Faurie, Nitrogen precursors in metalorganic vapor phase epitaxy of (Al,Ga)N, *J. Cryst. Growth* 156 (3) (1995) 140–146, [http://dx.doi.org/10.1016/0022-0248\(95\)00296-0](http://dx.doi.org/10.1016/0022-0248(95)00296-0), ISSN 0022-0248.
- [19] S. Kurtz, R. Reedy, G.D. Barber, J.F. Geisz, D.J. Friedman, W.E. McMahon, J. M. Olson, Incorporation of nitrogen into GaAsN grown by MOCVD using different precursors, *J. Cryst. Growth* 234 (2–3) (2002) 318–322, [http://dx.doi.org/10.1016/S0022-0248\(01\)01711-0](http://dx.doi.org/10.1016/S0022-0248(01)01711-0).
- [20] E. Sterzer, A. Beyer, L. Duschek, L. Nattermann, B. Ringler, B. Leube, A. Stegmüller, R. Tonner, C. von Hänisch, W. Stolz, K. Volz, Efficient nitrogen incorporation in GaAs using novel metal organic As–N precursor di-tertiary-butyl-arsano-amine (DTBAA), *J. Cryst. Growth*, 439, pp. 19–27, <http://dx.doi.org/10.1016/j.jcrysgro.2015.12.032>.

7.3 (GaIn)(NAs) Growth Using Di-Tertiary-Butyl-Arsano-Amine (DTBAA)*

E. Sterzer, B. Ringler, L. Nattermann, A. Beyer, C. von Hänisch, W. Stolz, K. Volz, *Journal of Crystal Growth* **467**, 132-136 (2017). DOI: 10.1016/j.jcrysgro.2017.01.014.

Abstract

III/V semiconductors containing small amounts of Nitrogen (N) are very interesting for a variety of optoelectronic applications. Unfortunately, the conventionally used N precursor 1,1-dimethylhydrazine (UDMHy) has an extremely low N incorporation efficiency in GaAs when grown using metal organic vapor phase epitaxy. Alloying Ga(NAs) with Indium (In) even leads to an exponential reduction of N incorporation. The huge amount of UDMHy in turn changes drastically the growth conditions. Furthermore, the application of this material is still hampered by the large carbon incorporation, most probably originating from the metal organic precursors. Hence, novel precursors for dilute nitride growth are needed. This paper will show (GaIn) (NAs) growth studies with the novel precursor di-tertiary-butyl-arsano-amine in combination with tri-ethyl-gallium and tri-methyl-indium. We show an extremely high N incorporation efficiency in the In containing (GaIn)(NAs). The (GaIn)(NAs) samples investigated in this study have been examined using high resolution X-Ray diffraction, room temperature photoluminescence and atomic force microscope measurements as well as secondary ion mass spectrometry.

The Authors contribution

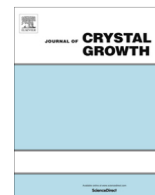
My contribution to this work was the planning, executing and investigation of all samples including MOVPE growth and HR-XRD, AFM as well as PL measurements. B. Ringler synthesized the precursor, which was used for the growth of the (GaIn)(NAs) layers. All co-authors helped to interpret the data for the publication which was written by me.

* Reprinted from *Journal of Crystal Growth* **467**, 132-136 (2017), Copyright 2017, with permission from Elsevier.



Contents lists available at ScienceDirect

Journal of Crystal Growth

journal homepage: www.elsevier.com/locate/jcrysgro

(GaIn)(NAs) growth using di-tertiary-butyl-arsano-amine (DTBAA)

E. Sterzer^{a,*}, B. Ringler^b, L. Nattermann^a, A. Beyer^a, C. von Hänisch^b, W. Stolz^a, K. Volz^a^a Material Sciences Center and Faculty of Physics, Philipps-Universität Marburg, Germany^b Material Sciences Center and Faculty of Chemistry, Philipps-Universität Marburg, Germany

ARTICLE INFO

Communicated by T.F. Kuech

Keywords:

A3. Metalorganic chemical vapor deposition

B1. Nitrides

B2. Semiconducting III-V materials

B2. Semiconducting gallium arsenide

ABSTRACT

III/V semiconductors containing small amounts of Nitrogen (N) are very interesting for a variety of optoelectronic applications. Unfortunately, the conventionally used N precursor 1,1-dimethylhydrazine (UDMHy) has an extremely low N incorporation efficiency in GaAs when grown using metal organic vapor phase epitaxy. Alloying Ga(NAs) with Indium (In) even leads to an exponential reduction of N incorporation. The huge amount of UDMHy in turn changes drastically the growth conditions. Furthermore, the application of this material is still hampered by the large carbon incorporation, most probably originating from the metal organic precursors. Hence, novel precursors for dilute nitride growth are needed. This paper will show (GaIn)(NAs) growth studies with the novel precursor di-tertiary-butyl-arsano-amine in combination with tri-ethyl-gallium and tri-methyl-indium. We show an extremely high N incorporation efficiency in the In containing (GaIn)(NAs). The (GaIn)(NAs) samples investigated in this study have been examined using high resolution X-Ray diffraction, room temperature photoluminescence and atomic force microscope measurements as well as secondary ion mass spectrometry.

1. Introduction

Nitrogen (N) incorporation in GaAs is used to reduce the band gap very strongly. An N content of only one percent reduces the band gap up to 180 meV, which has been described by the band anti crossing theory [1–5]. Dilute nitrides are therefore a promising tool for band gap engineering. Moreover, the small covalent radius of N compared to the other group V atoms allows an efficient reduction of the lattice constant. The gallium indium nitride arsenide (GaIn)(NAs) material, for instance, is discussed as the 1 eV layer in a four junction solar cell, lattice matched to Ge substrates [6–13]. Conventionally, 1,1-dimethyl-hydrazine (UDMHy) is used as N precursor in metal organic vapor phase epitaxy (MOVPE) growth. UDMHy, however, shows an extremely low N incorporation efficiency, which is even less when alloying Ga(NAs) with In (from tri-methyl-indium (TMIn)) [14]. Moreover, the best solar cells based on (GaIn)(NAs) as an 1 eV subcell were achieved with molecular beam epitaxy (MBE) growth. This 1 eV solar cell also contained up to 2% Sb. A similar growth of (GaIn)(NAsSb) is unfortunately not possible using MOVPE and UDMHy, as a huge excess of UDMHy has to be applied when In and Sb are incorporated in the alloy [15–22]. This makes the growth of high quality layers at a certain point impossible. On top of that, the MOVPE grown dilute nitride samples are still suffering from unintentional carbon (C) incorporation, which increases strongly with high UDMHy partial

pressure, which is however necessary to incorporate sufficient N into the material. This C incorporation is believed to reduce the solar cell efficiency [13]. It is still unclear where exactly the C incorporation is originating from. It stems either from the methyl part of the UDMHy or from other alkyl groups like methyl or ethyl radicals from the other metal organic precursors, which can bond to N on the surface and therefore incorporate easily.

Recent results show a high N incorporation efficiency of the molecule di-tertiary-butyl-arsano-amine (DTBAA) in Ga(NAs) [23]. To increase the understanding of DTBAA's incorporation nature and to investigate its potential also for the quaternary layers, (GaIn)(NAs) structures have been grown varying the growth conditions systematically.

In this paper we will present systematic growth experiments of (GaIn)(NAs) using TEGa, TMIn and DTBAA. HRXRD, PL, as well as AFM and SIMS will be shown. Moreover, we will also discuss the role of TMIn in terms of C incorporation.

2. Growth and characterization of (GaIn)(NAs) layers

All samples have been grown in an Aixtron AIX 200 horizontal gas foil rotation (GFR) reactor, heated by 6 halogen lamps. The reactor pressure was held constant at 50 mbar (37.5 Torr) with a total flux of 6800 sccm Pd-purified hydrogen carrier gas. The exact GaAs (001)

* Corresponding author.

E-mail address: eduard.sterzer@physik.uni-marburg.de (E. Sterzer).<http://dx.doi.org/10.1016/j.jcrysgro.2017.01.014>

Received 17 November 2016; Received in revised form 6 January 2017; Accepted 9 January 2017

Available online 10 January 2017

0022-0248/ © 2017 Elsevier B.V. All rights reserved.

semi-insulating samples were rotated at 60–70 rpm to ensure uniform growth.

To provide a high quality surface for subsequent growth, the first layer was a 250 nm thick GaAs buffer grown at 625 °C under optimized conditions. The temperature change from 625 °C to 500 °C (growth temperature of the dilute nitride alloy) was performed under TBAs stabilization to prevent As desorption. Structures with five, up to 10 nm thick, Ga(In)NAs quantum wells (QWs) and 15 nm thick GaAs barriers have been grown, finishing with the last (5th) (GaIn)(NAs) QW to be able to investigate the surface of the layer of interest. The samples were cooled to 350 °C under *tertiary*-butyl-arsine (TBAs) stabilization. All ternary and quaternary dilute nitride layers have been grown without TBAs, which was however used for growth of the GaAs barriers and buffer layer. Tri-ethyl-gallium (TEGa) and TMIn have been used as group III precursors. DTBAA was used as N as well as As precursor for the dilute nitride QW growth. Reference (GaIn)As samples with the same TEGa/TMIn ratio as in the (GaIn)(NAs) material have been grown in order to estimate the In incorporation in the quaternary material. With the assumption that the In incorporation is identical in the ternary and in the quaternary material, the high resolution X-ray diffraction (HRXRD) patterns have been simulated to obtain the N content. Room temperature photo luminescence (PL) measurements were undertaken to confirm that the so-derived N and In contents are plausible. The composition has also been verified via secondary ion mass spectrometry (SIMS) for one growth condition. (GaIn)(NAs) growth experiments were performed at a constant temperature of 500 °C, constant TEGa (8.15×10^{-3} mbar) and DTBAA (3.72×10^{-2} mbar) partial pressure, varying the TMIn partial pressure from 0.568×10^{-3} to 2.27×10^{-3} mbar linearly in four steps, one value for each sample growth.

The growth rate and strain of the layers have been determined by high resolution X-ray diffraction (HRXRD) using a Panalytical X'Pert Pro system using the Cu K α 1 wavelength (0.15405 Å). Diffraction patterns around the (004) GaAs reflection were obtained and simulated with the X'Pert Epataxy software. There is an infinite number of possible composition solutions for a quaternary material if only the strain of the layer is taken into account. Hence, not only HRXRD, but also PL was used to estimate the composition.

To investigate the optical properties, the samples have been excited at room temperature with the 512 nm line of an argon ion laser (100 mW with 163 μ m FWHM). A liquid N₂ cooled Ge detector with standard lock-in technique was used to collect the signal which was dispersed with a 1 m grating monochromator (THR 1000, Jobin-Yvon). All samples shown have been annealed after growth in a Jipelec JetFirst 200 C Rapid Thermal Annealer (RTA) at 700 °C for 10 s.

A Nanoscope IIIa atomic force microscope was used to investigate the surface morphology (in tapping mode).

A specific sample for SIMS analysis has also been grown, containing both a Ga(NAs) and (GaIn)(NAs) layer, to determine the oxygen (O), C, N and In incorporation.

3. Results and discussion

In Fig. 1 HRXRD measurements of 6 samples are shown. Sample 1 was grown without TMIn, just with TEGa and DTBAA with partial pressures of 8.151×10^{-3} and 3.72×10^{-2} mbar, respectively. The ternary (GaIn)As sample (sample 6) was grown with the same TEGa partial pressure and a TMIn partial pressure of 1.7×10^{-3} mbar. As no DTBAA was supplied, TBAs with a partial pressure of 3.26×10^{-2} mbar had to be applied for this sample. The (GaIn)(NAs) structures have subsequently been grown with different TMIn partial pressures. Starting from sample 2 over samples 3, 4 and 5, the TMIn partial pressure was increased from 0.568×10^{-3} mbar in 0.568×10^{-3} mbar steps up to 2.27×10^{-3} mbar. One clearly sees the strain changing from tensile to compressive with higher TMIn input (Fig. 1). Sample 4 was grown with the same TMIn partial pressure as sample 6 and with the same DTBAA

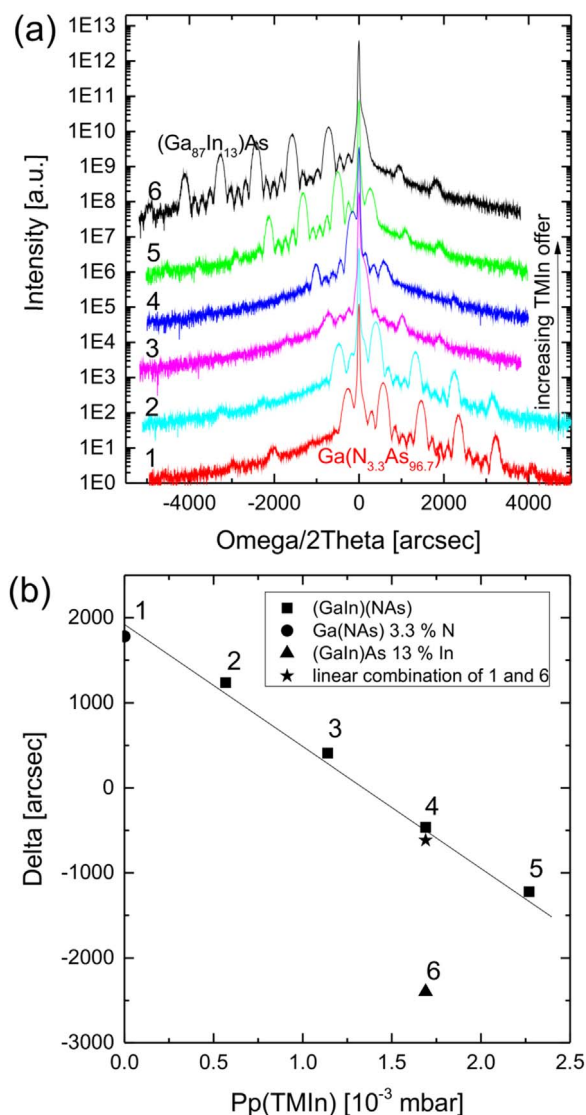


Fig. 1. (a) HRXRD of Ga(NAs) (1), (GaIn)(NAs) (2–5) and (GaIn)As (6) with different TMIn partial pressures. The sample no. 4 was grown with the same TEGa and TMIn partial pressures as sample no. 6 and with the DTBAA partial pressure of the sample no. 1. (b) Angular position of the maximum of the envelope of the MQW peaks with respect to the GaAs(004) substrate peak.

partial pressure as sample 1. By simulating the HRXRD pattern of sample 4 with the assumption of an In incorporation (13% In) independent from the N (and DTBAA), a good match was found for an N content of 3.7% N. This means an increase in N incorporation in (GaIn)(NAs) compared to the In-free Ga(NAs) case. The same is observed for the other samples grown in this study. In Fig. 1(b) the relative distance of the XRD layer envelope to the GaAs (004) peak is plotted versus TMIn partial pressure. To prove that TMIn and DTBAA incorporate independently, linear strain estimation for a combination of samples 1 and 6 was done and is seen in Fig. 1(b) as a star. Sample no. 4 reveals a strain which is close to the predicted one, proving a linear combination of N and In incorporation using DTBAA and TMIn.

To verify the In and N contents, PL measurements have also been performed. In Fig. 2 the PL-spectra of all six samples are plotted. If any significant decrease in N incorporation happened, the PL-peak position would shift to higher energies. Instead the PL-peak position shifts to lower energy with higher TMIn input/incorporation supporting the assumption of a linear combination of N and In incorporation. Fig. 2(b) shows the shift of the PL-peak positions in dependence of the TMIn partial pressure demonstrating the linearity of PL-peak position change.

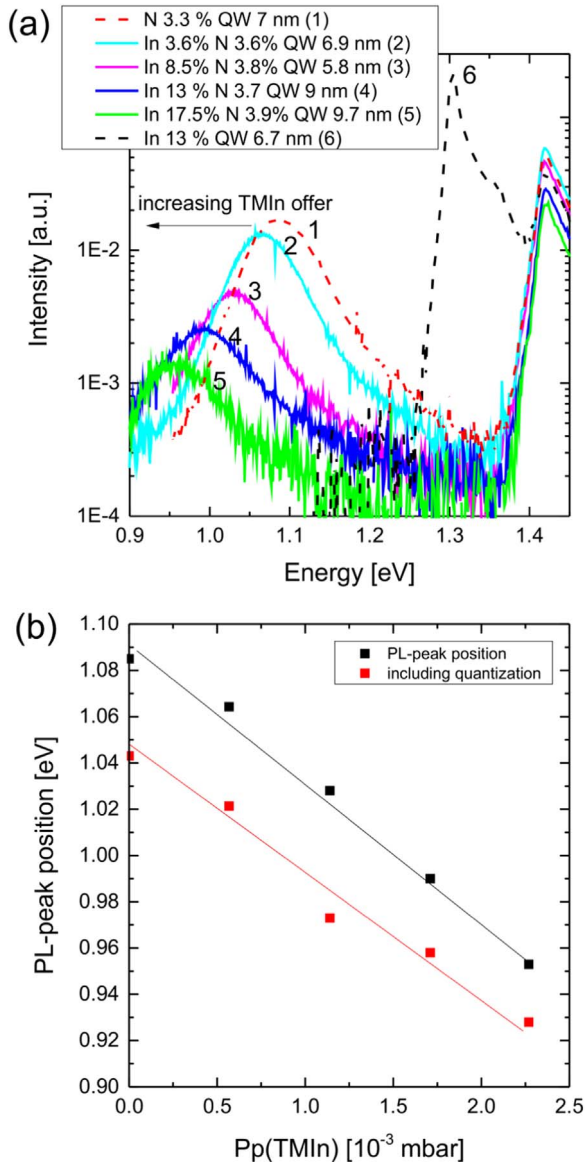


Fig. 2. (a) PL spectra of Ga(NAs), (GaIn)As and (GaIn)(NAs) (same samples as shown in Fig. 1). (b) PL peak position dependence on TMIn partial pressure (black data points). As the layer thickness was below 10 nm, quantization effects have to be taken into account (red data points denote the bandgap position). The solid lines are guides to the eye only. (For interpretation of the references to color in this figure legend, the reader is referred to the web version of this article.)

At this point we assume an In incorporation independent of the N (and the DTBAA), which was determined using ternary calibration materials. From HRXRD simulations of the quaternary layers, the corresponding N content is deduced then from the strain. The normalized N content in Fig. 3 shows the behavior of (GaIn)(NAs) growth with DTBAA in comparison to UDMHy. Whereas the N incorporation using UDMHy decreases exponentially with increasing In content, DTBAA grown samples even show an increase of N incorporation with increasing In. This makes the N incorporation efficiency with DTBAA even higher for (GaIn)(NAs) growth than for Ga(NAs) growth. Taking into account that the N incorporation efficiency in Ga(NAs) from DTBAA is roughly 10 times higher than UDMHy [23] the N incorporation efficiency in (GaIn)(NAs) solar cell material with a composition of roughly 8% In and 3% N increases up to 40x compared to (GaIn)(NAs) growth using UDMHy. MBE grown (GaIn)(NAs) samples show a similar behavior concerning the N incorporation increase with higher In content. Therefore we believe that the N incorporation increase

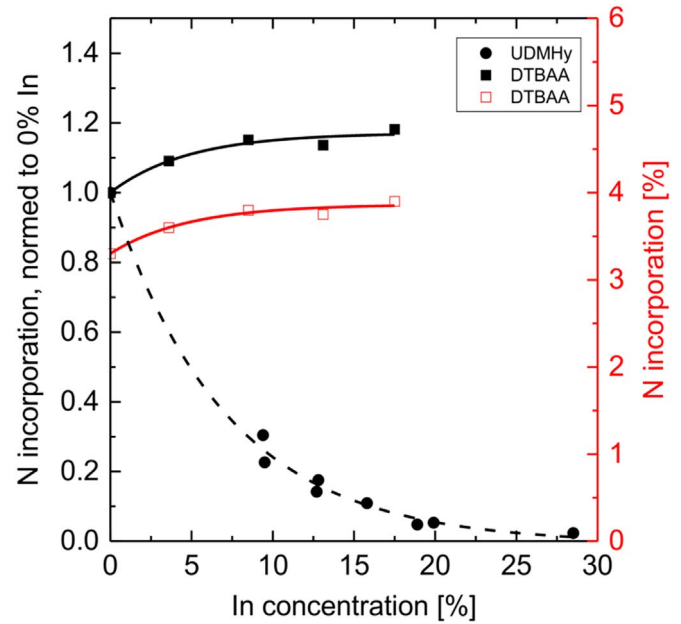


Fig. 3. N incorporation in (GaIn)(NAs) dependence on In concentration. The N incorporation in (GaIn)(NAs) grown with UDMHy (black spheres: normalized to the 0% In layer, data taken from [15]) drops by 75% in comparison to pure Ga(NAs) when alloyed with 8% In. The samples grown with DTBAA show a higher N incorporation when adding In compared to the In-free sample (black squares: normalized to the 0% In layer; red open squares: actual N incorporation in the layer). (For interpretation of the references to color in this figure legend, the reader is referred to the web version of this article.)

stems from lattice pulling [24]. The N incorporation drop in (GaIn)(NAs) grown with UDMHy can be related to N/In (UDMHy/TMIn) interaction in the gas phase or/and on the surface or to the UDMHy decomposition characteristics. As mentioned earlier, N incorporation in MOVPE grown (GaIn)(NAs) samples suffer from extremely low N incorporation in the quaternary material, probably due to the decomposition path of UDMHy (mainly N₂) and the In-induced N desorption [14], making DTBAA a preferable N precursor for dilute nitrides, especially for In containing dilute nitrides.

Fig. 4 shows the N and In incorporation dependence on the TMIn partial pressure. Here we see the linear behavior of In incorporation as well as the slightly increasing N incorporation. The growth rate seems not to change up to a TMIn partial pressure of 1.5×10⁻³ mbar; after that value the growth rate increases due to higher group III partial pressure. The reasons for this behavior will be clarified in the future. AFM measurements reveal a smooth surface with atomic steps with an RMS value of 0.14 ((GaIn)(NAs)) and 0.16 (Ga(NAs)) nm.

Low O and C levels in compound semiconductors are key points in terms of device efficiency. Therefore, a layer with a device favorable composition (3% N and 8% In) was grown and investigated with SIMS. Fig. 5 shows the SIMS depth profile for In, N, C and O in atoms/cm³. The growth direction is from right to left. The sample contains two layers: lattice matched (GaIn)(NAs) and a Ga(NAs) layer with 3% N which are separated by roughly 150 nm GaAs. Unfortunately both layers contain a fairly high amount of O which is around 3.5×10¹⁸ atoms/cm³. These high O levels are a hint that the DTBAA, which has been synthesized only at the laboratory scale and has not been purified sufficiently for this study, is still a source of O. Similar O levels are not observed when growing dilute nitrides using UDMHy. The purification by distillation in the lab is therefore not sufficient to exclude all O. The C incorporation using DTBAA has the same magnitude as the C incorporation in Ga(NAs) and (GaIn)(NAs) layers grown with UDMHy (around 10¹⁸ atoms/cm³) [13]. However, as the DTBAA is not sufficiently purified, the C contamination might also stem from impurities in the DTBAA. Hence, future studies will include growth and SIMS characterization using purified DTBAA.

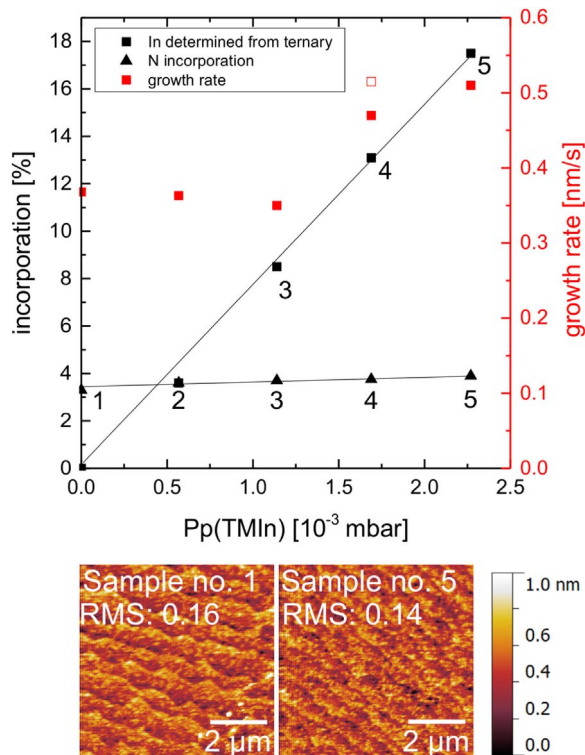


Fig. 4. Summary of N (black triangles) and In (black squares) incorporation vs. TMIn partial pressure. The growth rate for the samples is shown as red squares. The opened red square represents the growth rate of the (GaIn)As sample with the same In content as sample no. 4. The AFM micrographs of samples no. 1 and no. 5 are shown below the graph. (For interpretation of the references to color in this figure legend, the reader is referred to the web version of this article.)

As soon as In is present, incorporation of N, C and O changes. Fig. 5(b) shows the change in concentration depending on In incorporation. As mentioned previously and now proven by SIMS, the N incorporation is increasing with higher In concentration. The O incorporation increases similarly to the N incorporation, showing a connection between N and O incorporation due to impurities in the DTBAA precursor. The C incorporation, however, doubles with additional TMIn. This cannot only be explained by the impurity of DTBAA, as the N and O incorporation increased only by roughly 12–17%. As we use TMIn for the growth of the quaternary material, additional methyl radicals are supplied and can bond to N. Due to the strong N–C bond more C might be incorporated into the crystal. This means that also a novel In precursor will be needed when aiming to minimize the C content in dilute nitride alloys.

4. Summary and outlook

In this work systematic investigation of N and In incorporation in GaAs using TEGa, TMIn and DTBAA has been presented. HRXRD, PL and SIMS were used to obtain reliable information concerning the N and In contents of the quaternary material. A linear change in the strain with higher TMIn partial pressure, measured with HRXRD, could arise either from increasing In incorporation or N incorporation reduction. PL measurements showed a linear PL-peak shift towards lower energies. This red shift can be explained by increasing In content with higher TMIn without an N incorporation reduction in the quaternary material. Furthermore, SIMS measurements even revealed an increase in N incorporation when increasing the In content. The result is an increase in the N incorporation efficiency from DTBAA vs. UDMHy by up to a factor of 40 for a composition of (Ga_{0.92}In_{0.08}) (As_{0.97}N_{0.03}). A similar N incorporation behavior was never before

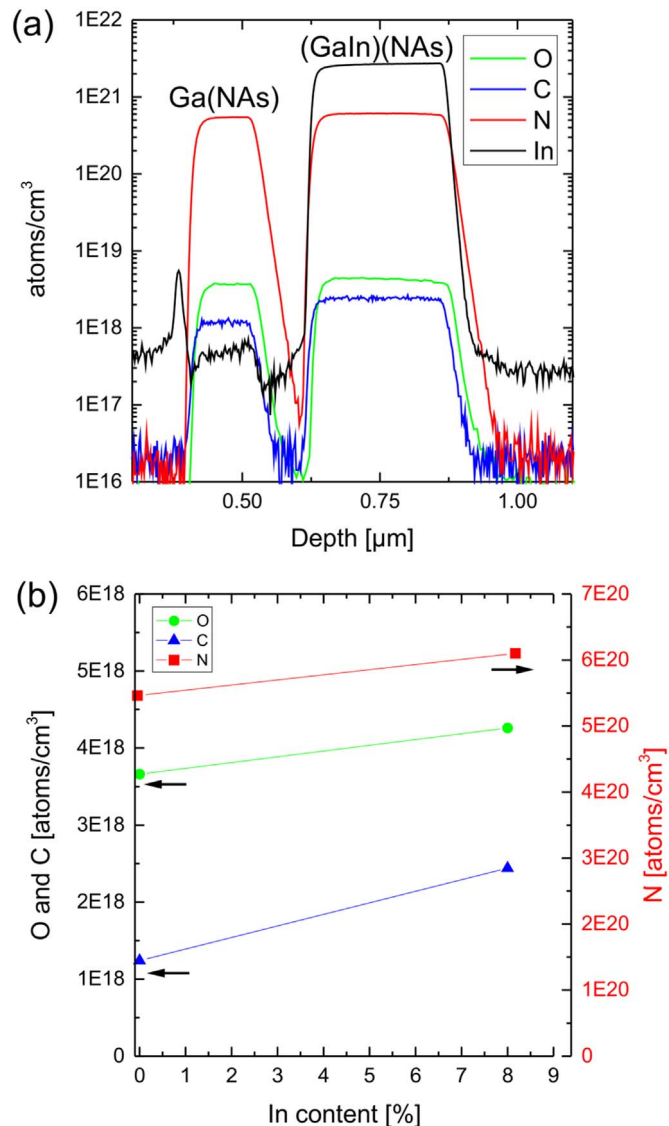


Fig. 5. (a) SIMS profiles for O, C, N and In in Ga(NAs) and (GaIn)(NAs) grown under the same conditions expect for the addition of In to the quaternary layer and excluding TBAs. (b) N, C and O incorporation change with In. (Arrows pointing towards corresponding scale).

observed in MOVPE growth using UDMHy. SIMS measurement also revealed O and C incorporation, which are increasing with additional In content. O is originating from the impurities in the new, laboratory scale synthesized, N precursor DTBAA and is incorporating together with N. C incorporation is increasing from Ga(NAs) to (GaIn)(NAs) by a factor of two, showing that at least as much C is originating from DTBAA as from TMIn. In future experiments (GaIn)(NAs) material will be grown with purified DTBAA in order to prevent O and C incorporation originating from DTBAA. Moreover, novel In precursors will be tested to examine the influence of the group III precursors on the C incorporation. Using this material, 1 eV cells will be realized and compared to existing UDMHy grown (GaIn)(NAs) cells. Furthermore, N incorporation studies in combination with tri-methyl-antimony and tri-ethyl-antimony will be performed on GaAs.

Acknowledgements

This work was supported by the German Science Foundation (GRK 1782: “Functionalization of Semiconductors”).

References

- [1] W. Shan, W. Walukiewicz, K.M. Yu, I.I.I., J.W. Ager, E.E. Haller, J.F. Geisz, D.J. Friedman, J.M. Olson, S.R. Kurtz, H.P. Xin, C.W. Tu, Band anticrossing in III–N–V alloys, *Physica Status Solidi (b)* 223 (1) (2001) 75–85. [http://dx.doi.org/10.1002/1521-3951\(200101\)223:1 < 75::AID-PSSB75 > 3.0.CO;2-1](http://dx.doi.org/10.1002/1521-3951(200101)223:1 < 75::AID-PSSB75 > 3.0.CO;2-1).
- [2] W. Shan, W. Walukiewicz, I.I.I., J.W. Ager, E.E. Haller, J.F. Geisz, D.J. Friedman, J.M. Olson, S.R. Kurtz, Band anticrossing in GaInNAs alloys, *Phys. Rev. Lett.* 82 (1999) 1221–1224. <http://dx.doi.org/10.1103/PhysRevLett.82.1221>.
- [3] W. Shan, K.M. Yu, W. Walukiewicz, J. Wu, J.W. Ager, E.E. Haller, Band anticrossing in dilute nitrides, *J. Phys.: Condens. Matter* 16 (31) (2004) S3355–S3372. <http://dx.doi.org/10.1088/0953-8984/16/31/024>.
- [4] J. Wu, W. Shan, W. Walukiewicz, Band anticrossing in highly mismatched III V semiconductor alloys, *Semicond. Sci. Technol.* 17 (8) (2002) 860–869. <http://dx.doi.org/10.1088/0268-1242/17/8/315>.
- [5] Jun Shao, Wei Lu, M. Sadeghi, Xiang Lü, S.M. Wang, Lili Ma, A. Larsson, Evolution of valence-band alignment with nitrogen content in GaNAs/GaAs single quantum wells, *Appl. Phys. Lett.* 93 (2008) 031904. <http://dx.doi.org/10.1063/1.2958232>.
- [6] D.J. Friedman, J.F. Geisz, S.R. Kurtz, J.M. Olson, 1-eV solar cells with GaInNAs active layer, *J. Cryst. Growth* 195 (1998) 409–415. [http://dx.doi.org/10.1016/S0022-0248\(98\)00561-2](http://dx.doi.org/10.1016/S0022-0248(98)00561-2).
- [7] J.F. Geisz, D.J. Friedman, J.M. Olson, S.R. Kurtz, B.M. Keyes, Photocurrent of 1 eV GaInNAs lattice-matched to GaAs, *J. Cryst. Growth*, 195, pp. 401–408, [http://dx.doi.org/10.1016/S0022-0248\(98\)00563-6](http://dx.doi.org/10.1016/S0022-0248(98)00563-6).
- [8] S. Kurtz, A.A. Allerman, E.D. Jones, J.M. Gee, J.J. Banas, B.E. Hammons, InGaAsN solar cells with 1.0 eV band gap, lattice matched to GaAs, *Appl. Phys. Lett.* 74 (1999) 729–731. <http://dx.doi.org/10.1063/1.123105>.
- [9] F. Hohnsdorf, J. Koch, S. Leu, W. Stolz, B. Borchert, M. Druminski, Reduced threshold current densities of (GaIn)(NAs)/GaAs single quantum well lasers for emission wavelengths in the range 1.28–1.38 μm , *Electron. Lett.* 35 (7) (1999) 571–572. <http://dx.doi.org/10.1049/el:19990421>.
- [10] S. Sato, S. Satoh, 1.3 μm continuous-wave operation of GaInNAs lasers grown by metal organic chemical vapour deposition, *Electron. Lett.* 35 (15) (1999) 1251–1252. <http://dx.doi.org/10.1049/el:19990858>.
- [11] M. Kawaguchi, T. Miyamoto, E. Gouardes, D. Schlenker, T. Kondo, F. Koyama, K. Iga, Lasing characteristics of low-threshold GaInNAs lasers grown by metalorganic chemical vapor deposition, *Jpn. J. Appl. Phys.* 40 (2001) L744. <http://dx.doi.org/10.1143/JJAP.40.L744>.
- [12] V. Polojärvi, A. Aho, A. Tukiainen, M. Raappana, T. Aho, A. Schramm, M. Guina, Influence of As/group-III flux ratio on defects formation and photovoltaic performance of GaInNAs solar cells, *Sol. Energy Mater. Sol. Cells* 149 (2016) 213–220. <http://dx.doi.org/10.1016/j.solmat.2016.01.024>.
- [13] K. Volz, T. Torunski, B. Kunert, O. Rubel, S. Nau, S. Reinhard, W. Stolz, Specific structural and compositional properties of (GaIn)(NAs) and their influence on optoelectronic device performance, *J. Cryst. Growth* 272 (1–4) (2004) 739–747. <http://dx.doi.org/10.1016/j.jcrysgro.2004.09.012>.
- [14] K. Volz, J. Koch, F. Höhnsdorf, B. Kunert, W. Stolz, MOVPE growth of dilute nitride III/V semiconductors using all liquid metalorganic precursors, *J. Cryst. Growth* 311 (8) (2009) 2418–2426. <http://dx.doi.org/10.1016/j.jcrysgro.2008.09.210>.
- [15] D.B. Jackrel, S.R. Bank, H.B. Yuen, M. a. Wistey, J.S. Harris, A.J. Ptak, S.R. Kurtz, Dilute nitride GaInNAs and GaInNAsSb solar cells by molecular beam epitaxy, *J. Appl. Phys.* 101 (11) (2007) 1–8. <http://dx.doi.org/10.1063/1.2744490>.
- [16] N. Miyashita, N. Ahsan, Y. Okada, Effect of antimony on uniform incorporation of nitrogen atoms in GaInNAs films for solar cell application, *Sol. Energy Mater. Sol. Cells* 111 (2013) 127–132. <http://dx.doi.org/10.1016/j.solmat.2012.12.036>.
- [17] N.A. Naoya Miyashita, Y. O. Generation and collection of photocarriers in dilute nitride GaInNAsSb solar cells, *Prog. Photovolt: Res. Appl.* (15) (2016). <http://dx.doi.org/10.1002/pip.2641>.
- [18] M.M. Islam, N. Miyashita, N. Ahsan, T. Sakurai, K. Akimoto, Y. Okada, Photocapacitance study of MBE grown GaInNAsSb thin film solar cells, *J. Cryst. Growth* 378 (2013) 57–60. <http://dx.doi.org/10.1016/j.jcrysgro.2012.12.150>.
- [19] A. Aho, A. Tukiainen, V. Polojarvi, M. Guina, Performance assessment of multi-junction solar cells incorporating GaInNAsSb, *Nanoscale Res. Lett.* 9 (2014) 1–7. <http://dx.doi.org/10.1186/1556-276X-9-61>.
- [20] D.B. Jackrel, S.R. Bank, H.B. Yuen, M.A. Wistey, J.S. Harris, A.J. Ptak, S.R. Kurtz, Dilute nitride GaInNAs and GaInNAsSb solar cells by molecular beam epitaxy, *J. Appl. Phys.* 101 (11) (2007). <http://dx.doi.org/10.1063/1.2744490>.
- [21] F. Höhnsdorf, J. Koch, C. Agert, W. Stolz, Investigations of (GaIn)(NAs) bulk layers and (GaIn)(NAs)/GaAs multiple quantum well structures grown using tertiarybutylarsine (TBAs) and 1,1-dimethylhydrazine (UDMH₂), *J. Cryst. Growth* 195 (1998) 391–396. [http://dx.doi.org/10.1016/S0022-0248\(98\)00651-4](http://dx.doi.org/10.1016/S0022-0248(98)00651-4).
- [22] I. Suemune, K. Uesugi, T.Y. Seong, Growth and structural characterization of III–N–V semiconductor alloys, *Semicond. Sci. Technol.* 17 (8) (2002) 755–761. <http://dx.doi.org/10.1088/0268-1242/17/8/303>.
- [23] E. Sterzer, A. Beyer, L. Duschek, L. Nattermann, B. Ringler, B. Leube, A. Stegmüller, R. Tonner, C. von Hänisch, W. Stolz, K. Volz, Efficient nitrogen incorporation in GaAs using novel metal organic As–N precursor di-tertiary-butyl-arsano-amine (DTBAA), *J. Cryst. Growth*, 439, pp. 19–27, <http://dx.doi.org/10.1016/j.jcrysgro.2015.12.032>.
- [24] J.-C.H. Dias, A. C. E. V. K. R. L. L., J. R. R. T. L. T., G. U. B. T. I. F. L., GaNAsSb: how does it compare with other dilute III–V-nitride alloys?, *Semicond. Sci. Technol.* 17 (8) (2002) 778. <http://dx.doi.org/10.1088/0268-1242/17/8/306>.

7.4 1 eV Ga(NAsSb) Grown in MOVPE Using Di-Tertiary-Butyl-Arsano-Amine (DTBAA)*

E. Sterzer, O. Maßmeyer, L. Nattermann, K. Jandieri, S. Gupta, A. Beyer, B. Ringler, C. von Hänisch, W. Stolz, K. Volz, *AIP Advances* **8**, 055329 (2018). DOI: 10.1063/1.5034083

Abstract

N containing lattice matched 1 eV materials, such as Ga(NAsSb) and (GaIn)(NAs), are discussed as potential solar subcells in a four junction solar cell alongside Ge, GaAs, and (GaIn)P, reaching theoretically conversion efficiencies of around 50 %. The solar subcell with the highest conversion efficiency, consisting of (GaIn)(NAsSb), was grown with molecular beam epitaxy (MBE). The growth of Sb/N containing materials have always been a challenge to metalorganic vapor phase epitaxy (MOVPE), as N incorporation is hindered drastically by even small amounts of Sb if 1,1-dimethylhydrazine is used. This strong N/Sb interaction was not observed by MBE, therefore gas phase reactions in MOVPE are held responsible for the N incorporation drop. In this work we will present a systematic study of Ga(NAsSb) on GaAs grown in MOVPE with the novel N/As precursor di-tertiary-butyl-arsano-amine, as well as triethylgallium and triethylantimony. The achieved 1 eV Ga(NAsSb) material opens up new possibilities for using MOVPE to grow further solar subcells like (GaIn)(NAsSb) or Ga(NAsSb) in the band gap range of 1.0 - 1.1 eV.

The Authors contribution

My contribution to this work was the planning, executing and investigation of all samples including MOVPE growth and HR-XRD, AFM as well as PL measurements. B. Ringler synthesized the precursor, which was used for the growth of the (GaIn)(NAs) layers. S. Gupta and A. Beyer performed the (S)TEM measurements. K. Jandieri calculated the Sb and N estimations. All co-authors helped to interpret the data for the publication which was written by me.

* Reprinted from *AIP Advances* **8**, 055329 (2018), Copyright 2018, with permission from AIP Publishing.

1 eV Ga(NAsSb) grown by MOVPE using di-tertiary-butyl-arsano-amine (DTBAA)

E. Sterzer,^{1,a} O. Maßmeyer,¹ L. Nattermann,¹ K. Jandieri,¹ S. Gupta,¹
 A. Beyer,¹ B. Ringler,² C. von Hänisch,² W. Stolz,¹ and K. Volz¹

¹Material Sciences Center and Faculty of Physics, Philipps-Universität Marburg,
 35032, Germany

²Material Sciences Center and Faculty of Chemistry, Philipps-Universität Marburg,
 35032, Germany

(Received 9 April 2018; accepted 18 May 2018; published online 29 May 2018)

N containing lattice matched 1 eV materials, such as Ga(NAsSb) and (GaIn)(NAs), are discussed as potential solar subcells in a four junction solar cell alongside Ge, GaAs, and (GaIn)P, reaching theoretically conversion efficiencies of around 50 %. The solar subcell with the highest conversion efficiency, consisting of (GaIn)(NAsSb), was grown with molecular beam epitaxy (MBE). The growth of Sb/N containing materials have always been a challenge to metalorganic vapor phase epitaxy (MOVPE), as N incorporation is hindered drastically by even small amounts of Sb if 1,1-dimethylhydrazine is used. This strong N/Sb interaction was not observed by MBE, therefore gas phase reactions in MOVPE are held responsible for the N incorporation drop. In this work we will present a systematic study of Ga(NAsSb) on GaAs grown in MOVPE with the novel N/As precursor di-tertiary-butyl-arsano-amine, as well as triethylgallium and triethylantimony. The achieved 1 eV Ga(NAsSb) material opens up new possibilities for using MOVPE to grow further solar subcells like (GaIn)(NAsSb) or Ga(NAsSb) in the band gap range of 1.0 – 1.1 eV. © 2018 Author(s). All article content, except where otherwise noted, is licensed under a Creative Commons Attribution (CC BY) license (<http://creativecommons.org/licenses/by/4.0/>). <https://doi.org/10.1063/1.5034083>

I. INTRODUCTION

Dilute nitrides (N), like (GaIn)(NAs) or Ga(NAsSb), are promising materials for use in various applications. The small covalent radius of N in comparison to As has a large influence on the lattice constant in a GaAs matrix. Furthermore, the strong band gap reduction of 120 - 180 meV/%N is explained by the band anti crossing model.^{1–5} This strong influence on lattice constant and band gap with rather small amounts of N makes the dilute nitrides a perfect candidate for band gap and lattice constant engineering. In combination with a fourth element, one can tune the band gap and lattice constant independently. For the growth of solar cells lattice matched to GaAs or Ge, one has to reduce the strain in Ga(NAs). This can be realized by incorporating an atom with a larger covalent radius than Ga or As. Additionally, the addition of these elements have to further reduce the band gap in order to achieve the desired 1 eV material. Suitable elements would be either In (substituting Ga) or Sb/Bi (substituting As). Accordingly, it is possible to achieve the 1 eV solar subcell with (GaIn)(NAs), Ga(NAsSb), Ga(NAsBi) or a combination of these.^{6–15}

In literature, Ga(NAsSb) and (GaIn)(NAsSb) materials have been reported as being lattice matched to GaAs and showing a 1 eV band gap.^{16–23} All of these samples were obtained with molecular beam epitaxy (MBE). The best multi junction solar cell efficiencies containing a 1 eV subcell were achieved with a (GaIn)(NAsSb) solar subcell grown with MBE.²³ In metalorganic vapor phase epitaxy (MOVPE) dilute nitrides are grown conventionally with 1,1-dimethylhydrazine (UDMHy)

^aE-Mail: eduard.sterzer@physik.uni-marburg.de

in combination with tri(m)ethylgallium (TMGa, TEGa), tertiarybutylarsine (TBAs) (or Arsine), and either trimethylindium (TMIn) or tri(m)ethylantimony (TMSb, TESb). Applying TEGa, TBAs, and UDMHy, the N incorporation is strongly reduced when alloying with TMIn.^{24,25} This effect is even stronger when alloying with TMSb or TESb instead of TMIn.^{26,27}

So far, MOVPE growth of Sb in combination with N is very complex^{26–28} and no high quality 1 eV cell lattice matched to GaAs have been realized as of yet. This is related to the dramatic N incorporation reduction when Ga(NAs) is alloyed with Sb. We recently presented the novel precursor for As and N namely di-tertiary-butyl-arsano-amine (DTBAA).²⁹ It not only provides N, which incorporates 10 - 20 times more efficiently in GaAs in comparison to UDMHy, but also shows no N incorporation decrease in (GaIn)(NAs) when grown with TEGa, TMIn, and DTBAA. This leads to an increase in the N incorporation efficiency by up to 80 times in comparison to UDMHy.³⁰ This result has motivated us to study Ga(NAsSb) growth in order to realize a 1 eV solar subcell material with MOVPE using DTBAA, TEGa, and TESb.

II. GROWTH AND CHARACTERIZATION OF Ga(NAsSb) LAYERS

All samples in this study were grown using an Aixtron AIX 200 GFR MOVPE machine with a horizontal reactor heated by six infrared lamps. Palladium purified H₂ was used as a carrier gas for the conventional precursors like TEGa, TESb, and TBAs, as well as the novel As/N precursor DTBAA. The reactor pressure was held constant at 50 mbar by a total gas flow of 6800 sccm. The graphite block embedded in the quartz liner is designed for a 2" substrate, which can be rotated with the gas foil rotation technique for homogeneous growth. To ensure a high quality GaAs surface, a 250 nm thick GaAs buffer was grown at 625 °C prior to each experiment. The layers of interest were grown at either 475 °C, 500 °C, or 550 °C. The temperature steps from buffer growth (625 °C) to layer growth were carried out in an ambient environment of TBAs to prevent As desorption. Roughly 10 nm thick 5QW Ga(NAsSb) structures with a 20 nm thick GaAs barrier were grown, and finished with the quaternary layer for a realistic surface roughness feedback. The Ga(NAsSb) layer was grown with TEGa, TESb, and DTBAA. No TBAs was applied, as the DTBAA provides N and As simultaneously. For the GaAs barrier growth however, TEGa and TBAs were used. Several techniques were applied for detailed material investigation. High resolution X-ray diffraction (HRXRD) using a Panalytical X'Pert Pro system with the Cu K α 1 wavelength (1.5405 Å) was utilized for strain as well as growth rate determination. In order to do this, patterns around the (004) reflex were scanned and simulated with the X'Pert Epitaxy software. A rapid thermal annealer (RTA), Jipelec JetFirst 200C, was used for post growth heat treatment to decrease the defect density and increase the optical signal of the Ga(NAsSb) material. Accordingly, samples were annealed for 10 seconds in the temperature range of 650 – 700 °C. Room temperature photoluminescence spectroscopy (RT-PL) of annealed samples was performed to determine the PL-peak position as well as PL-peak intensity. For the sample excitation a frequency doubled Nd:YAG laser with a 532 nm line was used. Additionally, a liquid N₂ cooled Ge detector in combination with a standard lock-in technique was used to obtain the PL signal, which was dispersed by a 1 m grating monochromator (THR 1000, Jobin-Yvon). With an atomic force microscope (AFM), Nanoscope IIIa, surface morphology of the Ga(NAsSb) layer was investigated. Lattice matched Ga(NAsSb) bulk layer of 140 nm thickness was investigated with secondary ion mass spectrometry (SIMS) by RTG Mikroanalyse GmbH in Berlin, detecting oxygen (O), carbon (C), nitrogen (N) and antimony (Sb). For scanning transmission electron microscopy (STEM) investigations cross-sectional samples were prepared in the [010] crystallographic direction by first grinding and polishing with a Multiprep System (Allied High Tech Systems) up to a thickness of approximately 40 μ m for investigation. The final preparation step was argon ion milling utilizing a Gatan precision polishing system. Plasma cleaning (Plasma Cleaner Model 1020 Fischione Instruments) was applied for 2 min to remove parasitic hydrocarbons. The STEM investigations were performed in a double-Cs corrected JEOL JEM 2200 FS field emission STEM operating at 200 kV using the high angle annular dark field (HAADF) technique.

For a quaternary material, HRXRD analysis gives an infinite combination of possible results. Therefore, additional experimental investigations are needed to determine the composition. In our case we correlated RT-PL of annealed samples with the strain obtained from HRXRD and compared to

the composition of a selected sample by SIMS. For the estimation of the PL peak energy as a function of the nitrogen and antimony contents, we apply the double-band anti crossing model suggested by Lin *et al.*³¹ when taking into account the quantization effects and the shift of the conduction and valence band edges due to the strain inherent in the studied QW structures.^{32,33}

III. RESULTS AND DISCUSSION

First we will present the results at 500 °C, in particular the variation of the individual partial pressures of TESb, DTBAA and TEGa as well as V/III variation and the impact on Sb and N incorporation. We will then discuss the surface roughness obtained by AFM for crystal quality analysis. Furthermore, Ga(NAsSb) samples will be discussed grown in the temperature range of 475 – 550 °C. Finally, we will present the 475 °C results including the near 1 eV Ga(NAsSb) structure. The trends in each graph are indicated with guides to the eye.

The N and Sb incorporation versus TESb supply for two different DTBAA partial pressures is depicted in Figure 1a). One can clearly see how the N incorporation decreases nonlinearly for a given DTBAA supply when increasing TESb. The Sb incorporation itself, however, seems to increase linearly for the lower DTBAA partial pressure. The Sb incorporation slope reduces drastically with higher DTBAA supply. It is thus obvious that the Sb incorporation is strongly affected by the supplied DTBAA, and therefore either the V/V or the V/III ratio. Figure 1b) shows the surface roughness on the right and the growth rate on the left hand side. We observe a higher surface roughness for higher TESb supply. This effect is more severe for higher DTBAA partial pressure. As the DTBAA provides As and N at the same time, we have to clarify which effects lead to this Sb/N/As interaction. It is known from pure Ga(AsSb) growth that the Sb incorporation is very sensitive to the As/Sb ratio,³⁴ which we would increase in our case with higher DTBAA. Furthermore, the growth rate is decreasing due to either higher TESb gas phase supply, higher Sb incorporation or Sb surfactant effect. This will be discussed in the results of the V/V experiments depicted in figure 3a).

The DTBAA variation results are plotted in figure 2. As expected, increasing the DTBAA supply leads to a higher N incorporation. However, as mentioned previously, Sb incorporation decreases with additional DTBAA. The surface roughness increases drastically with higher DTBAA supply. Higher

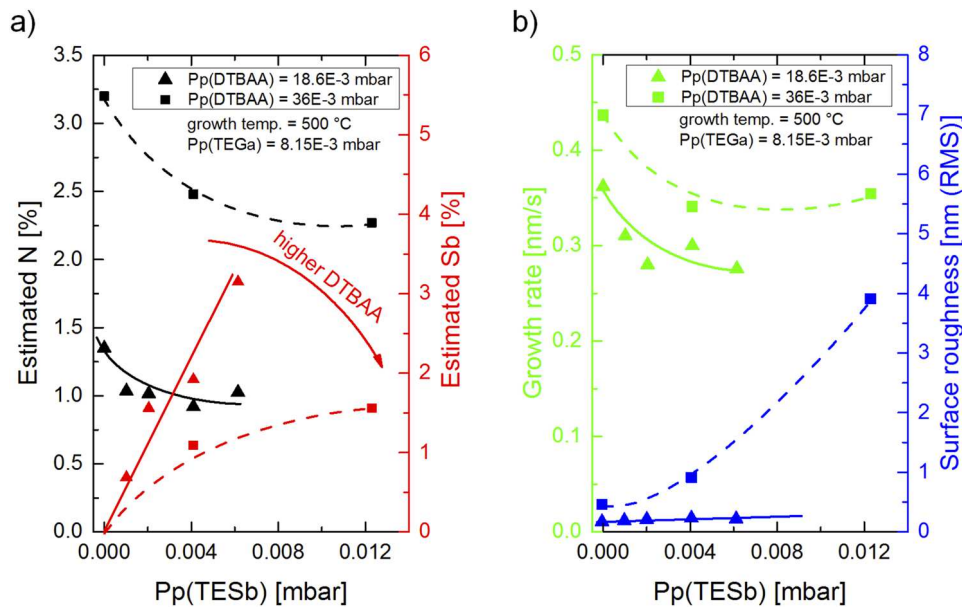


FIG. 1. Plot of calculated N and Sb values in a) as well as growth rate and the RMS value of the surface roughness versus TESb partial pressure in b). Higher TESb supply leads to linearly increasing Sb content and nonlinear decrease in N incorporation for low DTBAA. Higher DTBAA reduces the Sb incorporation drastically. Growth rate decreases with higher TESb supply or Sb incorporation. RMS value of the surface roughness increases with increasing TESb. (500 °C).

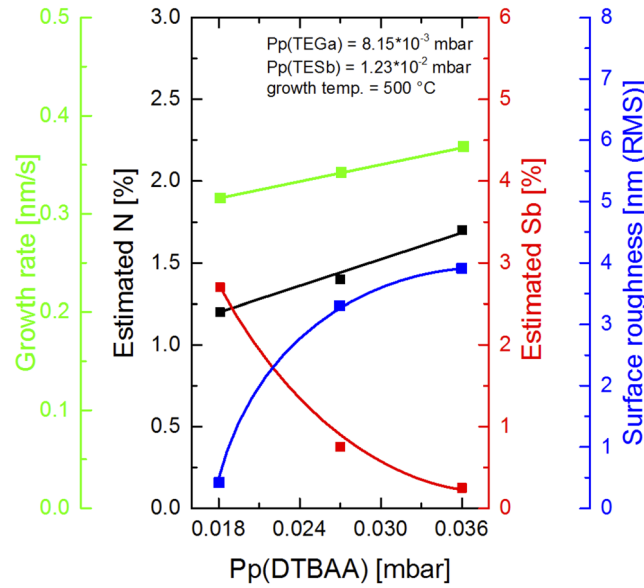


FIG. 2. N/Sb incorporation growth rate and RMS value in dependence to DTBAA supply. Slight increase in growth rate with higher DTBAA supply due to low V/III ratio and low growth temperature. Strong influence on the RMS value of the surface roughness. Higher DTBAA leads to N incorporation increase and Sb incorporation decrease. (500 °C).

N concentration itself leads to a slightly worse surface quality; nevertheless, roughness values of 4 nm (RMS) cannot be explained by an N incorporation of around 2 %. As the Sb incorporation decreases, Sb is either desorbing or segregating to the surface and causing defects during the growth, thus, increasing the surface roughness. At low growth temperatures and V/III ratios, group V elements also have an impact on growth rate. Therefore, a linear increase in growth rate is observed.

To understand whether the N/Sb incorporation processes or the gas phase ratio (either V/V or V/III) is accountable for the N/Sb interaction, V/III ratio experiments are performed. Figure 3a) shows results of an experiment with a constant DTBAA/TESb ratio of 9 and constant TEGa partial pressure of 8.15E-3 mbar. The V/III ratio was varied by changing the DTBAA/TESb gas phase supply at a fixed V/V ratio, thus, increasing the DTBAA and TESb supply by the same factor. This experiment reveals

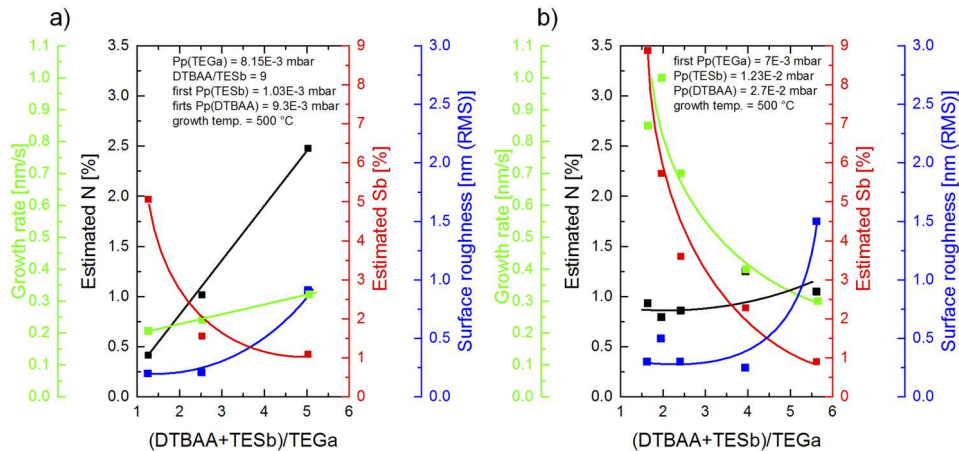


FIG. 3. V/III variation with fixed TEGa and fixed V/V ratio (a): Increasing group V supply leads to decreasing Sb incorporation, increasing N incorporation, increasing growth rate and increasing RMS value for surface roughness. V/III variation with fixed DTBAA and TESb (b): Higher TEGa supply reduces the V/III ratio, increases the growth rate, reduces the RMS value of the surface roughness and increases the Sb incorporation drastically.

that either the V/III ratio or the N incorporation process itself is responsible for the Sb incorporation decrease and not the V/V ratio. With increasing V/III ratio, the N incorporation increases linearly. Simultaneously, we observe an exponential decrease in the Sb incorporation together with a higher surface roughness. For a fixed V/V ratio we observe competing behavior in N and Sb incorporation by increasing all group V elements. Surprisingly, the growth rate increases despite a fixed TEGa supply. As the Sb incorporation is simultaneously decreasing, interactions on the surface (e.g. different surface reconstructions) may lead to a higher growth rate. At the same time the surface roughness is strongly increased, leading to the assumption of a 3D growth.

If low V/III ratios allow for sufficient Sb incorporation, while high DTBAA partial pressures are needed for N incorporation, varying TEGa may lead to an additional insight of N and Sb incorporation. Furthermore, one can distinguish whether it is the N incorporation or the V/III ratio which has a huge impact on the Sb incorporation. Therefore, the DTBAA and TESb supply were fixed while the TEGa supply was varied. Increasing TEGa supply (thus, lowering the V/III ratio) leads to a higher growth rate and slightly lower N incorporation as depicted in Figure 3b). The most important change is seen in simultaneously higher Sb incorporation. Additionally, the surface roughness decreases with lower V/III ratio (higher TEGa). The growth rate, however, does not double as we would expect by doubling the TEGa supply.

In the end, the variation of TESb, DTBAA, and TEGa makes it possible to control the Sb and N content. The challenge lies in finding the parameters as well as in understanding exactly which parameters interact with each other. All of the data in this publication shows that low V/III ratios are key for both a high quality surface as well as sufficient Sb incorporation for a given DTBAA partial pressure.

Temperature dependent investigations can be seen in figure 4. Therefore, samples are grown between 475 °C and 550 °C with a rather low V/III ratio of 2.5. One clearly sees how the N incorporation decreases drastically with higher temperature. At the same time, the Sb incorporation increases. In ternary Ga(AsSb), however, Sb incorporation decreases with higher temperature. This behavior shows that not only the gas phase ratios, but possibly both the N incorporation and temperature, have a large influence on the Sb incorporation. One certainly cannot distinguish between temperature induced precursor decomposition or temperature effect itself, but this gives us a further technique for N and Sb incorporation control. Furthermore, higher temperatures increase the growth rate by 35 %. This indicates that the effective V/III ratio changes with higher temperature, leading to a lower V/III ratio (higher TEGa decomposition with higher temperature) and therefore to a higher probability for Sb incorporation. As expected, almost no N incorporation

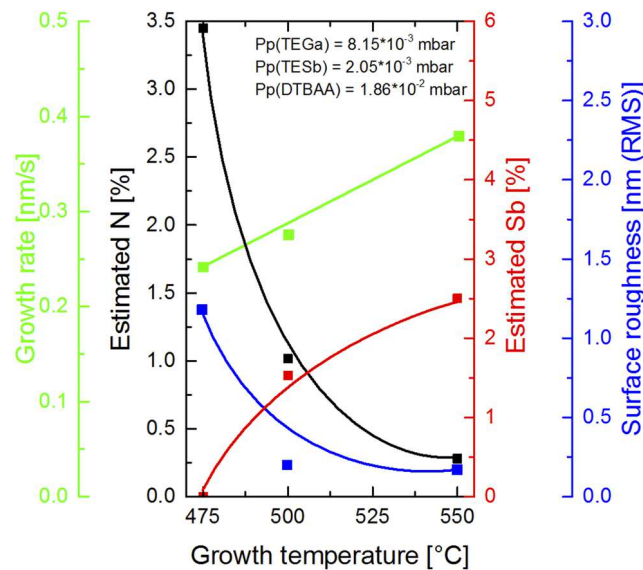


FIG. 4. Temperature variation: increasing temperature leads to lower N incorporation and higher Sb incorporation.

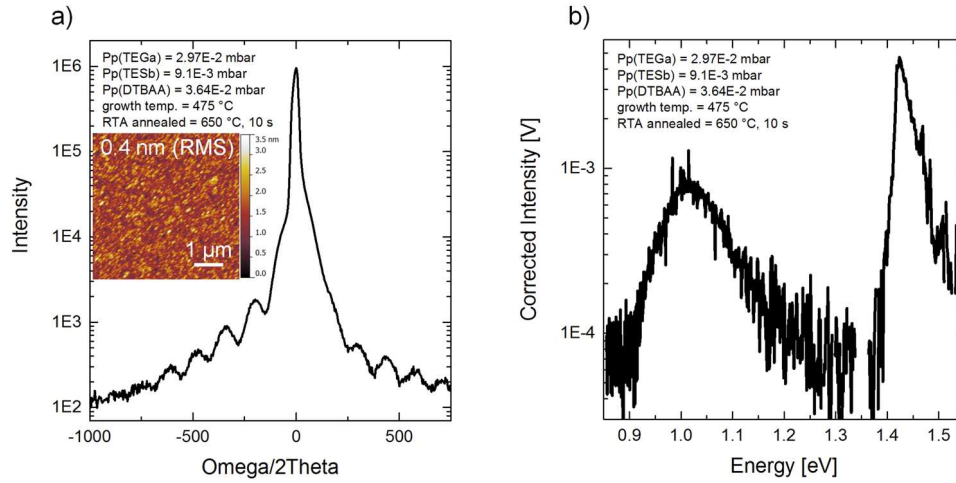


FIG. 5. a) HRXRD measurement and AFM micrograph of almost lattice matched Ga(NaAsSb) material. b) RT-PL of the RTA annealed sample (650°C , 10 s). The PL-peak position is around 1 eV.

is observed at high temperatures, underlining the need for low temperature growth for dilute nitrides.

For a 1 eV lattice matched Ga(NaAsSb) on GaAs material, concentrations of around 2.4 % N and 6 % Sb are needed. To take into account both decreasing N incorporation with increasing Sb supply and the sensitivity of Sb incorporation to the V/III ratio, an initial N incorporation of 3.2 % in Ga(NaAs) was chosen. These layers were realized at 475°C with V/III ratio around 1.3 or below. Afterwards, TESb was successively added, thus, increasing the V/III ratio up to 1.5. HRXRD pattern as well as AFM micrograph of the lattice matched 1 eV Ga(NaAsSb) bulk material grown with MOVPE are shown in Figure 5a). The annealed sample was investigated with RT-PL. Figure 5b) shows the PL spectrum with the PL peak position of 1.0 eV which corresponds to the Ga(NaAsSb) band gap. To verify the composition and to investigate the O and C incorporation, SIMS measurements were obtained. SIMS results of the same lattice matched 1 eV structure are depicted in Figure 6. One can clearly see the Sb concentration, which is higher than the N content. The calibrated SIMS data reveal an Sb incorporation of around 5.5 % Sb and 2.2 % N with an relative error of 10 %. Unfortunately, we also incorporated C in the $10^{18} \text{ atoms/cm}^3$ range. Furthermore, unintentional O incorporation due

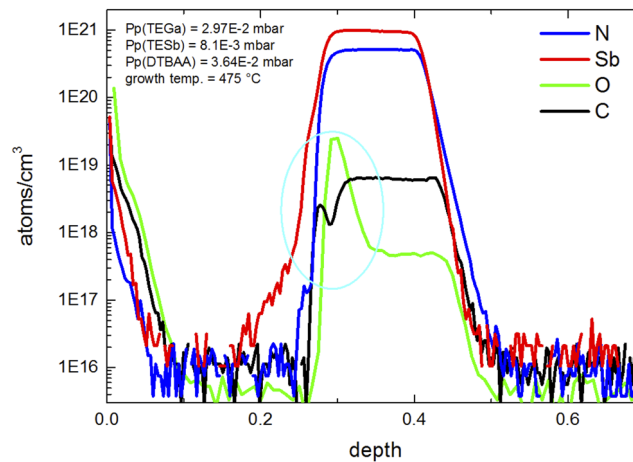


FIG. 6. SIMS measurement of the same sample as shown in figure 5. O incorporation stems from impurities in the DTBAA precursor. Ethyl groups of the Ga and Sb precursor as well as low temperature might be the reason for the high C concentration. The peaks highlighted with the cyan circle, occur due to regrowth of the Ga(NaAsSb) sample with GaAs.

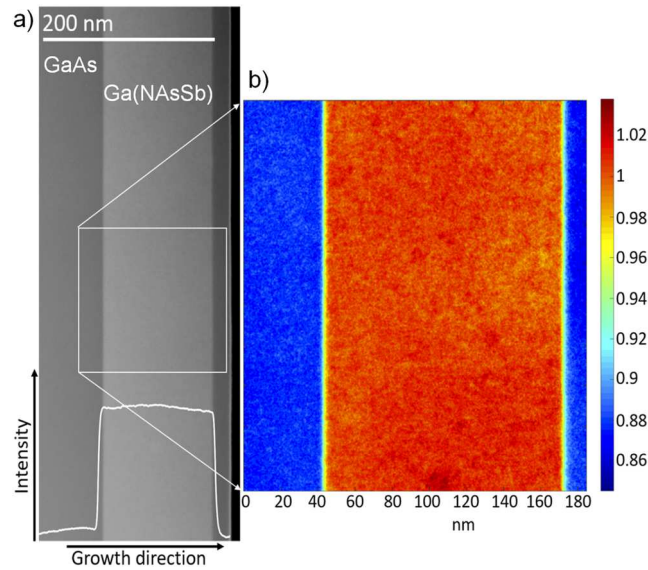


FIG. 7. Overview STEM image of the Ga(NAsSb) layer (a) and a color coded intensity map (b).

to impurities contained in the novel As/N precursor DTBAA were observed in the 10^{17} atoms/cm³ range. This precursor was produced on laboratory scale, no sophisticated purification steps have been applied to the synthesized precursor up to now. Furthermore, ethyl groups from the Ga and Sb source might also lead to unintentional C incorporation. The highlighted peaks occur due to regrowth of the Ga(NAsSb) sample with GaAs. Figure 7a) shows an overview image of the sample investigated by STEM. Images have been acquired at comparably low detector angles (41 - 164 mrad) of the Annular Dark Field (ADF) detector. Since N has a lower atomic number than the GaAs matrix and Sb has a higher one, their influences partially compensate each other, therefore the Ga(NAsSb) layer does not exhibit contrast in conventional high angle annular dark field images. The utilized low detector angles are sensitive to the static atomic displacements introduced by N and Sb.³⁵ Consequently, Ga(NAsSb) appears brighter than GaAs. The intensity profile which is shown as inset in Figure 7a) suggests that the lower interface between GaAs and Ga(NAsSb) is abrupt, whereas the upper interface is not quite abrupt which indicates a segregation of Sb and which will be investigated in more detail in the future. Figure 7b) shows the intensity map of the region selected in 7a) which has then been evaluated using the method developed by T. Wegele et al.³⁶ The evaluation shows the intensity fluctuation within Ga(NAsSb) layer is not significantly higher than that in GaAs layer, indicating that Ga(NAsSb) layer is also quite homogenous.

IV. SUMMARY AND OUTLOOK

In this work we presented the incorporation behavior of N and Sb in a Ga(NAsSb) material as a function of V/III, V/V ratios, DTBAA, TESb partial pressures and growth temperature. HRXRD, AFM, and RT-PL of annealed samples were used for the detailed characterization of the N and Sb content, as well as for the growth rate and surface morphology. The obtained data shows that low V/III values are favorable for simultaneously high N and Sb incorporation. Using this knowledge a 1 eV Ga(NAsSb) material lattice matched to GaAs was grown at 475 °C, which exhibited RT-PL after annealing at 650 °C for 10 s. The high C incorporation originating from low growth temperatures and possible hydro carbon groups can be decreased with higher growth temperatures. O incorporation is believed to come from the impurities in the DTBAA, which can be solved by high quality purification in the future. For the next stage in this research, a Ga(NAsSb) 1 eV solar cell device will be developed to compare the results to existing MBE grown cells, as well as to MOVPE grown (GaIn)(NAs) cells.

ACKNOWLEDGMENTS

This work was supported by the German Research Foundation (DFG) in the frame of the Research Training Group (GRK) 1782: “Functionalization of Semiconductors”. This project has also received funding from the European Union’s Horizon 2020 research and innovation program under the Marie Skłodowska-Curie grant agreement No 641899.

- ¹ W. Shan, W. Walukiewicz, J. W. Agar III, E. E. Haller, J. F. Geisz, D. J. Friedman, J. M. Olson, and S. R. Kurtz, “Band anticrossing in GaInNAs alloys,” *Physical Review Letters* **82**, 1221–1224 (1999).
- ² W. Shan, W. Walukiewicz, K. M. Yu, J. W. Ager III, E. E. Haller, J. F. Geisz, D. J. Friedman, J. M. Olson, S. R. Kurtz, H. P. Xin, and C. W. Tu, “Band anticrossing in III–N–V alloys,” *Physica Status Solidi (B)* **223**(1), 75–85 (2001).
- ³ J. Wu, W. Shan, and W. Walukiewicz, “Band anticrossing in highly mismatched III V semiconductor alloys,” *Semiconductor Science and Technology* **17**(8), 860–869 (2002).
- ⁴ W. Shan, K. M. Yu, W. Walukiewicz, J. Wu, J. W. Ager, and E. E. Haller, “Band anticrossing in dilute nitrides,” *Journal of Physics: Condensed Matter* **16**(31), S3355–S3372 (2004).
- ⁵ J. Shao, W. Lu, M. Sadeghi, X. Luä, S. M. Wang, L. Ma, and A. Larsson, “Evolution of valence-band alignment with nitrogen content in GaNAs/GaAs single quantum wells,” *Applied Physics Letters* **93**, 031904 (2008).
- ⁶ D. J. Friedman, J. F. Geisz, S. R. Kurtz, and J. M. Olson, “1-eV solar cells with GaInNAs active layer,” *Journal of Crystal Growth* **195**, 409–415 (1998).
- ⁷ J. F. Geisz, D. J. Friedman, J. M. Olson, S. R. Kurtz, and B. M. Keyes, “Photocurrent of 1 eV GaInNAs lattice-matched to GaAs,” *Journal of Crystal Growth* **195**, 401–408.
- ⁸ S. Kurtz, A. A. Allerman, E. D. Jones, J. M. Gee, J. J. Banas, and B. E. Hammons, “InGaAsN solar cells with 1.0 eV band gap, lattice matched to GaAs,” *Applied Physics Letters* **74**(1999), 729–731 (1999).
- ⁹ F. Höhnendorf, J. Koch, S. Leu, W. Stolz, B. Borchert, and M. Druminski, “Reduced threshold current densities of (GaIn)(NAs)/GaAs single quantum well lasers for emission wavelengths in the range 1.28–1.38 μm ,” *Electronics Letters* **35**(7), 571–572 (1999).
- ¹⁰ V. Polojärvi, A. Aho, A. Tukiainen, M. Raappana, T. Aho, A. Schramm, and M. Guina, “Influence of As/group-III flux ratio on defects formation and photovoltaic performance of GaInNAs solar cells,” *Solar Energy Materials and Solar Cells* **149**, 213–220 (2016).
- ¹¹ K. Volz, T. Torunski, B. Kunert, O. Rubel, S. Nau, S. Reinhard, and W. Stolz, “Specific structural and compositional properties of (GaIn)(NAs) and their influence on optoelectronic device performance,” *Journal of Crystal Growth* **272**(1–4), 739–747 (2004).
- ¹² D. B. Jackrel, S. R. Bank, H. B. Yuen, M. A. Wistey, J. S. Harris, A. J. Ptak, S. W. Johnston, D. J. Friedman, and S. R. Kurtz, “Dilute nitride GaInNAs and GaInNAsSb solar cells by molecular beam epitaxy,” *Journal of Applied Physics* **101**(11), 1–8 (2007).
- ¹³ N. Ahsan, N. Miyashita, M. M. Islam, K. M. Yu, W. Walukiewicz, and Y. Okada, “Effect of Sb on GaNAs intermediate band solar cells,” *IEEE Journal of Photovoltaics* **3**(2), 730–736 (2013).
- ¹⁴ I. Suemune, K. Uesugi, and T. Y. Seong, “Growth and structural characterization of III–N–V semiconductor alloys,” *Semiconductor Science and Technology* **17**(8), 755–761 (2002).
- ¹⁵ J.-C. Harmand, A. Caliman, E. V. K. Rao, L. Largeau, J. Ramos, R. Teissier, L. Travers, G. Ungaro, B. Theys, and I. F. L. Dias, “GaInNAsSb: How does it compare with other dilute III–V–nitride alloys?,” *Semiconductor Science and Technology* **17**(8), 778 (2002).
- ¹⁶ N. Miyashita, N. Ahsan, and Y. Okada, “Effect of antimony on uniform incorporation of nitrogen atoms in GaInNAs films for solar cell application,” *Solar Energy Materials and Solar Cells* **111**, 127–132 (2013).
- ¹⁷ N. Miyashita, N. Ahsan, and Y. Okada, “Generation and collection of photocarriers in dilute nitride GaInNAsSb solar cells,” *Prog. Photovolt: Res. Appl.* **15** (2016).
- ¹⁸ M. M. Islam, N. Miyashita, N. Ahsan, T. Sakurai, K. Akimoto, and Y. Okada, “Photocapacitance study of MBE grown GaInNAsSb thin film solar cells,” *Journal of Crystal Growth* **378**, 57–60 (2013).
- ¹⁹ A. Aho, A. Tukiainen, V. Polojärvi, and M. Guina, “Performance assessment of multijunction solar cells incorporating GaInNAsSb,” *Nanoscale Research Letters* **9**, 1–7 (2014).
- ²⁰ A. Maros, N. Faleev, S. H. Lee, J. S. Kim, C. B. Honsberg, and R. R. King, “1-eV GaInNAsSb for multijunction solar cells,” *2016 IEEE 43rd Photovoltaic Specialists Conference (PVSC)*, Portland, OR, 2016, pp. 2306–2309.
- ²¹ V. Braza, D. F. Reyes, A. Gonzalo, A. D. Utrilla, T. Ben, J. M. Ulloa, and D. González, “Sb and N incorporation interplay in GaAsSbN/GaAs epilayers near lattice-matching condition for 1.0–1.16-eV photonic applications,” *Nanoscale Research Letters* **12**, 356 (2017).
- ²² K. H. Tan, S. Wicaksono, W. K. Loke, D. Li, S. F. Yoon, E. A. Fitzgerald, S. A. Ringel, and J. S. Harris, Jr., “Molecular beam epitaxy grown GaNAsSb 1eV photovoltaic cell,” *Journal of Crystal Growth* **335**(1), 66–69 (2011).
- ²³ R. Jones-Albertus, E. Becker, R. Bergner, T. Bilir, D. Derkacs, O. Fidaner, D. Jory, T. Liu, E. Lucow, P. Misra, E. Pickett, F. Suarez, A. Sukiasyan, T. Sun, L. Zhang, V. Sabnis, M. Wiemer, and H. Yuen, “Using dilute nitrides to achieve record solar cell efficiencies,” *MRS Proceedings* **1538**, 161–166 (2013).
- ²⁴ K. Volz, J. Koch, F. Höhnendorf, B. Kunert, and W. Stolz, “MOVPE growth of dilute nitride III/V semiconductors using all liquid metalorganic precursors,” *Journal of Crystal Growth* **311**(8), 2418–2426 (2009).
- ²⁵ F. Höhnendorf, J. Koch, C. Agert, and W. Stolz, “Investigations of (GaIn)(NAs) bulk layers and (GaIn)(NAs)/GaAs multiple quantum well structures grown using tertiarybutylarsine (TBAs) and 1,1-dimethylhydrazine (UDMH₂),” *Journal of Crystal Growth* **195**, 391–396 (1998).
- ²⁶ T. Kim *et al.*, “Impact of Sb incorporation on MOVPE-grown ‘bulk’ InGaAs(Sb)N films for solar cell application,” *IEEE Journal of Photovoltaics* **6**(6), 1673–1677 (2016).

- ²⁷ F. Dimroth, A. Howard, J. K. Shurtleff, and G. B. Stringfellow, "Influence of Sb, Bi, Tl, and B on the incorporation of N in GaAs," *Journal of Applied Physics* **91**(6), 3687–3692 (2002).
- ²⁸ T. W. Kim, T. F. Kuech, and L. J. Mawst, "Impact of growth temperature and substrate orientation on dilute-nitride-antimonide materials grown by MOVPE for multi-junction solar cell application," *J. Cryst. Growth* **405**, 87–91 (2014).
- ²⁹ E. Sterzer, A. Beyer, L. Duschek, L. Nattermann, B. Ringler, B. Leube, A. Stegmüller, R. Tonner, C. von Hänisch, W. Stolz, and K. Volz, "Efficient nitrogen incorporation in GaAs using novel metal organic As–N precursor di-tertiary-butyl-arsano-amine (DTBAA)," *Journal of Crystal Growth* **439**, 19–27.
- ³⁰ E. Sterzer, B. Ringler, L. Nattermann, A. Beyer, C. von Hänisch, W. Stolz, and K. Volz, "(GaIn)(NAs) growth using di-tertiary-butyl-arsano-amine (DTBAA)," *Journal of Crystal Growth* **467**, 132–136 (2017).
- ³¹ K.-I. Lin, K.-L. Lin, B.-W. Wang, H.-H. Lin, and J.-S. Hwang, "Impact of growth temperature and substrate orientation on dilute-nitride-antimonide materials grown by MOVPE for multi-junction solar cell application," *Applied Physics Express* **6**, 121202 (2013).
- ³² C. G. Van de Walle, "Band lineups and deformation potentials in the model-solid theory," *Phys. Rev. B* **39**, 1871 (1989).
- ³³ Z. Batool *et al.*, "The electronic band structure of GaBiAs/GaAs layers: Influence of strain and band anti-crossing," *Journal of Applied Physics* **111**, 113108 (2012).
- ³⁴ G. B. Stringfellow and M. J. Cherng, "OMVPE growth of GaAsSb: Solid composition," *Journal of Crystal Growth* **64**(2), 413–415 (1983).
- ³⁵ V. Grillo *et al.*, "Strain, composition and disorder in ADF imaging of semiconductors," *J. Phys: Conf. Ser.* **326**(1), 012006 (2011).
- ³⁶ T. Wegele *et al.*, "Interface morphology and composition of Ga (NAsP) quantum well structures for monolithically integrated LASERs on silicon substrates," *J. Phys. D: Appl. Phys.* **49**(7), 07510 (2016).

7.5 Further Publications

Peer-Review Paper

Listed below are publications in which Eduard Sterzer did participate by either growing samples or interpreting data. These publications are not related to the dilute N growth which was the main focus of the thesis.

- E. Sterzer, N. Knaub, P. Ludewig, R. Straubinger, A. Beyer, W. Stolz, K. Volz, Investigation of the microstructure of metallic droplets on Ga (AsBi)/GaAs. *Journal of Crystal growth* **439**, 19 (2014). DOI: 10.1016/j.jcrysgro.2014.09.006
- L. Nattermann, P. Ludewig, N. Knaub, N. W. Rosemann, T. Hepp, E. Sterzer, S. R. Jin, K. Hild, S. Chatterjee, S. J. Sweeney, W. Stolz, K. Volz, MOVPE growth and characterization of quaternary Ga (PAsBi)/GaAs alloys for optoelectronic applications. *Applied Materials Today* **5**, 209 (2016). DOI: 10.1016/j.apmt.2016.09.018
- L. Nattermann, A. Beyer, P. Ludewig, T. Hepp, E. Sterzer, K. Volz, MOVPE growth of Ga(PBi) on GaP and GaP on Si with Bi fractions up to 8 %. *Journal of Crystal Growth* **463**, 151 (2017). DOI: 10.1016/j.jcrysgro.2017.02.021
- L. Nattermann, P. Ludewig, E. Sterzer, K. Volz, Exploiting strain to enhance the Bi incorporation in GaAs-based III/V semiconductors using MOVPE. *Journal of Crystal Growth* **470**, 15 (2017). DOI: 10.1016/j.jcrysgro.2017.04.005
- C. M. Krammel, L. Nattermann, E. Sterzer, K. Volz, P.M. Koenraad, Structural and electronic properties of isovalent boron atoms in GaAs. *Journal of Applied Physics* **123**, 161589 (2018). DOI: 10.1063/1.5011166
- L. Nattermann, O. Maßmeyer, E. Sterzer, V. Derpmann, H. Y. Chung, W. Stolz, K. Volz, An experimental approach for real time mass spectrometric CVD gas phase investigations. *Scientific Reports* **8**, 319 (2018). DOI: 10.1038/s41598-017-18662-7
- O. Maßmeyer, E. Sterzer, L. Nattermann, W. Stolz, K. Volz, Influence of UDMHy on GaAs(001) Surface Reconstruction Before and During Growth of Ga(NAs) by MOVPE. Submitted (2018)

Patent

- C. von Hänisch, K. Volz, W. Stolz, E. Sterzer, A. Beyer, D. Keiper, B. Ringler, Use of at least one binary group 15 element compound, a 13/15 semiconductor layer and binary group 15 element compounds.

PCT-Nummer: PCT/EP2015/072163

Conference Presentations (Talks)

- E. Sterzer, A. Beyer, K. Werner, R. Straubinger, W. Stolz, C. v. Hänisch, J. Sundermeyer, K. Volz, Nitrogen incorporation in GaAs using alternative precursors containing As-N and Ga-N bonds, GRK-Meeting (Jul/Aug 2014) San Sebastian, Spain
- E. Sterzer, A. Beyer, K. Werner, R. Straubinger, W. Schorn, K. Schlechter, J. Sundermeyer, W. Stolz, K. Volz, Nitrogen incorporation in GaAs using novel precursors with predefined N-Ga bonds in the molecule, DGKK Arbeitskreistreffen Epitaxie von III-V Halbleitern (Dec 2014) Magdeburg, Germany
- E. Sterzer, A. Beyer, B. Ringler, C. von Hänisch, W. Stolz, K. Volz, Nitrogen incorporation in GaAs using novel precursor with no direct C-N bond, 20th American Conference on Crystal Growth and Epitaxy (ACCGE-20) (Aug 2015) Big Sky, MT, USA
- E. Sterzer, A. Beyer, L. Duschek, L. Nattermann, B. Ringler, B. Leube, A. Stegmüller, R. Tonner, C. von Hänisch, W. Stolz, K. Volz, Nitrogen incorporation in GaAs and (GaIn)As using di-tert-butyl-arsano-amine (DTBAA) in MOVPE, DPG Tagung (Mar 2016) Regensburg, Germany
- E. Sterzer, A. Beyer, L. Duschek, L. Nattermann, B. Ringler, B. Leube, A. Stegmüller, R. Tonner, C. von Hänisch, W. Stolz, K. Volz, Nitrogen incorporation in GaAs and (GaIn)As using di-tert-butyl-arsano-amine (DTBAA) in MOVPE, 18th International Conference on Metal-Organic Vapor Phase epitaxy (IC-MOVPE) (Jul 2016) San Diego, CA, USA
- E. Sterzer, A. Beyer, L. Duschek, L. Nattermann, B. Ringler, C. von Hänisch, W. Stolz, K. Volz, Novel N precursor di-tertiary-butyl-arsano-amine (DTBAA) for (GaIn)(NAs) and Ga(NAsSb) growth in MOVPE, DGKK Arbeitskreistreffen Epitaxie von III-V Halbleitern (Dec 2016) Duisburg, Germany
- E. Sterzer, L. Nattermann, O. Maßmeyer, K. Jandieri, S. Gupta, B. Ringler, C. von Hänisch, W. Stolz, K. Volz, Lattice Matched Ga(NAsSb) 1 eV Material Grown by MOVPE using DTBAA, 21th American Conference on Crystal Growth and Epitaxy (ACCGE-21) (Aug 2017) Santa Fe, NM, USA

Bibliography

- [1] Key World Energy Statistics. *International Energy Agency*, 2017. URL <https://www.iea.org/publications/freepublications/publication/KeyWorld2017.pdf>.
- [2] Key World Energy Statistics. *International Energy Agency*, 2010. URL https://web.archive.org/web/20120301212427/http://www.iea.org/textbase/nppdf/free/2010/key_stats_2010.pdf.
- [3] Statistical Review of World Energy. *British Petrol*, 2017. URL <https://www.bp.com/content/dam/bp/en/corporate/pdf/energy-economics/statistical-review-2017/bp-statistical-review-of-world-energy-2017-full-report.pdf>.
- [4] A. Grunwald. Thermonuclear Fusion. *Office of Technology Assessment at the German Bundestag*, 2002. URL https://www.tab-beim-bundestag.de/en/pdf/publications/summaries/TAB-Arbeitsbericht-ab075_Z.pdf.
- [5] S. Lee et al. Nuclear Fusion Energy - Mankind's Giant Step Forward. *The Second International Conference on Nuclear and Renewable Energy Resources*, 2010. URL <http://www.plasmafocus.net/IPFS/2010%20Papers/LSmankind.pdf>.
- [6] A. Marti et al. Limiting efficiencies for photovoltaic energy conversion in multigap systems. *Sol. En. Mat. Sol. Cel.*, 43:203, 1996. doi: 10.1016/0927-0248(96)00015-3.
- [7] K. Volz. MOVPE growth of dilute nitride III/V semiconductors using all liquid metalorganic precursors. *J. Cryst. Growth*, 311:2418, 2009. doi: 10.1016/j.jcrysgro.2008.09.210.
- [8] C. H. Chen et al. Use of tertiarybutylarsine for GaAs growth. *Appl. Phys. Lett.*, 50: 218, 1987. doi: 10.1063/1.97666.
- [9] R. Beccard et al. Replacement of hydrides by TBAs and TBP for the growth of various III-V materials in production scale MOVPE reactors. *J. Cryst. Growth*, 170: 97, 1997. doi: 10.1016/S0022-0248(96)00625-2.
- [10] A. C. Jones et al. Developments in metalorganic precursors for semiconductor growth from the vapour phase. *Chem. Soc. Rev.s*, 26:101, 1997. doi: 10.1039/CS9972600101.

- [11] A. Stegmüller et al. A Quantum Chemical Descriptor for CVD Precursor Design: Predicting Decomposition Rates of TBP and TBAs Isomers and Derivatives. *Chem. Vap. Deposition*, 21:161, 2015. doi: 10.1002/cvde.201504332.
- [12] C. A. Larsen et al. Decomposition Mechanisms of Tertiarybutylarsine. *J. Cryst. Growth*, 94:663, 1988. doi: 10.1016/0022-0248(89)90090-0.
- [13] Y. Yamauchi et al. Decomposition of Arsine and Trimethylarsenic on GaAs Investigated by Surface Photo-Absorption. *Jpn. J. Appl. Phys*, 29:L1353, 1990. doi: 10.1143/JJAP.29.L1353.
- [14] L. Nattermann et al. An experimental approach for real-time mass spectrometric CVD gas phase investigations. *Sci. Rep.*, 8:19–27, 2018. doi: 10.1038/s41598-017-18662-7.
- [15] W. Stolz et al. Metalorganic Vapour Phase Epitaxy (MOVPE) of III/V-Semiconductor Heterostructures using Alternative Precursor Molecules: New Developments. *Physica Scripta*, T45:186, 1992. doi: 10.1088/0031-8949/1992/T45/039.
- [16] U. W. Pohl et al. Tertiarybutylhydrazine: a new precursor for the MOVPE of Group III-nitrides. *J. Cryst. Growth*, 59:20, 1999. doi: 10.1016/S0921-5107(98)00406-1.
- [17] W. Stolz. Novel N-Precursors. *Private Communication*, April 2018.
- [18] W. Stolz et al. Alternative N-, P- and As-precursors for III/V-epitaxy. *J. Cryst. Growth*, 209:272, 2000. doi: 10.1016/S0022-0248(99)00554-0.
- [19] E. Bourret-Courchesne. Pyrolysis of dimethylhydrazine and its co-pyrolysis with triethylgallium. *J. Cryst. Growth*, 217:47, 2000. doi: 10.1016/S0022-0248(00)00398-5.
- [20] A. J. Ptak et al. Incorporation effects in MOCVD-grown (In)GaAsN using different nitrogen precursors. *J. Cryst. Growth*, 243:231, 2002. doi: 10.1016/S0022-0248(02)01412-4.
- [21] D. C. Bradley et al. Novel Precursors for the Growth of III/V Semiconductors by MOVPE. *J. Cryst. Growth*, 75:101, 1986. doi: 10.1016/0022-0248(86)90230-7.
- [22] A. Brauers et al. Alternative precursors for III-V MOVPE criteria for evaluation. *J. Cryst. Growth*, 107:281, 1991. doi: 10.1016/0022-0248(91)90472-H.
- [23] R. A. Fischer et al. Erzeugung dünner Schichten: neue Herausforderungen für die Metallorganische Chemie. *Chem. unserer Zeit*, 3:141, 1995. doi: 10.1002/ciuz.19950290306.
- [24] M. A. Malik et al. *Chemical Vapour Deposition: Precursors, Processes and Applications*. Royal Society of Chemistry, Cambridge, 1 edition, 2009. doi: 10.1039/9781847558794-00207.

- [25] M. A. Malik et al. Precursor Chemistry for Main Group Elements in Semiconducting Materials. *Chem. Rev.*, 110:4417, 2010. doi: 10.1021/cr900406f.
- [26] J. Hu et al. Direct Liquid Injection of liquid ammonia solutions in chemical vapor deposition. *US Patent*, Patent No. US5968594A, 1996.
- [27] V. K. Agarwal et al. Direct liquid injection system with on-line cleaning. *US Patent*, Patent No. US6258171B1, 1998.
- [28] M. B. Abrams et al. Direct injection chemical vapor deposition method. *Patent*, Patent No. WO2006009872, 2006.
- [29] M. Vervaele et al. Development of a new direct liquid injection system for nanoparticle deposition by chemical vapor deposition using nanoparticle solutions. *Rev. Sci. Instrum.*, 87:025101, 2016. doi: 10.1063/1.4940937.
- [30] V. Grignard. Sur quelques nouvelles combinaisons organometalliques du magnesium et leur application a des syntheses d'alcools et d'hydrocarbures. *Compt. Rend.*, 130: 1322, 1900.
- [31] O. J. Scherer et al. Elementorganische amin/imin-verbindungen VII. Überführung eines N-silylierten aminoarsins in ein N-silylarsininimin. *J. Organomet. Chem.*, 16:69, 1969. doi: 10.1016/S0022-328X(00)89756-9.
- [32] E. Sterzer et al. Efficient nitrogen incorporation in GaAs using novel metal organic As-N precursor di-tertiary-butyl-arsano-amine (DTBAA). *J. Cryst. Growth*, 439: 19–27, 2016. doi: 10.1016/2015.12.032.
- [33] B. Ringler. *Über Interpnictogenverbindungen und MOVPE-Präkursoren sowie deren Reaktionsverhalten gegenüber Trielen*. PhD thesis, 2018.
- [34] B. Ringler et al. Novel Stibano Amines: Synthesis and Reactivity towards Group 13 Element Organics. *Z. Anorg. Allg. Chem.*, 642:294, 2016. doi: 10.1002/zaac.201500787.
- [35] B. Neumueller. Synthese und Eigenschaften von iPr_2InCl , iPrInCl_2 und $(\text{iPr}_2\text{InNHtBu})_2$. *Chem. Ber.*, 122:2281, 1989.
- [36] G. G. Hoffman. Zur Kenntnis von iPr_2InBr , iPr_2InI und iPrInI_2 . *J. Organomet. Chem.*, 391:1, 1990.
- [37] C. Kittel. *Introduction to Solid States Physics*. New York, 8 edition, 2013.
- [38] N. W. Ashcroft and D. N. Mermin. *Festkörperphysik*. Oldenbourg Verlag, 4 edition, 2014.

- [39] S. Hunklinger. *Festkörperphysik*. DeGruyter, 4 edition, 2014.
- [40] P. Dirac et al. On the Theory of Quantum Mechanics. *Proceedings of the Royal Society*, 112:726, 1926. doi: 10.1098/rspa.1926.0133.
- [41] P. Dirac et al. Sulla quantizzazione del gas perfetto monoatomico. *Rendiconti Lincei*, 3:145, 1926. doi: 10.1098/rspa.1926.0133.
- [42] H. Alt et al. Experimental Evidence for a Negative-U Center in Gallium Arsenide Related to Oxygen. *Phys. Rev. Lett.*, 65:3421, 1990. doi: 10.1103/PhysRevLett.65.3421.
- [43] D. Colleoni et al. Oxygen defects in GaAs: A hybrid functional study. *Phys. Rev. B*, 93:125208, 2016. doi: 10.1103/PhysRevB.93.125208.
- [44] H. Kan et al. Influence of Oxygen in Ambient Gas on LPE GaAs Layers. *Jpn. J. Appl. Phys.*, 16:461, 1977. doi: 10.7567/JJAPS.16S1.461.
- [45] M. Skowronski et al. Location of energy levels of oxygen-vacancy complex in GaAs. *Appl. Phys. Lett.*, 57:902, 1990. doi: 10.1063/1.103399.
- [46] J. Lagowski et al. Identification of oxygen-related midgap level in GaAs. *Appl. Phys. Lett.*, 44, 1984. doi: 10.1063/1.94751.
- [47] H. Jiang et al. P-type doping of GaAs by carbon implantation. *J. Elect. Mat.*, 23: 391, 1994. doi: 10.1007/BF02671219.
- [48] B. T. Cunningham et al. Carbon diffusion in undoped, n-type, and p-type GaAs. *Appl. Phys. Lett.*, 55, 1989. doi: 10.1063/1.101822.
- [49] S. G. Ayling et al. A comparison of carbon and zinc doping in GaAs/AlGaAs lasers bandgap-tuned by impurity- free vacancy disordering. *Semicond. Sci. Technol*, 9: 2149, 1994. doi: 10.1088/0268-1242.
- [50] S. J. Pearton et al. Carbon in GaAs: Implantation and isolation characteristics. *Appl. Phys. Lett.*, 55:678, 1989. doi: 10.1063/1.101820.
- [51] S. A. Stockman et al. Characterization of heavily carbon-doped GaAs grown by metalorganic chemical vapor deposition and metalorganic molecular beam epitaxy. *J. Appl. Phys.*, 72:981, 1992. doi: 10.1063/1.351776.
- [52] J. I. Pankove et al. *Optical Processes in Semiconductors*. Dover, 1 edition, 1975.
- [53] G. B. Stringfellow et al. Novel precursors for organometallic vapor phase epitaxy. *J. Cryst. Growth*, 128:503, 1993.
- [54] H. Ibach and H. Lüth. *Festkörperphysik*. Springer, 7 edition, 2009.

- [55] C. F. Klingshirn. *Semiconductor Optics*. Springer, 4 edition, 2012.
- [56] M. Grundmann. *The Physics of Semiconductors*. Springer, 2010.
- [57] M. I. Dyakonov. *Spin Physics in Semiconductors*. Springer, 1 edition, 2008.
- [58] R. Hall et al. Coherent Light Emission From GaAs Junctions. *Phys. Rev. Lett.*, 9: 366, 1962. doi: 10.1103/PhysRevLett.9.366.
- [59] Zh. Alferov et al. Solar-energy converters based on p-n $Al_xGa_{1-x}As - GaAs$ heterojunctions. *Fiz. Tekh. Poluprovodn*, 4:2378, 1970.
- [60] K. Berthold et al. High-field transport in GaAs transistors. *Appl. Phys. Lett.*, 54: 813, 1989. doi: 10.1063/1.100855.
- [61] L. Tohme et al. Terahertz wireless communication using GaAs transistors as detectors. *Elect. Lett.*, 50:323, 2014. doi: 10.1049/el.2013.3702.
- [62] K. Nigam et al. DC characteristics and analog/RF performance of novel polarity control GaAs-Ge based tunnel field effect transistor. *Superlattices and Microstructures*, 92:224, 2016. doi: 10.1016/j.spmi.2016.01.032.
- [63] J. S. Blakemore et al. Semiconducting and other major properties of gallium arsenide. *J. Appl. Phys.*, 53:R123, 1982. doi: 10.1063/1.331665.
- [64] L. Vegard. Die konstitution der mischkristalle und die raumfüllung der atome. *Z. Phys.*, 5:17, 1921. doi: 10.1007/BF01349680.
- [65] I. Vurgaftman et al. Band parameters for III-V compound semiconductors and their alloys. *J. Appl. Phys.*, 89:5815, 2001. doi: 10.1063/1.1368156.
- [66] Ioffe Institute. Semiconductor properties, February 2018. URL <http://www.ioffe.ru/SVA/NSM/Semicond>.
- [67] M. Kozhevnikov et al. Evolution of $GaAs_{1-x}N_x$ conduction states and giant $Au/GaAs_{1-x}N_x$ Schottky barrier reduction studied by ballistic electron emission spectroscopy. *Phys. Rev. B*, 61:R7861, 2000. doi: 10.1103/PhysRevB.61.R7861.
- [68] T. Makimoto et al. Excitonic luminescence and absorption in dilute $GaAs_{1-x}N_x$ alloy ($x < 0.3\%$). *Appl. Phys. Lett.*, 70:2984, 1997. doi: 10.1063/1.118764.
- [69] A. Ougazzaden et al. Metal organic vapor phase epitaxy growth of GaAsN on GaAs using dimethylhydrazine and tertiarybutylarsine. *Appl. Phys. Lett.*, 70:2861, 1997. doi: 10.1063/1.119025.
- [70] J. Sik et al. Near-band-gap optical functions spectra and band-gap energies of GaNAs/GaAs superlattice heterostructures measured by spectroscopic ellipsometry. *Appl. Phys. Lett.*, 76+:2859, 2000. doi: 10.1063/1.126497.

- [71] G. Pozina et al. Properties of molecular-beam epitaxy-grown GaNAs from optical spectroscopy. *J. Appl. Phys.*, 84:3830, 1998. doi: 10.1063/1.368562.
- [72] M. Kondow et al. Gas-Source Molecular Beam Epitaxy of $\text{GaN}_x\text{As}_{1-x}$ Using a N Radical as the N Source. *Jpn. J. Appl. Phys.*, 33:L1056, 1994. doi: 10.1143/JJAP.33.L1056.
- [73] S. Sakai et al. Band Gap Energy and Band Lineup of III-V Alloy Semiconductors Incorporating Nitrogen and Boron. *Jpn. J. Appl. Phys.*, 32:4413, 1993. doi: 10.1143/JJAP.32.4413.
- [74] W. Shan et al. Band anticrossing in GaInNAs alloys. *Phys. Rev. Lett.*, 82:1221, 1999. doi: 10.1103/PhysRevLett.82.1221.
- [75] M. Seifika et al. Analysis of band-anticrossing model in GaNAs near localised states. *Phys. Status Solidi B*, 248:1176, 2011. doi: 10.1002/pssb.201000784.
- [76] W. Shan et al. Band anticrossing in III-N-V alloys. *Phys. Status Solidi*, 223:75, 2001. doi: 10.1002/1521-3951(200101)223:1<75::AID-PSSB75>3.0.CO;2-1.
- [77] W. Shan et al. Band anticrossing in highly mismatched III V semiconductor alloys. *Semicond. Sci. Technol.*, 17:860, 2002. doi: 10.1088/0268-1242/17/8/315.
- [78] W. Shan et al. Band anticrossing in dilute nitrides. *J. Phys. Condens. Matter*, 16:S3355, 2004. doi: 10.1088/0953-8984/16/31/024.
- [79] J. Shao et al. Evolution of valence-band alignment with nitrogen content in GaNAs/GaAs single quantum wells. *Appl. Phys. Lett.*, 93:031904, 2008. doi: 10.1063/1.2958232.
- [80] S. Wei et al. Giant and Composition-Dependent Optical Bowing Coefficient in GaAsN Alloys. *Phys. Rev. Lett.*, 76:664, 1996. doi: 10.1103/PhysRevLett.76.664.
- [81] J. Neugebauer et al. Electronic structure and phase stability of $\text{GaAs}_{1-x}\text{N}_x$ alloys. *Phys. Rev. B*, 51:10568, 1995. doi: 10.1103/PhysRevB.51.10568.
- [82] A. Lindsay et al. Theory of enhanced bandgap non-parabolicity in $\text{GaN}_x\text{As}_{1-x}$ and related alloys. *Solid State Commun.*, 112:443, 1999. doi: 10.1016/S0038-1098(99)00361-0.
- [83] T. Mattila et al. Localization and anticrossing of electron levels in $\text{GaAs}_{1-x}\text{N}_x$ alloys. *Phys. Rev. B*, 60:R11245, 1999. doi: 10.1103/PhysRevB.60.R11245.
- [84] L. Bellaiche et al. Band gaps of GaPN and GaAsN alloys. *Appl. Phys. Lett.*, 70:3558, 1997. doi: 10.1063/1.119232.

- [85] L. Bellaiche et al. Localization and percolation in semiconductor alloys: GaAsN vs GaAsP. *Phys. Rev. B*, 54:17568, 1996. doi: 10.1103/PhysRevB.54.17568.
- [86] A. Rubio et al. Quasiparticle excitations in $\text{GaAs}_{1-x}\text{N}_x$ and $\text{AlAs}_{1-x}\text{N}_x$ ordered alloys. *Phys. Rev. B*, 51:4343, 1995. doi: 10.1103/PhysRevB.51.4343.
- [87] D. J. Welford et al. The Nitrogen Isoelectronic Trap in GaAs. *Proceedings of the 17th International Conference on the Physics of Semiconductors*, page 627, 1984. doi: 10.1007/978-1-4615-7682-2_138.
- [88] R. Kudrawiec et al. Alloying of $\text{GaN}_x\text{As}_{1-x}$ with $\text{InN}_x\text{As}_{1-x}$: A simple formula for the band gap parametrization of $\text{Ga}_{1-y}\text{In}_y\text{N}_x\text{As}_{1-x}$ alloys. *J. Appl. Phys.*, 101: 023522, 2007. doi: 10.1063/1.2424528.
- [89] Y. Zhang et al. Formation of an impurity band and its quantum confinement in heavily doped GaAs:N. *Phys. Rev. B*, 61:7479, 2000. doi: 10.1103/PhysRevB.61.7479.
- [90] P. N. Hai et al. Direct determination of electron effective mass in GaNAs/GaAs quantum wells. *Appl. Phys. Lett.* 77, 77:1843, 2000. doi: 10.1063/1.1311324.
- [91] M. Hetterich et al. Influence of indium on the electronic states in GaInNAs/GaAs quantum well structures. *J. Appl. Phys.*, 94:1810, 2003. doi: 10.1063/1.1591078.
- [92] M. Kondow et al. GaInNAs: A Novel Material for Long-Wavelength-Range Laser Diodes with Excellent High-Temperature Performance. *Jpn. J. Appl. Phys.*, 35:1273, 1996. doi: 10.1143/JJAP.35.1273.
- [93] S. R. Kurtz et al. Projected performance of three- and four-junction devices using GaAs and GaInP. *Proc. 26th IEEE Photovoltaic Specialists Conf., IEEE, New York*, page 875, 1999. doi: 10.1109/PVSC.1997.654226.
- [94] S. Sato et al. 1.3 μm continuous-wave operation of GaInNAs lasers grown by metal organic chemical vapour deposition. *Electron. Lett.*, 35:1251, 1999. doi: 10.1049/el:19990858.
- [95] D. J. Friedman et al. 1-eV solar cells with GaInNAs active layer. *J. Cryst. Growth*, 195:409, 1998. doi: 10.1016/S0022-0248(98)00561-2.
- [96] J. F. Geisz et al. Photocurrent of 1 eV GaInNAs lattice-matched to GaAs. *J. Cryst. Growth*, 195:401, 1998. doi: 10.1016/S0022-0248(98)00563-6.
- [97] S. Kurtz et al. InGaAsN solar cells with 1.0 eV band gap, lattice matched to GaAs. *Phys. Lett.*, 74:729, 1999. doi: 10.1063/1.123105.
- [98] F. Höhnsdorf et al. Reduced threshold current densities of (GaIn)(NAs)/GaAs single quantum well lasers for emission wavelengths in the range 1.28-1.38 μm . *Electron. Lett.*, 35:571, 1999. doi: 10.1049/el:19990421.

- [99] M. Kawaguchi et al. Lasing characteristics of low-threshold GaInNAs lasers grown by metalorganic chemical vapor deposition. *Jpn. J. Appl. Phys.*, 40:L744, 2001. doi: 10.1143/JJAP.40.L744.
- [100] K. Volz et al. Specific structural and compositional properties of (GaIn)(NAs) and their influence on optoelectronic device performance. *J. Cryst. Growth*, 272:739, 2004. doi: 10.1016/j.jcrysgro.2004.09.012.
- [101] V. Polojvi et al. Influence of As/group-III flux ratio on defects formation and photovoltaic performance of GaInNAs solar cells. *Sol. Energy Mater. Sol. Cells*, 149: 213, 2016. doi: 10.1016/j.solmat.2016.01.024.
- [102] A. J. Ptak et al. A comparison of MBE- and MOCVD-grown GaInNAs. *J. Cryst. Growth*, 251:392, 2003. doi: 10.1016/S0022-0248(02)02201-7.
- [103] A. Tukiainen et al. High-efficiency GaInP/GaAs/GaInNAs solar cells grown by combined MBE-MOCVD technique. *Progress in Photovoltaics*, 24:914, 2016. doi: 10.1002/pip.2784.
- [104] D. Jackrel et al. MBE grown gainnas solar cells for multijunction applications. *Conference Record of the IEEE Photovoltaic Specialists Conference*, page 845, 2005. URL <https://web.stanford.edu/group/OTL/lagan/07169/mjcs-PVSC-05.pdf>.
- [105] A. J. Ptak et al. Enhanced-Depletion-Width GaInNAs Solar Cells Grown by Molecular-Beam Epitaxy. *DOE Solar Energy Technologies*, 2005. URL <https://www.nrel.gov/docs/fy05osti/37025.pdf>.
- [106] H. P. Xin et al. Observation of quantum dot-like behavior of GaInNAs in GaInNAs/GaAs quantum wells. *Appl. Phys. Lett.*, 74:2337, 1999. doi: 10.1063/1.123843.
- [107] M. A. Pinault et al. Influence of alloy stability on the photoluminescence properties of GaAsN/GaAs quantum wells grown by molecular beam epitaxy. *Appl. Phys. Lett.*, 79:3404, 2001. doi: 10.1063/1.1418263.
- [108] S. Gwo et al. Atomic-scale nature of the (3x3)-ordered GaAs(001):N surface prepared by plasma-assisted molecular-beam epitaxy. *Appl. Phys. Lett.*, 71:362, 1997. doi: 10.1063/1.119538.
- [109] N. Q. Thinh et al. Formation of nonradiative defects in molecular beam epitaxial GaN_xAs_{1-x} studied by optically detected magnetic resonance. *Appl. Phys. Lett.*, 79:3089, 2001. doi: 10.1063/1.1416155.
- [110] W. Li et al. Origin of improved luminescence efficiency after annealing of Ga(In)NAs materials grown by molecular-beam epitaxy. *Appl. Phys. Lett.*, 79:1094, 2001. doi: 10.1063/1.1396316.

- [111] K. M. Kim et al. Thermal annealing effect on nitrogen related defects of GaInNAs semiconductors. *Journal of Ceramic Processing Research*, 16:45, 2015. URL http://jcpr.kbs-lab.co.kr/file/JCPR_vol.16_2015/JCPR16-1/_092013-079_45-48.pdf.
- [112] S. B. Zhang et al. Nitrogen Solubility and Induced Defect Complexes in Epitaxial GaAs:N. *Phys. Rev. Lett.*, 86:1789. doi: 10.1103/PhysRevLett.86.1789.
- [113] P. Carrier et al. Evolution of structural properties and formation of N-N split interstitials in GaAs_{1-x}N_x alloys. *Phys. Rev. B*, 71:165212, 2005. doi: 10.1103/PhysRevB.71.165212.
- [114] X. Liu et al. Nitrogen pair luminescence in GaAs. *Appl. Phys. Lett.*, 56:1451, 1990. doi: 10.1063/1.102495.
- [115] A. Lindsay et al. Unification of the Band Anticrossing and Cluster-State Models of Dilute Nitride Semiconductor Alloys. *Phys. Rev. Lett.*, 93:196402, 2004. doi: 10.1103/PhysRevLett.93.196402.
- [116] F. Natku et al. Effect of thermal annealing and nitrogen composition on quantum transport in GaInNAs alloy based modulation doped quantum well structures. *J. Alloys and Compounds*, 695:404, 2017. doi: 10.1016/j.jallcom.2016.11.101.
- [117] M. Kondow et al. Annealing in GaInNAs system. *J. Phys.: Condens. Matter*, 16:S3229, 2004. doi: 10.1088/0953-8984/16/31/017.
- [118] V. Liverini et al. Effects of rapid thermal annealing conditions on GaInNAs band gap blueshift and photoluminescence intensity. *J. Appl. Phys.*, 99:113103, 2006. doi: 10.1063/1.2200877.
- [119] A. Khan et al. Correlation of nitrogen related traps in InGaAsN with solar cell properties. *Appl. Phys. Lett.*, 90:243509, 2007. doi: 10.1063/1.2747664.
- [120] W. G. Schmidt et al. Antimony-stabilized GaAs(001)(2x4) reconstructions. *Phys. Rev. B*, 55:13051, 1997. doi: 10.1103/PhysRevB.55.13051.
- [121] W. K. Cheah et al. Low antimony-doped GaN_xAs_{1-x} on GaAs grown by solid-source molecular-beam epitaxy. *J. Cryst. Growth*, 254:305, 2003. doi: 10.1016/S0022-0248(03)01171-0.
- [122] C. M. Fetzer et al. The use of a surfactant (Sb) to induce triple period ordering in GaInP. *Appl. Phys. Lett.*, 76:1440, 2000. doi: 10.1063/1.126057.
- [123] S. Oberhoff. Morphologie innerer Grenzflächen in verdünnt stickstoffhaltigen III/V-Materialsystemen, PhD thesis. *Philipps-Universität Marburg*, (2007).

- [124] M. Copel et al. Surfactants in epitaxial growth. *Phys. Rev. Lett.*, 63:632, 1989. doi: 10.1103/PhysRevLett.63.632.
- [125] J. Massies et al. Surfactant effect on the surface diffusion length in epitaxial growth. *Phys. Rev. B*, 48:8502, 1993. doi: 10.1103/PhysRevB.48.8502.
- [126] B. Voigtländer et al. Modification of growth kinetics in surfactant-mediated epitaxy. *Phys. Rev. B*, 51:7583, 1995. doi: 10.1103/PhysRevB.51.7583.
- [127] K. Schroeder et al. Reexchange controlled diffusion in surfactant-mediated epitaxial growth: Si on As-terminated Si(111). *Phys. Rev. Lett.*, 80:2873, 1998. doi: 10.1103/PhysRevLett.80.2873.
- [128] D. Kandel et al. Surfactant mediated crystal growth of semiconductors. *Phys. Rev. Lett.*, 75:2742, 1995. doi: 10.1103/PhysRevLett.75.2742.
- [129] C. W. Oh et al. Kinetic role of a surfactant in island formation. *Phys. Rev. Lett.*, 76:776, 1996. doi: 10.1103/PhysRevLett.76.776.
- [130] J. K. Shurtleff et al. Surfactant effects on doping of GaAs grown by organometallic vapor phase epitaxy. *Appl. Phys. Lett.*, 78:3038, 2001. doi: 10.1063/1.1371790.
- [131] R. T. Lee et al. Time dependent surfactant effects on growth of GaInP heterostructures by organometallic vapor phase epitaxy. *J. Cryst. Growth*, 234:327, 2002. doi: 10.1016/S0022-0248(01)01713-4.
- [132] G. B. Stringfellow et al. Surface processes in OMVPE - the frontiers. *J. Cryst. Growth*, 221:1, 2000. doi: 10.1016/S0022-0248(00)00640-0.
- [133] R. R. Wixom et al. Theory of Sb-induced triple-period ordering in GaInP. *Phys. Rev. B*, 64:201322, 2001. doi: 10.1103/PhysRevB.64.201322.
- [134] F. Dimroth et al. Influence of Sb, Bi, Tl, and B on the incorporation of N in GaAs. *J. Appl. Phys.*, 91:3687, 2002. doi: 10.1063/1.1450053.
- [135] T. Sato et al. Sb surfactant-mediated growth of strained InGaAs multiple-quantum wells by metalorganic vapor phase epitaxy at low growth temperatures. *J. Cryst. Growth*, 312:359, 210. doi: 10.1016/j.jcrysgro.2009.11.003.
- [136] T. Kageyama et al. Sb surfactant effect on GaInAs/GaAs highly strained quantum well lasers emitting at 1200 nm range grown by molecular beam epitaxy. *J. Appl. Phys.*, 96:44, 2004. doi: 10.1063/1.1760841.
- [137] J. C. Harmand et al. GaInAs/GaAs quantum-well growth assisted by Sb surfactant: Toward 1.3 μ m emission. *Appl. Phys. Lett.*, 84:3981, 2004. doi: 10.1063/1.1751221.

- [138] K. G. Sadasivam et al. Antimony Surfactant Effect on Green Emission InGaN/GaN Multi Quantum Wells Grown by MOCVD. *J. Nanosc. Nanotech.*, 11:1787–1790, 2011. doi: 10.1166/jnn.2011.3387.
- [139] W. K. Cheah et al. Surfactant and impurity properties of antimony on GaAs and GaAs_{1-x}N_x on GaAs [100] by solid source molecular beam epitaxy. *Thin Solid Films*, 488:56–61, 2005. doi: 10.1016/j.tsf.2005.04.040.
- [140] H. B. Yuen et al. The role of antimony on properties of widely varying GaInNAsSb compositions. *J. Appl. Phys.*, 99:093504, 2006. doi: 10.1063/1.2191745.
- [141] A. A. Khandekar et al. Effects of Ga- and Sb-precursor chemistry on the alloy composition in pseudomorphically strained GaAs_{1-y}Sb_y films grown via metalorganic vapor phase epitaxy. *J. Cryst. Growth*, 303:456–465, 2007. doi: 10.1016/j.jcrysgro.2006.12.034.
- [142] A. D. Howard et al. Effects of surfactants Sb and Bi on the incorporation of zinc and carbon in III/V materials grown by organometallic vapor-phase epitaxy. *J. Appl. Phys.*, 100:044904, 2006. doi: 10.1063/1.2227707.
- [143] G. B. Stringfellow et al. Methods using surfactants to control unintentional dopant in Semiconductors. *US Patent*, 2006. doi: PatentNo.US20110215275.
- [144] R. Kudrawiec et al. Band-gap discontinuity in GaN_{0.02}As_{0.87}Sb_{0.11}/GaAs single-quantum wells investigated by photorefectance spectroscopy. *Appl. Phys. Lett.*, 86: 141908, 2005. doi: 10.1063/1.1897849.
- [145] R. Kudrawiec et al. Interband transitions in GaN_{0.02}As_{0.98-x}Sb_x/GaAs single quantum wells studied by contactless electroreflectance spectroscopy. *Phys. Rev. B*, 73:245413, 2006. doi: 10.1103/PhysRevB.73.245413.
- [146] A. Moto et al. Hydrogen and carbon incorporation in GaInNAs. *J. Cryst. Growth*, 221:485, 2000. doi: 10.1016/S0022-0248(00)00749-1.
- [147] R. Jones-Albertus et al. Using Dilute Nitrides to Achieve Record Solar Cell Efficiencies. *MRS Proceedings*, 1538:161–166, 2013. doi: 10.1557/opl.2013.656.
- [148] N. Miyashita et al. Effect of antimony on uniform incorporation of nitrogen atoms in GaInNAs films for solar cell application. *Solar Energy Materials and Solar Cells*, 111:127, 2013. doi: 10.1016/j.solmat.2012.12.036.
- [149] N. Miyashita et al. Generation and collection of photocarriers in dilute nitride GaInNAsSb solar cells. *Prog. Photovolt: Res. Appl.*, 24:28, 2016. doi: 10.1002/pip.2641.

- [150] A. Aho et al. Performance assessment of multijunction solar cells incorporating GaInNAsSb. *Nanoscale Research Letters*, 9:1, 2014. doi: 10.1186/1556-276X-9-61.
- [151] A. Maros et al. 1-eV GaNAsSb for multijunction solar cells. *IEEE 43rd Photovoltaic Specialists Conference (PVSC)*, page 2306, 2016. doi: 10.1109/PVSC.2016.7750048.
- [152] V. Braza et al. Sb and N Incorporation Interplay in GaAsSbN/GaAs Epilayers near Lattice-Matching Condition for 1.0-1.16-eV. *Photonic Applications. Nanoscale Research Letters*, 12:356, 2017. doi: 10.1186/s11671-017-2129-2.
- [153] T. Kim et al. Impact of Sb Incorporation on MOVPE-Grown InGaAs(Sb)N Films for Solar Cell Application. *IEEE J. Phot.*, 6:1673–1677, 2016. doi: 10.1109/JPHOTOV.2016.2598262.
- [154] T. W. Kim et al. Impact of growth temperature and substrate orientation on dilute-nitride-antimonide materials grown by MOVPE for multi-junction solar cell application. *J. Cryst. Growth*, 405:87, 2016. doi: 10.1109/JPHOTOV.2016.2598262.
- [155] A. Luque et al. *Handbook of Photovoltaic Science and Engineering*. Wiley, 1 edition, 2003.
- [156] H. G. Wagemann et al. *Photovoltaik*. Vieweg+Teubner, 2 edition, 2010.
- [157] W. Shockley et al. Detailed Balance Limit of Efficiency of pn Junction Solar Cells. *J. Appl. Phys.*, 32:510, 1961. doi: 10.1063/1.1736034.
- [158] S. M. Sze et al. *Physics of Semiconductor Devices*. Wiley, 1981.
- [159] NREL. Efficiency Chart. 2018. doi: <https://www.nrel.gov/pv/assets/images/efficiency-chart.png>.
- [160] J. B. Lasky et al. Wafer bonding for silicon-on-insulator technologies. *Appl. Phys. Lett.*, 48:78, 1986. doi: 10.1063/1.96768.
- [161] M. Niemeyer et al. Next Generation of Wafer-Bonded Multi-Junction Solar Cells. *29th European Photovoltaic Solar Energy Conference and Exhibition*, page 1991, 2014. doi: 10.4229/EUPVSEC20142014-4BO.10.2.
- [162] F. Dimroth et al. Wafer bonded four-junction GaInP/GaAs//GaInAsP/GaInAs concentrator solar cells with 44.7 % efficiency. *Progress in Photovoltaics: Research and Applications*, 22:277, 2014. doi: 10.1002/pip.2475.
- [163] T. N. D. Tibbits et al. New Efficiency Frontiers with Wafer-Bonded Multi-Junction Solar Cells. *29th European Photovoltaic Solar Energy Conference and Exhibition*, page 1975, 2014. doi: 10.4229/EUPVSEC20142014-4CP.2.1.

- [164] L. Vauche et al. Development of III-V on Si Multijunction Photovoltaics by Wafer Bonding. *33rd European Photovoltaic Solar Energy Conference and Exhibition*, page 1228, 2017. doi: 10.4229/EUPVSEC20172017-4DO.4.3.
- [165] M. A. Green et al. Solar cell efficiency tables (version 51). *Prog. Photovolt. Res. Appl.*, 26:3, 2018. doi: 10.1002/pip.2978.
- [166] R. King et al. Band-gap- engineered architectures for high-efficiency multijunction concentrator solar cells. *Proceedings of the 24th European Photovoltaic Solar Energy Conference and Exhibition*, page 55, 2009. doi: 10.4229/24thEUPVSEC2009-1AO.5.2.
- [167] J. Geisz et al. 1-eV GaInNAs solar cells for ultrahigh-frequency multijunction devices. *2nd World Conference and Exhibition on Photovoltaic Solar Energy Conversion*, 1998. doi: <https://www.osti.gov/biblio/305644>.
- [168] NREL Demonstrates 45.7% Efficiency for Concentrator Solar Cell. *News Release NR-4514*, 2014. doi: <https://www.nrel.gov/news/press/2014/15436.html>.
- [169] R. M. France et al. Quadruple- Junction Inverted Metamorphic Concentrator Devices. *IEEE Journal of Photovoltaics*, 5:432, 2015. doi: 10.1109/JPHOTOV.2014.2364132.
- [170] T. J. Mountziaris et al. Gas-Phase and Surface Reaction Mechanisms in MOCVD of GaAs with Trimethyl-Gallium and Arsine. *J. Electrochem. Soc.*, 138:2426, 1991. doi: 10.1149/1.2085990.
- [171] A. Stegmüller et al. From Molecules to Thin Films: GaP Nucleation on Si Substrates. *High Performance Computing in Science and Engineering*, page 185, 2013. doi: 10.1007/978-3-319-02165-2_14.
- [172] A. Stegmüller et al. GaP/Si: Studying Semiconductor Growth Characteristics with Realistic Quantum-Chemical Models. *High Performance Computing in Science and Engineering*, page 205, 2014. doi: 10.1007/978-3-319-10810-0_15.
- [173] L. Pecher et al. Modeling the Complex Adsorption Dynamics of Large Organic Molecules: Cyclooctyne on Si(001). *J. Phys. Chem. C*, 121:26840, 2017. doi: 10.1021/acs.jpcc.7b09148.
- [174] W. Hagen et al. Tetragonal distortion in heteroepitaxial layers: Ge on GaAs. *J. Cryst. Growth*, 43:739, 1978. doi: 10.1016/0022-0248(78)90154-9.
- [175] R. N. Hall et al. Electron-Hole Recombination in Germanium. *Phys. Rev.*, 87:387, 1952. doi: 10.1103/PhysRev.87.387.
- [176] W. Shockley et al. Statistics of the Recombinations of Holes and Electrons. *Phys. Rev.*, 57:835, 1952. doi: 10.1103/PhysRev.87.835.

- [177] R. Fehse et al. Evidence for large monomolecular recombination contribution to threshold current in 1.3 μm GaInNAs semiconductor lasers. *Electron. Lett.*, 37:1518, 2001. doi: 10.1049/el:20011033.
- [178] I. A. Buyanova et al. Hydrogen-induced improvements in optical quality of GaNAs alloys. *Appl. Phys. Lett.*, 82:3662, 2003. doi: 10.1063/1.1578513.
- [179] D. Sentosa et al. Thermal annealing effect on GaNAs epilayers with different nitrogen compositions grown by MOCVD. *J. Cryst. Growth*, 307:229, 2007. doi: 10.1016/j.jcrysgro.2007.06.018.
- [180] I. A. Buyanova et al. Hydrogen passivation of nitrogen in GaNAs and GaNP alloys: How many H atoms are required for each N atom? *Appl. Phys. Lett.*, 90:021920, 2007. doi: 10.1063/1.2425006.
- [181] D. Dagnelund et al. Effects of hydrogenation on non-radiative defects in GaNP and GaNAs alloys: An optically detected magnetic resonance study. *J. Appl. Phys.*, 111: 023501, Dagnelund. doi: 10.1063/1.3676576.
- [182] P. J. Klar et al. (Ga, In)(N, As)-fine structure of the band gap due to nearest-neighbor configurations of the isovalent nitrogen. *Phys. Rev. B*, 64:121203(R), 2001. doi: 10.1103/PhysRevB.64.121203.
- [183] H. Zhao et al. Post-growth and in situ annealing on GaInNAs(Sb) and their application in 1.55 μm lasers. *Semicond. Sci. Technol.*, 21:279, 2006. doi: 10.1088/0268-1242/21/3/011.
- [184] L. J. van der Pauw. A method of measuring the resistivity and Hall coefficient on lamellae of arbitrary shape. *Philips Technical Review*, 20:220, 1958. URL <http://electron.mit.edu/~gsteele/vanderpauw/vanderpauw.pdf>.
- [185] J. Hilibrand et al. Determination of the Impurity Distribution in Junction Diodes From Capacitance-Voltage Measurements. *RCA Review*, 21:245, 1960. URL <http://garfield.library.upenn.edu/classics1983/A1983QT44200001.pdf>.
- [186] A. C. Diebold et al. *Handbook of Silicon Semiconductor Metrology*. CRC press, 1 edition, 2001.
- [187] U. Hashima et al. Shallow junction determination and boron profiling using electrochemical capacitance-voltage (ECV). *Jurnal Fizika Malaysia*, 30:37, 2009. URL <http://ifm.org.my/sites/default/files/publications/%5B037-041%5D-hashim.pdf>.
- [188] E. N. Kaufmann et al. *Characterisation of Materials*. John Wiley & Sons, 2 edition, 2012.

- [189] M. Sterzer. Wachstum und Charakterisierung verdünnt N-haltiger Schichten mittels MOVPE mit alternativen Präkursoren. *Master's thesis, Philipps-Universität Marburg*, 2014.
- [190] O. Massmeyer. Real time mass spectrometric MOVPE gas phase investigations. *19th International Conference on MOVPE*, 2018.
- [191] O. Massmeyer et al. Influence of UDMHy on GaAs(001) Surface Reconstruction Before and During Growth of Ga(NAs) by MOVPE. *Appl. Surf. Scie.*, Submitted, 2018.
- [192] E. Sterzer et al. (GaIn)(NAs) growth using di-tertiary-butyl-arsano-amine (DTBAA). *J. Cryst. Growth*, 467:132–136, 2017. doi: 10.1016/2017.01.014.
- [193] P. Strässer. Einfluss von Rapid Thermal Annealing auf verdünnt stickstoffhaltige III/V-Materialsysteme für die Anwendung in Multi-Junction Solarzellen. *Master's thesis, Philipps-Universität Marburg*, 2015.
- [194] O. Massmeyer. Einfluss von Antimon und thermischem Ausheizen auf die elektrischen Eigenschaften von (GaIn)(NAs) - Solarzellenmaterial. *Bachelor's thesis, Philipps-Universität Marburg*, 2015.
- [195] M. Longo et al. Controlled intrinsic carbon doping in MOVPE-grown GaAs layers by using TMGa and TBAs. *J. Cryst. Growth*, 248:119, 2003. doi: 10.1016/S0022-0248(02)01846-8.
- [196] S. Tanaka et al. Spatial distribution of deep level traps in GaNAs crystals. *J. Cryst. Growth*, 221:467, 2000. doi: 10.1016/S0022-0248(00)00746-6.
- [197] S. J. C. Irvine et al. A new N-type doping precursor for MOCVD-IMP growth of detector quality MCT. *J. Electr. Mat.*, 22:859, 1992. doi: 10.1007/BF02817498.
- [198] G. B. Stringfellow. *Organometallic vapor-phase epitaxy: theory and practice*. Academic Press, 2 edition, 1998.
- [199] J. Ohlmann. TIPIn incorporation behavior. *Private Communication*, April 2018.
- [200] M. Kapitein. TIPIn incorporation behavior. *Private Communication*, Mai 2018.
- [201] V. Swaminathan et al. Defects in GaAs. *Bull. Mater. Sci.*, 4:403, 1982. URL <https://link.springer.com/content/pdf/10.10072FBF02748739.pdf>.
- [202] V. Bondarenko et al. Positron annihilation study of equilibrium point defects in GaAs. *Martin-Luther-Universität Halle-Wittenberg*, 2003. URL <https://sundoc.bibliothek.uni-halle.de/diss-online/04/04H067/prom.pdf>.

-
- [203] J. Mimila-Arroyo et al. Carbon site switching in carbon doped GaAs, its dependence on carbon concentration. *Superficies y Vacío*, 16:37, 2003. URL http://www.fis.cinvestav.mx/~smcsyv/supyvac/16_1/SV1613703.PDF.
- [204] J. W. Huang et al. Compensation of shallow impurities in oxygen-doped metalorganic vapor phase epitaxy grown GaAs. *J. Appl. Phys.*, 80:6819, 1996. doi: 10.1063/1.363811.
- [205] E. Sterzer et al. 1 eV Ga(NAsSb) grown by MOVPE using di-tertiary-butyl-arsanoamine (DTBAA). *J. Cryst. Growth*, 2018. doi: 10.1063/1.5034083.
- [206] G. B. Stringfellow et al. OMVPE growth of GaAs_{1-x}Sb_x: solid composition. *J. Cryst. Growth*, 64:413, 1983. doi: 10.1016/0022-0248(83)90156-2.

List of abbreviations

AFM	atomic force microscope
As	arsenic
AsCl₃	arsenic trichloride
AsH₃	arsine
BAC	band anti crossing
C	carbon
Et₂O	diethyl ether
DTBAA	di-tertiary-butyl arsano amine
DTBSbTBA	di-tertiary-butyl antimony tertiary-butyl amine
ECV	electrochemical capacitance voltage
EQE	external quantum efficiency
fcc	face centered cubic
FF	fill factor
FWHM	full width of half maximum
Ga	gallium
GaAs	gallium arsenide
Ga(AsSb)	gallium arsenide antimonide
Ga(NAs)	gallium nitride arsenide
(GaIn)(NAs)	gallium indium nitride arsenide
(GaIn)As	gallium indium arsenide
(GaIn)(NAs):Sb	gallium indium nitride arsenide: antimony

(GaIn)(NAsSb)	gallium indium nitride arsenide antimonide
(GaIn)P	gallium indium phosphide
Ga(NAsSb)	gallium nitride arsenide antimonide
GaN	gallium nitride
GaSb	gallium antimonide
Ge	germanium
GaP	gallium phosphide
H	hydrogen
\hbar	reduced planck constant $6.582119514(40) \times 10^{-16} \text{ eV}\cdot\text{s}$
HR-XRD	high resolution X-ray diffraction
In	indium
InAs	indium arsenide
InI₃	indium(III) iodide
<i>i</i>PrCl	iso-propyl chloride
<i>i</i>PrMgCl	iso-propyl magnesium chloride
IQE	internal quantum efficiency
k	wave vector
I_{SC}	short circuit current
J_{SC}	short circuit current density
LASER	light amplification by the stimulated emission of radiation
LED	light emitting diode
LiCl	lithium chloride
m[*]	effective mass normed to m_0
MBE	molecular beam epitaxy
MFC	mass flow controller
Mg	magnesium

MgCl₂	magnesium chloride
MgClI	magnesium chloride iodide
MO	metal organic
MOVPE	metalorganic vapor phase epitaxy
MPP	maximum power point
N	nitrogen
<i>n</i>Butane	normal-butane
<i>n</i>Pentane	normal-pentane
<i>n</i>BuLi	normal-butyl lithium
NH₃	ammonia
NH₄Cl	ammonium chloride
Ni	nickel
O	oxygen
PC	pressure controller
PL	photoluminescence
QW	quantum well
RMS	root mean square
RTA	rapid thermal annealer
Sb	antimony
Si	silicon
SIMS	secondary ion mass spectrometry
TBA_s	tertiary-butyl arsine
<i>t</i>Bu	tertiary-butyl
<i>t</i>Bu₂AsCl	di-tertiary-butyl arsano chloride
<i>t</i>BuCl	tertiary-butyl chloride
<i>t</i>BuMgCl	tertiary-butyl magnesium chloride

<i>t</i>BuNH₂	tertiary-butyl amine
<i>t</i>BuNLi	lithium tertiary-butyl amide
<i>t</i>Bu₂SbCl	di-tertiary-butyl antimony chloride
TMGa	tri-methyl gallium
TEGa	tri-ethyl gallium
TESb	tri-ethyl antimony
TIPIn	tri-iso-propyl indium
TMIn	tri-methyl indium
TMSb	tri-methyl antimony
UDMH_y	1,1-dimethylhydrazine
V_{OC}	open circuit voltage
W_{OC}	$E_{gap}/q - V_{OC}$